Rotating Stall and Passive Flow Control on Blade Profiles and in Centrifugal Compressors

Andrew P. Heffron

Thesis submitted for the Degree of Doctor of Philosophy at University of London

School of Engineering and Materials Science

Queen Mary, University of London

28/04/2017

Details of Presentations and Publications

Journal Papers

[1] **Heffron, A.P.**, Avital, E., and Williams, J.J., "Numerical and Experimental Study of Microvortex Generators," *Journal of Aircraft*, under review.

Conference Papers

[1] **Heffron, A.P.**, Avital, E., and Williams, J.J., "Flow Separation and Passive Flow Control on E387 Airfoil," *54th AIAA Aerospace Sciences Meeting*, San Diego, CA, 2016.

Presentations

[1] **Heffron, A.P.**, Avital, E., and Williams, J.J.R., "Modelling a Low-Speed Centrifugal Compressor with *Code_Saturne*," Presented at *Code_Saturne* User Meeting, Poster Session, Chatou, France, 2015.

[2] **Heffron, A.P.**, Avital, E., and Williams, J.J., "Large Eddy Simulations of Flow Separation and Flow Control on E387 Airfoil," *UKTC Annual Review*, Poster Session, Southampton, UK, September 2015.

[3] **Heffron, A.P.**, Avital, E., and Williams, J.J.R., "Study of Rotating Stall in Centrifugal Compressors," Presented at *Code_Saturne* User Meeting, Chatou, France, 2016.

[4] **Heffron, A.P.**, Avital, E., and Williams, J.J., "Behavior of Microvortex Generators in Turbulent Flows," *UKTC Annual Review*, Poster Session, Cambridge, UK, September 2016.

[5] **Heffron, A.P.**, Avital, E., and Williams, J.J., "Modelling High-Speed Compressors with *Code_Saturne*," Presented at *Code_Saturne* User Meeting, Poster Session, Paris-Saclay, France, 2017.

Abstract

The operating range and efficiency of a centrifugal compressor is limited by the development of rotating stall and surge at low mass flow rates. To extend the operating range of a compressor, flow control in the compressor can be used to suppress secondary flow structures that lead to rotating stall. The presented work seeks to use the novel idea of placing passive vortex generators (VG) upstream of the impeller to suppress rotating stall, while also developing new concepts and optimization of microvortex generators (MVG).

To accomplish this goal, a new SIMPLE-type algorithm for compressible flows was written in *Code_Saturne* along with a 2nd-order MUSCL scheme for convective terms and an AUSM^{+}-up scheme for mass flux computation. The new algorithm was successfully validated against several widely-used test cases. The new algorithm was used to model the flow of the NASA CC3, a high-speed centrifugal compressor, from choke to rotating stall with a vaneless and vaned diffuser. The new algorithm predicted the performance of the compressor with a vaneless diffuser very well; satisfactory results were obtained for the compressor with a vaned diffuser. The full compressor with a vaned diffuser was used to model rotating stall. A complex stall cycle between the inlet of the impeller and diffuser was observed and studied.

The fundament behavior of MVG, i.e. micro (sub-boundary layer) vortex generator, in a turbulent boundary layer was investigated in a channel flow with RANS and LES. Complementary wind tunnel testing was conducted to validate the computational predictions. The configuration of the MVG was studied to determine an optimal configuration and several conclusions were reached on the design of MVG. Most importantly triangle MVG were found to be the most efficient shape followed by NACA0012 and e423-type MVG, and a MVG angle of 18˚ to 20˚ was found to be optimal. Rectangle MVG were observed to suffer flow separation on the vanes which reduced their performance. The circulation and drag of a MVG was found to have a logarithmic relationship with the device's Reynolds number. These findings were incorporated in a LES study to control separated flow on the e387 airfoil and achieved an improvement in lift-to-drag ratio of 11.27%. Additional recommendations for MVG implementation were given.

Combining the work on the NASA CC3 with the work on MVG, vortex generators were implemented near the inlet of the impeller. A detailed optimization study was conducted for the implementation vortex generators in the compressor. It was found vortex generators equal to the boundary layer thickness were the most efficient on controlling the downstream flow. The best

configuration was implemented into the full compressor with a vaned diffuser to assess the ability of vortex generators to suppress rotating stall. The vortex generators were found to suppress rotating stall and extend the operating range of the compressor.

Acknowledgements

I wish to express my gratitude to my doctoral research advisors, Dr. Eldad Avital and Prof John Williams, for their support, encouragement, and guidance during my research. I thank my postdoc Dr. Zaheer Ikram for his research advice and assistant on conducting my wind tunnel tests. I also would to like to thank Dr. Zainab Saleh, Dr. Xiang Shen, and Ms. Vasana Don for their guidance and advice.

I express my gratitude to Mr. Mick Etheridge for his technical support with conducting my wind tunnel tests along with the other SEMS technicians that made my experiments possible. I would like to thank the development team of Code_*Saturne* at EDF, particularly Mr. Martin Ferrand, Mr. Erwan Le Coupanec, and Mr. Yvan Fournier, for their assistants on using *Code_Saturne* and understanding the code. I am also grateful to Mr. Jonathan Hills and other staff at QMUL for their help throughout my studies at QMUL.

Lastly I would to thank my family and friends for their support. I am thankful for all the great people I met and friendships I made at QMUL. I am immensely grateful to all my friends, especially Dr. Karla Corbitt, Ms. Anuroopa Kalyan, Dr. Jonathan Wheatland, Dr. Estelle Collin, Dr. Daniela Ferreira, Dr. Ewa Spiesz, and Dr. Reshma Tilwani, for their endless support during my doctoral studies and continual friendship. Most importantly, I would like to thank my parents for their continual encouragement and support which made my studies possible.

List of Contents

List of Figures

List of Tables

List of Symbols

Roman Symbols

c	Speed of sound
c_p	Heat capacity at constant pressure
c_v	Heat capacity at constant volume
C_f	Skin friction
D	Drag
e	Total energy or length of vortex generator vane
f	Function
h	Vortex generator height
h^+	Effective height of vortex generator vane
k	Turbulent kinetic energy
L	Lift
M	Mach number
$\dot{m}$	Mass flow rate
P	Pressure
P_o	Stagnation (or total) pressure
Pr	Prandtl number
q	Heat flux
r, θ, z	Cylindrical coordinate system
$R_{ij} = \langle u_i' u_j' \rangle$	Reynolds stress
Re	Reynolds number
s	Spacing between vortex generators
t	Time
T	Temperature
T_o	Stagnation (or total) temperature
u	Velocity
u_τ	Friction velocity
u^+	Non-dimensional velocity
U_o	Freestream velocity
V_m	Meridional velocity
w	Spacing for counter-rotating pair
y^+	Non-dimensional wall distance
γ	Ratio of specific heats or Poisson constant
Δt	Time step
x, y, z	Cartesian coordinate system

Greek Symbols

α	Angle
δ	Boundary layer thickness
δ_{ij}	Kronecker delta
ε	Internal energy
Γ	Vortex circulation
ρ	Density

λ	Thermal conductivity
μ	Laminar Viscosity
μ_t	Turbulent Viscosity
τ_{ij}	Shear stress tensor
τ_w	Wall shear stress
Ω	Cell volume
ω	Vorticity
ω_r	Rotational velocity

Notation

a_i	Vector
a_{ij}	Tensor
$\hat{a}$	Test filtered variable
$\bar{a}$	Mean variable
$\tilde{a}$	Filtered variable
∇a or $a_{,i}$	Gradient of variable a

Abbreviations

AoA	Angle of Attack
CC3	Centrifugal Compressor 3
CFD	Computational Fluid Dynamics
DSM	Dynamic Smagorinsky Model
LE	Leading Edge
LES	Large Eddy Simulation
LSCC	Low-Speed Centrifugal Compressor
MVG	Microvortex Generator
PIV	Particle Image Velocimetry
PS	Pressure Side of a blade
RANS	Reynolds Averaged Navier-Stokes
SS	Suction Side of a blade
TE	Trailing Edge
TKE	Turbulent Kinetic Energy
VG	Vortex Generator
WALE	Wall-Adapting Local Eddy-Viscosity

1. Introduction

In the modern world, gas turbines have become a critical technology for power generation and propulsion for a variety of vehicles. There is an ever-present need for improvements in efficiency and operating range of gas turbines that can be passed onto the applied application. Gas turbines are composed of several subcomponents with the compressor strongly dictating the operating range and the performance of the whole machine. Improvements in the operation of the compressor can easily lead to improvements in the overall operation of the gas turbine. This chapter introduces the concepts, research questions and objectives of this PhD project that has sought and gained improvements in the aerodynamic operation of centrifugal compressors and in the aerodynamic efficiency of blade sections.

1.1 Gas Turbine Compressors

The concept of an engine that compresses air and then combusts the air with a fuel to generate thrust has been around for centuries but was hindered by metallurgy and knowledge of fluid dynamics. It was not until the early twentieth century when technology and the understanding of fluid dynamics had matured far enough to allow multiple researchers working in many countries to make significant progress towards a jet engine. The first working jet engine is credited to Frank Whittle, who in 1937 successfully tested an engine with a centrifugal compressor. Later in 1937, Hans von Ohain successfully tested a similar engine independently of Whittle and by 1939 had successfully powered an aircraft with a jet engine. In competition to the centrifugal compressor is the axial compressor. Anselm Franz produced a working jet engine using an axial compressor in 1940, and by 1950's the majority of jet engines were using axial compressors because of their ability to achieve a higher compression ratio across multiple blade stages. Axial compressors compress air by accelerating the flow by rotating a row of blades (rotor) and then diffusing the flow across a row of stationary blades (stator) to obtain an increase of pressure across a stage. In contrast, centrifugal compressors compress air through a combination of accelerating and diffusing the flow within the impeller and further diffusing the flow within a diffuser to obtain the desired pressure ratio. Centrifugal compressors have the benefit of being rugged and the ability to achieve a high compression ratio in a single stage and are preferred in applications such as helicopters and small aircraft.

In the performance of a jet engine, the mass flow rate, total pressure, and adiabatic efficiency of the compressor is of interest. Along a speed line (constant rotational speed), the total pressure ratio and adiabatic efficiency is a function of the mass flow rate. A compressor map can be constructed, with the

total pressure ratio and mass flow rate, Fig. 1-1. In the figure, five speed lines are plotted with key features of the operating range noted. The operating range of a compressor is limited by choking at higher mass flow rate and surge at low mass flow rate. When a compressor is choked, the flow in the throat of the impeller passageway becomes sonic. Choking limits the mass flow rate and the pressure ratio becomes independent of the mass flow rate. At the other end of the operating range is surge. Surge occurs when the compressor flow is no longer able to maintain the pressure ratio across the compressor at a given mass flow rate; the flow becomes unstable and reverses. Before surge occurs, local instabilities may appear leading to rotating stall. Both instabilities degrade the compressor performance and induce stress vibrations in the compressor. To avoid these phenomena, a safety margin from the surge line is enforced; which takes into consideration inlet distortions, blade imperfections, and throttling. To shift this limit and obtain better performance from the compressor, a costly re-design of the compressor and/or implementation of a mechanism to manipulate the flow is needed. Significant amount of research has been direct towards axial compressors on this matter because of their wide use in industry and relatively simple flow dynamics. Centrifugal compressors in contrast have received less attention because of their smaller industrial use and much more complex flow dynamics. To contribute to understanding of centrifugal compressors, this thesis is directed towards the modelling of rotating stall inside of a compressor and the use of vortex generators to increase the stable operating range of the compressor.

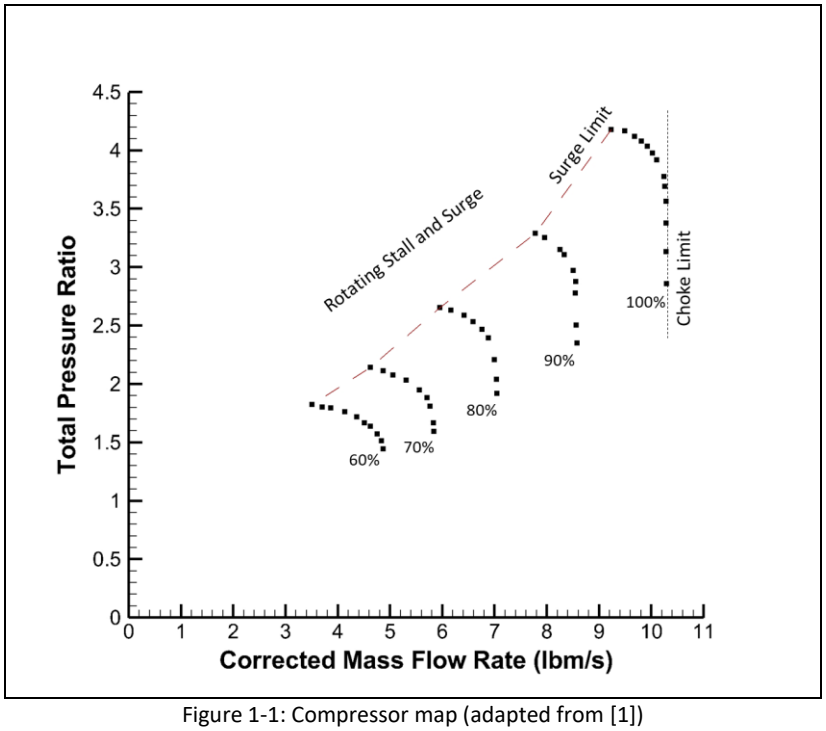

Figure 1-1: Compressor map (adapted from [1])

1.1.1 Rotating Stall

Rotating stall has been meticulously examined to determine its inception and behavior. Due to a large variety of compressor geometries, a wide set of behavior and inception for rotating stall has been observed in literature. At the reduced mass flow rate, the flow is unable to maintain the pressure gradient across the compressor. In an attempt by the compressor to compensate for the diminished flow, the flow is restricted to a limited number of passages, thereby maintaining a constant overall or time-averaged mass flow rate. One or more stalled cells (group of stalled passages) propagate around the compressor at a rotational speed of 20% to 70% of the rotational speed of the impeller [2, 3]. The stalled cells propagate around the compressor by a stalled passageway diverting the flow to a neighboring passageway. The diverted flow causes the flow angle to increase for the neighboring passageway which causes it to stall, the flow angle for a previously stalled passageway returns to normal. Through this process the disturbance rotates around the compressor at a fraction of the rotational speed of the impeller as shown in Fig. 1-2. The number of stalled cells varied from one or more in literature depending on the compressor geometry and flow conditions. Rotating stall is categorized as either abrupt or progressive stall. As much as the names suggests, progressive stall is the gradual deterioration of the total pressure ratio, while abrupt stall is the sudden drop of the total pressure ratio. Rotating stall has also been categorized on whether the stall is part-span, full-span, or small/large-scale [3, 4].

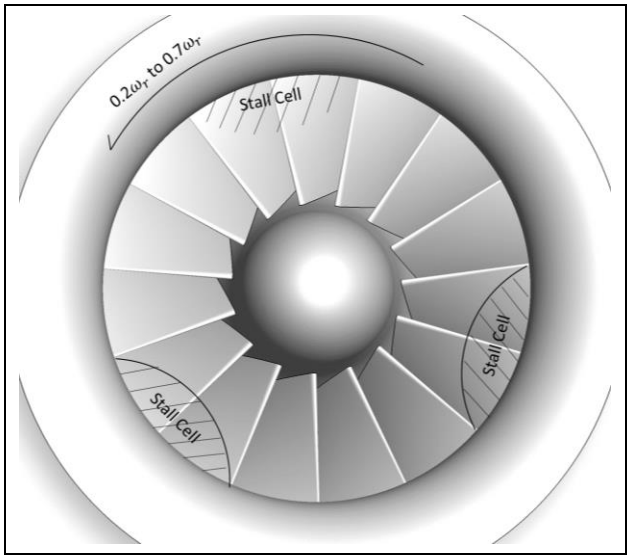

Figure 1-2: Illustration of rotating stall in a compressor

Two types of inception of stall have been observed in literature, long-wavelength model stall waves and short-wavelength spikes [3, 5, 6]. These stall inception patterns were first discovered in axial compressors, but were later identified in centrifugal compressors as well [7, 8]. The spike pattern occurs

with a sudden appearance of a short length-scale disturbance that quickly initiates rotating stall. Modal oscillation patterns involve a gradual build-up of long length-scale perturbations that can be detected up to hundreds of revolutions before the initiation of stall. In axial compressors, Camp and Day [6] found that spike stall inception is localized separation on a blade while modal stall inception is circumferential oscillation of the flow-field. Whether modal or spike stall inception is observed is dependent on the relative relationship of the critical incidence of the rotor to the peak of the pressure rise characteristic. Unlike axial compressors, the impeller and diffuser of a centrifugal compressor can stall independently or simultaneously; however, stall can only progress to surge if both components are stalled [4].

Rotating stall frequently triggers surge, causing the compressor to oscillate between a stalled and unstalled state with the time averaged flow through the compressor being unsteady. In the extreme case of deep surge, the flow in the entire compressor reverses and the total pressure ratio collapses. Less severe is mild surge where the flow does not reverse but the total pressure ratio oscillates. In between is classic surge, which is similar to mild surge but the oscillations are larger and with a lower frequency, and modified surge, which is a combination of classic surge and rotating stall [4].

To combat the instabilities in the compressor at off-design conditions, various approaches have been proposed that avoid an expensive redesign of the compressor blades. Work has been devoted to casing treatment in the form of slots or honeycomb structures, which minimizes tip leakage and increasing kinetic energy of the flow to increase stability. Additional studies have shown the effectiveness of casing treatment in delaying stall, however casing treatments induces additional losses throughout the operating range [9, 10]. Casing treatment has been applied to centrifugal compressors with similar success [11]. In the recent decades, active and passive vortex generators have been successfully used to suppress stall and surge, which are detailed in section 1.2.3.

1.2 Flow Separation and Control

Flow separation is a problem that has plagued aerodynamics since its inception and is often encountered on blades/wings, diffusers, and many other aerodynamic objects. Turbomachinery is composed of several complex geometries (i.e. blades and diffuser) that can experience many adverse flow conditions through the operation range of the machinery, leading to many opportunities for flow separation to occur on components. Flow separation can be benign, leading only to a lost in performance

and efficiency, or being a critical issue, instrumental in the formation of rotating stall and surge as discussed in the previous section.

The phenomenon of flow separation occurs when the boundary layer, particularly the inner boundary layer, is stripped of kinetic energy. The reduction of kinetic energy along with wall friction causes a stagnation region to form in the inner boundary layer, which in turn causes the flow to separate and reverse direction, along with an increase of boundary layer thickness. At the point of separation, acceleration of the flow equals zero. Likewise, the wall shear stress equals zero, which is typically used to determine the point of separation in a flow.

$$\tau_w = \mu \frac{\partial u}{\partial y}\bigg|_w = 0 \tag{1.1}$$

The loss of kinetic energy in the boundary layer can be caused by adverse pressure conditions, wall curvature, and shock-wave/boundary layer interactions, which are all conditions typically found in turbomachinery. Common approaches to counteract flow separation are carefully constructing wall curvature or adding/transferring momentum to the near-wall boundary layer. The later method makes use of active or passive vortex generators to add and transfer momentum within a boundary layer. In the following section, a review of previous research in both types of vortex generators will be discussed.

1.2.1 Passive Vortex Generators

Passive vortex generators (VG) transfer momentum from the outer to the inner boundary layer to suppress flow separation and improve the shape factor of the boundary layer by a vortex generated by a device embedded in the flow. In the boundary layer, vortex generators are typically described by their height (h) relative to the boundary layer thickness (δ). The first implementation of a vortex generator was in diffusers by Taylor [12] in the late-1940's and were in the form of a simple vane placed at an angle to the flow. Vortex generators were quickly applied to other aerodynamic applications such as the on P-51D fighter plane to improve flight performance [13]. The following decades saw further applications and testing of vortex generators in a variety of applications.

Before proceeding further into the development and behavior of VGs, it is important to describe the geometry of these devices. Shown in Fig. 1-3 and 1-4 is the geometry of a vane-type VG in an array. *h* is the height and *e* is the length of the vane, which are often non-dimensionalized by the boundary layer thickness. The vane is placed at an angle of α relative to the freestream flow. In an array of VGs, vanes can

be placed as pairs with an angle of $\pm\alpha$ as shown in Fig. 1-4 to produce counter-rotating vortices. The vane pairs have spacing of *w* and are spaced *s* from other vane pairs. VGs can also be assembled as an array of vanes with equal angles that are spaced at a distance of *s* to produce co-rotating vortices as shown in Fig. 1-3.

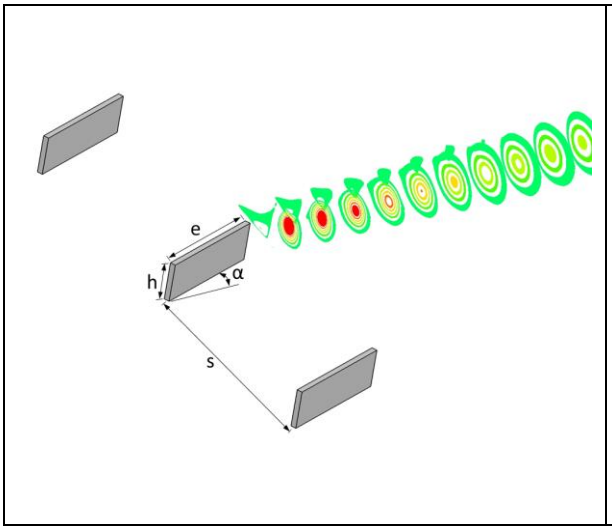

Figure 1-3: Co-rotating VG geometry

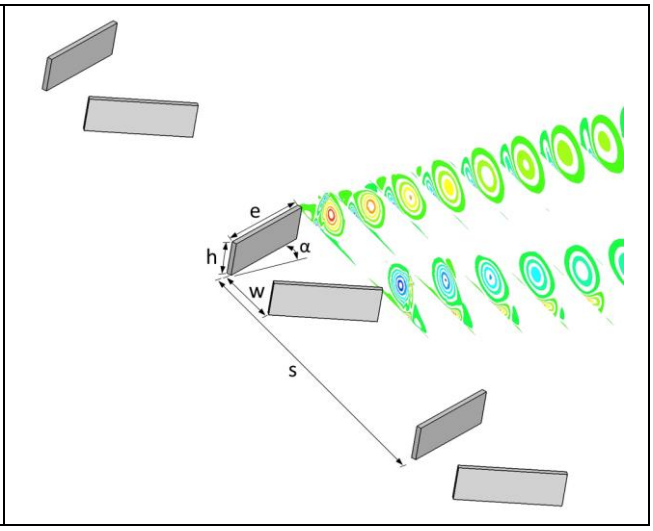

Figure 1-4: Counter-rotating VG geometry

Early vortex generators were on the scale of $h/\delta \sim 1$, or the height of the boundary layer, which caused excessive drag. Rao and Kariva [14] tested vane-type VG's with a height of $h/\delta \leq 0.65$ and found these smaller VG's could still provide sufficient momentum transfer within the boundary layer while having a lower associated drag cost. Research by Lin et al. [15] on several different VG configurations found that the size of a VG could be reduced to $h/\delta \sim 0.1$ and still retain their effectiveness in controlling flow separation. Further research by Lin et al. [16] showed that a vane-type VG with a height of 0.2δ was just as effective as a VG with a height of 0.8δ. However, further reduction in the height caused it to be inside the inner boundary layer thereby reducing its ability to transfer momentum inside the boundary layer [16, 17]. Subsequent research in diffusers by Canepa et al. [18] up held Lin et al. [16] conclusion on the effectiveness of sub-boundary layer VG. Vortex generators that are $h/\delta \leq 0.5$ have been called microvortex generators (MVG) [16], elsewhere in literature they have been called low-profile VG [19], submerged VG [20], and sub-boundary layer VG [21, 22]. In this thesis, VG will be used to reference vortex generators as a whole, while MVG will be used to directly reference vortex generators that are less than 50% of the boundary layer thickness.

Besides the typical vane-type VG, many different vortex generator shapes have been considered in literature. Wheeler's doublet, wishbone VGs, spanwise cylinders, LEBU and elongated arches at +10˚ angle of attack, Viet's flapper, and transverse groove VGs have all been tested in literature. Vane-type,

Wheeler's doublet, and wishbone VGs produce streamwise vortices, while the others produce transverse vortices. Lin et al. [16] tested several different VG shapes and found that VGs that generated streamwise, or longitudinal, vortices were the most effective in reducing flow separation on an airfoil when compared to VGs that generated quasi-coherent dynamic transverse vortices. On a high-lift airfoil, Lin et al. [23] observed that trapezoidal vanes were overall better in suppressing separation. However, Godard and Stanislas [24] observed a significant improvement in the flow with triangular vanes versus rectangular vanes. In regards to the VG vane angle, Pauley and Eaton [25] found that the optimum angle was 18˚ on a flat plate and Godard and Stanislas [24] similarly found 18˚ to be the optimum angle on an airfoil section.

In the application of vane-type vortex generators, vortex generators are placed into an array to sufficiently suppress flow separation. The vortices from an array of MVG interact strongly making the distance between vanes a critical factor in the performance of an array of MVG. An array of VGs can be grouped as pairs of counter-rotating vanes to produce vortices of counter-rotating vorticity as shown in Fig. 1-3 or as co-rotating vanes that produce vortices with co-rotating vorticity as shown in Fig. 1-4. Whether counter-rotating or co-rotating vanes is better at suppressing separation and improving the boundary layer is case dependent. Lin [16] found that co-rotating vanes suppressed separation better on a high-lift airfoil while various authors [21, 24, 25] found counter-rotating vanes were superior on an airfoil section. Another study by Lin et al. [23] found the best configuration was dependent on the location of the vanes; all of authors noted that both type of vane configurations still improved the flow. Pauley and Eaton [25] conducted an extensive experimental study on the interaction of vortices in an array. Co-rotating vortices were observed to remain stable and within the boundary layer if the spacing between vanes were large enough (*s/h* = 3). The behavior of counter-rotating vortices, which can be classified as "common flow down" and "common flow up" [25] [26], was more complex. Pauley and Eaton found that "common flow up" pairs interact strongly and convected each other out of the boundary layer, negating their effectiveness in transferring momentum. "Common flow down" vortex pairs interact strongly too, but the vortices moved apart while thinning the boundary layer in-between the pair. Counter-rotating vanes were the most efficient with a spacing of w/h = 2 and s/h = 6-10 [24] and for co-rotating vanes, spacing of s/h = 4-6 were found to be optimal [24].

In addition to the potential interaction with other vortices, the wall strongly dictates the behavior of a vortex. The circulation of an isolated vortex in a turbulent boundary layer decays by the wall skin friction [25]. Shabaka et al. [27] noted that the skin friction is strongest at the downdraft of the vortex on the wall and weakest at the updraft of the vortex. The vortex diffuses by strong gradients in the

($\langle v'v' \rangle - \langle w'w' \rangle$) and $\langle v'w' \rangle$ stresses of the flow [25, 28]. However, the decay and diffusion of the vortex is slow, allowing for the vortex to persist up to 100h behind the vane [16, 29]. Lin et al. [16] suggested that the optimum distance was 5h to 10h between a MVG and the separation point. The vortex has been observed to wander in the spanwise and normal direction with the motion being controlled by the wall (vortex image) and the turbulent boundary layer. [30]. For vortex pairs, the spanwise movement is further influenced by the neighboring vortex as discussed by Angele and Grewe [30]. Mehta and Bradshaw [31] stated that the wandering of the vortex was on a small scale that does not significantly hinder RANS modelling of the vortex.

Aside from vortex and its effect on the downstream flow, several researchers have looked at the drag of VGs. As mentioned earlier, Lin et al. [16, 17] found that the VG's drag increases greatly when height was greater than 0.2δ without an increase of effectiveness in flow control. Lin et al. conducted the drag measurements via a force balance. Ashill et al. [22] used the momentum defect to determine the drag on VGs in the presence of a zero and an adverse pressure gradient. They found the drag was much greater in an adverse pressure gradient than in tests without one. Ashill et al. also made a comparison between their experimental results for zero pressure gradient and numerical predictions by a CFD solver, and found a reasonable agreement between the two.

1.2.2 Numerical Modelling of Vortex Generators

In the numerical modelling of vortex generators, two approaches have been taken in literature. The most obvious approach is directly modeling the VG and the generated vortex, alternatively modeling of the VG can be neglected and a vortex is imposed onto the flow. The former approach is more accurate while the latter approach simplifies and lowers the computational cost of a case involving VGs. The Bender-Anderson-Yagle (BAY) model proposed by Bender et al. [32] imitates the influence of a VG by the inclusion of a source term in the momentum equation to enforce flow tangency on the VG. An improved version was developed by Jirásek [33] called the jBAY model. An alternative model to the BAY/jBAY was proposed by Wallin and Eriksson [34] which uses a body force formulation to represent the influence of a VG.

Allan et al. [35] modelled a solitary MVG vane on a flat plate and found that RANS predicted the vortex trajectory well in comparison to experimental data. However, RANS under predicted the peak vorticity and overestimated the vortex circulation. RANS was found to diffuse the vortex faster than was experimentally observed; the diffusion was found to be independent of the mesh resolution and Allan et

al. concluded that it was deficiency of the turbulent modelling. Yao et al. [29] and Wik et al. [36] observed similar behavior with RANS modelling of a MVG vane, however both their models yielded closer matches for the vortex circulation when compared to experimental results. Wet al. [36] found the prediction the vortex parameters to be strongly independent of the mesh resolution and the vane thickness could be neglected without significantly impacting the results. Allan et al. [35] and Wik et al. [36] noted that the k-ω SST model performed better in predicting the vortex parameters than the Spalart-Allmaras model, but Wik et al. observed the Reynolds Stress model gave better predictions than the k-ω SST model.

Manolesos et al. [37] conducted PIV measurements of VGs on a wing section to assess capability of CFD to predict the behavior of VGs. Manolesos et al. used the S-A and k-ω SST turbulence models in conjunction to fully resolve the VG vanes and using the jBAY model. Comparing the peak vorticity, they found the numerical results underestimated the vorticity. Fully resolving the VG gave some benefits; however, they decided the benefits were negligible with the increase computational cost when compared to the jBAY model. Florentie et al. [38] found the BAY and jBAY models to be very dependent on the mesh resolution and resolving the VG vane lead to better results when compared to experimental results.

1.2.3 Prior Applications in Turbomachinery

Flow inside of turbomachinery is very complex, as expressed earlier, with many secondary flow structures that can affect the overall performance of the gas turbine. Many strategies can be used to tackle these adverse flow conditions, but VG offer a simple and cheap method to control secondary flow structures. These attributes have led to VG to being applied to compressors, diffusers, inlets, intermediate ducts, and turbines. Vortex generators have been frequently implemented in diffusers to diminish the losses generated by flow separation that is caused by extreme wall curvature and adverse pressure gradients [18, 39, 40]. VG has also been used to control flow inside of supersonic inlets [41, 42] and S-duct inlets [43].

The application of VG within compressors and turbines are complicated by rotating blades and the transient nature of the flow. Hergt et al. [44] used MVG to control corner stall and reduce pressure loss by up to 4.6% in a compressor cascade. Further work by Hergt et al. [45] achieved a 9% reduction in pressure loss. Law et al. [46] used VG on the casing of an axial compressor stage to increase both the efficiency and stall margin in 1976. And Chima [47] modelled VG in an axial compressor to reduce secondary flows at the endwalls. Applying VG to casing, Chima [47] found that preswirl vanes improved the stall margin while decreasing the total pressure ratio, counterswirl vanes decrease the stall margin

but increase the total pressure ratio. Applying the VG to the blade itself reduce secondary flow, but did not reduce losses. Furthermore, Chima found that VG height of 0.5δ was optimum for the heights considered; taller VG could turn the boundary flow better but with a higher pressure loss while smaller VG had negligible influence on the boundary flow. Lastly in axial turbines, active vortex generators [48] have been used on turbine blades to successfully suppress shock induce boundary layer separation and to decrease heat transfer on the blade.

Majority of the implementation of VG in centrifugal compressors has been done with the NASA CC3 [49]. Skoch [50, 51] used vortex jets inside the semi-vaneless region of the diffuser. He observed a 1.7% improvement in the surge margin with a pressure loss of 1% while using a forward-tangent jet, but the vortex jets decreased the overall performance when in use. Spakovszky [52] used a steady air injection in between the impeller and diffuser with an injection of air at 0.5% of the compressor mass flow rate to obtain a 25% increase in the surge margin. Halawa et al. [53] successfully modelled vortex jets in the vanless region of a vaned diffuser to stabilize the flow at stall conditions ($\dot{m} = 3.9\ kg/s$). Additional optimization study by Halawa et al. [54] increased the stall margin ($\dot{m} = 3.8\ kg/s$). Stein et al. [55] numerically modelled vortex jets upstream of the impeller blades to eliminate leading-edge separation and increase the operating range of the NASA LSCC below 60% of the design operating point.

1.3 Research Questions and Thesis Objectives

Rotating stall, and related surge, degrades the performance and efficiency of a compressor. The unsteady behavior of the flow in the impeller also places an imbalance load on the blades causing vibration and fatigue on the blades which can cause severe damage. To suppress these instabilities and extend the operating range of a compressor, extensive redesign of the compressor needs to be conducted and/or implementation of flow control techniques as detailed earlier. As discussed in section 1.2.3, a number of authors have experimented with vortex generators in axial compressors and active vortex generators in centrifugal compressors to reduce losses from secondary flow and extend the operating range. Most research has focused on controlling the flow inside the diffuser to increase stability and extend the operating range of a centrifugal compressor. This poses a question on whether vortex generators implemented in the inlet of a centrifugal compressor can be as effective as other forms of the flow control implemented elsewhere in the compressor.

The rotating stall in the impeller and the separation on the impeller blades affects the downstream flow and stability of the compressor. The implementation of vortex generators upstream of the impeller may suppress the unstable flow in the impeller and impart stability in the overall compressor. Placing vortex generators upstream of the impeller may offer additional benefits such as working with a more uniform flow than the unsteady, non-uniform flow of the diffuser which may induce lower pressure losses. Although active vortex generators can potentially achieve the same effect as passive vortex generators, passive vortex generators are simple and rugged and do not require any complicated mechanisms to function. In the pursuit of this hypothesis, several additional questions are posed such as the detailed dynamics of separation and rotating stall on the impeller and the most efficient vortex generator configuration.

A variety of centrifugal compressor geometries are available in publications, the NASA CC3 [49] was chosen due to the extensive publications on the performance and rotating stall of the compressor. To facilitate the modelling of rotating stall and flow control inside the NASA CC3, the full compressor needs to be modelled with a sufficient distance upstream and downstream of the compressor. This scale of modelling is in the realm of high-performance computing (HPC) and the open-source code *Code_Saturne* was chosen. *Code_Saturne* has been written to work on and has been extensively validated for HPC [56]. However, *Code_Saturne* has primarily been applied to incompressible flow application and the algorithm for compressible flow has been greatly neglected. A new algorithm was written by the author in *Code_Saturne* to allow for the code to solve a rotating, compressible flow that is found in turbomachinery. Spatial accuracy of the compressible flow algorithm was increased with a 2nd-order MUSCL scheme written for the convective terms. These improvements, along with the numerical methods in general are presented in Chapter 2. In Chapter 3, the new compressible flow algorithm is validated against several test cases.

Expanding upon prior published works, the fundamental flow dynamics of microvortex generators (MVGs) in a turbulent boundary layer are studied in Chapter 4. LES is used to look at MVG vanes with varying shapes and angles to better understand their behavior. The LES results along with experimental results and prior published results are used to validate the capability of RANS to accurately model the flow of on a MVG. RANS modelling is then used to determine the optimum vane shape and angle along with assessing the affect that Reynolds number, vane height, and vane thickness has on a MVG vane. The lesson learned from Chapter 4 is then applied in Chapter 5 to study MVG implementation on the e387 airfoil that is undergoing stall.

Applying the newly constructed compressible flow algorithm to the NASA CC3 compressor, a single impeller blade/splitter is modelled with a vaneless diffuser to determine the optimum mesh resolution in Chapter 6. The pressure and efficiency curve is obtained at the design operating speed. With satisfactory results from this work, the complete compressor with a vaned diffuser is modelled. The mass flow rate is manipulated to induce rotating stall. The unstable flow field is studied and compared to prior published works. Finally in Chapter 7, vortex generators are placed in the impeller passage to determine the best configuration to control the downstream boundary layer. The best configuration is then placed upstream of the impeller blades to study the ability of the vortex generator to control the rotating stall.

2. Numerical Methods

In the numerical work that was conducted for this project, ANSYS Fluent and *Code_Saturne* were used. *Code_Saturne* is an open source, industrial code developed by Électricité de France (EDF) [57, 58]. It solves the Navier-Stokes equations with the finite volume method and cell-centered approach, and has been validated against a wide variety of CFD test cases. *Code_Saturne* can solve steady or unsteady problems with several different Reynolds-Averaged turbulence models (k-ω, k-ε, Reynolds Stress Model, Spalart-Allmaras) or with Large Eddy Simulation. The code itself is written in Fortran and C, and has been optimized to run in a HPC environment [56]. Majority of the work used v4.0, although v3.3 was used for some initial work. Using v4.0 as a baseline, a new compressible flow algorithm was written by the author with the capability of solving flows with rotating reference frames. ANSYS Fluent [59] is a commercial CFD software that can also solve a wide variety of numerical problems. Similar to *Code_Saturne*, Fluent uses the finite-volume method to solve the Navier-Stokes equations and offers many different choices for spatial and temporal discretization, and turbulence modelling.

In the following chapter, the numerical setup used for *Code_Saturne* and any changes made to the algorithm will be discussed. For ANSYS Fluent, the detail workings of the algorithms are proprietary and a generalized theory of the code is given in ANSYS Fluent Theory Guide [59]. Comparing the source material of the two codes, both codes in theory follow the same methods to numerically solving the Navier-Stokes equations. It is therefore assumed that the numerical methods used for *Code_Saturne* will also hold true for ANSYS Fluent, but any known differences will be discussed when applicable.

2.1 Governing Equations

A system of governing equations can be constructed to describe a fluid based on the principles of conservation of mass, momentum, and energy, which are known as the Navier-Stokes equations.

$$\frac{\partial \rho}{\partial t} + \nabla_i \cdot (\rho u_i) = 0 \tag{2.1}$$

$$\frac{\partial (\rho u_i)}{\partial t} + \nabla_j \cdot \left(\rho u_j u_i\right) = -\nabla_i P + \nabla_j \cdot \tau_{ij} \tag{2.2}$$

$$\frac{\partial (\rho e)}{\partial t} + \nabla_i \cdot \left(\rho u_i \left(e + \frac{P}{\rho} \right) \right) = \nabla_i \cdot \left(u_j \cdot \tau_{ji}\right) - \nabla_i \cdot q_i \tag{2.3}$$

To close the Navier-Strokes equations, an equation of state is defined to describe the gas or fluid. For most applications, the Ideal gas law is adequate, Eq. 2.4.

$$P = \rho RT = (\gamma - 1)\rho\left(e - \frac{1}{2}u^2\right) \tag{2.4}$$

Studying the momentum and energy equations, there are two terms that are undefined, the shear stress tensor and the heat flux. For majority of cases, the fluid or gas can be assumed to be Newtonian, meaning the viscous stresses are linearly proportional to the local strain rate. The viscous stresses can therefore be expressed as:

$$\tau_{ij} = \mu\left(\frac{\partial u_i}{\partial x_j} + \frac{\partial u_j}{\partial x_i}\right) - \frac{2}{3}\mu\frac{\partial u_k}{\partial x_k}\delta_{ij} \tag{2.5}$$

where μ is the dynamic viscosity. For incompressible flows the dynamic viscosity can be assumed to be constant while for compressible flows the temperature dependency of viscosity is accounted for by Sutherland's law.

The heat flux is described by the law of the heat conduction, or Fourier's law. The heat flux is equal to the product of the thermal conductivity λ and the negative temperature gradient.

$$q = -\lambda\nabla T \tag{2.6}$$

With the equation of state, the temperature can be written in terms of the total, kinetic, and internal energy to give:

$$q = -\frac{\lambda}{c_v}\nabla\left(e - \frac{1}{2}u^2 - \varepsilon\right) \tag{2.7}$$

where ε is the internal energy and c_v is the specific heat at constant volume. The thermal conductivity is replaced by the effective thermal conductivity, the summation of the laminar and turbulent thermal conductivity.

$$\lambda = c_p\frac{\mu}{Pr} \tag{2.8}$$

where c_p is the specific heat at constant pressure and Pr is the Prandtl number.

Although the Navier-Stokes equations accurately describe fluid motion within a continuum limit, the equations are non-linear, non-unique, and very difficult to solve. Without a general exact solution to the Navier-Stokes equations, the equations must be solved numerically. In this chapter, the numerical methods used to solve the governing equations in the studied cases are discussed.

2.1.1 Incompressible Flows

Solving the complete set of Navier-Stokes equations are not always required and for many cases simplifications and assumptions can be made to aid in the task of numerically solving the equations. At Mach numbers of less than 0.3, the compressibility of the flow can be neglected allowing for density to be assumed to be constant which simplifies the continuity equation to the divergence of the velocity field. And without heat transfer in the flow and assuming viscosity is constant, the energy equation does not affect the continuity and momentum equations and can be neglected. These simplifications reduce the Navier-Stokes equations to its incompressible form, where it is only a function of pressure and velocity.

$$\nabla_i \cdot u_i = 0 \tag{2.9}$$

$$\rho \frac{\partial u_i}{\partial t} + \nabla_j \cdot \left(\rho u_j u_i\right) = -\nabla_i P + \nabla_j \cdot \tau_{ij} \tag{2.10}$$

2.1.2 Rotating Frame Flows

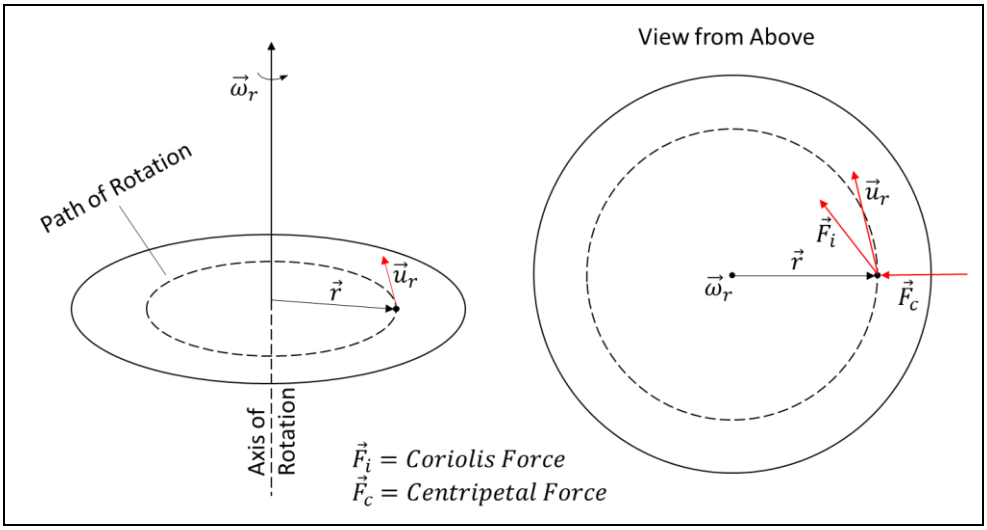

Figure 2-1: Rotating reference frame

The specific case of the Navier-Stokes equations in a rotating frame needs to be considered. The Navier-Stokes equations are reformulated simply by substituting the solved variables by their relative forms. The momentum equation also includes a Coriolis acceleration term ($-2\rho(\vec{\omega} \times \vec{r})$) and a centripetal acceleration term ($-\rho\, \vec{\omega} \times (\vec{\omega} \times \vec{r})$) on the right-hand side. Fig. 2-1 visualizes the forces on a particle in rotating system. The velocity from relative frame can be related to the velocity in the absolute frame by:

$$\vec{u} = \vec{u}_r + \vec{\omega} \times \vec{r} \tag{2.11}$$

Alternatively, the Navier-Stokes equations can be written again into an absolute velocity formulation. This version is beneficial for cases when the domain is both rotating and stationary, allowing for only one set of variables to be solved. The only quantity that is not solved in absolute terms is the mass flux. The Navier-Stokes equations written in absolute formulation are:

$$\frac{\partial \rho}{\partial t} + \nabla_i \cdot (\rho (u_r)_i) = 0 \tag{2.12}$$

$$\frac{\partial (\rho u_i)}{\partial t} + \nabla_j \cdot \left(\rho u_j (u_r)_i\right) = -\nabla_i P + \nabla_j \cdot \tau_{ij} - \rho\left((\omega_r)_i \times r_j\right) \tag{2.13}$$

$$\frac{\partial (\rho e)}{\partial t} + \nabla_i \cdot \left(\rho (u_r)_i \left(e + \frac{P}{\rho}\right) + (\omega_i \times r_i) P\right) = \nabla_i \cdot \left(u_j \cdot \tau_{ji}\right) - \nabla_i \cdot q_i \tag{2.14}$$

The absolute formulation can also be easily re-used for a moving/rotating mesh.

2.2 Turbulence Modelling

A key area of numerically solving the Navier-Stokes equations, and fluid dynamics in general, is the turbulence. Turbulence commonly arises in the presence of shear in the flow and from instabilities at high Reynolds numbers. The characterization of turbulent flows has long been sought after and with many notable researchers contributing to the understanding of this phenomenon. However, the theory of turbulence is still not complete and no exact solution currently exists [60-62]. A series of assumptions can be made to allow for a turbulent flow to be either simulated or numerically modelled with some degree of accuracy.

Turbulent flows are characterized as being unsteady, three-dimensional, vortex stretching, diffusive, dissipative, and having many length and time scales. With all these properties, simulating a turbulent flow becomes a difficult undertaking and there are three common approaches to this problem. The most straightforward path is to simulate everything and resolve all the turbulent structures, which is known as Direct Numerical Simulation (DNS). Even though DNS is conceptually straightforward, DNS requires a very fine mesh and high order discretization schemes to properly resolve the broad range of length and time scales. Rogallo and Moin [63] calculated the grid requirement for DNS computation was $Re^{2.25}$. An approach for overcoming the strict requirements for DNS is to simulate the large eddies while modelling the small-scale structures which alleviates the mesh requirement to properly resolve the flow. Large scale eddies in turbulent flows are much more energetic and stronger than small scale eddies, allowing for such approximation to be made. This approach is known as the Large-Eddy Simulation (LES).

Although the computational cost of LES is less than DNS, LES still requires a relatively fine mesh and high-order schemes. Chapman [64] estimated that the wall-resolved LES computation requirement was proportional to $Re^{1.8}$. Further approximation can be made by assuming that the whole turbulent flow can be modelled based on the Reynolds-Averaged Navier-Stokes (RANS) equations, or for compressible flows, Favre-Averaged Navier-Stokes (FANS). Reynolds averaging is the process of averaging a variable over time while Favre averaging uses density weighted variables for the time averaging.

Due to prohibitively large computational cost of DNS, particularly for high Reynolds number and turbomachinery flows, it was not considered as an option for this project. LES was used to study low to moderate Reynolds number applications, and in numerical experiments where it was necessary to accurately resolve the large-scale flow structures. Otherwise, RANS modelling was used to model the turbulent flow that was encountered in this project.

2.2.1 Large-Eddy Simulation

LES is based on the idea of simulating the large-scale eddies while modelling the small-scale eddies, therefore a filter needs to be imposed on the Navier-Stokes equations to filter out the small-scale eddies. Using one-dimensional notation for simplicity, a filtered variable is given by:

$$\tilde{\phi} = \int G(x, x')\phi(x')dx' \tag{2.15}$$

where the G is a localized function, the filter kernel. Filter functions that have been used are box filter, Gaussian, and Fourier cutoff. The filter has an associated length scale, $\tilde{\Delta}$, with any eddies smaller than the length scale being modelled. This results in a variable being expressed with a filtered and an unresolved component.

$$\phi = \tilde{\phi} + \phi' \tag{2.16}$$

Filtering the incompressible[1] Navier-Stokes equations yields:

$$\nabla_i \cdot (\rho \tilde{u}_i) = 0 \tag{2.17}$$

$$\frac{\partial(\rho \tilde{u}_i)}{\partial t} + \nabla_j \cdot \left(\rho \tilde{u}_j \tilde{u}_i\right) = -\nabla_i \tilde{P} + \nabla_j \cdot \left(\tilde{\tau}_{ij} + \tau^*_{ij}\right) \tag{2.18}$$

[1] All of the numerical experiments conducted with LES assumed the flow was incompressible.

where τ_{ij}^{*} represents the subgrid stress tensor, or residual stress. The filtered Navier-Stokes equations are solvable except for the subgrid stress tensor, which is unknown and must be modelled. The subgrid stresses can be approximated by Boussinesq hypothesis.

$$\tau_{ij}^{*} - \frac{1}{3}\tau_{kk}\delta_{ij} = 2\mu_t \tilde{S}_{ij} \tag{2.19}$$

For incompressible flows, τ_{kk} is negligible and is generally not computed. S_{ij} is the strain rate tensor.

There are several models to calculate the turbulent viscosity, μ_t. One of the simplest models is the Smagorinsky-Lilly model [65], and is model by:

$$\mu_t = \rho\left(c_s\tilde{\Delta}\right)^2\sqrt{2\tilde{S}_{ij}\tilde{S}_{ij}} \tag{2.20}$$

$\tilde{\Delta}$ is the filter width and is equal to $2(\Omega)^{1/3}$ and the Smagorinsky constant c_s is equal to 0.1838 in *Code_Saturne*. However, the shortcoming of the Smagorinsky-Lilly model is the assumption that c_s is constant. For simple flows, c_s can be adjusted to an optimum value for the given case, but for complex flows, the assumption that c_s is constant is no longer valid. The fix to this problem is to use the dynamic model proposed by Germano et al. [66].

The model proposed by Germano et al. [66] uses a second filter (called a test filter), with twice the width of the original filter to be applied to the Navier-Stokes equations. The difference between the two filtered velocity fields allows for the quality of the model to be assessed and a parameter to be constructed for the unresolved stress for each cell.

$$c_s^2 = \frac{\langle L_{ij}M_{ij}\rangle}{\langle M_{ij}M_{ij}\rangle} \tag{2.21}$$

where

$$M_{ij} = \hat{\Delta}^2\widehat{\left|\tilde{S}\right|\tilde{S}_{ij}} - \Delta^2\left|\hat{\tilde{S}}\right|\hat{\tilde{S}}_{ij} \tag{2.22}$$

$$L_{ij} = \widehat{\tilde{u}_i\tilde{u}_j} - \hat{\tilde{u}}_i\hat{\tilde{u}}_j \tag{2.23}$$

In solving for c_s^2, the numerator and denominator are locally averaged to dampen fluctuations and the equation is clipped to 0.65 when the denominator is less than 10^{-12}. The dynamic model fixes many of problems of the constant Smagorinsky-Lilly model; however, it is slightly more expensive computationally. Most subgrid models, such as the constant and dynamic Smagorinsky-Lilly models, are observed to behave incorrectly near the wall leading to excessive viscosity near the wall and incorrect predictions of skin friction. A fix to this problem is to dampen the viscosity with the Van Driest damping function.

A third subgrid model is the Wall-Adapting Local Eddy-Viscosity (WALE) model proposed by Nicoud and Ducros [67]. They observed that the velocity derivatives expressed the expected asymptotic behaviour of $\mu_t \propto (y^+)^3$. y^+ is the non-dimensional distance from the wall. Drawing on this observation, they proposed the subgrid viscosity to be defined as:

$$\mu_t = \rho\tilde{\Delta}^2 \frac{\left(S_{ij}^d S_{ij}^d\right)^{3/2}}{\left(\bar{S}_{ij}\bar{S}_{ij}\right)^{3/2} + \left(S_{ij}^d S_{ij}^d\right)^{5/4}} \tag{2.24}$$

where

$$\tilde{\Delta} = c_w^2(\Omega)^{1/3} \tag{2.25}$$

$$S_{ij}^d = \frac{1}{2}\left(\tilde{g}_{ij}^2 + \tilde{g}_{ji}^2\right) - \frac{1}{3}\delta_{ij}\tilde{g}_{kk}^2 \tag{2.26}$$

$$\tilde{g}_{ij} = \frac{\partial \tilde{u}_i}{\partial x_j} \tag{2.27}$$

The WALE model has the inherent property of the subgrid viscosity vanishing near the wall and well suited for complex geometries. The constant c_w is equal to 0.5 in *Code_Saturne*.

2.2.2 Reynolds Averaged Naiver-Stokes Equations

Turbulence can be ideally characterized as random fluctuations in the velocity field; however, in reality turbulence is deterministic. Assuming the turbulence is random, statistical methods can be used to construct a model of the turbulent flow. The instantaneous velocity can therefore be split between a mean and a fluctuating component. The mean is averaged over an infinitely large time step. This approach is known as the Reynolds averaging, which yields the Reynolds averaged Navier-Stokes (RANS) equations.

$$\phi = \bar{\phi} + \phi' \tag{2.28}$$

$$\bar{\phi} = \lim_{t\to\infty} \frac{1}{t}\int_0^t \phi(x,t)\, dt \tag{2.29}$$

Reynolds averaging the incompressible Navier-Stokes equations yields:

$$\frac{\partial \rho}{\partial t} + \nabla_i \cdot (\rho \bar{u}_i) = 0 \tag{2.30}$$

$$\frac{\partial(\rho\bar{u}_i)}{\partial t} + \nabla_j \cdot \left(\rho\bar{u}_j\bar{u}_i\right) = -\nabla_i P + \nabla_j \cdot \left(\bar{\tau}_{ij} - \overline{\rho u_i' u_j'}\right) \tag{2.31}$$

where

$$\bar{\tau}_{ij} = 2\mu\bar{S}_{ij} \tag{2.32}$$

Except for the last term on the right-hand side of the momentum equation, the computation of RANS solution is relatively straight forward. The modelling of the last term is described later in section 2.2.4.

2.2.3 Turbulence Closure

The RANS equations contain a nonlinear, fluctuating term $-\overline{\rho u_i' u_j'}$ that is unknown, but is generally computed by a first or second order closure model. First order closure models, or eddy viscosity models, assume that the turbulent viscosity is isotropic and used the Boussinesq hypothesis to provide closure. The Boussinesq hypothesis relates the Reynolds stresses to the strain rate as:

$$-\overline{\rho u_i' u_j'} = \mu_t \left(\frac{\partial u_i}{\partial x_j} + \frac{\partial u_j}{\partial x_i} - \frac{2}{3}\frac{\partial u_k}{\partial x_k}\delta_{ij}\right) - \frac{2}{3}\rho k \delta_{ij} \tag{2.39}$$

In contrast, second order closure models, or Reynolds Stress models, directly solve for the Reynolds stresses by set of seven Reynolds stress transport equations. Second order closure models have increased accuracy over eddy viscosity models, particularly for flows with streamline curvature, swirl, or other complex 3D flows. The second order closure models are however more computationally expensive.

Eddy viscosity models can be broken down further into zero-equation (algebraic), one-equation, and two-equation. Zero-equation models close the system without solving additional equations and solves for turbulence viscosity from the mean flow properties and as a function of the characteristic length. One-equation models introduce a transport equation to solve for turbulent kinetic energy k while imposing a length scale. The most popular one-equation model is the Spalart-Allmaras model [68]. Two-equation models take it one step further and use a transport equation for both *k* and its rate of dissipation (absolute ε or specific ω). Common two-equation models are the *k*-ε [69] and the *k*-ω [70] model. The turbulent viscosity, μ_t, is solved from an algebraic equation. The Reynolds stress model is effective for complex three-dimensional turbulent flows, but it is computationally intensive.

Code_Saturne has several popular turbulence models: Spalart-Allmaras, *k*-ε, *k*-ω SST, $R_{ij} - \epsilon$, and v2f models. The turbulence models in *Code_Saturne* are formulated in a compressible form. Fluent has

similar turbulence models available. For the work that was carried out, the Spalart-Allmaras and the *k*-ω SST models were used and will be discussed in detailed in the following sections. The Reynolds Stress models was considered, but was determined to be too computationally expensive.

2.2.3.1 Spalart-Allmaras Model

The Spalart-Allmaras model is a one-equation model that solves a transport equation for the kinematic turbulent viscosity [68]. The model was developed for aeronautical applications and is well suited for wall-bounded flows and boundary layers with adverse pressure gradients. It however performs poorly for complex 3D flows, free shear flows, and flows with strong separation.

The transport equation for kinematic turbulent viscosity ($\tilde{\nu}$) is given by:

$$\frac{\partial \bar{\rho}\tilde{\nu}}{\partial t} + \nabla_i \cdot (\bar{\rho}\tilde{u}_i\tilde{\nu}) = c_{b1}\bar{\rho}\tilde{S}\tilde{\upsilon} - c_{w1}f_w\bar{\rho}\left(\frac{\tilde{\nu}}{d}\right)^2 + \frac{1}{\sigma}\left[\nabla \cdot \left((\mu + \bar{\rho}\tilde{\nu})\nabla\tilde{\nu}\right) + c_{b2}\bar{\rho}|\nabla\tilde{\nu}|^2\right] \tag{2.40}$$

where the individual terms are defined as:

$$\chi = \frac{\tilde{\nu}}{\nu}$$

$$f_{v1} = \frac{\chi^3}{\chi^3 + c_{v1}^3}$$

$$f_{v2} = 1 - \frac{\tilde{\nu}}{\nu + \tilde{\nu}f_{v1}}$$

$$\tilde{S} = \Omega + \frac{\tilde{\nu}}{\mathrm{K}^2 d^2} f_{v2} \tag{2.41}$$

$$r = min\left[\frac{\tilde{\nu}}{\tilde{S}K^2 d^2}, 10\right]$$

$$g = r + c_{w2}(r^6 - r)$$

$$f_w = g\left[\frac{1 + c_{w3}^6}{g^6 + c_{w3}^6}\right]$$

where *d* is the distance to the nearest surface and the stated constants are given in Table 2-1.

σ	c_{b1}	c_{b2}	K	c_{w2}	c_{w3}	c_{v1}	c_{w1}
2/3	0.1355	0.622	0.41	0.3	2	7.1	$\frac{c_{b1}}{K^2}+\frac{1+c_{b2}}{\sigma}$

Table 2-1: Constants for the Spalart-Allmaras model

After solving the transport equation of $\tilde{\nu}$, the turbulent eddy viscosity is computed by

$$\mu_t = \rho f_{v1} \tilde{\nu} \tag{2.42}$$

The Spalart-Allmaras model neglects the kinetic energy containing term of the Boussinesq hypothesis. The turbulent quantities are imposed by the user at the inlet and extrapolated from within the domain for the outlet. At the wall, a value of null is imposed for the kinematic turbulent viscosity.

2.2.3.2 k-ω SST Model

The original, well-known k-ω model was proposed by Wilcox in 1988 [71] and solves a transport equation for turbulent kinetic energy (k) and specific dissipation rate (ω). The k-ω is similar to the k-ε turbulence model; however, the specific dissipation rate is solved instead of the dissipation rate. The k-ω model performs well for wall-bounded cases, particularly for adverse pressure gradient. However, a weakness of the k-ω model is its sensitivity of the specific dissipation rate to the freestream. Menter [70] overcame the shortcomings of the original k-ω model by employing the model only in the inner region of the boundary layer and switching to the k-ε model in the outer region of the boundary layer and mixing regions. The reformulated model is called the k-ω SST model.

$$\frac{\partial(\rho k)}{\partial t} + \nabla_i \cdot (\rho k u_i) - \nabla \cdot \left[\left(\mu + \frac{\mu_t}{\sigma_k}\right)\nabla k\right] = P_k - \beta^* \rho \omega k \tag{2.43}$$

$$\frac{\partial(\rho \omega)}{\partial t} + \nabla_i \cdot (\rho \omega u_i) - \nabla \cdot \left[\left(\mu + \frac{\mu_t}{\sigma_\omega}\right)\nabla \omega\right] = \frac{\rho\gamma}{\upsilon_t} P_\omega - \beta \rho \omega^2 + 2(1-F_1)\frac{\rho \sigma_{\omega 2}}{\omega}\nabla k \nabla \omega \tag{2.44}$$

The production terms are approximated as [72]:

$$P_\omega = \mu_t S^2 - \frac{2}{3}\rho k \nabla \cdot u_i \tag{2.45}$$

$$P_k = \begin{cases} c_1 c_\mu \rho \omega k, & P_\omega > c_1 c_\mu \rho \omega k \\ P_\omega \quad , & P_\omega \leq c_1 c_\mu \rho \omega k \end{cases} \tag{2.46}$$

The production term for kinetic energy is limited as shown in Eq. 2.46. The constants used in the k-ω SST model is a blending of an inner (1) and outer (2) constant via Eq. 2.47.

$$\phi = \phi_1 F_1 + (1 - F_1)\phi_2 \tag{2.47}$$

Function F_1 is defined as:

$$CD_{k\omega} = max\left(\frac{2\rho}{\sigma_{\omega 2}\omega}\nabla k \nabla \omega, 10^{-20}\right) \tag{2.48}$$

$$arg_1 = \min\left[\max\left(\frac{\sqrt{k}}{c_\mu \omega d}, \frac{500}{\omega d^2}\frac{\mu}{\rho}\right), \frac{4\rho k}{\sigma_{w2} CD_{k\omega} d^2}\right] \tag{2.49}$$

$$F_1 = \tanh(arg_1^4) \tag{2.50}$$

Function F_2 is defined as:

$$arg_2 = max\left(\frac{2\sqrt{k}}{c_\mu \omega d}, \frac{500\mu}{\rho d^2 \omega}\right) \tag{2.51}$$

$$F_2 = \tanh(arg_2^2) \tag{2.52}$$

The constants used are given in Table 2-2.

γ_1	β_1	σ_{k1}	$\sigma_{\omega 1}$	c_1	κ
$\beta_1/c_\mu - \kappa^2/\left(\sigma_{\omega_1}\sqrt{c_\mu}\right)$	0.075	1.1765	2	0.31	0.42
γ_2	β_2	σ_{k2}	$\sigma_{\omega 2}$	c_μ	
$\beta_2/c_\mu - \kappa^2/\left(\sigma_{\omega_2}\sqrt{c_\mu}\right)$	0.0828	1	1.1682	0.09	

Table 2-2: Coefficients for k-ω SST model

The turbulent viscosity is equal to [73]:

$$\mu_t = \frac{a_1 \bar{\rho} k}{max(a_1\omega, SF_2)} \tag{2.53}$$

The turbulent quantities are imposed by the user at the inlet and extrapolated from within the domain for the outlet. At the wall, a value of null is imposed for the turbulent kinetic energy and a Neumann boundary condition for ω.

2.2.3.3 Curvature/Rotation Correction

Eddy viscosity models are insensitive to streamline curvature and rotation. To overcome the insensitivity, a correction can be introduced to the production term to improve the modelling of the

turbulence, which is called Spalart-Shur Correction [74]. Smirnov and Menter extended the correction to the k-ω SST model [75]. The Spalart-Shur correction is given in *Code_Saturne* by:

$$f_{rot} = (1 + c_{r1})\frac{2r^*}{1 + r^*}(1 - c_{r3}\tan^{-1}(c_{r2}\hat{r})) - c_{r1} \tag{2.54}$$

$$f_{r1} = max[f_{rot}, 0] \tag{2.55}$$

where the terms are defined as:

$$r^* = \frac{S}{W} \tag{2.56}$$

$$\hat{r} = \frac{2W_{ik}S_{jk}}{\widetilde{D}^4}\left[\frac{DS_{ij}}{Dt} + \left(\varepsilon_{imn}S_{jn} + \varepsilon_{jmn}S_{in}\right)(\omega_r)_m\right] \tag{2.57}$$

and

$$S_{ij} = \frac{1}{2}\left(\frac{\partial u_i}{\partial x_j} + \frac{\partial u_j}{\partial x_i}\right) \tag{2.58}$$

$$W_{ij} = \frac{1}{2}\left[\left(\frac{\partial u_i}{\partial x_j} + \frac{\partial u_j}{\partial x_i}\right) + 2\varepsilon_{mji}\Omega'_m\right] \tag{2.59}$$

$$S^2 = 2S_{ij}S_{ij} \tag{2.60}$$

$$W^2 = 2W_{ij}W_{ij} \tag{2.61}$$

$$D = \left[\frac{1}{2}\left(S_{ij} + W_{ij}\right)\right]^{1/2} \tag{2.62}$$

For the Spalart-Allmaras model

$$\widetilde{D} = D \tag{2.63}$$

For the k-ω SST model

$$\widetilde{D} = max\left(D, c_\mu\omega\right) \tag{2.64}$$

The constants for the rotation/curvature correction are given in Table 2-4.

c_{r1}	c_{r2}	c_{r3}
1.0	12.0	1.0

Table 2-3: Constants for rotation/curvature correction

From the use of rotation/curvature correction for k-ω SST model in *Code_Saturne*, it was found the original correction led to significant over production of turbulence in the boundary layer. The correction for the k-ω SST model was rewritten to replicate exactly the correction of Smirnov and Menter [75]. In the revised correction written in *Code_Saturne*, the correction is given by:

$$f_{r1} = max[min(f_{rot}, 1.25), 0] \tag{2.65}$$

The calculated variables D and $\widetilde{D}$ are given by:

$$D^2 = max(S^2, 0.09\omega^2) \tag{2.66}$$

$$\widetilde{D} = WD^3 \tag{2.67}$$

The constants for the revised correction are given in Table 2-4. The revised rotation/curvature correction is validated in Appendix A.

c_{r1}	c_{r2}	c_{r3}
1.0	2.0	1.0

Table 2-4: Constants for revised rotation/curvature correction

2.2.3.4 Wall Modelling

In the boundary layer of a turbulent flow, high gradients can be encountered, requiring fine mesh resolution even for RANS modelling. A turbulent boundary layer can however be approximated as a wall function to alleviate the mesh requirements. The boundary layer can be split into an inner and outer boundary layer. The inner boundary layer is described by the non-dimensional wall distance y^+, and the outer boundary layer is described by the non-dimensional wall distance y/δ. The inner boundary layer can be further broken down into a viscous sublayer, log-law region, and a buffer region. The viscous sublayer is $y^+ \leq 5$, the buffer region is $5 < y^+ < 30$, and the log-law region is $y^+ \geq 30$. Through non-dimensional analysis of experiments on turbulent boundary layers, Ludwig Prandtl and Theodore von Kármán developed the law of the wall to describe the mean boundary layer profile. The equation of the law of the wall is defined as:

$$u^+ = \frac{u}{u_\tau} = \frac{1}{\kappa}\ln(y^+) + 5.2 \tag{2.68}$$

where u^+ is the non-dimensional wall velocity and u_τ is the friction velocity. The law is typically valid from $15 < y^+ < 100$, however this range varies from case to case. Below a limit of y^+_{lim} (defined as κ^{-1} in *Code_Saturne*), the boundary profile is defined as:

$$u^+ = y^+ \tag{2.69}$$

With the above approximations, a two-scale model is used for the k-ω SST model.

$$u_\tau = \begin{cases} \dfrac{u}{\kappa^{-1}\ln(y^+) + 5.2}, & if\ y^+ > y^+_{lim} \\ \dfrac{u}{y^+}, & if\ y^+ \le y^+_{lim} \end{cases} \tag{2.70}$$

where u is the magnitude of the velocity vector tangential to the wall. For the wall function, the non-dimensional distance from the wall, y^+, is defined as:

$$y^+ = \frac{u_k y}{\mu} \tag{2.71}$$

where

$$g = \exp\left(-\frac{1}{11}\frac{k^{1/2}}{\mu}y\right) \tag{2.72}$$

$$u_k = \left((1-g)c_\mu^{1/2}k + g\mu\frac{u}{y}\right)^{1/2} \tag{2.73}$$

Contrary to the k-ω SST model, the Spalart-Allmaras model is not designed to resolve the boundary layer. In *Code_Saturne*, a one-scale model is used for the Spalart-Allmaras model but with the constraint that the wall is not resolved ($y^+ > 30$). If cell centre of the cell closest to the wall is in the log layer, the friction velocity is equal to:

$$u_k = u_\tau = \frac{\kappa u + u_\tau}{\ln\left(\frac{y}{\mu}u_\tau\right) + 5.2\kappa + 1} \tag{2.74}$$

Otherwise the friction velocity is equal to:

$$u_k = u_\tau = \sqrt{\frac{\mu}{y}u} \tag{2.75}$$

The non-dimensional wall distance is computed with Eq. 2.71.

2.3 Discretization

To solve the Navier-Stokes and any associated transport equations, the equations need to be numerically discretized. Each of the equations are composed of a temporal, convection, diffusion, and source terms.

$$\frac{\partial \phi}{\partial t} + \nabla_i \cdot (\rho u_i \phi) - \nabla_i \cdot (\mu \nabla \phi) = f_s \tag{2.76}$$

The finite volume method divides the solution domain into a number of control volumes to solve the governing equations on. The governing equations can be appropriately rewritten in an integral form.

$$\int_\Omega \frac{\partial \phi}{\partial t} d\Omega + \int_{\partial\Omega} (\rho u_i \phi) \cdot dS_i - \int_{\partial\Omega} (\mu \nabla \emptyset) \cdot dS_i = \int_\Omega f_s d\Omega \tag{2.77}$$

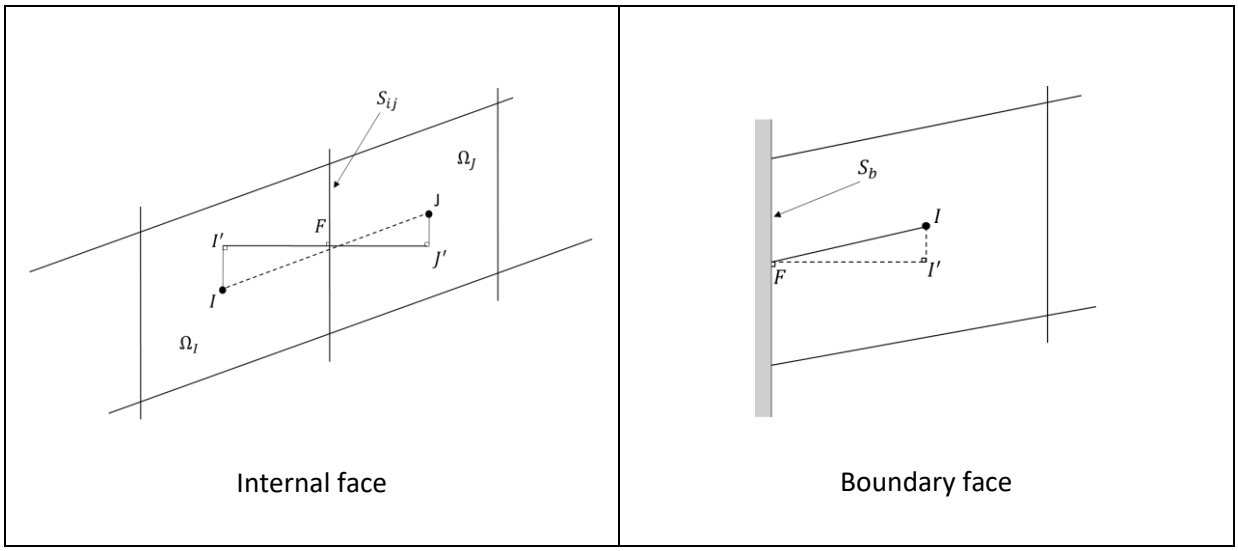

Figure 2-2: Sketch of advection scheme

Over each control volume, Eq. 2.74 can be approximated as:

$$\frac{\partial \phi}{\partial t}\Omega + \sum_{CS} \phi_f (\rho u_i)_f \cdot dS_i - \sum_{CS} \mu_f \frac{\phi_{J'} - \phi_{I'}}{\|I'J'\|} \|S_i\| = f_s \Omega \tag{2.78}$$

where I and J are the cells boarding a given cell face f, as shown in Fig. 2-2. I' and J' are respectively the projection of I and J along the orthogonal line to the centroid of cell face f. The temporal and source terms are approximated as the product of the quantities at the cell center with the cell volume. The convective and diffusive terms use the Gauss' theorem to approximate the divergence of the two terms as the summation of fluxes on all the control surfaces (CS) of the cell, Eq. 2-78. The extrapolation of the

variables for the convective term is discussed later in section 2.3.2 and mass flux extrapolation in section 2.3.3. Similarly, the diffusive term needs a discretization scheme for the viscosity and variable ϕ.

2.3.1 Time Discretization

The time derivative of a given variable can be treated explicitly or implicitly, with first- or second-order accuracy. With each scheme, time is advanced with a time step of Δt.

Explicit Euler Scheme $$\phi^{n+1} = \phi^n + f(t_n, \phi^n)\Delta t \quad (2.79)$$

Implicit Euler Scheme $$\phi^{n+1} = \phi^n + f(t_{n+1}, \phi^{n+1})\Delta t \quad (2.80)$$

Adam-Bashforth Scheme $$\phi^{n+1} = \phi^n + \tfrac{1}{2}[3f(t_n, \phi^n) - f(t_{n-1}, \phi^{n-1})]\Delta t \quad (2.81)$$

Crank-Nicholson Scheme $$\phi^{n+1} = \phi^n + \frac{1}{2}[f(t_n, \phi^n) + f(t_{n+1}, \phi^{n+1})]\Delta t \quad (2.82)$$

Euler scheme is first-order accurate and either implicitly or explicitly updates the function with time. The Crank-Nicholson scheme updates the solution with the average of current and future states, which is also known as the trapezoidal rule. The Adam-Bashforth method updates the solution with the current and past states. Both Crank-Nicholson and Adam-Bashforth schemes are second-order, but the Crank-Nicholson scheme is implicit while Adam-Bashforth scheme is explicit. The explicit schemes are computationally cheaper than the implicit schemes; however, implicit schemes are more stable. *Code_Saturne* uses implicit Euler and Crank-Nicholson schemes to discretize the transported variables (velocity, density, pressure, and energy). Explicit Euler and Adam-Bashforth schemes are used to discretized physically properties (viscosity, specific heat, …) and source terms. For most cases, first-order temporal schemes are used, however LES requires higher order discretization and the Crank-Nicholson scheme is used.

2.3.2 Spatial Discretization of Convective Terms

To resolve the convective and diffusion terms, variables stored at the cell-centre needs to be extrapolated to the cell faces. The use of an unstructured mesh, which both *Code_Saturne* and Fluent are based on, limits the available information for the discretization schemes to the two neighbouring cells of the face. Information of the flow field beyond the two neighbouring cells of the face are unknown in data storage method of *Code_Saturne* and Fluent, more advance data storage methods can however extend connectivity of the face to overcome this problem. The construction of a discretization can be characterized by its accuracy, numerical stability and boundness.

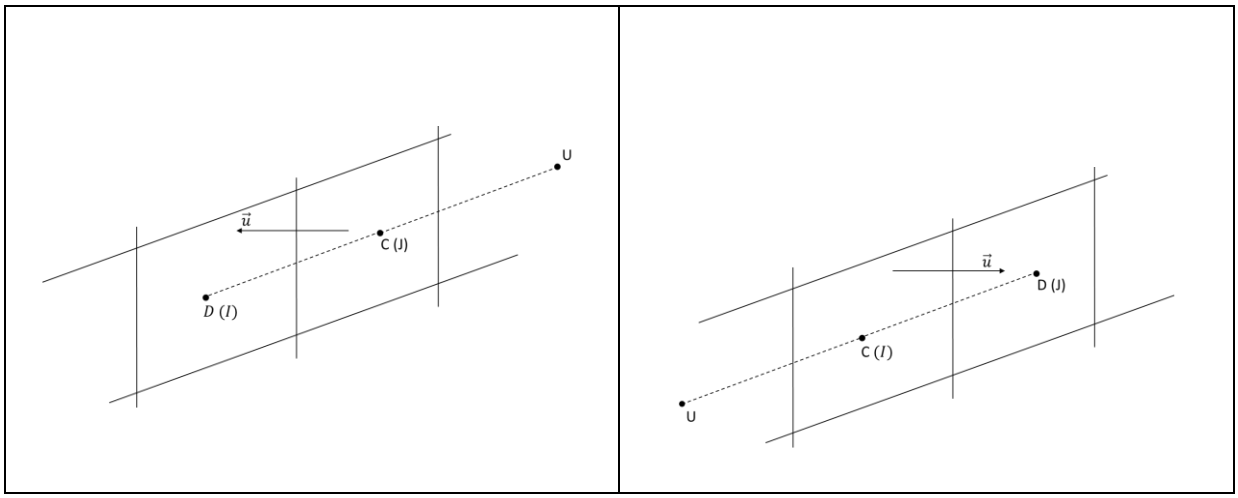

Figure 2-3: Sketch of upwind convection scheme

Given in Fig. 2-2 and 2-3, is a sketch of the geometric notation for the extrapolating of the variables to the face F. Fig. 2-3 expresses the notation used for the upwind schemes, with cell C being the cell upstream of face F and cell D being the cell downstream of face F. Cell U is the 'virtual' cell being upstream of cell C.

A first-order approximation can be made by extrapolating the variable from the cell upwind of the face.

$$\phi_f^{upwind} = \phi_c \tag{2.83}$$

Although simple, the upwind scheme is very diffusive. To improve the accuracy of the discretization, a second-order approximation can be made by extrapolating the variables from both the bordering cells.

$$\phi_{ij}^{centred} = \alpha_{ij}\phi_{I'} + \left(1 - \alpha_{ij}\right)\phi_{J'} \tag{2.84}$$

where α_{ij} is a weighting factor of the distance between cell centre I and face f_{ij} with respect to the distance between the cell centre of I and J. In reality, the points I' and J' are used, which are the projection of I and J along the orthogonal line to the face f_{ij} passing through its centre, F. This is done to increase the accuracy for non-orthogonal mesh.

$$\alpha_{ij} = \frac{\overrightarrow{FJ'}}{I'J'} \tag{2.85}$$

To further account for any non-orthogonality of the mesh, the centred scheme includes the average gradient dotted with the spatial vector of the distance between the centre of the face and the line between points I and J.

$$\phi_{ij}^{centred} = \alpha_{ij}\phi_{I'} + \left(1-\alpha_{ij}\right)\phi_{J'} + \frac{1}{2}\left[(\nabla\phi)_I + (\nabla\phi)_J\right]\cdot\overrightarrow{OF} \tag{2.86}$$

Although the centred scheme is second-order accurate, the scheme can produce an unbounded solution, which can introduce unphysical oscillation in presence of strong convection and discontinuities in the flow. Second-order accuracy can also be achieved by taking the first-order upwind scheme and adding an anti-diffusive term. The anti-diffusive term is the gradient within the upwind cell dotted with the spatial vector between the face and the cell-centre, Eq. 2.87. This scheme is called the second-order linear upwind (SOLU).

$$\phi_f^{solu} = \phi_c + (\nabla\phi)_c \cdot \left(\vec{r}_f - \vec{r}_c\right) \tag{2.87}$$

The gradient used in the anti-diffusive term is however unbounded, and can cause stability issues and oscillations in the solutions. This presents a conundrum for flows with strong convection or discontinuities, either accept lower accuracy in the solution, or have oscillations and stability issues.

To achieve high order accuracy and monotonicity preserving, or non-oscillatory, a new scheme needs to be introduced. Several early schemes were proposed that met these criteria but with shortcomings. A practical scheme that satisfied these criteria was developed by Van Leer [76] called the Monotonic Upstream-Centered Scheme for Conservation Laws (MUSCL) scheme. The MUSCL scheme introduces a limiter function φ applied to the linear piecewise reconstruction.

$$\phi_f^{MUSCL} = \phi_c + \varphi\left(r_f\right)(\nabla\phi)_c \cdot \left(\vec{r}_f - \vec{r}_c\right) \tag{2.88}$$

Harten [77] introduced a further criterion, the concept of total variation diminishing (TVD), which requires oscillations to remain constant or shrink with increase of time step. Harten further showed that TVD schemes are also monotonicity preserving. Sweby [78] expressed the TVD criterion with a $r-\varphi$ diagram to develop a limiter function. With the aid of the Sweby's diagram, numerous limiters have been proposed by researchers. Three of the most popular, and that have been implemented into *Code_Saturne*, are the minmod [79], superbee [79], and Van Albada [80] limiters.

Minmod
$$\varphi(r) = max[0, min(1, r)] \tag{2.89}$$

Superbee
$$\varphi(r) = max[0, min(1{,}2r), min(2, r)] \tag{2.90}$$

Van Albada
$$\varphi(r) = \frac{r^2 + r}{r^2 + 1} \tag{2.91}$$

where r_f (computed at a cell face), Sweby's r-factor, is equal to:

$$r_f = \frac{\phi_C - \phi_U}{\phi_D - \phi_C} \tag{2.92}$$

Setting the limiter to unity recovers the SOLU scheme. The determination of r_f is straightforward for structured meshes where the neighbouring cells are known, but the implementation on unstructured meshes where the neighbouring cells are not easily 'known' poses an obstacle. A popular and simple approach to this problem was proposed by Barth and Jespersen (BJ) [81]. BJ scheme requires that the reconstructed value within a cell does not exceed the extrema of the neighbouring cells, which is a modification of Speikreijse monotonicity criterion [82]. However, many of the ideas developed for limiters in structured meshes cannot be applied for the BJ scheme. Building on the Sweby's r-factor, Bruner [83] extended Sweby's r-factor to unstructured meshes by using the cells gradient to recover the upstream cell value. Darwish and Moukalled [84] further refined the method to the r-factor as:

$$r_f = \frac{2\nabla\phi_C \cdot r_{CD}}{\phi_D - \phi_C} - 1 \tag{2.93}$$

2.3.3 Spatial Discretization of Diffusive Terms

The discretization of the diffusive term uses a second-order central difference scheme and is determined by:

$$D = \nabla_i \emptyset \cdot dS_i = \frac{\phi_{J'} - \phi_{I'}}{\|I'J'\|} \|S_i\| \tag{2.94}$$

However, to increase spatial accuracy, the diffusive term can be reconstructed to account for any non-orthogonalities in the mesh.

$$D = \frac{\phi_{J'} - \phi_{I'}}{\|I'J'\|} \|S_i\| + \frac{1}{2} \frac{\nabla\phi_I + \nabla\phi_J}{\|I'J'\|} \|S_i\| \cdot \left(\overrightarrow{II'} - \overrightarrow{JJ'}\right) \tag{2.95}$$

The viscosity for the diffusion term is determined by a linear interpolation (Eq. 2.96), although a harmonic interpolation (Eq. 2.97) can be used instead.

$$\mu_f = \frac{1}{2}\left(\mu_I + \mu_J\right) \tag{2.96}$$

$$\mu_f = \frac{\mu_I \mu_J}{\alpha_{ij}\mu_I + \left(1 - \alpha_{ij}\right)\mu_J} \tag{2.97}$$

2.3.4 Treatment of Boundary Conditions

Lastly is the implementation of the convective and diffusive flux at the boundary. Information of the boundary condition is stored in the coefficients A^g and B^g for the convective term, and A^f and B^f for the diffusive term. The boundary value for the convective flux is computed by Eq. 2.98 and the boundary flux is computed by Eq. 2.99.

$$\phi_f = A^g + B^g \phi_{I'} \tag{2.98}$$

$$\frac{D}{\|S_i\|} = A^f + B^f \phi_{I'} \tag{2.99}$$

A full description of the boundary conditions will be described later in the chapter, but the coefficients for Dirichlet and Neumann boundary conditions are given in Table 2-5. ϕ^{imp} and q^{imp} are the boundary variable and flux defined by the user, respectively. h_{int} is the 'viscosity' coefficient.

$\begin{cases} A^g = \phi^{imp} \\ B^g = 0 \end{cases}$	$\begin{cases} A^f = -h_{int}\phi^{imp} \\ B^f = h_{int} \end{cases}$	$\begin{cases} A^g = -q^{imp}/h_{int} \\ B^g = 1 \end{cases}$	$\begin{cases} A^f = q^{imp} \\ B^f = 0 \end{cases}$
Dirichlet		Neumann	

Table 2-5: Coefficient values for Dirichlet and Neumann Boundaries

2.3.5 Mass Flux and AUSM$^+$-up Interpolation

In determination of the mass flux at the cell face, *Code_Saturne* uses a centred scheme to interpolate $(\rho u)_i$ to the cell face for the incompressible flow, Eq. 2.100.

$$(\rho u_i)_f = \alpha_{ij}(\rho u_i)_I + \left(1 - \alpha_{ij}\right)(\rho u_i)_J + \frac{1}{2}\left(\nabla(\rho u_i)_I + \nabla(\rho u_i)_J\right) \cdot \overrightarrow{OF} \tag{2.100}$$

Similar to the centred scheme for convective flux, *Code_Saturne* uses a correction for non-orthogonality in the mesh to increase accuracy. This scheme works well for incompressible flows, however as the Mach number of the flow is increased to the supersonic regime, information of the flow no longer travels both upstream and downstream. For supersonic flows, information travels upstream to downstream. The native compressible flow algorithm in *Code_Saturne* uses a central difference scheme for velocity and an upwind scheme for the density. A more suitable approach to mass flux discretization would be to use a flux vector splitting scheme. Numerous flux vector splitting schemes have been described in literature, one of the popular scheme is the Advection Upstream Splitting Method (AUSM) developed by Liou and Steffen [85].

The AUSM scheme computes cell interface Mach number from the characteristic speed from the left and right state. The interface Mach number is then used to extrapolate quantities for the interface fluxes. Differing from other schemes, AUSM scheme splits the pressure term from convective terms of the flux. Several different versions of the scheme have been developed culminating in the AUSM$^+$-up scheme [86, 87]. The AUSM$^+$-up scheme improves upon earlier versions by being efficient at all Mach numbers, and fixing pressure oscillations and inefficiencies at low Mach numbers in previous versions. Overall, the scheme has been shown to exactly capture contact discontinuities, entropy-satisfying, positivity-preserving, free of carbuncle phenomenon, accurate of slow moving discontinuities, and smooth transition through the sonic point.

Described below is the implementation of the AUSM$^+$-up scheme in *Code_Saturne* by the author. The cell face velocity is equal to the common speed of sound and Mach number at the face.

$$u_f = a_f M_f \tag{2.101}$$

The speed of sound at the cell face is:

$$a_f = \min(\hat{a}_L, \hat{a}_R) \tag{2.102}$$

where the left- and right-states are defined as:

$$\hat{a}_L = \frac{(a^*)^2}{\max(a^*, u_L)} \tag{2.103}$$

$$\hat{a}_R = \frac{(a^*)^2}{\max(a^*, -u_R)}$$

The critical speed of sound, a^*, for a perfect gas is calculated via:

$$a^* = \sqrt{\frac{2(\gamma - 1)}{\gamma + 1} H_t} \tag{2.104}$$

where H_t is the total enthalpy and is defined as:

$$H_t = e + \frac{P}{\rho} \tag{2.105}$$

The velocity of the left and right states, u_L and u_R, are extrapolated with an upwind scheme. At the face, the extrapolated left and right states are multiplied by the unit normal vector of the cell face, $u = u_i \cdot (S_i)_f$.

The Mach number of the left and right states are simply:

$$M_L = \frac{u_L}{a_f}$$
$$M_R = \frac{u_R}{a_f} \tag{2.106}$$

The face Mach number can be written as a function of the left and right state Mach numbers, and a pressure diffusion term.

$$M_f = M_{(4)}^{+}(M_L) + M_{(4)}^{-}(M_R) + M_p \tag{2.107}$$

The split Mach numbers $M_{(4)}^{\pm}$ are polynomial functions of fourth-order and are evaluated as:

$$M_{(4)}^{\pm}(M) = \begin{cases} M_{(2)}^{\pm}(M)\left(1 \mp 16\beta M_{(2)}^{\mp}(M)\right) & |M| < 1 \\ M_{(1)}^{\pm}(M) & |M| \geq 1 \end{cases} \tag{2.108}$$

where the first and second order functions are

$$M_{(1)}^{\pm}(M) = \frac{1}{2}(M \pm |M|) \tag{2.109}$$

$$M_{(2)}^{\pm}(M) = \pm\frac{1}{4}(M \pm 1)^2 \tag{2.110}$$

The pressure diffusion term in Eq. 2.105 has the benefit of coupling the pressure and velocity at low speeds. The pressure diffusion term is evaluated as:

$$M_p = -\frac{K_p}{f_a}\max(1 - \bar{M}^2, 0)\frac{p_R - p_L}{\rho_f a_f^2} \tag{2.111}$$

where

$$\bar{M}^2 = \frac{1}{2}(M_L^2 + M_R^2) \tag{2.112}$$

and K_p is a dissipation coefficient with a value of $0 \leq K_p \leq 1$. Following literature, a value of 0.25 was used. The density at the face, ρ_f, is simply the average of the left- and right-states. The variable $f_a$is a scaling function dependent on the reference Mach number M_o.

To properly scale the numerical dissipation with the flow speed, an introduction of a scaling function f_a is required. The simplest form of the scaling factor is a function of a reference Mach number (M_o).

$$f_a(M_o) = M_o(2 - M_o) \geq 0 \tag{2.113}$$

$$M_o^2 = min(1, \max(\bar{M}^2, M_\infty^2) \tag{2.114}$$

where M_∞ is the freestream Mach number that can be set equal to the Mach number of the inlet or as a user defined value. For algorithm written in *Code_Saturne*, this value is set equal to the average Mach number of the domain.

A similar procedure can be conducted to calculate the face pressure.

$$P_f = P_{(5)}^{+}(M_L)p_L + P_{(5)}^{-}(M_R)p_R + p_u \tag{2.115}$$

where the $P_{(5)}^{\pm}$ is 5th-order polynomial function given by:

$$P_{(5)}^{\pm}(M) = \begin{cases} M_{(2)}^{\pm}(M)\left((\pm 2 - M) \mp 16\alpha M_{(2)}^{\mp}(M)\right) & |M| < 1 \\ \frac{1}{M} M_{(1)}^{\pm}(M) & |M| \geq 1 \end{cases} \tag{2.116}$$

The velocity diffusion term, p_u, is:

$$p_u = -K_u P_{(5)}^{+}(M_L) P_{(5)}^{-}(M_R)(\rho_L + \rho_R) f_a a_f (u_R - u_L) \tag{2.117}$$

where the pressure diffusion term, K_u is a dissipation coefficient with a value of $0 \leq K_u \leq 1$, following literature, a value of 0.75 was used.

In the implemented algorithm, the AUSM^{+}-up scheme is used to compute the mass flux and the convective pressure flux in the pressure correction equation. Density is a transport quantity and is upwinded with either a simple first-order scheme or a second-order MUSCL scheme.

$$\dot{m}_f = \frac{1}{2}\left[u_f(\rho_L + \rho_R) - |u_f|(\rho_R - \rho_L)\right] \tag{2.118}$$

Similarly, for the convective pressure flux, which transports the compressibility coefficient, ψ.

$$F_f = \frac{1}{2}\left[u_f(\psi_L + \psi_R) - |u_f|(\psi_R - \psi_L)\right] \tag{2.119}$$

2.3.6 Solution of Linear System of Equations

With the discretization methods discussed, the last step is the solution of the linear equations that are formed from the governing and any transport equations. At the beginning of each step in the segregated algorithm, *Code_Saturne* calculates the explicit terms, implicit terms, viscosity, and boundary conditions, and then assembles a linear equation to solve. Eq. 2.78 can easily be rewritten as:

$$f^{imp}(\phi^{n+1} - \phi^n) + \nabla_i \cdot (\phi^{n+1}(\rho u_i) - \mu \nabla \phi^{n+1}) = f^{exp} \tag{2.120}$$

The source terms are split between an implicit and an explicit term, f^{imp} and f^{exp} respectively. The temporal term is included in the implicit term. Alternatively, Eq. 2.120 can be written as an algebraic equation:

$$A_p\phi_p + \sum A_l\phi_l = b \tag{2.121}$$

where the subscript p represents the node of interest and l represents the neighboring nodes. The coefficient A contains the implicit, convective, and diffusion terms. b contains all the terms that are known or are treated explicitly. Because the linear system must be solved for each control volume and the solution to each control volume is interdependent on their neighbors, a system of linear equations is constructed.

$$[A][\phi] = [b] \tag{2.122}$$

The system of linear equations can be solved directly or iteratively. Direct method gives a solution to the system in a finite number of operations and is suitable for small problems. Alternatively, iterative method makes an initial guess and then iteratively solves the system until a specified tolerance is met. *Code_Saturne* offers several different iterative solvers for linear systems: Jacobi, preconditioned conjugate gradient, Bi-conjugate gradient stabilized, and generalized minimal residual. Jacobi linear solver is the default solver in *Code_Saturne*. For pressure equations, a multigrid method combined with the conjugate gradient solver is used to solve for such equations.

2.4 Solution of the Navier-Stokes Equations

In the solution of the Navier-Stokes equations, the system of equations can be solved with a segregated or a coupled approach. Furthermore, there are two approaches to enforce the continuity equation upon the constructed algorithm that are known as the density-based and pressure-based solvers.

In the coupled approach, all of equations of the Navier-Stokes equations are solved simultaneously. This approach has the benefit of being robust and quickly converging to a solution but with a larger memory requirement. Alternatively, the equations can be solved in a segregated manner, which is much easier to implement and uses less memory at the cost of requiring multiple iterations around the Navier-Stokes equations to reach a converged state.

The distinction between the density-based and pressure-based solver is the approach to enforcing the continuity equation. Density-based solvers enforce the continuity equation directly by solving the equation and then updating the pressure field with the equation of state. In contrast, pressure-based solvers update the pressure field with a pressure or pressure correction equation which is constructed from the continuity and momentum equation. Historically, pressure-based solvers were used for low-speed incompressible flows while density-based solvers were used for high-speed compressible flows. Early pressure-based algorithms were built on the assumption that the flow being solved was incompressible. In contrast, density-based algorithms had the problem that density becomes constant at the incompressible limit causing the continuity equation to reduce the divergence of the velocity field. The velocity then becomes decoupled from the pressure due to the continuity equation no longer being a viable method to update the pressure. In recent decades, these restrictions have been overcome by introducing the artificial compressibility method [88] to density-based solvers and the inclusion of compressibility effects in pressure-based solvers. Pressure-based solvers are still more efficient than density-based solvers when solving incompressible flows or flows that are dominated by incompressible flow which why this project focused on pressure-based solvers.

2.4.1 Incompressible Flow Algorithm

The incompressible flow algorithm in *Code_Saturne* uses a pressure-correction method that can solve steady and unsteady flows. For steady flows, *Code_Saturne* uses a SIMPLE (Semi-Implicit Method for Pressure-Linked Equations) algorithm which was developed by Patankar and Spalding [89]. In principle, *Code_Saturne* follows a SIMPLE method for unsteady flows too, but in reality a non-iterative pressure-correction algorithm is used by default. However, additional inner iterations on the pressure-velocity coupling may be imposed to increase accuracy. A summary of the steady and unsteady incompressible flow algorithm can be found in Fig. 2-4 and 2-5, respectively.

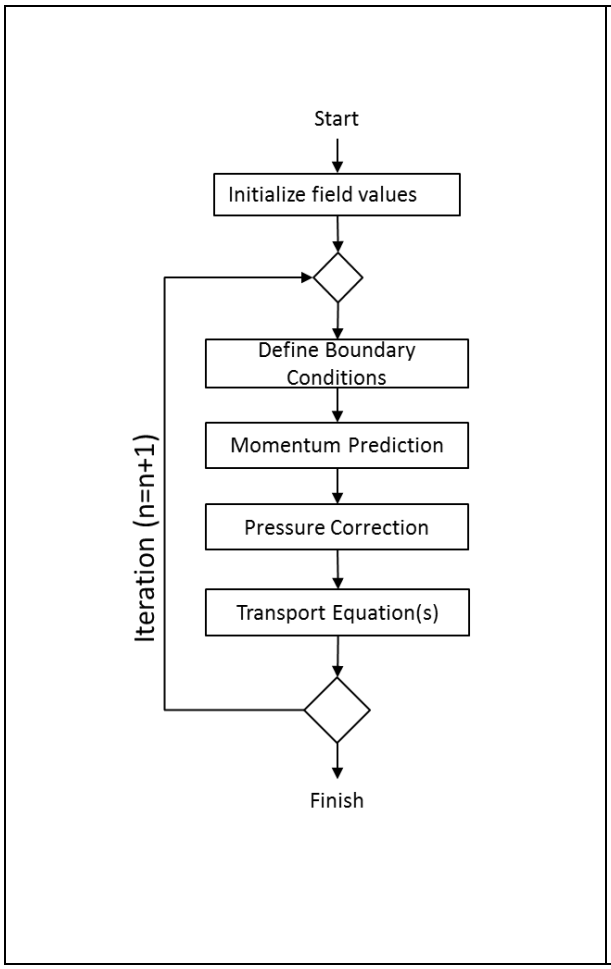

Figure 2-4: Steady, incompressible flow algorithm

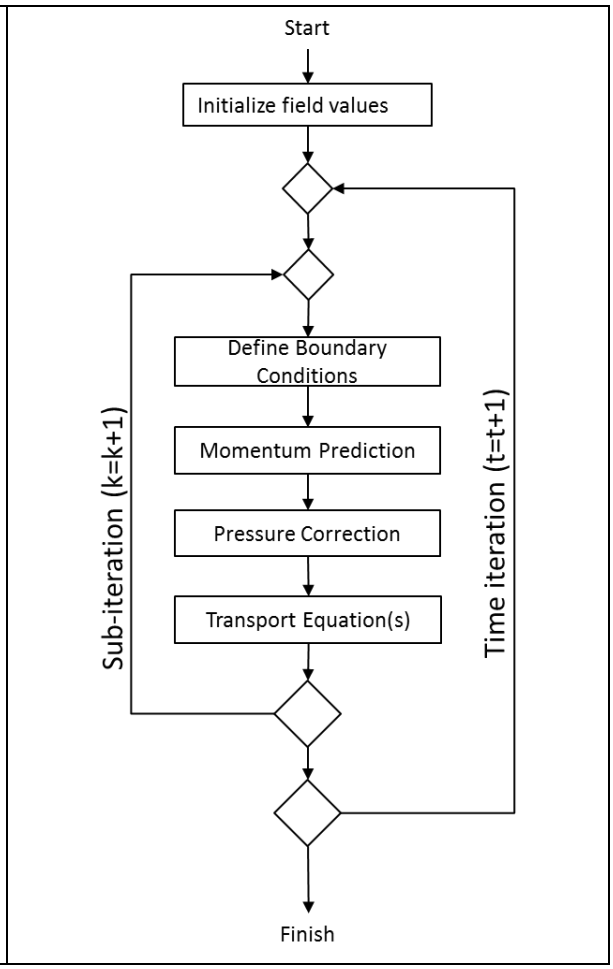

Figure 2-5: Unsteady, incompressible flow algorithm

During each iteration, the momentum equation (Eq. 2-2) is solved for a new velocity field, but the newly predicted velocity does not satisfy the continuity equation. To satisfy the continuity equation, the velocity field needs to be corrected by correcting the pressure field. An equation can be constructed by combining the momentum and continuity equation to solve for the corrected pressure field. The first step to constructing the pressure correction equation is to write the momentum equation.

The convection and diffusion terms can be split into a diagonal (D) and a non-diagonal (N) component.

$$\nabla_i \cdot \left(\rho u_i u_j - \tau_{ij}\right) = A_{ji}^{D} u_i + \sum A_{ij}^{N} u_i \tag{2.123}$$

Rewriting the momentum equation with the auxiliary velocity u^*, which does not satisfy the continuity equation.

$$\left(\frac{\rho\Omega}{\Delta t}\delta_{ij} + A_{ji}^{D}\right)u_i^* + \sum A_{ij}^{N}u_i^* = -\nabla_j P^n + \frac{\rho\Omega}{\Delta t}u_j^n + S^n \tag{2.124}$$

A reformulated momentum equation can be constructed a pressure field P^* and a velocity field u_i^{**} that satisfies the continuity equation.

$$\left(\frac{\rho\Omega}{\Delta t}\delta_{ij} + A_{ji}^{D}\right)u_i^{**} + \sum A_{ij}^{N}u_i^* = -\nabla_j P^* + \frac{\rho\Omega}{\Delta t}u_j^n + S^n \tag{2.125}$$

In the new equation, the pressure effect on the non-diagonal term is assumed to be negligible. Eq. 2.124 can now be subtracted from Eq. 2.125 and the divergence of the resulting equation can be taken.

$$\nabla_i \cdot u_i^* = \nabla_i \cdot \left[\frac{1}{A_p}\nabla_j(P^* - P^n)\right] \tag{2.126}$$

where

$$A_p = \frac{\rho\Omega}{\Delta t}\delta_{ij} + A_{ji}^{D} \tag{2.127}$$

The non-diagonal component can be neglected in the coefficient A_p, which yields the SIMPLE method. However, to increase efficiency and accuracy of the algorithm, the non-diagonal component can be included to give the SIMPLEC method.

$$A_p = \left(\frac{\rho\Omega}{\Delta t}\delta_{ij} + A_{ji}^{D}\right) + \sum A_{ij}^{N} \tag{2.128}$$

Code_Saturne calculates an estimator to the coefficient by:

$$\left[\left(\frac{\rho\Omega}{\Delta t}\delta_{ij} + A_{ji}^{D}\right) + \sum A_{ij}^{N}\right]a_i = \Omega \cdot I \tag{2.129}$$

where *I* is an identity matrix.

$$A_p = (a_i)^{-1} \tag{2.130}$$

But for most cases in *Code_Saturne*, the coefficient A_p is equal to Δt^{-1}.

The new pressure field allows for the velocity field and mass flux to be corrected.

$$u_j^{**} = u_j^* - \frac{1}{\rho}\frac{1}{A_p}\nabla_j P^* \tag{2.131}$$

$$\dot{m}^{**} = (\rho u)^* - \sum \frac{1}{A_p}\nabla P \cdot S_{ij} \tag{2.132}$$

Linear interpolation of cell-centred values to cell face results in unphysical checker-boarding of the pressure field, to prevent this, the Rhie-Chow interpolation scheme is used [90]. After resolving the pressure and velocity fields, the final step is to solve any additional transport equations for turbulence models.

2.4.2 Original Compressible Flow Algorithm

The compressible flow algorithm in *Code_Saturne* relies upon a non-iterative segregated solver, known as the SLK algorithm [91]. The algorithm is broken down into three steps, an acoustic prediction, a momentum prediction, and an energy prediction. Earlier versions of *Code_Saturne* solved an acoustic prediction equation to implicitly predict density, which was used to update the pressure and mass flux. Current versions of *Code_Saturne* implicitly solve for pressure instead, and update the density and the mass flux.

The acoustic equation is constructed by simplifying the continuity (Eq. 2.1) and momentum equations (Eq. 2.2):

$$\frac{\rho^{n+1}-\rho^{n}}{\Delta t}+\nabla_i\cdot(\rho u_i)^{n+1}=0 \tag{2.133}$$

$$\frac{(\rho u_i)^{n+1}-(\rho u_i)^{n}}{\Delta t}=\rho^{n} f_i^{n}-\nabla_i P^{*} \tag{2.134}$$

where the advection and source terms of the momentum equations are combined into f. Pressure and density can be related with the following relation:

$$\frac{\partial P}{\partial t}=c^2\frac{\partial \rho}{\partial t}+\beta\frac{\partial s}{\partial t} \tag{2.135}$$

where $c^2=\left.\frac{\partial P}{\partial \rho}\right|_s$ (speed of sound squared), $\beta=\left.\frac{\partial P}{\partial s}\right|_\rho$, and s is entropy. The acoustic step is assumed to be isentropic, which allows for the change in entropy in Eq. 2.135 to be neglected. Merging Eq. 2.133 and 2.134, and using Eq. 2.135 to relate density to pressure yields:

$$\frac{1}{c^2}\frac{P^{*}-P^{n}}{\Delta t}+\nabla_i\cdot\left(\rho^{n}(u_i^{n}+\Delta t\, f_i^{n})\right)-\nabla_i\cdot(\Delta t\,\nabla P^{*}) \tag{2.136}$$

Solving the acoustic equation updates the pressure and the density can be updated through the ideal gas equation. f is normally set to zero to stabilized the algorithm, which consequently eliminates the advection terms contribution to the mass flux and pressure. The effects of the advection terms are therefore only

taken account from the previous iteration. An update to the mass flux can be made with the new pressure field.

$$(\rho u_i)^{n+1} = (\rho u_i)^n - \Delta t \, \nabla_i P^* \tag{2.137}$$

After implicitly predicting the new pressure field and calculating the acoustic mass flux, the momentum (Eq. 2-2) and energy (Eq. 2-3) equations can be solved. The momentum equation updates the velocity field and the energy equations update the total energy. With the new total energy field, the temperature and pressure field is updated. The final step is solving for any transport equations for the turbulence models.

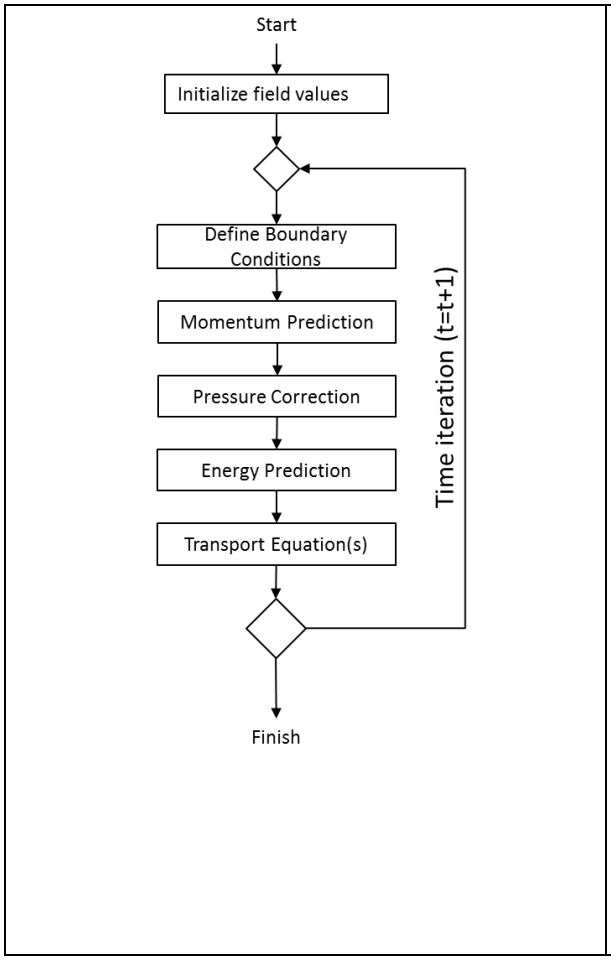

Figure 2-6: SLK compressible flow algorithm

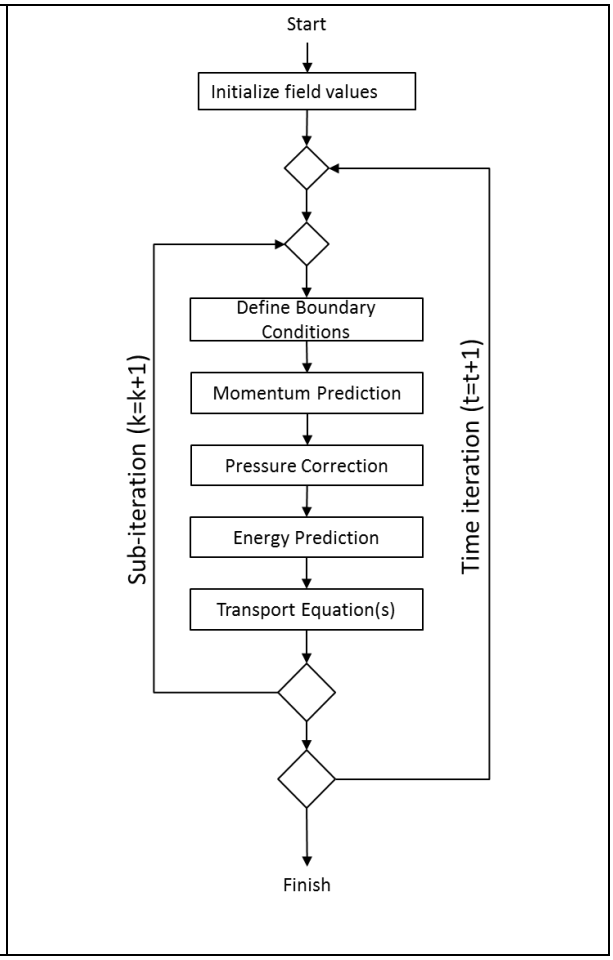

Figure 2-7: New compressible SIMPLE algorithm

As presented by Archambeau et al. [91], the SLK algorithm is highly efficient for inviscid flow problems, assuming the CFL number is below 0.5. To achieve a non-iterative algorithm, the algorithm assumes the convective contribution is negligible to the acoustic contribution to the mass flux. If this is not true, the continuity equation is fulfilled only at the conclusion of the acoustic prediction step, not at

the end of each iteration. Therefore, the SLK algorithm is greatly limited by the CFL number to remain stable and accurate.

2.4.3 New Compressible (SIMPLE) Algorithm

To improve upon the on the SLK compressible flow algorithm in *Code_Saturne*, a number of changes were made by the author. To ensure the governing equations are satisfied at each time iteration and to increase stability, a SIMPLE-type algorithm was adopted by adding a pressure correction step after the momentum prediction. The mass flux was interpolated with an AUSM$^+$-up scheme instead of upwinding the flux. Similarly, the pressure for convective terms were interpolated with the AUSM$^+$-up scheme. The AUSM$^+$-up scheme eliminates the need to use the Rhie-Chow interpolation for the pressure correction equation [92]. The implementation of the AUSM$^+$-up scheme is explained in the following section. And as discussed earlier, a 2nd order upwind scheme with a slope limiter was implemented to increase spatial accuracy for compressible flows.

The new algorithm retains the acoustic prediction step, Eq. 2.136, because it was observed to increase the rate of convergence and the step is computationally inexpensive compared to the rest of the algorithm. From the acoustic prediction, the density is updated via the ideal gas equation and the mass flux is updated by Eq. 2.137. This is followed by the solution of the momentum equation.

To ensure the continuity equation is satisfied with the newly predicted velocity, a pressure correction equation is constructed and solved. Although similar to the pressure correction equation constructed for incompressible flow, the new equation needs to account for the compressibility of the flow. The momentum equation, Eq. 2.138, is solved for the velocity field u_i^{**} with the density field ρ^* and pressure field P^* that was obtained from the acoustic prediction step.

$$\left(\frac{\Omega}{\Delta t}\delta_{ij} + A_{ji}^D\right)\rho^* u_i^{**} + \sum A_{ij}^N u_i^{**} = -\nabla_j P^* + \frac{\Omega}{\Delta t}\rho^n u_j^n + S^n \tag{2.138}$$

$$\left(\frac{\Omega}{\Delta t}\delta_{ij} + A_{ji}^D\right)\rho^* u_i^{***} + \sum A_{ij}^N u_i^{**} = -\nabla_j P^{**} + \frac{\Omega}{\Delta t}\rho^n u_j^n + S^n \tag{2.139}$$

A momentum equation, Eq. 2.139, with the velocity field u_i^{***} and pressure field P^{**} is constructed that satisfies the continuity equation. Subtracting Eq. 2.138 from Eq. 2.139 and taking the divergence of the resulting equation yields:

$$\nabla_i \cdot (\rho^* u_i^{***}) - \nabla_i \cdot (\rho^* u_i^{**}) = -\nabla_i \cdot \frac{1}{A_p}\nabla_j (P^{**} - P^*) \tag{2.140}$$

where

$$A_p = \left(\frac{\Omega}{\Delta t}\delta_{ij} + A_{ji}^D\right) + \sum A_{ij}^N \tag{2.141}$$

As with the incompressible flow algorithm in *Code_Saturne*, the coefficient A_p can be estimated by $(\Delta t)^{-1}$.

Unlike for incompressible flows where the term $\nabla_i \cdot (\rho^* u_i^{***})$ was assumed to be zero because divergence of the velocity is zero in incompressible flows, the term is unknown. An expression can be constructed for the unknown term using the continuity equation and expanding the equation.

$$\frac{\Omega}{\Delta t}(\rho^{**} - \rho^n) = -\nabla_i \cdot (\rho^{**} u_i^{***}) = -\nabla_i \cdot (\rho^* u_i^{***} + \rho' u_i^{**} + \rho' u_i') \tag{2.142}$$

where $\rho' = \rho^{**} - \rho^*$ and $u_i' = u_i^{***} - u_i^{**}$. The last term of the expression on the right can be neglected under the assumption that the product of the two corrections quickly converges to zero. The density correction in the equation can be expressed as a pressure correction using ideal gas equation and substituted into Eq. 2.142 to give:

$$\frac{1}{\Delta t}\frac{1}{c^2}\delta P + \nabla_i \cdot \left(\frac{1}{c^2} u_i^{**} \delta P\right) - \nabla_i \cdot \frac{1}{A_p}\nabla_j \delta P = -\frac{1}{\Delta t}(\rho^* - \rho^n) - \nabla_i \cdot (\rho^* u_i^{**}) \tag{2.143}$$

where

$$\delta P = P^{**} - P^* \tag{2.144}$$

After solving the pressure correction for the corrected pressure field, the velocity field, mass flux, and density field can be corrected.

$$u_j^{***} = u_j^{**} - \frac{1}{\rho^*}\frac{1}{A_p}\nabla \delta P \tag{2.145}$$

$$\rho^{**} u^{***} = \rho^* u^{**} - \frac{1}{A_p}\nabla \delta P \tag{2.146}$$

$$\rho^{**} = \rho^* + \frac{1}{c^2}\delta P \tag{2.147}$$

The last step in the algorithm is to solve for the total energy equation, Eq. 2.3, with the new density, pressure, and velocity fields.

2.5 Residual

To ensure convergence in the newly implemented algorithm, the residuals of the governing equations are calculated at the end of each iteration and are monitored. The residual for the continuity equation is:

$$R(\rho) = \sum_{i\ cells}^{n} \left| \frac{\Omega}{\Delta t}\left(\rho_i^{n+1} - \rho_i^n\right) + \nabla \cdot \left(\rho_i^{n+1} u_i^{n+1}\right) \right| \tag{2.148}$$

The residual for the momentum equation is:

$$R(u) = \sum_{i\ cells}^{n} \left| \frac{\Omega}{\Delta t}\left(\rho^{n+1} u_i^{n+1} - \rho^n u_i^n\right) + \nabla \cdot \left((\rho u)_j^{n+1} u_i^{n+1}\right) - \nabla \cdot \mu_{eff} \nabla u_i^{n+1} + \nabla P^{n+1} - S \right| \tag{2.149}$$

Similarly, the residual for the energy equation is:

$$R(e) = \sum_{i\ cells}^{n} \left| \frac{\Omega}{\Delta t}(\rho_i^* - \rho_i^n) + \nabla_i \cdot \left(\rho u_i \left(e + \frac{P}{\rho} \right) \right) - \nabla_i \cdot \left(u_j \cdot \tau_{ji}\right) + \nabla_i \cdot q_i \right| \tag{2.150}$$

The residual for the continuity equation is left unweighted. While the residual for the momentum and energy equations are weighted by Eq. 2.151 and 2.152, respectively.

$$RW_i(u) = \sum_{i\ cells}^{n} \frac{\Omega}{\Delta t} \rho^{n+1} u_i^{n+1} \tag{2.151}$$

$$RW(e) = \sum_{i\ cells}^{n} \frac{\Omega}{\Delta t} \rho^{n+1} e^{n+1} \tag{2.152}$$

The number of inner loops per time step within the new compressible flow algorithm was altered to ensure that residual for the continuity equation was less than 10^{-12}, and 10^{-6} for the momentum and energy equation.

2.6 Boundary Conditions

Within the computational domain, the governing equations control the dynamics of the flow, however the boundaries of the domain need to be carefully treated to properly model an application. In

Code_Saturne, boundary conditions are needed for the convective terms, diffusion terms, and calculation of cell gradients. Using a finite volume formulation, *Code_Saturne* imposes the boundary conditions at the boundary faces.

Numerically, three types of the boundaries can be imposed: Dirichlet, Neumann, and Robin boundary conditions. Dirichlet imposes a fixed value, Neumann imposes a flux, and Robin imposes a combination of a value and a derivative flux at the boundary face. Normally, only the Dirichlet and Neumann boundary conditions are used.

For incompressible flows, imposing the boundary conditions is a straightforward process. For inlet boundaries, the velocity vector and a zero-pressure gradient are imposed, along with turbulent scalars. For outlet boundaries, the pressure value is specified and a Neumann condition imposed for velocity. Wall boundaries use a Neumann condition for pressure and a Dirichlet condition for velocity with mass flux set to zero. Except for moving walls, the wall has a null velocity vector. Symmetric boundaries have Neumann conditions for all variables.

For compressible flows, the implementation of the boundary conditions is not as straightforward as for incompressible flows. Using the same method for the boundary condition as for incompressible flows leads to numerical instabilities. To overcome this, the characteristics of the boundaries need to studied [93]. There are 5 characteristics, or eigenvalues, for three-dimensional cases ($\lambda_1 = u - c$, $\lambda_{2,3,4} = u$, $\lambda_5 = u + c$).

Condition	λ_1	λ_2	λ_3	λ_4	λ_5	Specify
Subsonic Inflow	<0	>0	>0	>0	>0	P_o, T_o, α
Subsonic Outlet	<0	<0	<0	<0	>0	P
Supersonic Inflow	>0	>0	>0	>0	>0	All
Supersonic Outlet	<0	<0	<0	<0	<0	None

Table 2-6: Boundary characteristics

Subsonic inlet has four incoming and one outgoing characteristic, therefore the total pressure, total temperature, and flow angle α is imposed while the pressure is extrapolated from within the domain. Alternatively, the mass flux, total temperature, and flow angle can be imposed instead. Subsonic outlet has four outgoing and one incoming characteristic, the static pressure is imposed while the all other variables use a zero gradient. In supersonic flows, all the characteristics are incoming at the inlet and all the characteristics are outgoing for the outlet. All the variables are specified at a supersonic inlet and all the variables are extrapolated with a Neumann boundary condition for a supersonic outlet. Wall and symmetry boundaries are implemented in a similar fashion to incompressible flows.

For subsonic boundaries, the imposed total pressure and temperature need to be translated into the flow variables. *Code_Saturne* solves a Riemann problem at the boundary between an inner and an outer state to calculate the flow variables. If the diffusive and source terms are neglected, a set of quasi-linear Euler equations can be constructed:

$$\frac{\partial \vec{W}}{\partial t} + \frac{\partial}{\partial n}\vec{F}_n(\vec{W}) = 0 \tag{2.153}$$

where

$$\vec{F}_n(\vec{W}) = \sum_{i=1}^{3} n_i \vec{F}_i(\vec{W}) \tag{2.154}$$

$$\frac{\partial}{\partial n} = \sum_{i=1}^{3} n_i \frac{\partial}{\partial x_i} \tag{2.155}$$

The quasi-linear equation is orientated relative to the normal direction of the boundary face. The vector $\vec{W}$ is composed of the primitive variables ρ, u, v, w, and e. Using Riemann invariants and the equation of state, the set of the equations can be iteratively solved to determine the boundary variables.

Instead of setting up and solving a Riemann problem, isentropic relations can be used. Although both approaches resolve the inlet and outlet boundaries equally well, a method using isentropic relations was implemented by the author to allow for the mass flux to be imposed. The isentropic equations for total pressure and total temperature, respectively, are:

$$\frac{P_o}{P} = \left(1 + \frac{1}{2}(\gamma - 1)M^2\right)^{\gamma/\gamma - 1} \tag{2.156}$$

$$\frac{T_o}{T} = 1 + \frac{1}{2}(\gamma - 1)M^2 \tag{2.157}$$

The two equations are solved with the Newton method to find the Mach number and temperature at the boundary. Alternatively, if the mass flux and total temperature is imposed at the inlet, total temperature can instead be defined as:

$$T + \frac{1}{2}\frac{u^2}{c_p} = T_o \tag{2.158}$$

A quadratic equation can be formed from Eq. 2.156, and extrapolating the pressure and substituting in the definition of mass flow rate that leads to:

$$\frac{1}{2}\left(\frac{\dot{m}R}{PA}\right)^2 T^2 + c_p T - c_p T_o = 0 \tag{2.159}$$

where R, A, and c_p is the ideal gas constant, surface area, and specific heat at constant pressure, respectively. Solving the quadratic equation for the maximum root yields the boundary temperature and the other boundary variables. For subsonic outlet, the static pressure is simply imposed and a Neumann boundary conditions is used for all other flow variables as discussed earlier.

Lastly, periodic boundary conditions can be imposed for cases where the flow repeats, such as an impeller passageway or infinitely wide channel. Periodic boundaries are built by copying the cells of one boundary and then moving the cells by a periodic step. This set of cells is than joined and linked with their new neighbours, creating a set of halo cells that can transmit information of the flow field during the solution of the governing equations. The periodic step is a user-defined translation or rotation that will match the two periodic faces.

2.7 Sliding Mesh

The interface between a moving and a static mesh poses a problem in the solution of the flow field. At the interface between the two meshes, a numerical method must be constructed that allows for information of the flow field to be transferred across it unimpeded. The two common methods to linking the two meshes is an overset (chimera) mesh or a sliding mesh interface. An overset mesh involves two overlapping meshes where the flow field is interpolated back and forth. A sliding mesh interface is composed of two matching mesh geometries where the flow field is interpolated across the shared interface. Francois et al. [94] found that both methods give similar results but the sliding mesh scheme required much less memory and was slightly quicker.

The sliding mesh scheme in *Code_Saturne* operates by joining the two meshes at the interface together. A mesh joining algorithm constructs new sub-faces from the intersections of the edges as shown in Fig. 2-8. In Fig. 2-8, the bold solid line represents Mesh A, the bold dashed line represents Mesh B, and the lighter dashed line represents the reconstructed internal face.

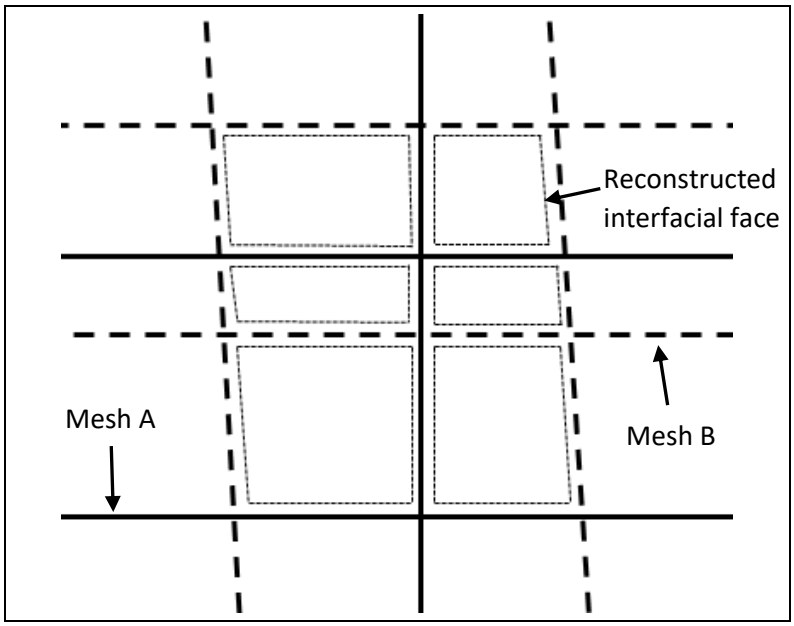

Figure 2-8: Mesh joining

The new sub-faces are then treated as internal faces and the fluxes are computed upon these new internal faces to compute the solution to the governing equation. The scheme has been shown to be conservative. In the next time iteration, the joined mesh is broken, rotated, and joined again. This process is conducted between the momentum prediction and pressure correction step.

The process in Fluent is quite similar to the sliding mesh algorithm in *Code_Saturne*, however Fluent constructs a zone in-between the two meshes. Where the two meshes join together, the zone is treated as an interior zone, but where the two meshes do not meet, a 'wall' zone is created. This scheme allows for the use of periodic repeats on the interface, allowing the use of a rotating mesh for a single passageway.

2.8 Turbulent Recycling Inflow for LES

The requirements for the inlet conditions for LES are much more demanding than RANS. As stated earlier, RANS rely upon the turbulent properties of the flow to be modelled, while LES simulates the large-scale eddies of the flow and models the small-scale features. To properly simulate a case where an inlet involves a turbulent inflow, it becomes necessary to impose a three-dimensional, time-dependent turbulent inflow. Many methods have been used to model the necessary turbulent inflow on a flat plate, such as the vortex method [95] and synthetic eddy method [96]. However, the method that yields the best results is simulating the inflow with a prior simulation, but this method adds additional computational

expense by requiring another simulation to be run. A compromise can be found by assuming that the mean boundary layer through the domain of interest can be reduced to a single curve through similarity variables. With this assumption, a scaled boundary layer from within the domain can be imposed onto the inlet. Lund et al. [34] developed an efficient method on this principle to generate a turbulent boundary layer at the inlet with desired parameters.

Below is a brief description of the method described by Lund et al. [97] that has been implemented into *Code_Saturne* by the author. The algorithm implemented here assumes that the pressure gradient zero and the flow is incompressible. The instantaneous velocity field can be decomposed into fluctuations u'_i and mean value $\bar{u}_i$.

$$u'_i(x,y,z,t) = u_i(x,y,z,t) - \bar{u}_i(x,y) \tag{2.160}$$

The coordinates x, y, and z denotes the streamwise, vertical, and spanwise directions, respectively. Similarly, *u*, *v*, and *w* denotes the streamwise, vertical, and spanwise velocity components, respectively. Splitting the velocity field into its mean and fluctuations allow for each quantity to be scaled independently. The mean velocity field can be rescaled according to the law of the wall for the inner boundary layer (Eq. 2.161) and defect law for the outer boundary layer (Eq. 2.162).

$$\bar{u}^{inner} = u_\tau(x) f_1(y^+) \tag{2.161}$$

$$U_\infty - \bar{u}^{outer} = u_\tau(x) f_2(\eta) \tag{2.162}$$

Where f_1 and f_2 are universal functions which are dependent upon the non-dimensional wall coordinate, y^+, and outer wall coordinate, η, respectively. The mean velocity at the recycle plane, $\bar{u}_{recy}$, and the inlet plane, $\bar{u}_{in}$, can be related with the law of the wall and the defect law leading to:

$$\bar{u}_{in}^{inner} = \gamma \bar{u}_{recy}(y_{in}^+) \tag{2.163}$$

$$\bar{u}_{in}^{outer} = \gamma \bar{u}_{recy}(\eta_{in}) + (1-\gamma) U_\infty \tag{2.164}$$

where gamma is the ratio of the friction velocity at the inlet to the recycle plane.

$$\gamma = \frac{u_{\tau,in}}{u_{\tau,recy}} \tag{2.165}$$

The friction velocity can be calculated at the recycle plane while the friction velocity at the inlet is unknown and has to be defined.

The velocity fluctuations of the inner and outer boundary layer at the inlet can be related from the recycle plane via:

$$(u')_{in}^{inner} = \gamma(u')_{recy}(y_{in}^{+}, z, t) \tag{2.166}$$

$$(u')_{in}^{outer} = \gamma(u')_{recy}(\eta_{in}, z, t) \tag{2.167}$$

The mean and fluctuating velocity components (Eq. 2.163, 2.164, 2.166, 2.167) can be assembled into a single, weighted function to give the velocity profile at the inlet.

$$u_{in} = \left[\bar{u}_{in}^{inner} + (u')_{in}^{inner}\right][1 - W(\eta_{in})] + \left[\bar{u}_{in}^{outer} + (u')_{in}^{outer}\right]W(\eta_{in}) \tag{2.168}$$

The weighting function $w(\eta)$ is defined by Lund et al. as:

$$W(\eta) = \frac{1}{2}\left\{1 + \tanh\left[\frac{\alpha(\eta - b)}{(1-2b)\eta + b}\right]\tanh^{-1}(\alpha)\right\} \tag{2.169}$$

where $\alpha = 0.4$ and $b = 0.2$.

The velocity normal to the wall can be decomposed in a similar manner into mean and fluctuation components, however the fluctuations can be assumed to be negligible. The mean normal velocity can be described as:

$$\bar{v}^{inner} = \bar{u}_{\infty}(x) f_3(y^{+}) \tag{2.170}$$

$$\bar{v}^{outer} = \bar{u}_{\infty}(x) f_4(\eta) \tag{2.171}$$

The normal velocity can be scaled, but in reality the mean normal velocity in a boundary layer is small and calculations can be approximated by directly extrapolating the values from the recycle plane.

$$\bar{v}_{in}^{inner} = \bar{v}_{recy}(y_{in}^{+}) \tag{2.172}$$

$$\bar{v}_{in}^{outer} = \bar{v}_{recy}(\eta_{in}) \tag{2.173}$$

The velocity in the spanwise direction is assumed to be negligible.

In solving the set of equations for rescaling the flow, u_τ and δ at the recycle plane can be determined directly from the flow. However, at the inlet the boundary layer thickness is imposed by the user and the friction velocity is equivalent to

$$u_{\tau,in} = u_{\tau,recy}\left(\frac{\theta_{recy}}{\theta_{in}}\right)^{1/8} \tag{2.174}$$

In the scheme that Lund et al. suggested, the fluctuations of the turbulent boundary layer abruptly transitions to the freestream flow at the inlet. The sharp transition negatively affects the outer boundary layer. To transition the boundary layer to the freestream, Bohr [98] suggested using Heaviside function to smoothly limit the fluctuations outside the boundary layer.

$$H(\emptyset) = \begin{cases} 1 & if\ \emptyset\ < -\epsilon \\ \frac{1}{2}\left[1 - \frac{\emptyset}{\epsilon} - \frac{1}{\pi}\sin\left(\frac{\pi\emptyset}{\epsilon}\right)\right] & if\ |\emptyset| \leq\ \epsilon \\ 0 & if\ \emptyset\ >\ \epsilon \end{cases} \quad (2.175)$$

where

$$\emptyset = y - 1.2\delta_{in} - \epsilon \quad (2.176)$$

$$\epsilon = 0.25\delta_{in} \quad (2.177)$$

The function begins to limit the fluctuations at $1.2\delta_{in}$ and eliminates the fluctuations beyond $1.3\delta_{in}$.

2.9 Conclusion

The numerical methods that are implemented in ANSYS Fluent and *Code_Saturne*, which are used in this study, have been described in detail. A number of changes were made to the baseline code of *Code_Saturne* by the author and were discussed in further details in this chapter which allows for compressible flows inside of turbomachinery to be modelled. In *Code_Saturne*, a new compressible flow algorithm, similar to the SIMPLE method, was implemented along with the capability to model flows with rotating reference frames. The new algorithm made use of the AUSM^{+}-up flux splitting scheme for mass flux discretization and convective pressure terms. To improve numerical accuracy in the presence of shocks and discontinuities, a 2nd-order MUSCL scheme was included. In the following chapter, a series of validation tests were conducted to ensure the numerical accuracy of the new algorithm.

In addition to the implementation of a new compressible flow algorithm, a turbulent recycling inflow method for large-eddy simulations was implemented into *Code_Saturne* by the author. The method allows for the generation of an accurate, turbulent flow at the inlet while being relatively computationally inexpensive. The usage of this method is discussed in Chapter 5.

3. Validation of New Compressible Flow Algorithm

Five different validation cases were used to test the new algorithm for compressible, rotating flows that was introduced in section 2.4.3. The cases were selected to validate the capability of the new algorithm to accurately resolve shocks with high-order schemes, turbulent flows, and rotating flows. The Sod shock tube and a channel flow with a bump was used to test the accuracy for inviscid flows in one- and two-dimensional flows, respectively. The Sajben diffuser and RAE2822 airfoil was modelled to demonstrate the accuracy of RANS modelling with a shock for internal and external flows. Finally, the NASA Low-Speed Centrifugal Compressor was modelled to demonstrate the new compressible flow algorithm in turbomachinery applications with a rotating frame. Unless otherwise noted, 2nd-order schemes for spatial discretization and 1st-order implicit time scheme were used.

3.1 Sod Shock Tube

To compare the accuracy of several different numerical schemes, Sod [99] used a shock tube problem with several discontinuities to assess the order of accuracy of schemes. The shock tube problem is in fact composed of three discontinuities: an expansion fan, a contact discontinuity, and a shock wave. The problem assumes the flow is inviscid and one-dimensional. After being used by Sod to compare the accuracy of schemes in capturing discontinuities, the problem has become a standard test case and been accordingly called Sod shock tube problem.

The case is initialized with a gas at rest, but with two regions of gas with differing pressure and density separated by an imaginary diaphragm, as shown in Fig. 3-1. Temperature of both regions are equal. At t=0 s, the diaphragm is broken. A shock wave propagates to the right and an expansion wave to the left. In between the shock and expansion waves, a contact discontinuity slowly drifts to the right. Between the discontinuities, the flow variables are ideally constant.

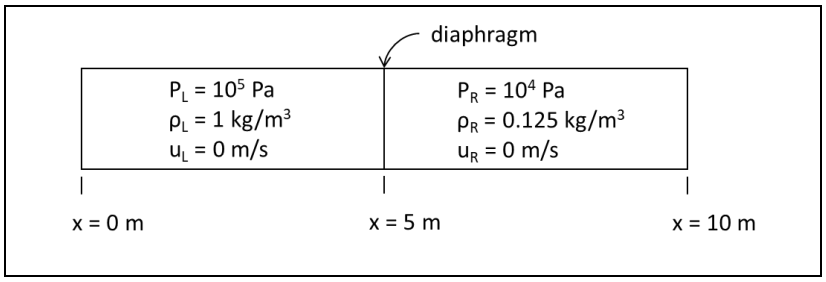

Figure 3-1: Initial conditions of Sod shock tube

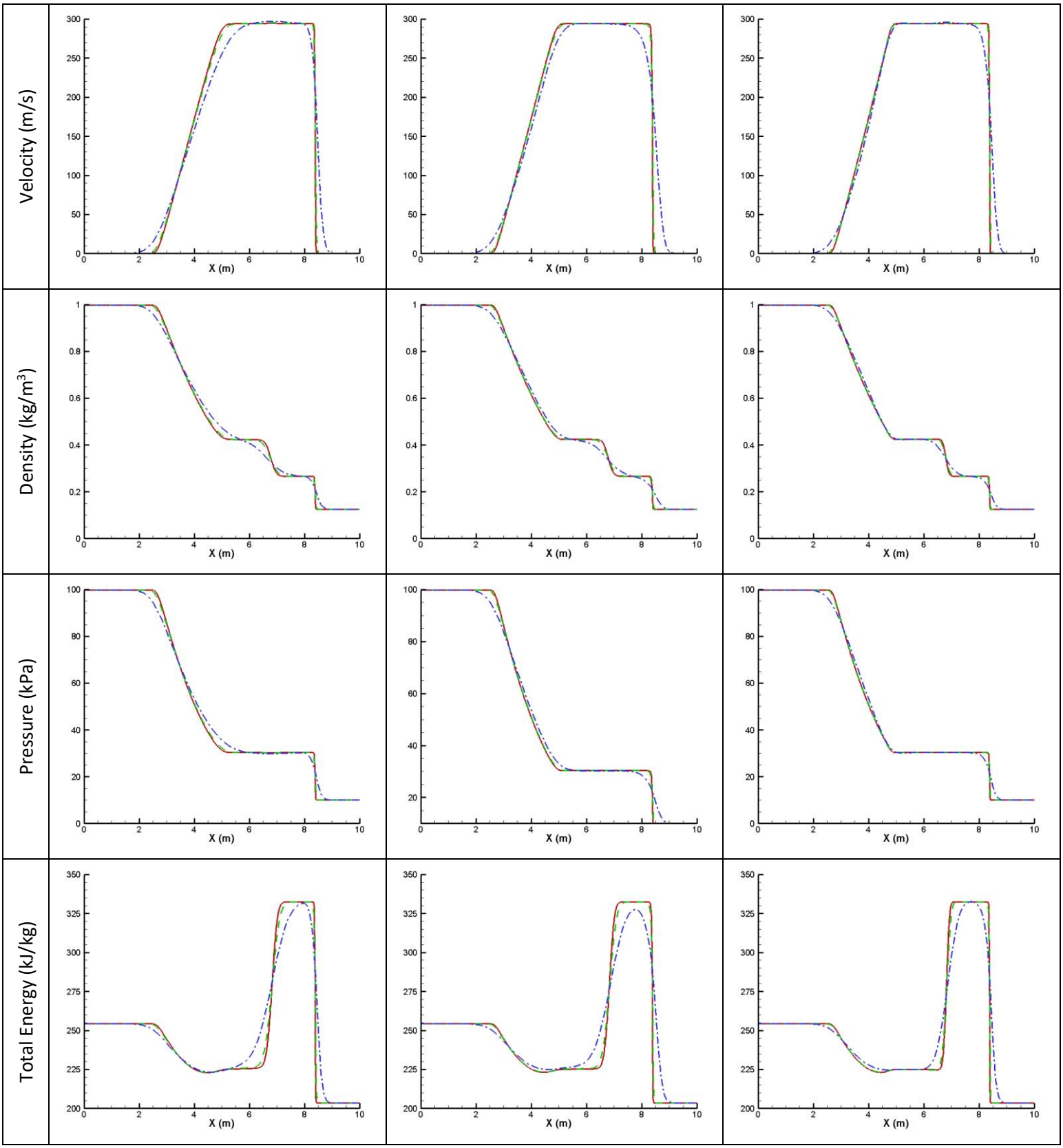

Figure 3-2: Sod shock tube problem (---- 1000 cells, - - - - 500 cells, - · - · - 100 cells)

Sod shock tube problem was used to test the default (SLK) compressible flow algorithm in *Code_Saturne* and the new compressible flow algorithm with first- and second-order schemes. The default algorithm in *Code_Saturne* uses first-order schemes for the mass flux and convective terms. A time step was selected to maintain the CFL number below 0.2 and results were collected 0.0062 s after the diaphragm was broken. The results are shown in Fig. 3-2.

The SLK algorithm gives fairly accurate resolution of the shock tube problem and as expected the accuracy of the results improves with an increase of mesh resolution. However, comparing the 1st-order results of new algorithm to the original SLK algorithm, the SLK algorithm overshoots the velocity prediction while undershooting the density prediction between the expansion and the shock waves. Even for the finer meshes, there is still a bump in the velocity profile at the location of the contact discontinuity. The SLK algorithm does give a sharper resolution of the shock wave, which is due to the velocity using a 2nd-order centered-scheme for the mass flux interpolation. Alternatively, the new algorithm yields a sharper resolution of the expansion wave. As expected, increasing the order of the convective schemes to 2nd-order for the new algorithm improves the resolution of the shock tube problem. However, using a 2nd-order scheme for the density discretization leads to a prediction of a bump in the velocity profile at the contact discontinuity.

3.2 Channel Flow with Bump

To assess the numerical accuracy of the algorithm in two-dimensions, Rizzi and Viviand [100] proposed a case with a transonic channel flow with a bump at the GAMM workshop in 1981. This case assumes the flow is inviscid. The geometry of the problem is given in Fig. 3-3, with a total pressure and temperature assigned at the inlet to produce the desired inlet Mach number and a static pressure at the outlet. For supersonic flows, all of the flow variables are imposed at the inlet and the flow is extrapolated at the outlet. Inviscid wall boundary conditions are imposed at the top and bottom of the domain. The bump in the channel is centered at 1.5L and has a chord of 1L. For subsonic and transonic flows, the bump has a height of 0.1L, and for supersonic flows the bump has a height of 0.04L.

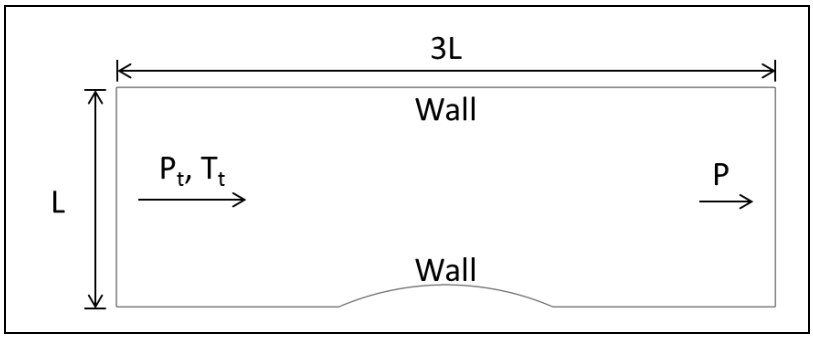

Figure 3-3: Sketch of a channel flow with a bump

For the test case, three different inlet Mach numbers are considered: 0.1, 0.675, and 1.4. At Mach 0.1, the flow is purely subsonic and should ideally by symmetric across the bump in the channel. At Mach 0.675, the flow is transonic and a shock develops on the bump. At Mach 1.4, the flow is completely supersonic. An initial shock wave forms at the front of the bump which is reflected off the top wall where it interacts with a second shock wave that forms at the end of the bump. The initial shock wave reflects a second time off the lower wall. To assess the accuracy of the algorithm on different resolutions of meshes, three different mesh sizes were generated: 75x40, 159x80, 225x120.

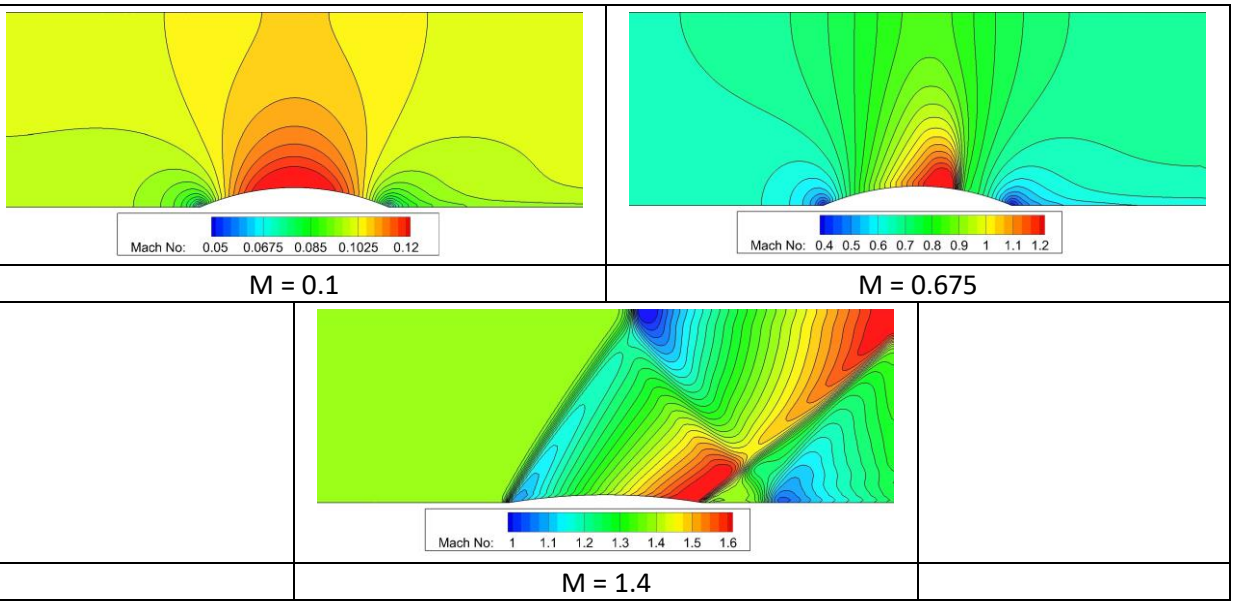

M = 0.1 | M = 0.675

M = 1.4

Figure 3-4: Mach contours for a channel flow with a bump

Shown in Fig. 3-4 are the Mach contours on the 159x80 mesh of the three tested Mach numbers. Shown below in Fig. 3-5 is the Mach distribution on the upper and lower walls for the three different mesh resolutions and three test Mach numbers. At M=0.1, the three meshes show good agreement except for the low-resolution mesh on the lower wall, which slightly under predicts the Mach number. At M=0.675, the low-resolution mesh predicts a diffused shock, while the medium and high resolution meshes predict a much sharper shock on the bump. The three meshes are good agreement on the upper wall Mach

distribution. At M=1.4, three meshes predict a very similar shock structure, however like the transonic case, the high resolution meshes yields sharper shocks. Overall, the new algorithm gives a good prediction for a channel flow with a bump.

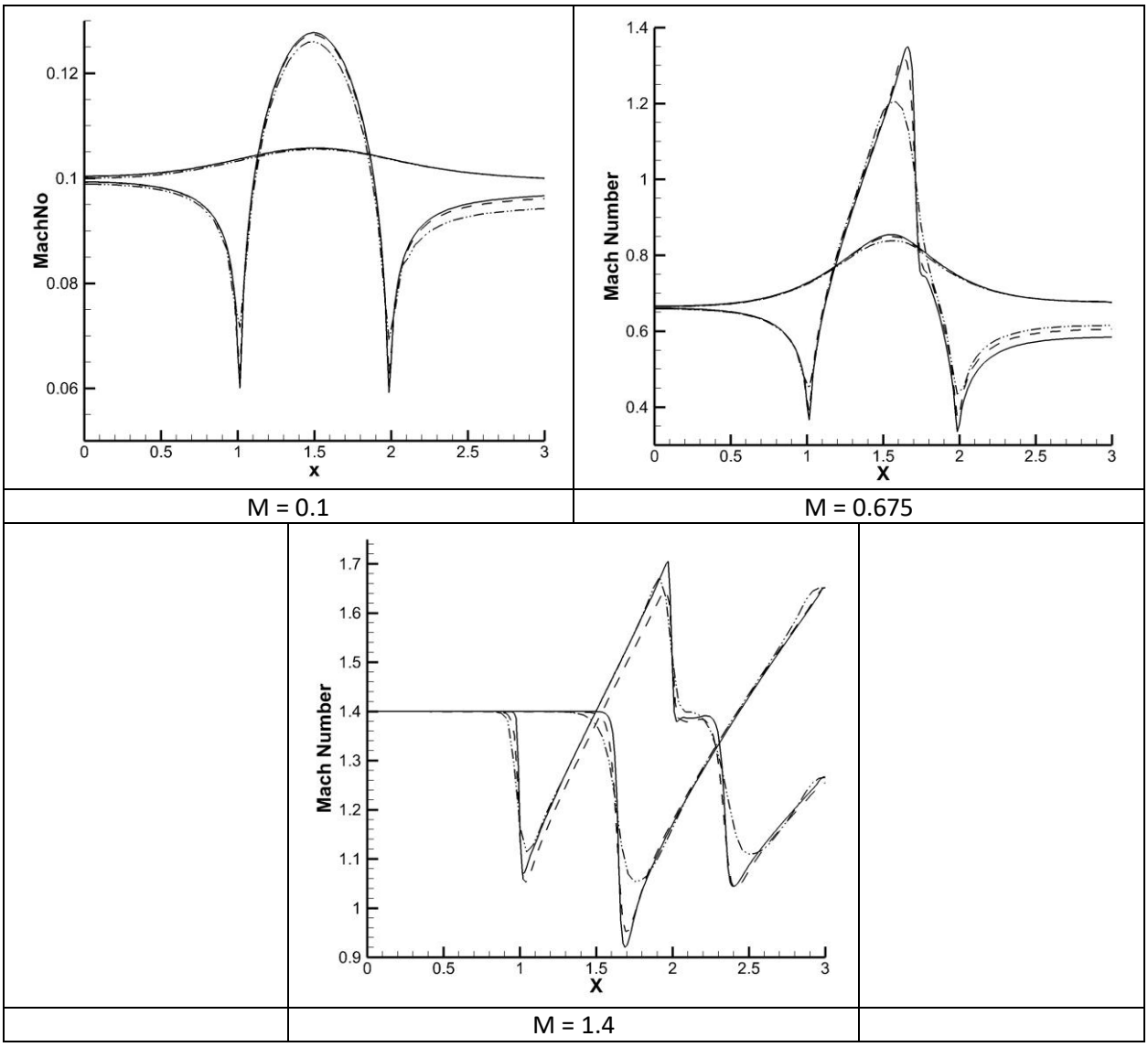

Figure 3-5: Mach distribution for a channel flow with a bump (— 225x120, – – 159x80, – ·· – 75x40)

3.3 RAE 2822 Airfoil

To test the capability of modelling turbulence with the new algorithm, the transonic RAE2822 airfoil is simulated. The RAE2822 airfoil was experimentally tested and published by the AGARD advisory group [101] to provide validation data for numerical models. Experimental data was published for

freestream Mach numbers of 0.600 to 0.745, angles of 2.40˚ to 3.19˚, and Reynolds number of 2.7 to 6.5 ($x10^6$). Pressure distribution and boundary layer measurements on the airfoil are given in the report.

To test the new algorithm, two flows conditions were selected which are given in Table 3-1. Case R1 yields a subsonic flow on the airfoil while case R2 yields a transonic flow with a shock forming on the upper surface of the airfoil.

Case	Angle	Mach No	Re
R1	2.40˚	0.676	$5.7x10^6$
R2	2.92˚	0.725	$6.5x10^6$

Table 3-1: Flow parameters for the RAE2822 airfoil

The chord length of the airfoil is 0.61 m. An inlet boundary was imposed 10c upstream of the leading edge of the airfoil and a pressure outlet boundary 14c downstream of the trailing edge of the airfoil. Total pressure and temperature to obtain the desire Mach number was specified at the inlet and a static pressure of 58175.19 Pa was specified at the outlet. Symmetric boundaries were placed 14c above and below the airfoil. A 2D mesh was generated for the two cases, shown in Fig. 3-6, had a mean y^+ of 25.5 and contained 837216 cells. Turbulence on the airfoil was modelled with the k-ω SST model using a wall function. A turbulence intensity of 2% was specified at the inlet.

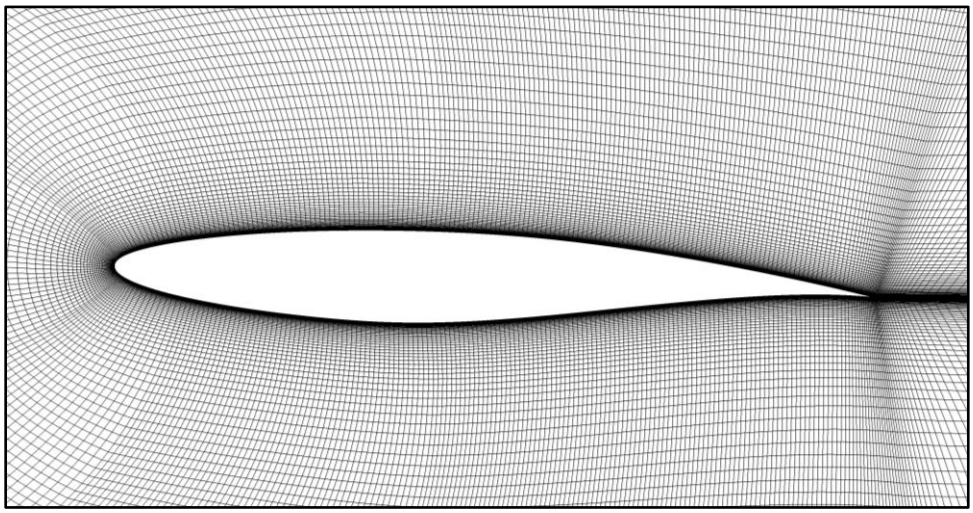

Figure 3-6: Mesh of RAE2822 airfoil

The Mach contours for the two cases are shown in Fig. 3-7. For case R1, the flow remains subsonic on the airfoil. While for case R2, with a higher angle of attack and freestream Mach number, the flow on airfoil becomes supersonic and a shock forms near the midpoint of the airfoil. Shown below in Fig. 3-8 is the pressure distribution for the two cases compared to experimental results for the modelled flow conditions. The new algorithm predicts the pressure distribution on the airfoil for both cases quite well, however there is a slight deviation in the pressure distribution on the upper surface of the airfoil after the leading edge. The deviation may be caused by the assumption of a completely turbulent flow, neglect of

the turbulence transition from a laminar to turbulent flow, and non-wall resolving boundary layer mesh. As with case R1, the new compressible flow algorithm predicts pressure distribution for case R2 quite well too, except for the leading edge. The new algorithm does correctly predict the shock position for case R2.

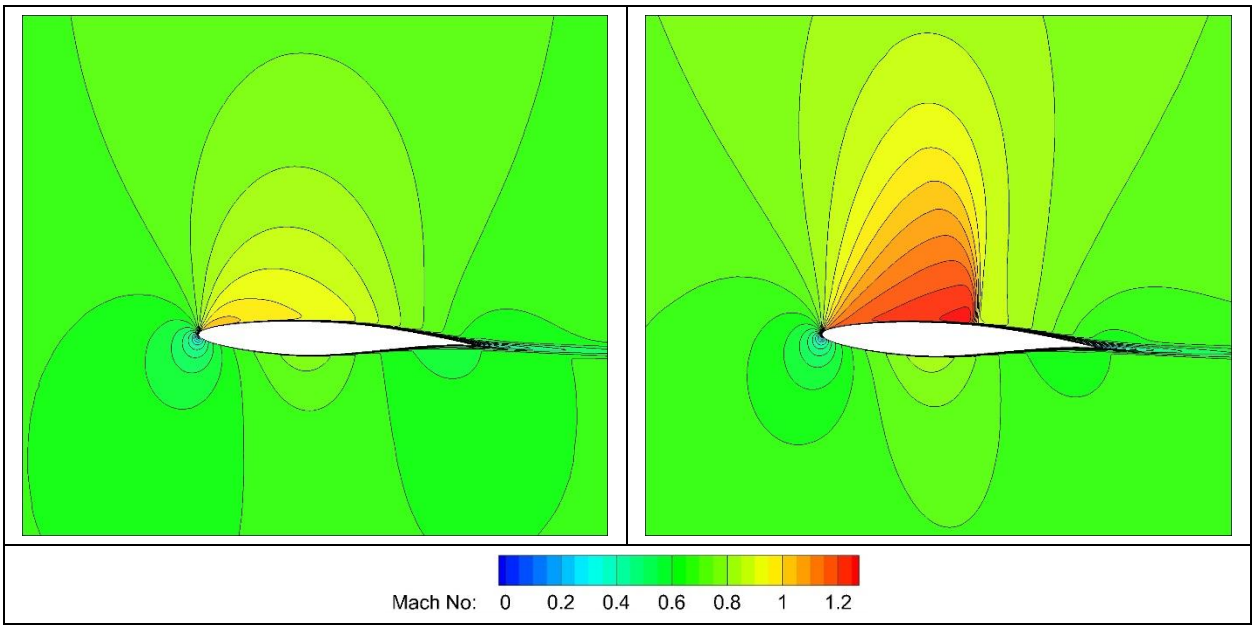

Figure 3-7: Mach contours of RAE2822 airfoil (Left – Case R1, Right – R2)

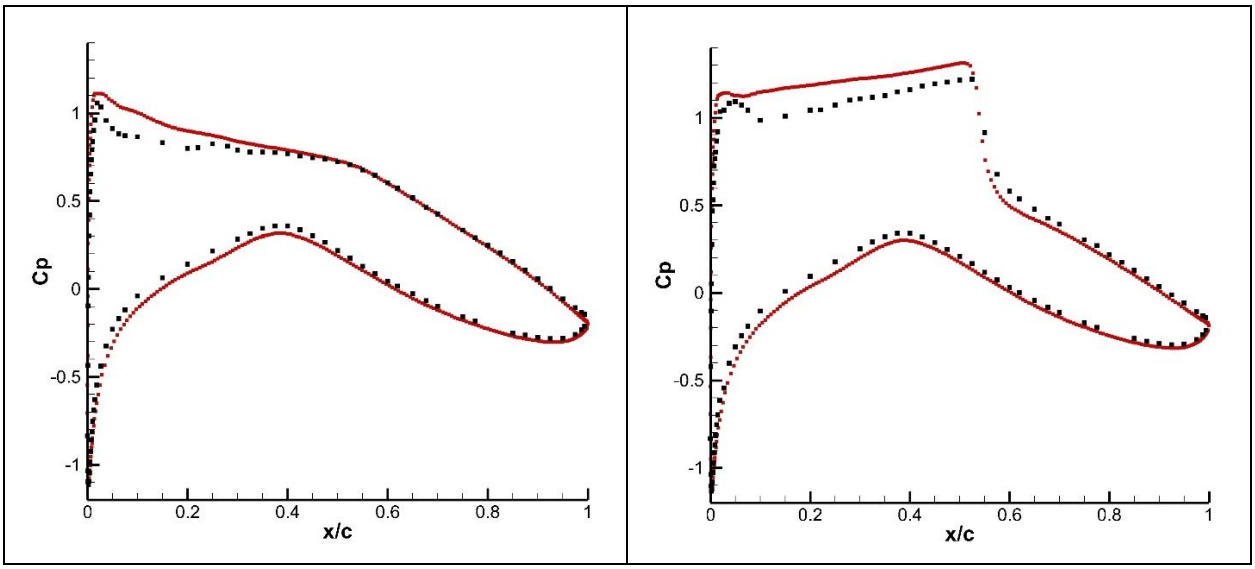

Figure 3-8: Pressure distribution on the RAE2822 airfoil (Left – Case R1, Right – R2) (■ Exp [101], --- CFD)

3.4 Sajben Diffuser

A more challenging case to the RAE2822 airfoil is the transonic Sajben diffuser. The Sajben diffuser was originally an experimental study on transonic flows in convergent/divergent channels and was later

used by NASA as a validation case for numerical models. In the presences of a strong shock in the diffuser's throat, a shock/boundary-layer interaction (SBLI) occurs. The separation from the SBLI is amplified by the presence of an adverse pressure gradient in the diffuser. Although several flow conditions were investigated in the original studies, a weak and strong shock case with a back pressure of 0.82 and 0.72, respectively, are considered. The weak shock case fails to cause shock induced separation, but separation does form from the presence of an adverse pressure gradient. The strong shock does contain a shock induced separation. Due to the nature of the diffuser, the shock in the diffuser oscillates. Salmon et al. [102] experimentally found that the shock-displacement spectra for the weak shock was 60 and 230 Hz, and for the strong case was 217 Hz.

The geometry of the Sajben diffuser is shown in Fig. 3-9. The height of the throat is 0.0440 m. A total pressure of 135 kPa and a total temperature of 277.78 K is imposed at the inlet, and the static pressure is specified at the outlet. Turbulent intensity of 2% is prescribed at the inlet. A time step was chosen to keep the maximum CFL number to less than 0.75.

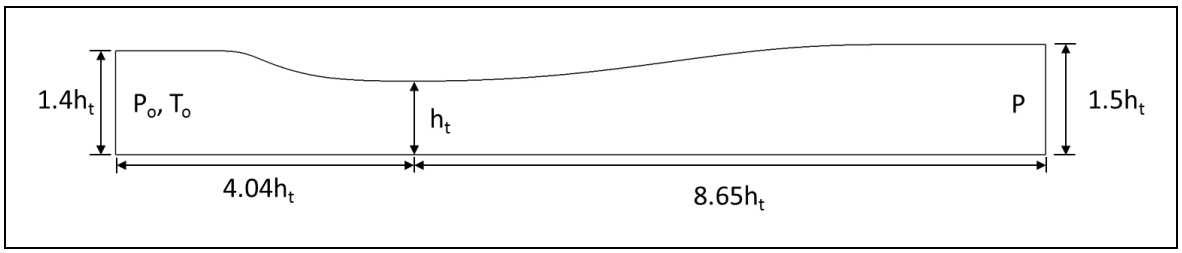

Figure 3-9: Geometry of the Sajben diffuser

Each of the cases were initialized by allowing for 10 flow through periods to be completed before the flow field was recorded. In preliminary tests, the weak shock case was observed to converge to a static state and fails to oscillate. The flow was therefore averaged over 3 flow though periods for the weak shock cases. For the strong shock cases, the flow was observed to oscillate and was averaged over 10 oscillations periods. Two different meshes were generated for this case with 17,472 and 14,664 cells and were called Mesh 4c and 4e, respectively. Mesh 4c and 4e had an average y^+ of 4 and 50, respectively. The two mesh densities were used to determine the effect that resolving the boundary layer had on predicted flow field. The unsteady RANS models k-ω SST and Spalarat-Allmaras were used.

Shown in Fig. 3-10 are the Mach contours of the weak shock case using the k-ω SST turbulence model. A weak shock is present slightly downstream of the throat of the diffuser. A pocket of flow separation, due to an adverse pressure gradient, forms further downstream.

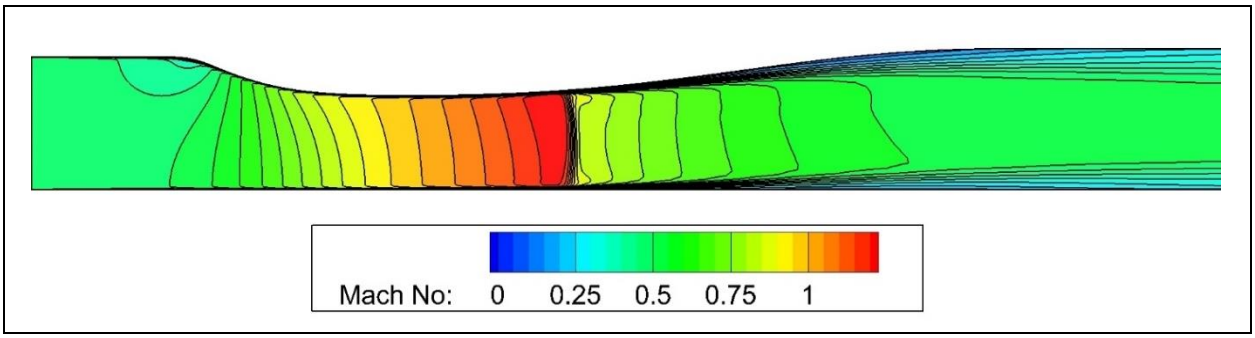

Figure 3-10: Mach contours of the weak shock case

The pressure distribution on the upper and lower walls are compared to published experimental results in Fig. 3-11. The presented results match experimental results reasonably well; however, the calculated shock was slightly downstream of the experimentally observed shock. Surprisingly the Spalart-Allmaras model gave the best prediction of the shock position on the wall resolved mesh with the k-ω SST model following close behind. On the coarser mesh, both turbulence models performed equally well.

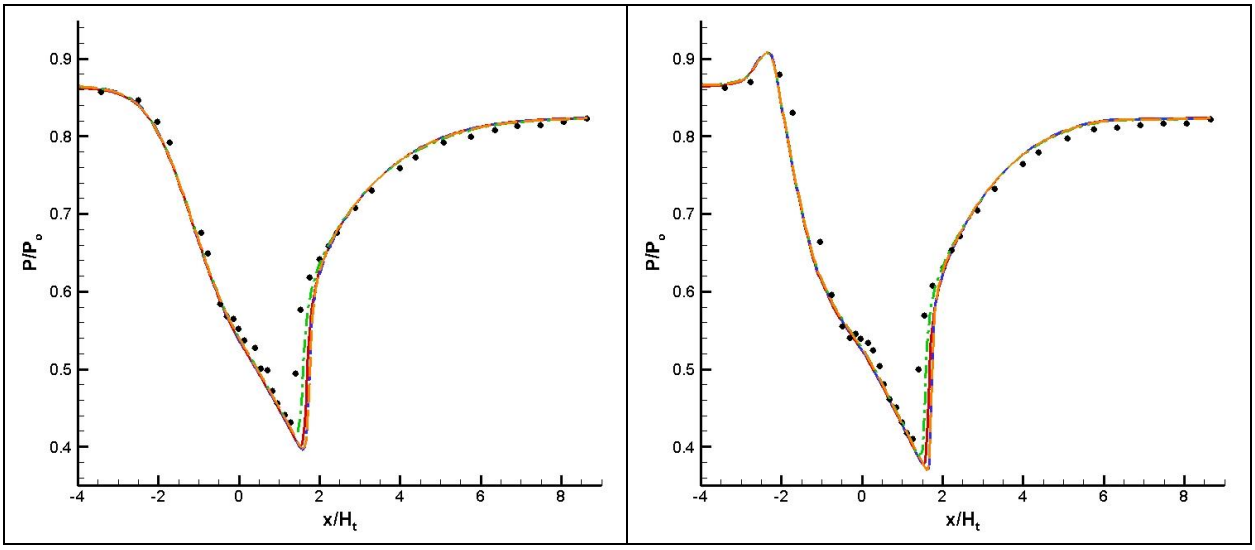

Figure 3-11: Pressure distribution for the weak shock case (left – lower wall, right – upper wall)
(● Exp, --- Mesh 4c – k-ω SST, - · - · - Mesh 4c – S-A, - - - Mesh 4e – k-ω SST, -- -- -- Mesh 4e – S-A)

The velocity profiles at several downstream locations from the shock are plotted in Fig. 3-12. At x/H_t = 1.73, the Spalart-Allmaras model under predicted while the k-ω SST model over predicted the velocity on the wall resolved mesh when compared to experimental data. On the coarser mesh, both models gave very similar predictions and over predicted the velocity. Although at this location, much variation is expected due to the shock being located nearby. Further downstream there is little variation observed between the different models and mesh resolution, and all the models under predicted the velocity.

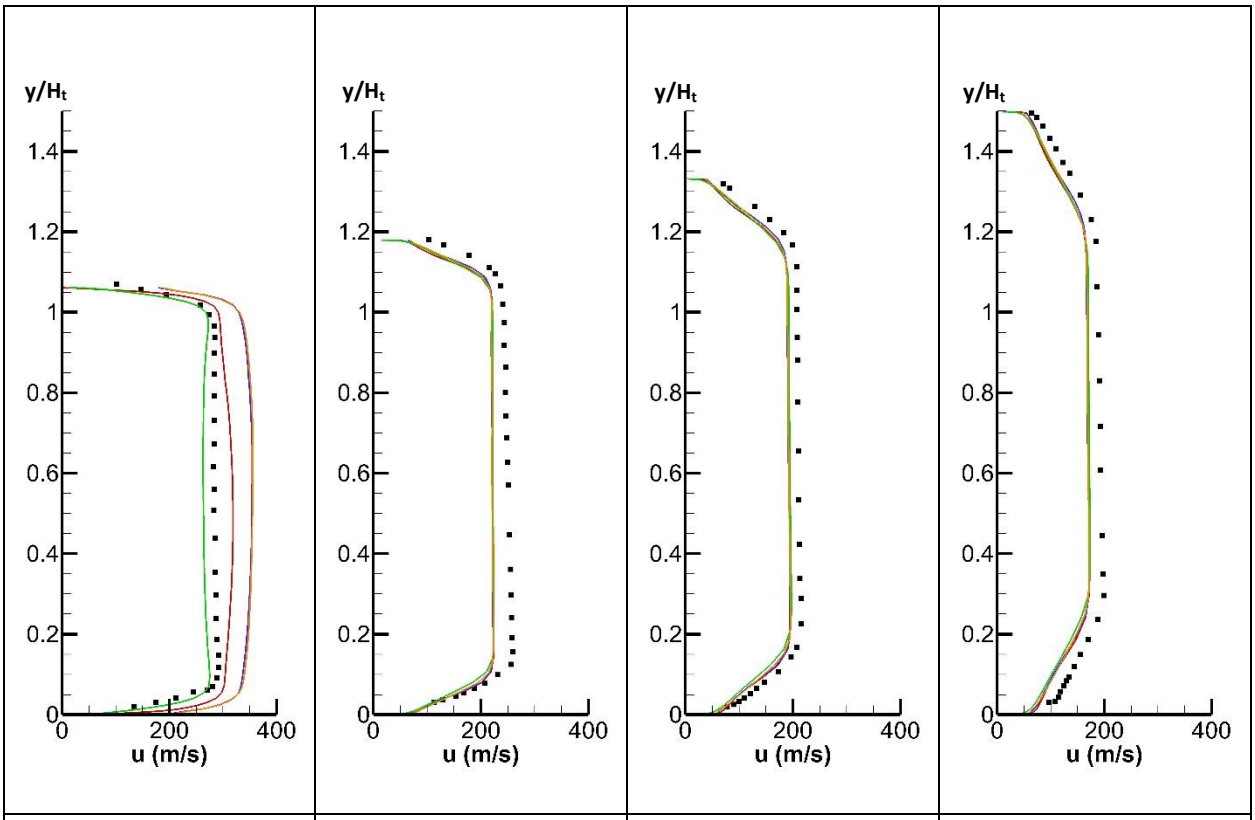

Figure 3-12: Velocity profiles for the weak shock case

(● Exp [102], --- Mesh 4c – k-ω SST, --- Mesh 4c – S-A, --- Mesh 4e – k-ω SST, --- Mesh 4e – S-A)

The strong shock case was much more difficult to test than the weak shock case. As with the weak shock, the k-ω SST and Spalart-Allmaras models were tested with a wall resolved mesh and non-wall resolved mesh (y^+ of approximately 4 and 50). Shown in Fig. 3-13 is the time averaged flow field with the k-ω SST model using a wall resolved mesh.

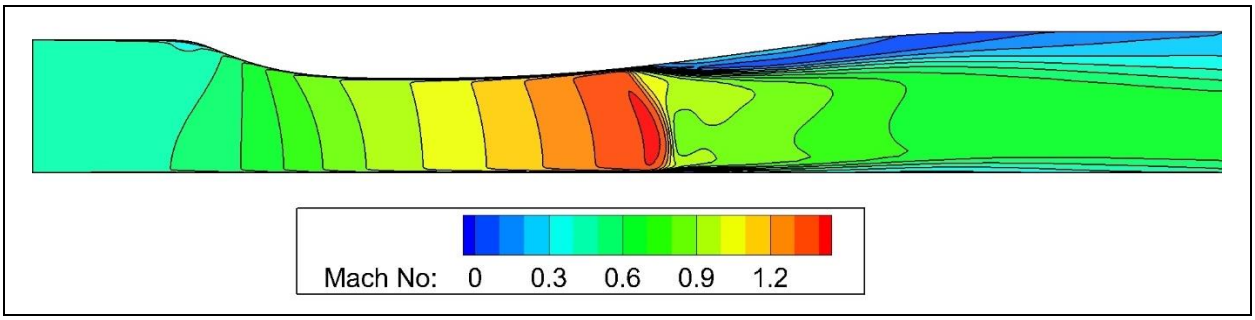

Figure 3-13: Mach contours of the strong shock case

The solution of the problem was found to be very dependent on the prediction of the boundary layer turbulence. If the mesh resolution at the wall was unresolved, both models were incapable of predicting the flow field and predicted that the zone of separation from the SBLI occurred on the low wall and no separation occurred on the upper wall. No oscillation of the shock was observed either. Using a

wall resolved mesh, the k-ω SST model gave a reasonable prediction of the flow field, but the Spalart-Allmaras model failed to accurately predict the flow field even with a finer mesh. Although the failure of the Spalart-Allmaras model was expected because the model is implemented with the assumption that the wall is not resolved and that the y^+ is greater than 30. These results are reflected in the pressure distribution plots in Fig. 3-14.

Shown in Fig. 3-15 are the velocity profiles at the several different cross-sections in the Sajben diffuser using the k-ω SST model and a wall resolved mesh. The prediction of the velocity field compares reasonably well with the published experimental results, although the boundary layer is slightly under predicted. The mass flow rate at the outlet was monitored and the main frequency was found to be 282.6 Hz compared to the experimental frequency of 217 Hz.

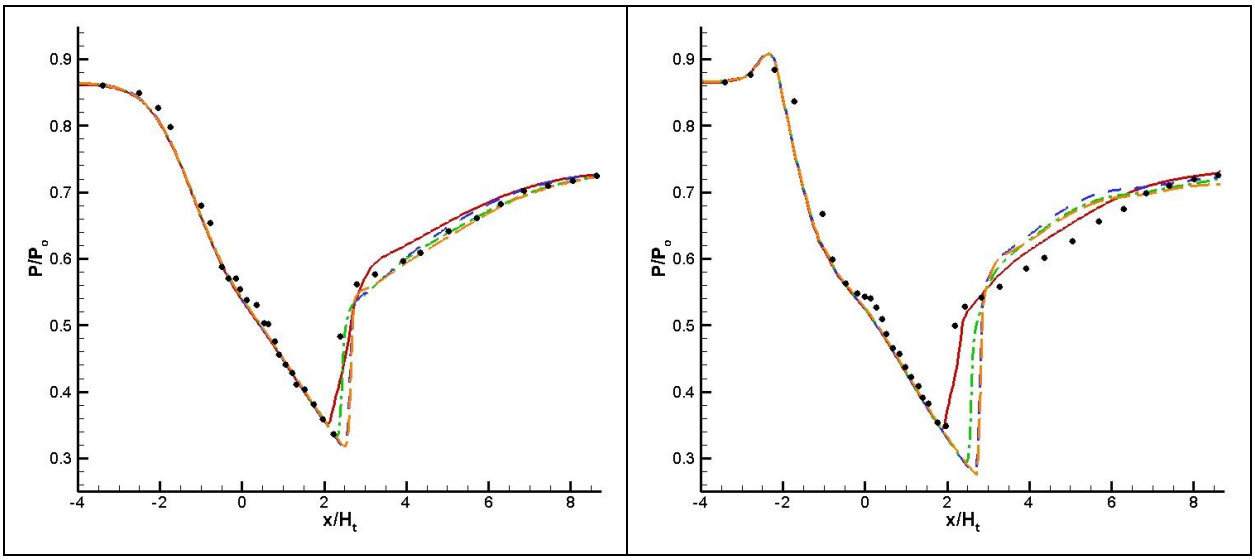

Figure 3-14: Pressure distribution for the strong shock case (left – lower wall, right – upper wall)
(● Exp, --- Mesh 4c – k-ω SST, - · - · - Mesh 4c – S-A, - - - Mesh 4e – k-ω SST, -- -- -- Mesh 4e – S-A)

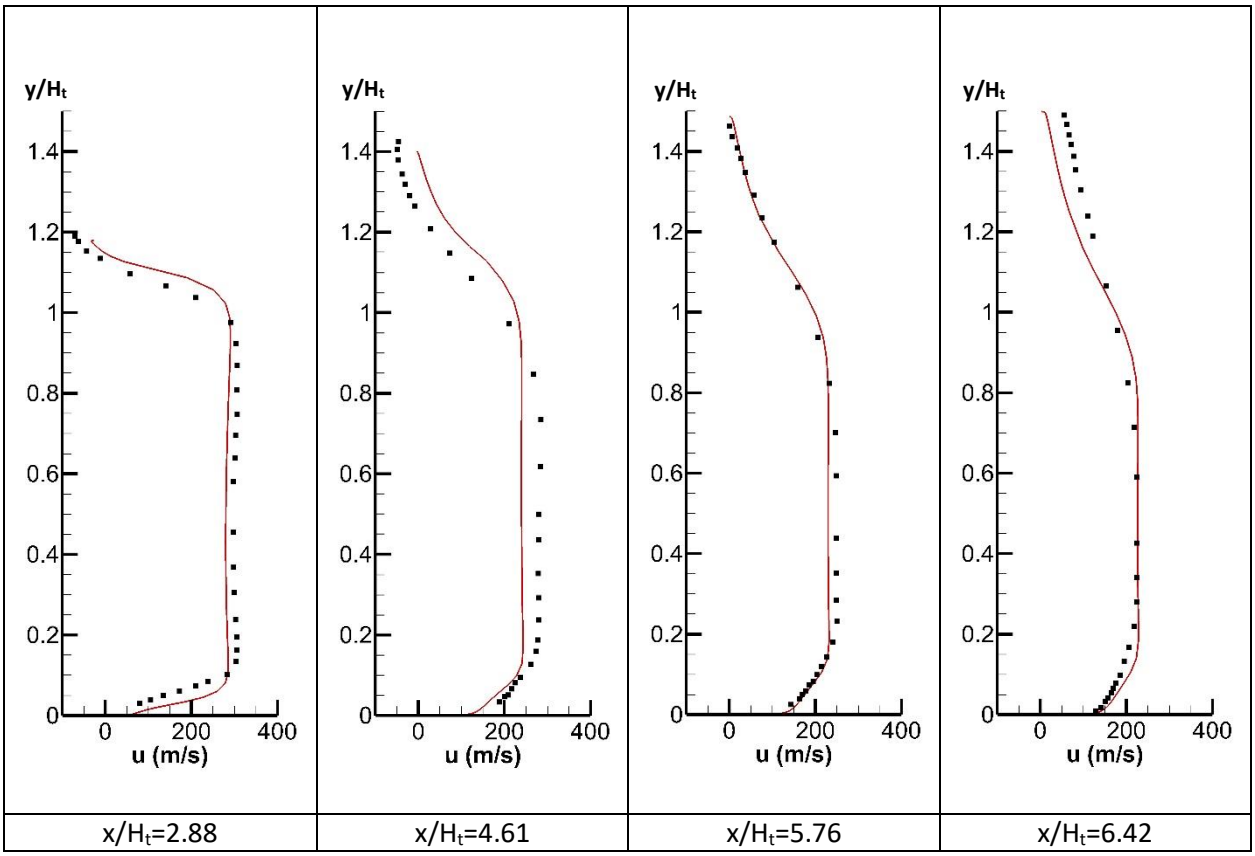

Figure 3-15: Velocity profiles for the strong shock case (● Exp [102], --- k-ω SST)

Before considering the next test case, the effect of the CFL number and the numerical method to impose the boundary conditions are considered. One of the benefits of the new compressible flow algorithm, which was implemented by the author was the removal of the strict CFL condition on the original compressible flow algorithm. The original algorithm was limited to a CFL number of less than 0.8, otherwise a numerical simulation would become unstable. The new algorithm allows for numerical simulations to be conducted at CFL numbers greater than one while remaining stable and producing accurate results. Fig. 3-16 demonstrates this capability by comparing numerical simulations that had CFL numbers of 0.75, 1.5, and 2.2. for the weak shock case. Increasing the CFL number had the effect of increasing the computing time per time iteration, however the total computing time for simulation is decreased by the need for less time iterations to reach a given simulation time. Higher CFL numbers were tested, but the numerical simulations were unstable. In Fig. 3-17 is the comparison of using isentropic relations versus Riemann invariants to calculate the boundary conditions at the inlet and outlet. Both methods for the calculations of the boundaries gave identical results.

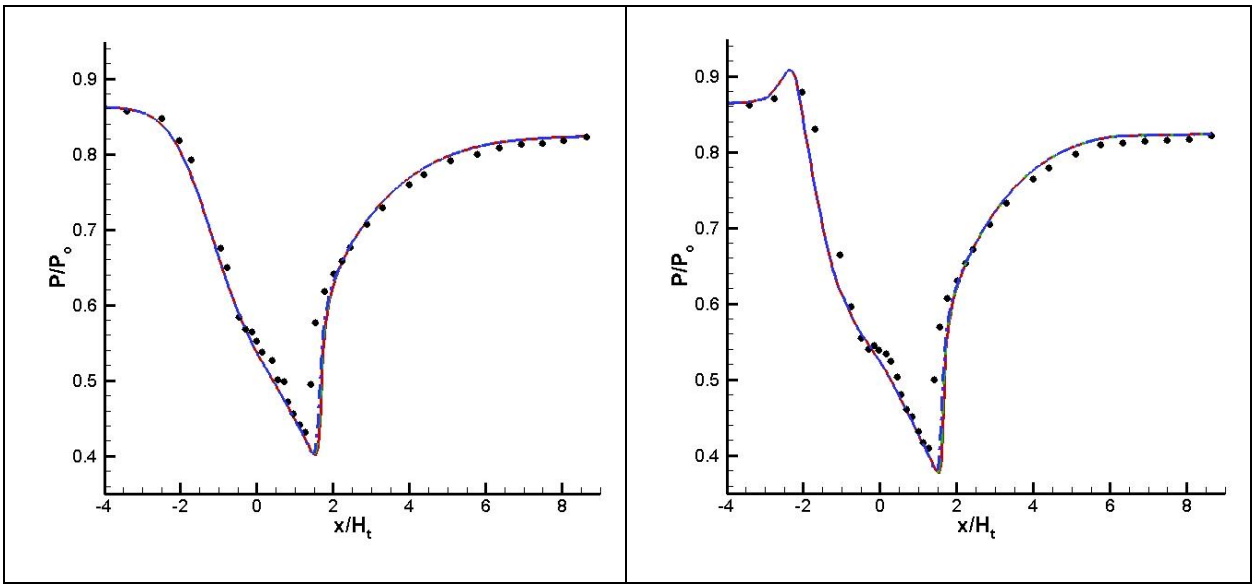

Figure 3-16: Pressure distribution for the weak shock case with CFL greater than unity
(left – lower wall, right – upper wall) (● Exp, --- CLF < 0 .75, - - - CFL < 1.5, - · - · - CFL < 2.2)

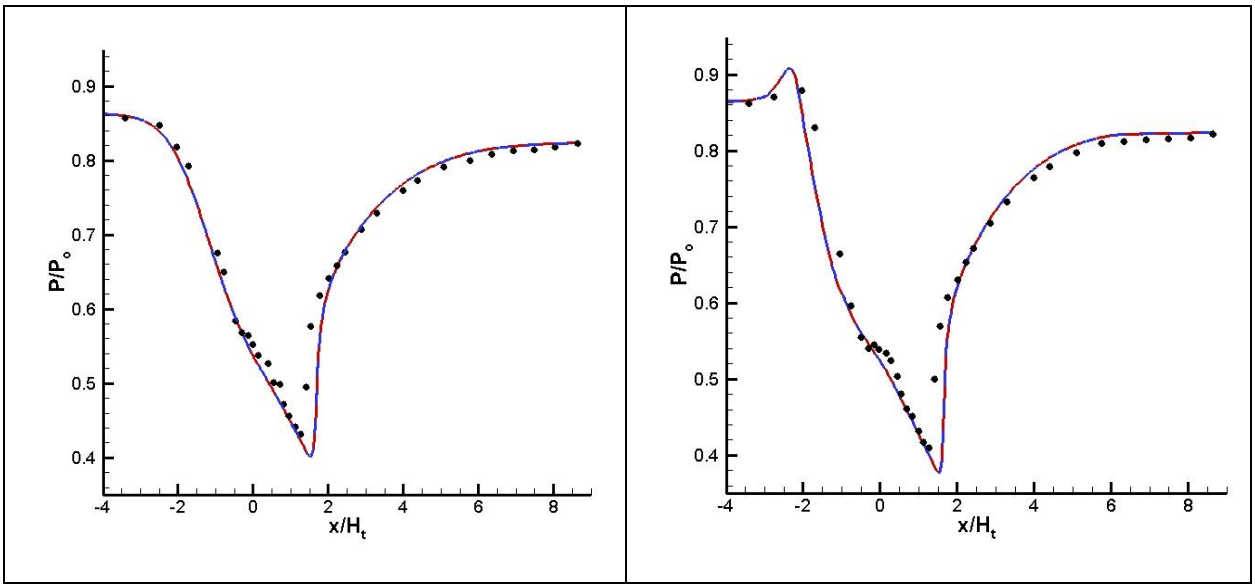

Figure 3-17: Pressure distribution for the weak shock case with boundaries using Riemann Invariants and isentropic relations
(left – lower wall, right – upper wall) (● Exp, --- Riemann Invariant BC, - - - Isentropic BC)

3.5 NASA Low-Speed Centrifugal Compressor

The final case that was considered with the new compressible flow algorithm was the NASA Low-Speed Centrifugal Compressor (LSCC). The LSCC was designed and tested with the intent that the compressor would serve to assess and develop numerical codes. The compressor was designed to replicate the flow physics in a high-speed subsonic compressor in a large low-speed compressor. A full detailed description of the geometry was published by Hathaway et al. [103]. The compressor is composed

of 20 impeller blades with a 55˚ back sweep paired with a vaneless diffuser. The blade inlet diameter is 0.87 m and the exit diameter is 1.52 m. The tip clearance is 2.54 mm. The design condition for the compressor has a mass flow rate of 30 kg/s and a total pressure ratio of 1.14 at a rotational speed of 1,862 rpm. The adiabatic efficiency is 92.2% at the operating design point. Hathaway et al. [103] and Wood et al. [104] experimentally tested the compressor, collecting and publishing the performance and detailed PIV data.

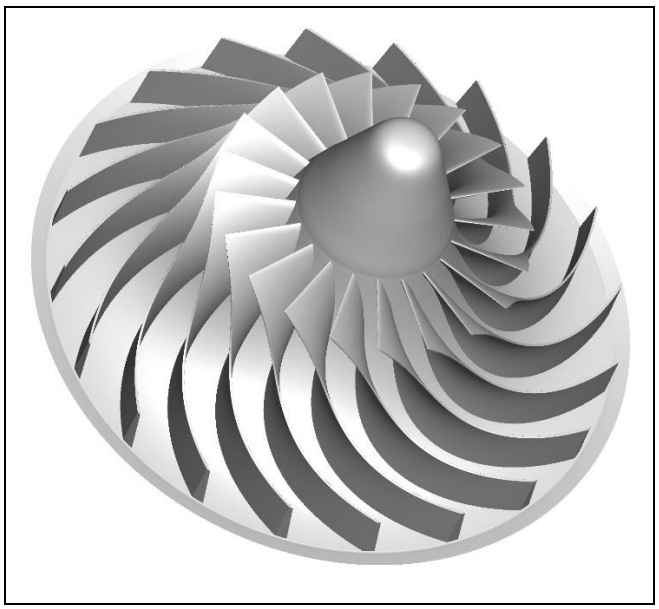

Figure 3-18: NASA LSCC 3D geometry

The LACC was modelled with the new compressible flow algorithm developed by the author and with *Code_Saturne*'s incompressible flow algorithm and with Fluent's compressible, pressure solver. Fluent simulation was used to solve for a steady-state solution while *Code_Saturne*'s incompressible flow algorithm was used to solve for an unsteady solution. All three solvers used the same mesh.

For the computational model, a single passage was modelled with an inlet boundary placed 0.4653 m upstream of the leading edge of the impeller and an outlet boundary placed at a radial distance of 1.3716 m. For *Code_Saturne*'s incompressible flow algorithm, the mass flow rate was specified at the inlet. For the new compressible flow algorithm and Fluent, a total pressure of 101325 Pa and a total temperature of 288.15 K were imposed. The static pressure was specified at the outlet. Periodic boundaries were imposed in the midspan of the passageway. The shroud and walls of the diffuser were stationary relative to the computational domain. The hub of the impeller and blades used a rotating wall boundary. The mesh constructed for the LSCC was composed of 2.3 million cells and had an average y^+ of 56. The geometry was split into an inlet, impeller, and diffuser domain. The individual domains were meshed independently and mesh joining was used to join the domains. The tip gap was resolved with 8

cells. The k-ω SST turbulence model with curvature correction was used for both *Code_Saturne* and Fluent. For the transient simulations, the flow was allowed to reach a converged state with the mass flow rate difference between the inlet and outlet being less than 1%. The transient simulation was then averaged over the time it took for the impeller to rotate two passageways.

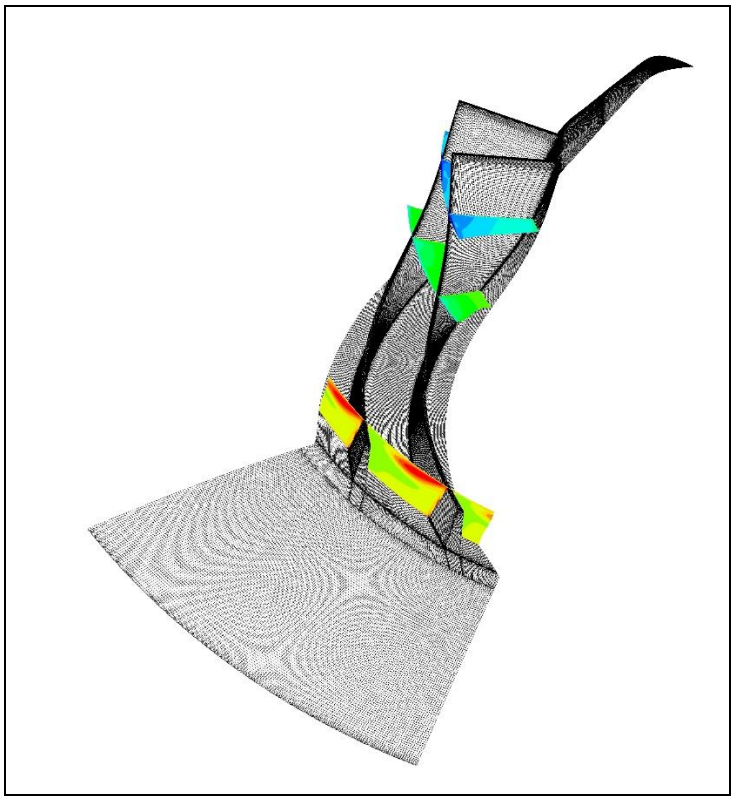

Figure 3-19: Mesh used for NASA LSCC with meridional planes

Conforming to the experimental results of Hathaway et al. [5], the area weighted averaged of the total pressure and temperature were obtained at the axial position of z = -0.204 and the radial position of r = 0.813 m. The total pressure ratio and efficiency of the compressor is plotted against the corrected mass flow rate in Fig. 3-20. Numerical prediction by *Code_Saturne*'s incompressible flow algorithm woefully under-predict the pressure curve due to assuming the flow is incompressible. Fluent and the new compressible flow algorithm gave a more accurate prediction of the pressure curve and both codes only slightly under predict the curve. At the design mass flow rate, Fluent predicted a total pressure ratio of 1.1369 and *Code_Saturne* predicted a ratio of roughly 1.1333. The new compressible flow algorithm gave a slightly better pressure ratio above the design mass flow rate and Fluent gave a slightly better prediction below the design mass flow rate. Overall the difference between Fluent and the new algorithm was only marginal. The difference between the two codes was more observable in the adiabatic efficiency curves.

Fluent matches the experimental results quite well while the new algorithm over predict the efficiency by about 3%.

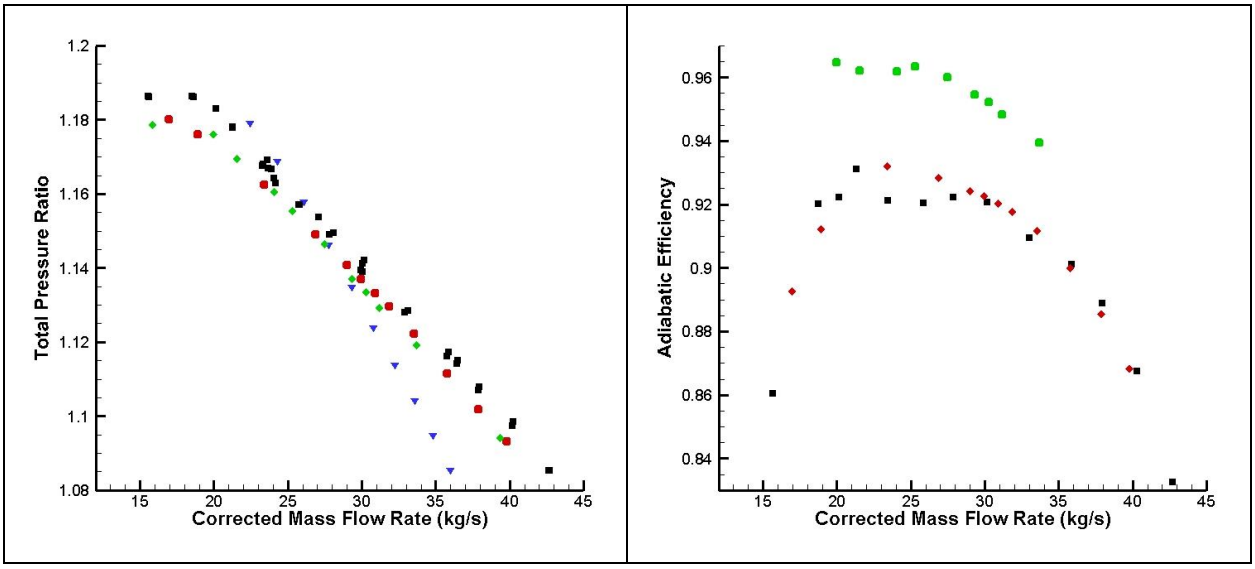

Figure 3-20: Performance and efficiency curves for NASA LSCC
(Exp [103] - ■, CS-Incompressible - ▼, New Algorithm - ♦, Fluent - ●)

In addition to the overall performance of the compressor, meridional planes were extracted at three points inside the compressor, the relative positions of the planes in relation to the compressor are shown in Fig. 3-19. The contour plots of the meridional planes are shown in Fig. 3-21. The results were taken at the design point of the compressor and compared to experimental results [103]. The meridional planes are plotted with the meridional velocity, the summation of the axial and radial velocity components.

$$V_m = \sqrt{V_r^2 + V_z^2} \tag{3.1}$$

Comparing the results in Fig. 3-21, the numerical results for all three solvers compared very well to PIV results of Hathaway et al. [103]. Fluent's compressible and the new compressible flow algorithm predict a slightly greater meridional velocity than the PIV results and the incompressible results.

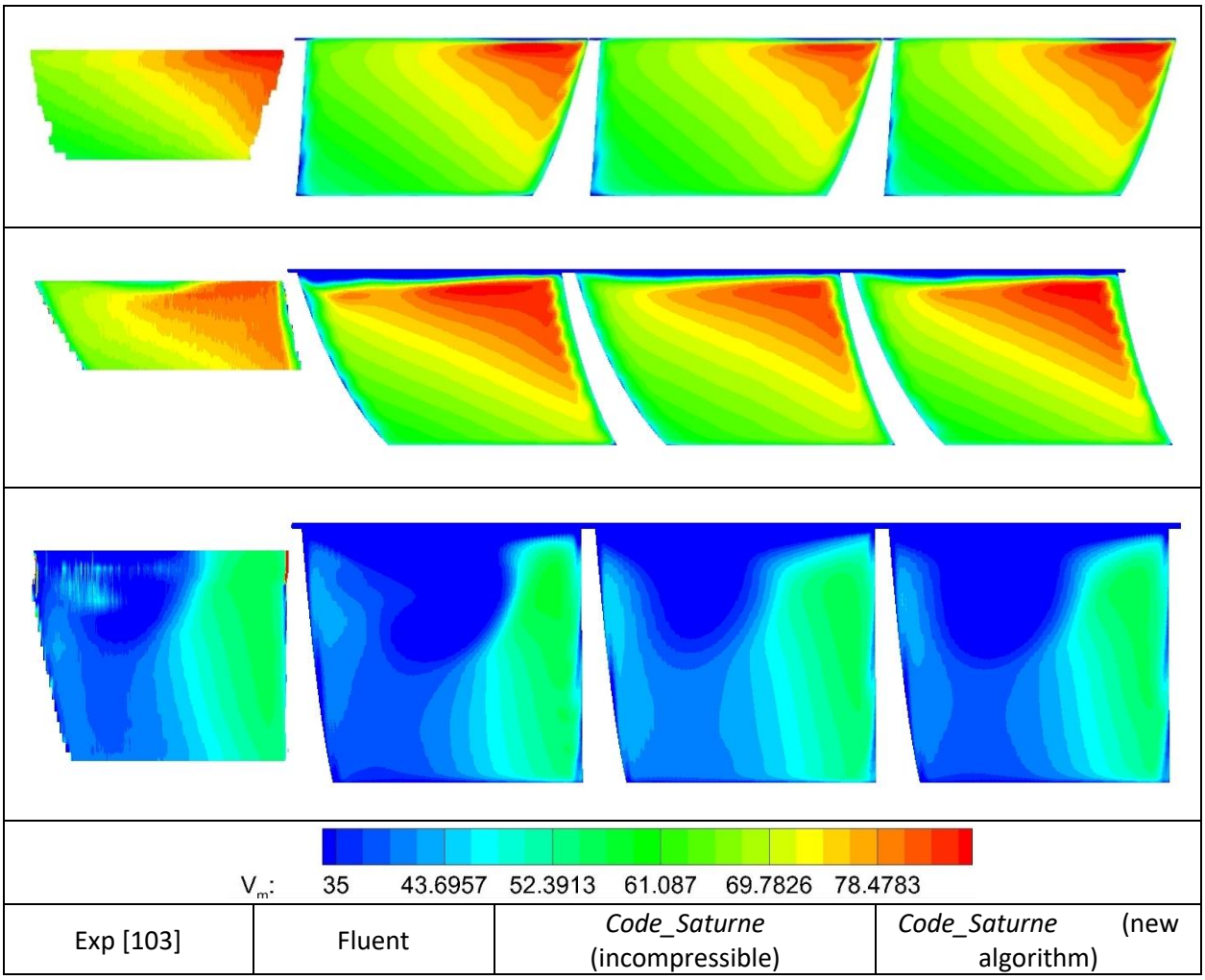

Figure 3-21: Meridional planes in the NASA LSCC (from top to bottom – M/M_o = 0.149 (J=85), M/M_o = 0.396 (J=110), M/M_o = 0.941 (J=165))

The pressure distribution on the blades was also extracted and compared to experimental results. The non-dimensional, reduced pressure on the impeller blades is defined as [105]:

$$\frac{P_r}{P_o} = \frac{P}{P_o}\left(1 + \frac{0.5\omega^2 r^2}{c_p T + 0.5(W^2 - \omega^2 r^2)}\right)^{-\gamma/\gamma-1} \tag{3.2}$$

The normalized pressure distributions at 20%, 49%, 79%, and 98% from the hub were plotted against experimental results in Fig. 3-22. At 20% and 49% from the hub, Fluent and the new compressible flow algorithm gave very similar predictions of the pressure distributions. 79% and 98% from the hub, there was a slight deviation in the pressure prediction, particularly for the pressure side of the blade, but the deviation was only minor. Likewise, the computational results matched experimental results the closest at 20% and 49% from hub with a slightly bigger deviation at 79% and 98%.

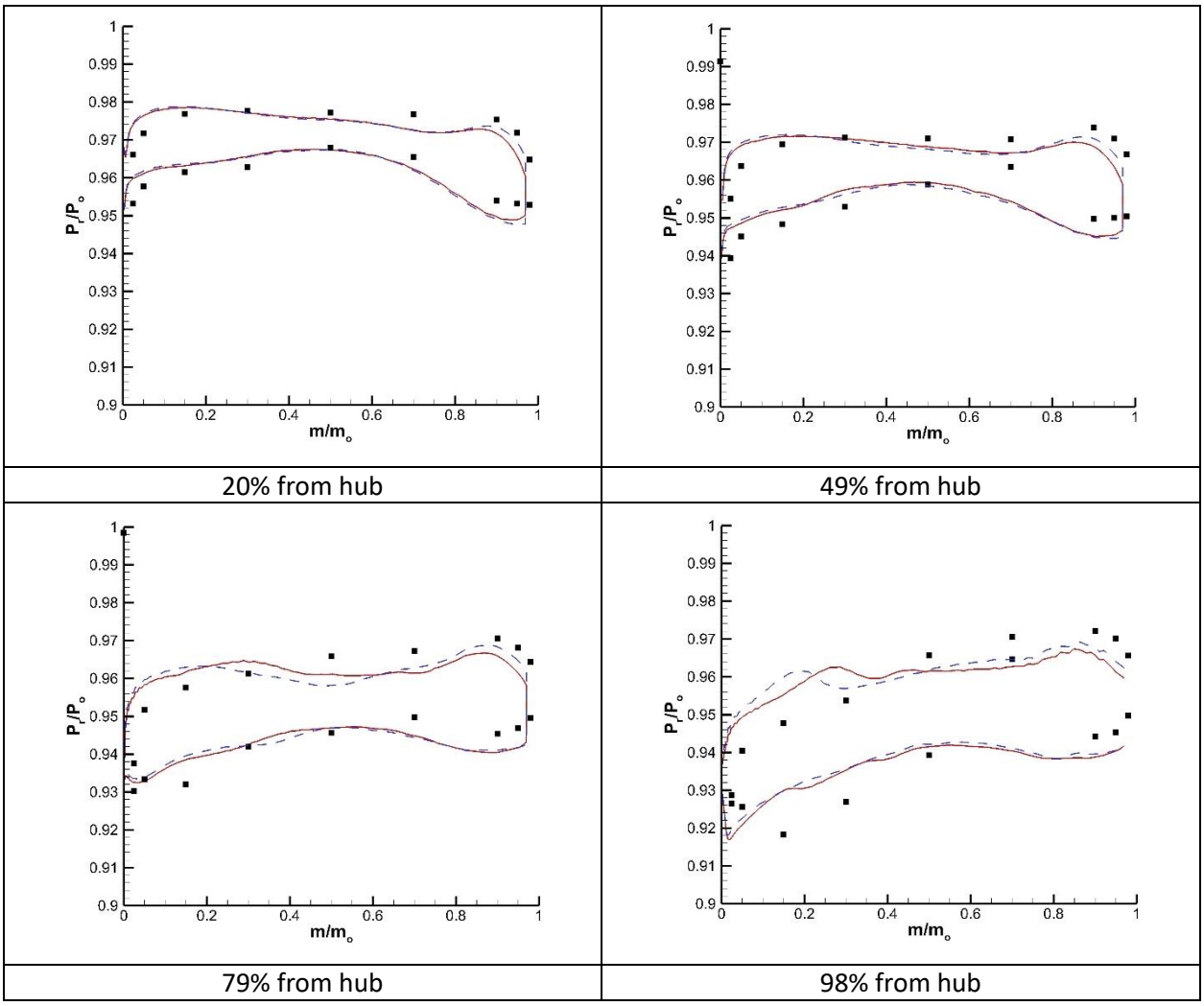

Figure 3-22: Normalized blade pressure distribution (■ Exp [103], ----- New Algorithm, - - - - Fluent)

3.6 Conclusion

The new compressible flow algorithm developed by the author was validated against several test cases (shock tube problem, channel flow with a bump, RAE2822 airfoil, and Sajben diffuser) and was found to give reasonably accurate results for the tested cases. The algorithm was also validated against the NASA LSCC with a rotating reference frame and shown to perform very well. These test cases validate the ability of the new compressible flow algorithm to efficiently handle turbomachinery flows that may contain many flow regimes with turbulence. The new algorithm was found to be less sensitive to high CFL numbers (>2.2) allowing for a reduction of the total time of a simulation, however the cost for an individual is increased in comparison to the SLK algorithm. The new algorithm made use of the Spalart-Allmaras and k-ω SST turbulence models that are found in *Code_Saturne*, with both models performing well. The newly

validated compressible algorithm in *Code_Saturne* will used later in Chapter 6 and 7 for modelling the NASA CC3.

There is however still room for future improvement in the newly written compressible flow algorithm. More work can be done to test the algorithm and possibly implement 3rd order spatial schemes to yield better results for the Sod's shock tube. For viscous problems, the algorithm used turbulence models originally written for incompressible flow. Investing more time to ensure these models and their wall functions work correctly for compressible flow problems may also yield better results. This may improve the prediction of the flow separation caused by the shock/boundary-layer interaction in the Sajben diffuser without using a wall-resolved mesh and produce a closer match of the efficiency curve of the LSCC compressor to experimental data.

4. Dynamics of Vortex Generators

In chapter 1, previous research into using microvortex generators (MVG) to control flow separation were discussed. Great amount of published work by numerous researchers has been devoted to the subject of MVG; to add to this body of research, a set of studies was conducted on the basic flow dynamics of MVG. Building off of Lin [16] work that found vane-type VGs were the most effective, this study investigated different MVG vanes as shown in Fig. 4-1 to provide new insight into the underlying physics of the flow around the vanes and to improve efficiency. The study used rectangle and triangle vanes that have been widely used in published works before. To improve the efficiency of the studied MVG, airfoil shaped vanes in the form of the NACA0012 and e423 airfoils were also tested. A simplified version of the e423 airfoil was also tested with a constant thickness for the vane.

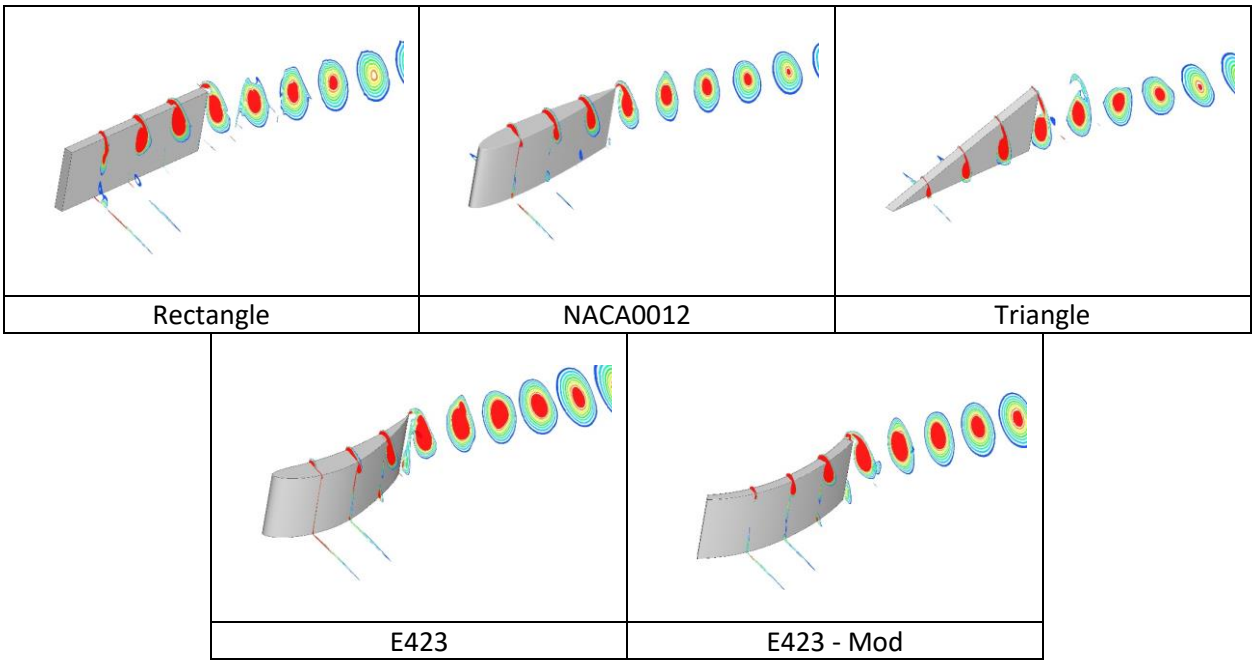

Figure 4-1: MVG vane geometry

From Lin et al.'s [16, 19] work that found MVG height could be reduced down to 20% of the boundary layer thickness, δ, while retaining their effectiveness , the height of the MVG vanes were studied primarily at 0.2δ. However, different MVG heights were also considered in section 4.3.5 in the event that the boundary layer thickness was variable or difficult to determine. The effect of the MVG thickness on the generated vortex was also investigated in section 4.3.4. For this chapter, incompressible flow was assumed; the maximum Mach number for any of the cases in this chapter was 0.21.

The geometric parameters for a MVG vane are shown in Fig. 4-2. In the work described in this chapter, x is the streamwise direction, y is the normal/vertical direction, and z is the spanwise direction. h is the height of the vane and e is the length of the vane given in height units. The vane is placed at angle of α relative to the freestream flow.

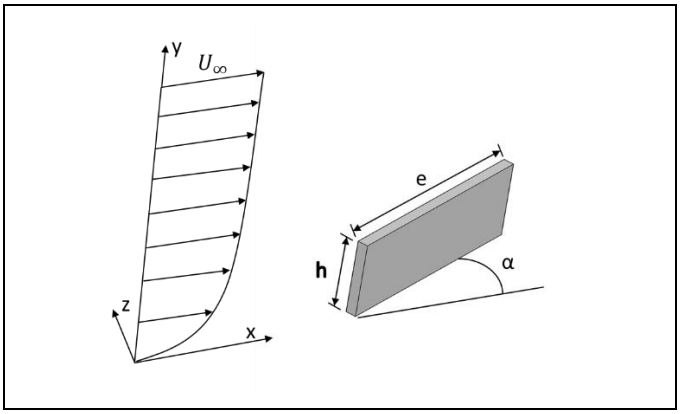

Figure 4-2: MVG vane configuration

4.1 Method of Analysis

A VG and the associated vortex can be defined by several parameters. The VG itself can be defined by its drag and initial strength of circulation while the evolution of the downstream vortex can be defined by the strength of circulation, peak vorticity, radius, skin friction on the wall, and trajectory of the vortex core at a measured point. Different techniques and methods can be used to evaluate these parameters.

The drag of the MVG can be calculated via two approaches, the direct drag of the MVG and the overall total drag of the MVG system. The direct drag of the MVG is the drag force on the MVG itself while the overall total drag is the net change in the drag of the system with the addition of a MVG. The total drag can either be negative or positive, negative being that MVG decreases the drag of the system while positive being that MVG increases the system's drag. In the numerical solution of a MVG, the direct and total drag can be calculated individually with the summation of the pressure and viscous forces. Experimentally, the 'total drag' of the system can only be determined, and is determined by measuring the momentum deficit at the measurement plane.

The other parameters were determined at incremental streamwise slices of the flow downstream of the MVG vane. The proper approach on identifying and characterizing vortices has been debated greatly. Peak vorticity is a simple approach to identifying a vortex core, however Jeong and Hussian [106] noted that in wall-bounded or homogenous shear flows the peak vorticity may not correspond to the core

of the vortex. Their work concluded that the Lambda-2 method was the best method in identifying the vortex core. The Lambda-2 criterion was used in the following work; however, it was found that using peak vorticity for identifying the vortex core gave very similar results. The zeroth point used for the vortex trajectory in the following sections is the center of the VG vane for the horizontal position and the wall for the vertical position. The size of the vortex core is approximated by assuming the vortex is a circle and calculating the radius of the vortex [4]. The radius of the vortex is determined by calculating the mean distance from the vortex core to isocline of half of the peak vorticity. This approximation is valid when the vortex core is circular but becomes less valid further downstream of the vane when the vortex stretches. A more applicable method is to measure the area of the vortex in a streamwise slice.

The circulation was evaluated by taking the surface integral of the vorticity vector dotted with the tangential unit vector of the wall.

$$\Gamma = \iint \boldsymbol{\omega} \cdot \hat{\boldsymbol{t}}\, dS \tag{4.1}$$

In the calculation of the circulation, the vorticity was clipped to 2.5% of the peak vorticity at x/h=1 to eliminate any background noise that was present. For sections 4.3.2 to 4.3.5, the vorticity was clipped to 1% for the RANS models. Clipping the vorticity for RANS had little impact on the calculation of the circulation, but for LES, where the turbulence structures are simulated, clipping had a far greater effect. Immediately downstream of the vane, the calculated circulations with clipping and non-clipping were equal, but much further downstream, the use of clipping has the negative effect of reducing the calculated circulation. The circulation was non-dimensionalized with the height of the MVG and the local friction velocity at the MVG location [21, 22].

4.2 Validation

To assess the accuracy of the numerical models in the following sections, a grid sensitivity study was conducted to determine the sensitivity of the vortex parameters to the grid resolution. Additionally, to validate the numerical prediction of the MVG drag, an experimental wind tunnel test on MVG vanes was conducted.

4.2.1 Grid Sensitivity

A numerical grid convergence study was conducted in an attempt to quantify the influence that mesh resolution had on the different parameters of a MVG and its vortex. The study used the experimental results of Yao et al. [29] to check the sensitivity of the mesh resolution. The numerical model used the k-ω SST model in ANSYS® Fluent with the SIMPLEC algorithm. A 2nd-order upwind scheme was used for the convective terms and a 2nd-order centered scheme for the diffusion terms. A block-based unstructured mesh was generated with ANSYS® ICEM to generate three different mesh densities to demonstrate the independence of the MVG and the generated vortex to the mesh resolution. The three different mesh densities are given in Table 4-1. The three meshes had a y^+ of less than 1 on the wall and the y^+ on the MVG had an average of 6.3. Following Yao et al. [29] work, the circulation, the trajectory, and the radius of the vortex were calculated as shown in the Fig. 4-3, 4-4, and 4-5.

	Number of Cells	C_D		
		23°	16°	10˚
Mesh C	3.8M	0.2343	0.4807	0.9733
Mesh B	6.1M	0.2298	0.4773	0.9762
Mesh A	11.6M	0.2303	0.4808	0.9751

Table 4-1: Mesh densities and drag for mesh sensitivity study

From Table 4-1, the drag from the MVG vane varied little between the three meshes with the largest deviation being 1.8% and a slight increase of drag was assumed with an increase of mesh resolution. The initial circulation also showed a slight sensitivity to the mesh resolution, but overall the circulation matches well to the experimental data, as shown in Fig. 4-4. The biggest sensitivity in the mesh resolution was observed for the vane placed at 23° after the vortex was initially formed, vanes placed at smaller angles showed less of a variation. Further downstream, the circulation was observed to be less sensitive to the mesh resolution for all three vanes. The trajectory of the vortex proved to be more sensitive to the mesh resolution and there was a slight discrepancy between the computationally predicted path of the vortices and what Yao et al. [29] experimentally observed as shown in Fig. 4-3. The discrepancies between the computational and published results were most clearly seen in vertical displacement of the vortex. The vortices were seen to depart from the vane further from the wall than published results as shown for all three vanes. However, the horizontal displacement matches quite well to the experimental results.

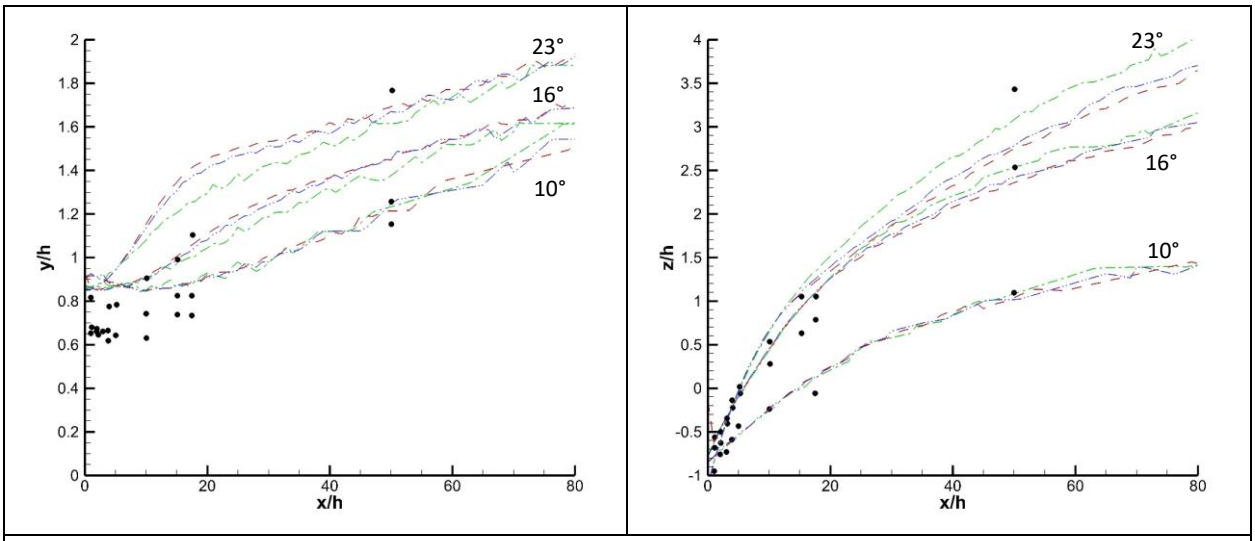

Mesh A - - - , Mesh B - · · · · · - , Mesh C - · - · - , Yao et al. [29] •

Figure 4-3: Vortex trajectory sensitivity to mesh (Right – y-position, Left – z-position)

Lastly, shown in Fig. 4-5 and Fig. 4-6 is the sensitivity of the vorticity and radius of the vortices to mesh resolution, respectively. The vorticity was observed to have a slight variation with an increase of mesh resolution but the overall numerical results under predicted the vorticity when compared to the results of Yao et al. [29]. There is a slight variation in the sensitivity of the vortex radius to mesh resolution, but the numerical results for the radius agree well with the published results.

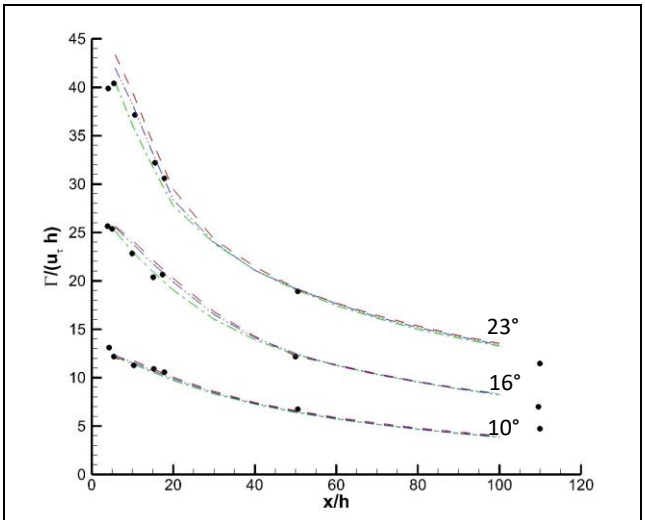

Mesh A - - - , Mesh B - · · · · · - , Mesh C - · - · - , Yao et al. [29] •

Figure 4-4: Vortex circulation sensitivity to mesh

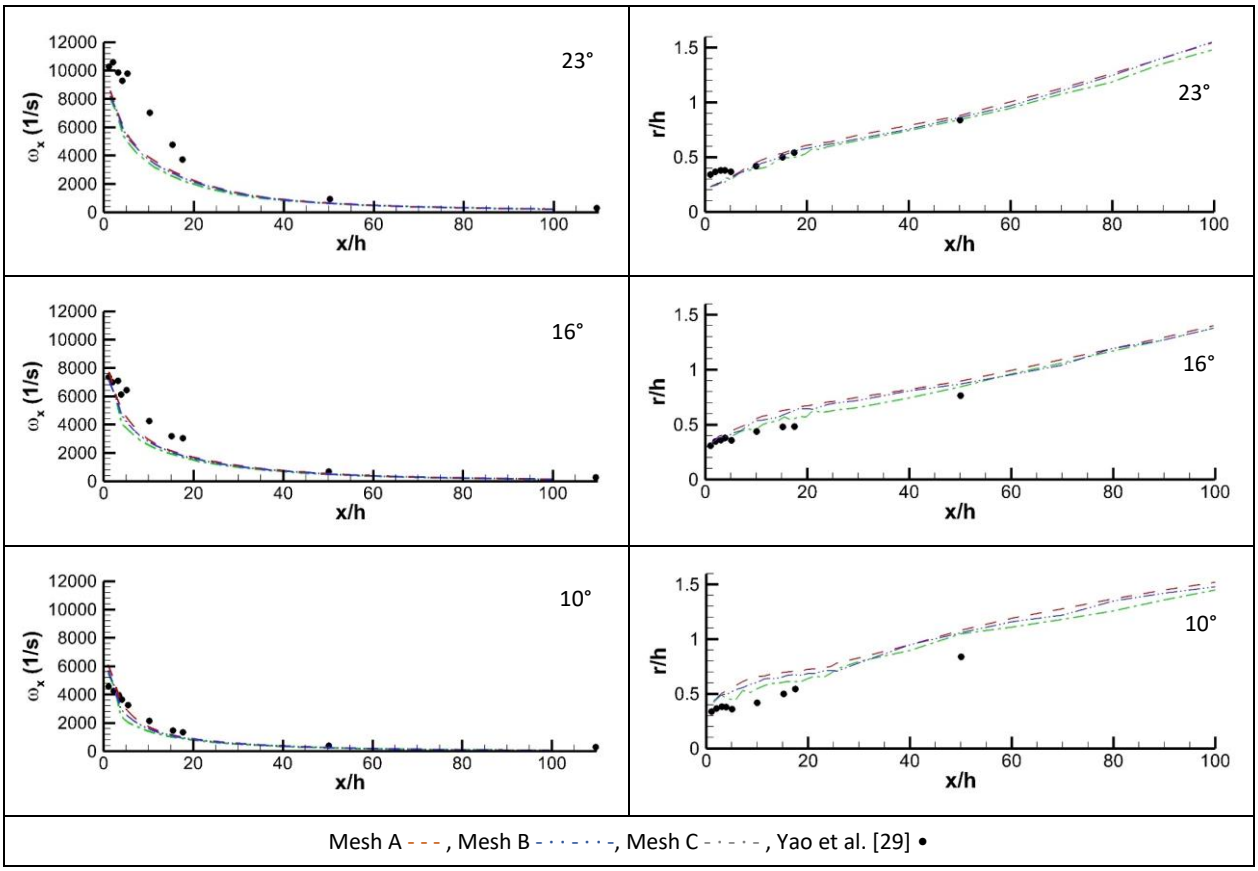

Figure 4-5: Vortex vorticity sensitivity to mesh

Figure 4-6: Vortex radius sensitivity to mesh

4.2.2 Experimental Drag Measurements

In literature, little research has been conducted to experimentally determine the drag force on MVG. To compensate for this gap, an experiment was conducted by the author with a number of MVG vanes to serve as a validation for computational results and provide further evidence for the flow development.

4.2.2.1 Setup

The QMUL wind tunnel No. 4 is a closed-circuit wind tunnel that can be operated up to 35 m/s. The working section has a length of 2 m, a width of 0.52 m wide, and a normal height of 0.38 m, the walls are slightly divergent to compensate for boundary layer growth. The test section is split in the center by a precisely machined flat plate to generate a boundary layer on, reducing the width of the test section to 0.25 m. The boundary layer was tripped 0.065 m from the leading edge of the flat plate with a metal rod. The center of the flat plate has 18 static pressure taps distributed in the streamwise direction and the stagnation pressure was measured with a pitot tube mounted on a traverse. The traverse allows for the Pitot tube to be moved three dimensionally with increments of 5 µm. The pressure measurements were

measured with a DSA3217 scanning valve that takes 32 scans per pressure measurement. The freestream turbulence intensity in the test section was measured to be 0.1%. The wind tunnel was run for at least 12 hours to allow the for the wind tunnel's temperature to stabilize; temperature affects the wind tunnel flow's air density and viscosity. A view of the work section of the wind tunnel is shown in Fig. 4-7.

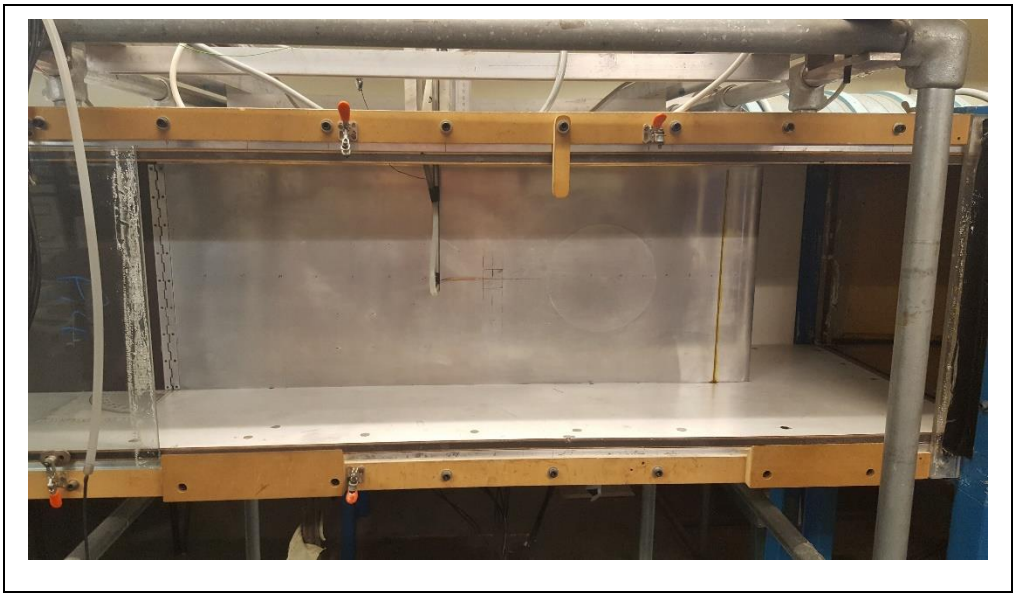

Figure 4-7: QMUL wind tunnel No. 4

The tested MVG vanes were mounted 0.515 m from the leading edge of the plate in the center of the test section to ensure a steady boundary layer. The measured freestream velocity was 15.79 ± 0.33 m/s. The boundary layer thickness and the momentum thickness were measured to be 16 mm and 1.37 mm at this point, respectively. The MVG vanes were scaled to 0.2δ and were placed 23° relative to the flow direction. Five different MVG shapes were tested: two rectangular vanes (e/h = 3,7), a triangular vane, a vane based on the NACA0012 airfoil, and a vane based on the E423 airfoil.

The flow field was surveyed at 53h behind the MVG vane. The survey was composed of 24 boundary layer profiles that were taken in the spanwise direction along a 104 mm space. The boundary layer profiles were composed of 45 measurements in the normal direction. The first measurement was taken 0.15 mm away from the wall and measurements were taken until the pitot tube was 22.15 mm above the wall. Each survey took 12 to 14 hours to complete. To reduce the uncertainty of the final drag measurement, each MVG was surveyed multiple times. The number of surveys conducted for each MVG is shown below in Table 4-2.

4.2.2.2 Method of Calculation

From each survey the stagnation and static pressure is known for a 104 mm by 22 mm grid, 53h behind the MVG. The grid contains 24 boundary layer profiles. At each surveyed point, the velocity was determined and non-dimensionalized by the freestream velocity. Making use of the equation for the momentum thickness of a boundary layer, the drag per unit distance in the spanwise direction can be determined by:

$$\frac{\partial D_{mvg}}{\partial z} = \rho U_o^2 \int \frac{u}{U_o}\left(1 - \frac{u}{U_o}\right) dy \tag{4.2}$$

The resulting value for each boundary layer profile is subtracted by the base case without a MVG vane. Each profile is then numerical integrated in the spanwise direction.

$$C_D = \frac{2}{\rho U_o^2 h^2} \int \left(\frac{\partial D_{mvg}}{\partial z} - \frac{\partial D_{base}}{\partial z}\right) dz \tag{4.3}$$

From Eq. 4-3, the drag coefficient is determined for a MVG vane. Because the drag value is measured at 53h behind the vane, the value is composed of the drag of the vane itself and the viscous forces on the wall induced by the vortex.

The friction velocity at the location of the MVG was calculated via two methods, a curve fitting method suggested by Kendall et al. [107] and a correlation method developed by Patel [8]. The method developed by Kendall et al. [107] makes use of the Spalding profile to calculate the mean boundary layer profile:

$$y^+ = u^+ + \exp(-\kappa B)\left[exp(\kappa u^+) - \kappa u^+ - \frac{1}{2}(\kappa u^+)^2 - \frac{1}{6}(\kappa u^+)^3 - 1\right] \tag{4.4}$$

where

$$y^+ = \frac{y u_\tau}{\nu} \tag{4.5}$$

$$u^+ = \frac{U}{u_\tau} \tag{4.6}$$

and $\kappa = 0.5$ and $B = 0.5$. With Eq. 4-4, a MATLAB routine was written to find the u^+ that matched the Spalding profile with the experimental data. The written programme found the correct u^+ by finding the minimum residual.

$$R = \frac{1}{N}\sum_{i=0}^{N}\frac{|u_i^+(data) - u_i^+(model)|}{u_i^+(model)} \tag{4.7}$$

Patel's correlation method [108] is an extension of Preston's method [109]. Preston's method uses a simple pitot tube, called a Preston tube, which rests on the wall of the wind tunnel. Assuming that the Preston tube is placed in a region that scales with the inner boundary layer variables, a similarity function can be constructed between dynamic pressure and wall shear stress.

$$\frac{\tau_w d^2}{4\rho u^2} = f\left(\frac{\Delta p D^2}{4\rho u^2}\right) \tag{4.8}$$

Through experiments, Preston [109] empirically determined and calibrated a function to match experimental measurements. Patel [8] expanded and improved the empirical function, the new function is valid from $1.5 < y^* < 3.5$ and $11.2 < Re_D < 110$. Re_D is the Reynolds number based on the outer diameter of the Pitot tube and friction velocity. The empirical relation that Patel determined was:

$$y^* = 0.8287 - 0.1381x^* + 0.1437x^{*2} - 0.0060x^{*3} \tag{4.9}$$

The variables x^* and y^* are defined as:

$$x^* = log_{10}\left(\frac{\tau_w D^2}{4\rho v^2}\right) \tag{4.10}$$

$$y^* = log_{10}\left(\frac{\Delta p\, D^2}{4\rho v^2}\right) \tag{4.11}$$

The uncertainty of the measured experimental values and the uncertainty of the final calculated drag coefficient was determined by the procedure published by the AGARD advisory report on "Quality Assessment for Wind Tunnel Testing" [110].

4.2.2.3 Results

The five MVG vanes were experimentally tested, which are shown in Table 4-2. The averaged Reynolds number for the experimental tests was 3,326, based on the freestream velocity at the MVG position and the height of the MVG. The friction velocity was calculated via two methods: a curve fitting method suggested by Kendall et al. [107] and a correlation method developed by Patel. The curve fitting method suggested by Kendall et al. [107] gave a friction velocity of 0.744 and h^+ of 155.03. Patel [108] correlation method is an extension of Preston's method [109] which uses the dynamic pressure at the

wall to obtain the friction velocity through a correlation. The correlation method proposed by Patel gave a friction velocity of 0.767 and h^+ of 159.80.

A numerical comparison to the experimental data was made with ANSYS Fluent by matching the Reynolds number of the MVG vane. Keeping with the experimental setup, the MVG height was scaled to 0.2δ, and the freestream and boundary layer thickness at the MVG was varied to obtain the required Reynolds number. To account for the drag caused by the viscous interaction of the vortex with the wall and to give a good comparison, the numerical results were evaluated at 53h behind the vane. The drag coefficient is based on the freestream velocity.

Experimental					Numerical
MVG Shape	e/h	No. of Trials	Avg C_D	± (%)	C_D
Rectangle	7	6	1.0020	3.52	1.0512
Rectangle	3	6	0.5707	16.78	0.6153
NACA0012	3	5	0.4907	19.74	0.4332
Triangle	3	7	0.2626	31.51	0.2316
E423	3	5	0.7704	3.96	0.8076

Table 4-2: Experimentally and computationally obtained drag values

The average experimental drag coefficient compares well between numerical and experimental results. The uncertainty in error for the drag measurements for the rectangle e/h=7 and E423 vanes was found to be small but was significant for the other vanes, particularly for the triangle vane. It is postulated that the uncertainty is proportional to the magnitude of the drag. As shown and discuss later, the drag is also proportional to the circulation, and the rectangle e/h=7 and E423 vanes were observed to generate the strongest circulation.

From the experimental data that was collected, a contour plot of the velocity field can be constructed as shown in Fig. 4-8. The velocity field is from a rectangle MVG vane with a length of e/h = 3. Computational results are compared to the experimentally obtained velocity field in Fig. 4-8. The predicted vortex by ANSYS Fluent shows less of a displacement in spanwise direction than was experimentally observed.

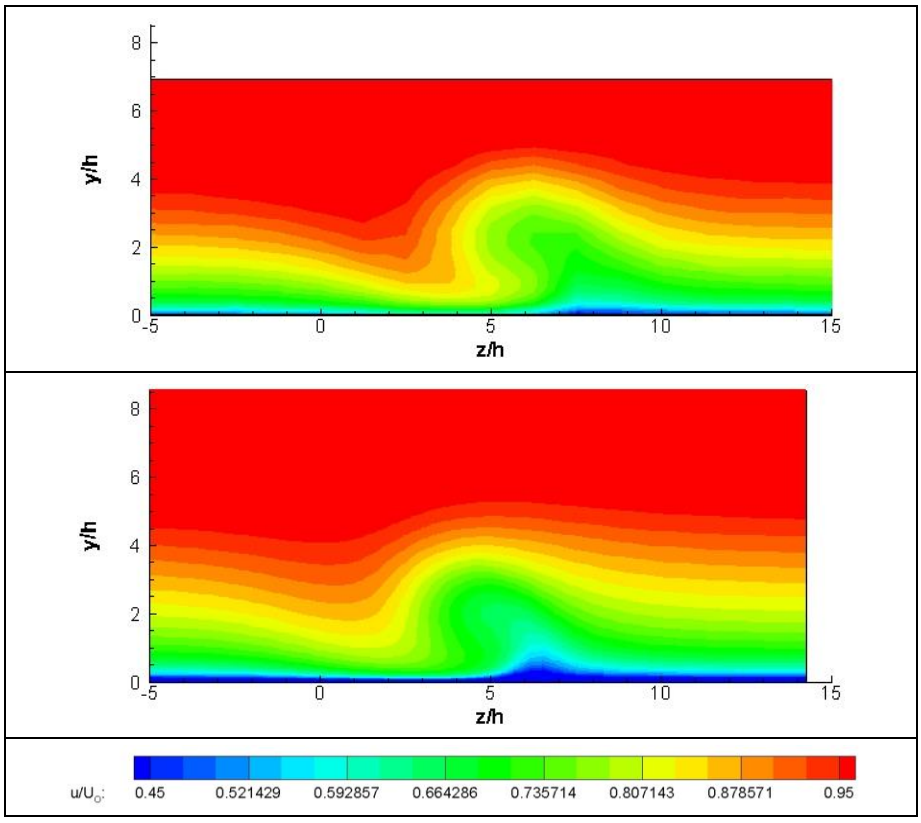

Figure 4-8: Experimental and computational velocity contours (Top – Exp, Bottom – CFD)

4.3 Fundamental Flow Dynamics

The following section conducts a high-fidelity simulation of a set of MVG vanes with LES to study in detail the behavior of the MVG vanes. With RANS, a variety of vane shapes and angles were modelled to determine the optimize configuration. The effect of the Reynolds number, vane thickness, and vane height was also studied. *Code_Saturne* was used for the LES modelling in section 4.3.1 while ANSYS Fluent was used for the RANS modelling in sections 4.3.2 to 4.3.5.

4.3.1 High-Fidelity Simulation of MVG

RANS modelling of MVG and their vortices has been shown to be adequate in section 4.2.1 and in literature; however, RANS is unable to capture the instantaneous behavior of MVGs in a turbulent flow and complex flow fields. To obtain a better understanding of the flow dynamics of a MVG in a turbulent flow, it becomes necessary to use LES. To properly resolve the flow field with LES, mesh and time requirements for a numerical simulation is much stricter than with RANS modelling. To accommodate these restrictions within the provided computational resources, a Reynolds Number based on the

freestream velocity and MVG height of 2900 was chosen. The Reynolds number used is slightly below the Reynolds number of the experiment in section 4.2.2, which was 3,326. The actual Reynolds number for the LES modelling was 2,894. The Reynolds Number based on the momentum friction velocity (h^+) is 86.36. In addition to the LES simulation, a parallel RANS model at a similar Reynolds number is conducted to further assess the accuracy of RANS modelling of a MVG.

The computational domain for the LES model is shown in Fig. 4-9. An inlet boundary condition was placed 16δ upstream of the MVG. At the inlet boundary, the flow was recycled from a recycle plane using the turbulent recycling inflow method described in section 3.8. The boundary layer at the inlet was scaled to 36 mm with a freestream velocity of 6.176 m/s. The recycle place was placed 10δ downstream of the inlet, or 6δ upstream of the MVG vane. An outlet boundary was placed 10.69δ downstream of the leading edge of the MVG vane. A sample time- and spatially-averaged boundary layer profile from a case without a MVG at the recycle plane is shown in Fig. 4-10. Periodic boundaries were enforced in the spanwise direction at a distance of 5.71δ and a symmetric boundary was enforced 6δ away from the wall. A no-slip boundary condition was used on the wall and on the MVG vane. The MVG vane was centered in the spanwise direction of the domain.

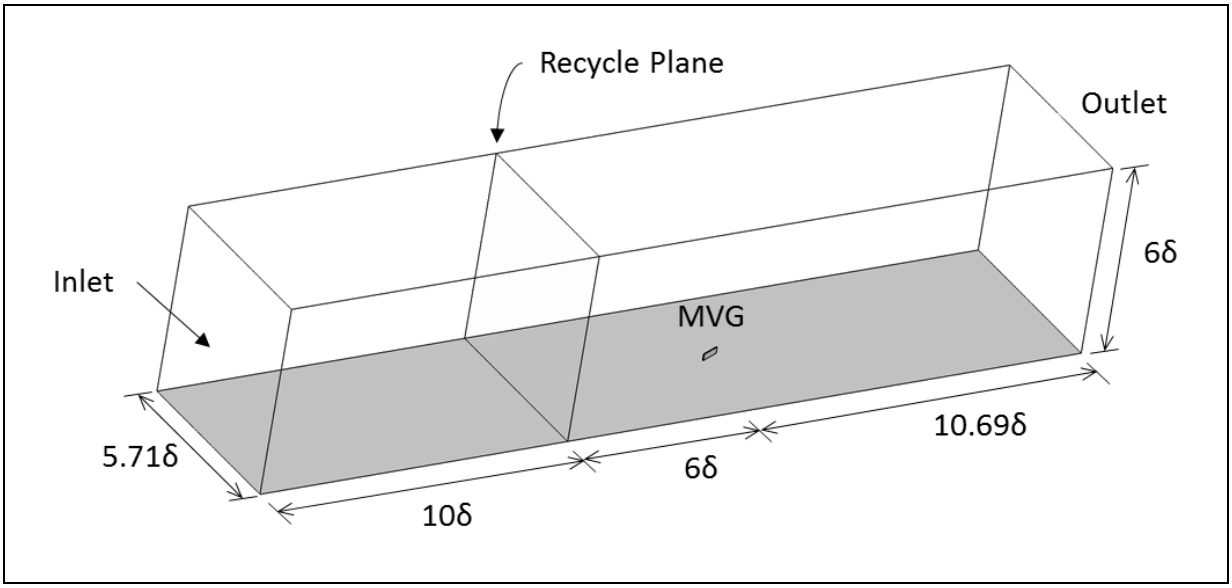

Figure 4-9: Computational domain for LES modelling of a MVG

Code_Saturne with the WALE subgrid model was used to simulate the incompressible flow. A 2nd-order centered scheme was used for the convective and diffusive terms, and an implicit 2nd-order Crank-Nicholson time scheme was used to advance the time. The simulation was run with a time increment that kept the CFL number to less than 0.5. The generated meshes contained 14.03 million cells for rectangle

vanes, 16.60 million cells for triangle vane, and 13.83 million cells for the E423 – mod vane. The y^+ on the wall was 0.5 and the y^+ on the MVG vane was on average 2. The x^+ and z^+ was less than 12.5. The simulation was allowed to run for at least 20 flow through periods before statistics of the flow were recorded for another 10 flow through periods.

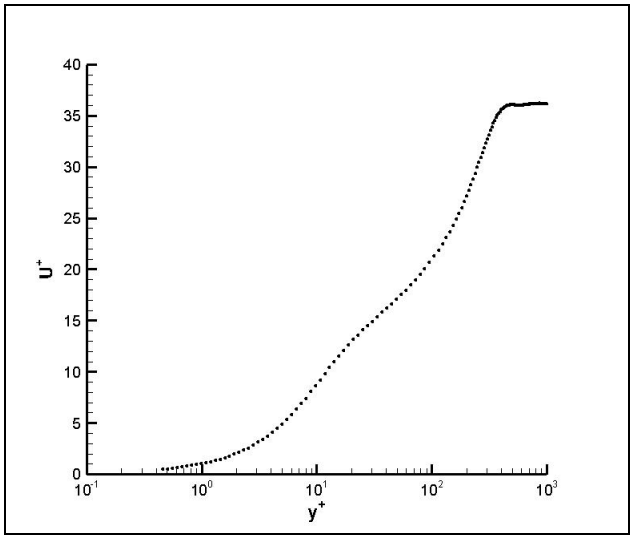

Figure 4-10: Boundary layer at the recycle plane

The RANS models setup was similar to the setup of the LES simulation, but ANSYS Fluent with the SIMPLEC pressure solver was used to solve for a steady-state solution. Since the turbulent inflow to the domain is no longer simulated, the inlet for the RANS model was moved further downstream and closer to the MVG vane. A boundary layer was generated from a prior simulation on a flat plate with an inlet turbulent viscosity of 1% and was imposed on the inlet to produce the desire freestream velocity and boundary layer thickness. The mesh was constructed to ensure that the y^+ was less than 1. The turbulent viscosity was modelled with the k-ω SST model.

A comparison of the instantaneous LES, time-averaged LES, and RANS simulations of the flow field on a rectangle vane at 18.5˚ is made in Fig. 4-11. At an instantaneous moment, the vortex formation on the vane is dynamic and disorganized in comparison to the time-averaged results and RANS. The instantaneous vortex may be composed of several cores, particularly near the end of the vane. The instantaneous vortex was also observed to have a higher vorticity. In the comparison of the time-averaged LES and RANS in Fig. 4-11, LES predicted a vortex that contained much less vorticity, however the vortex formation process between LES and RANS is very similar. The flow rapidly rolls-up on the leading edge of the vane tip. The vortex continues to roll-up until about 50% to 75% of the vane length when it detaches from the vane.

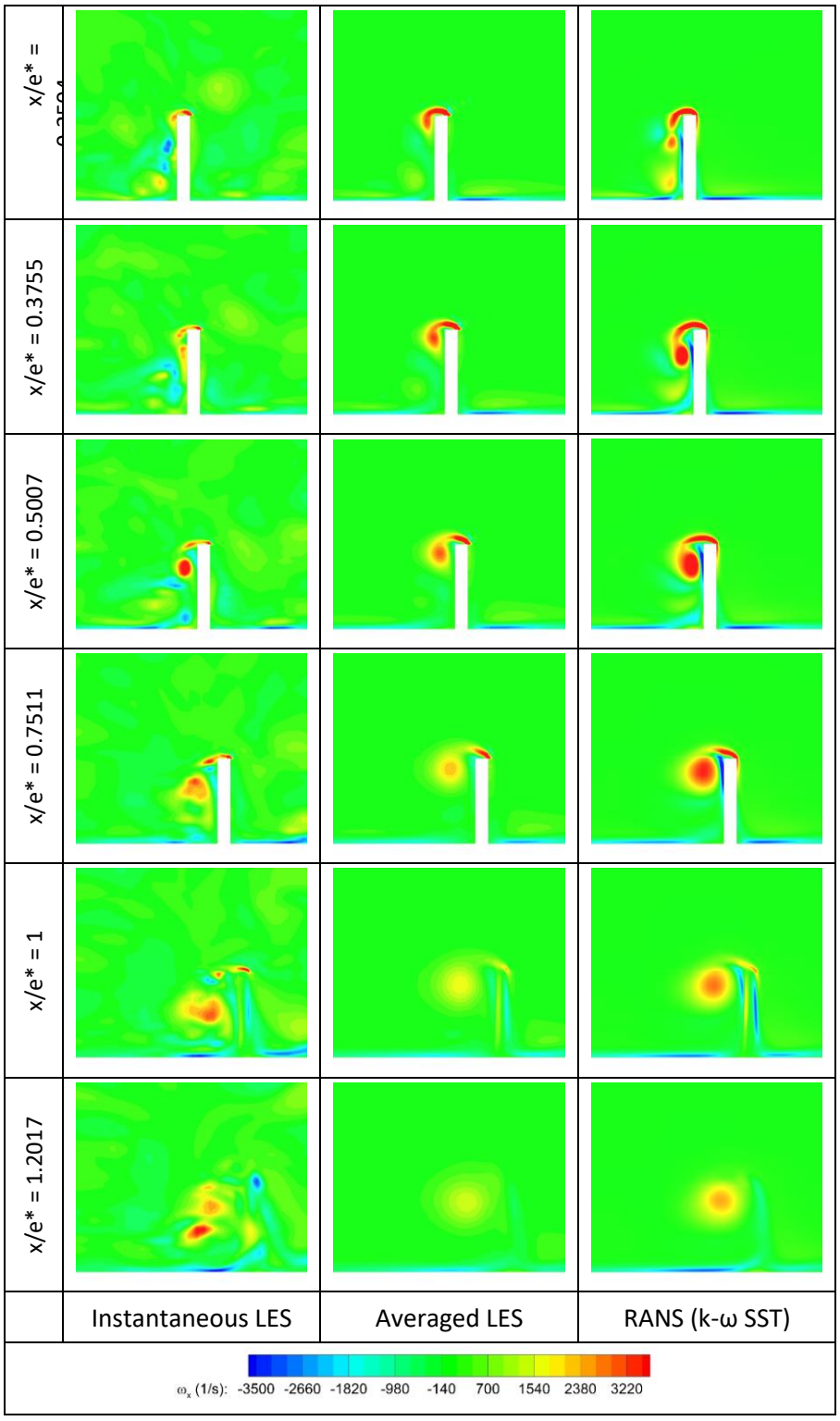

Figure 4-11: Vorticity comparison of instantaneous and averaged LES to RANS

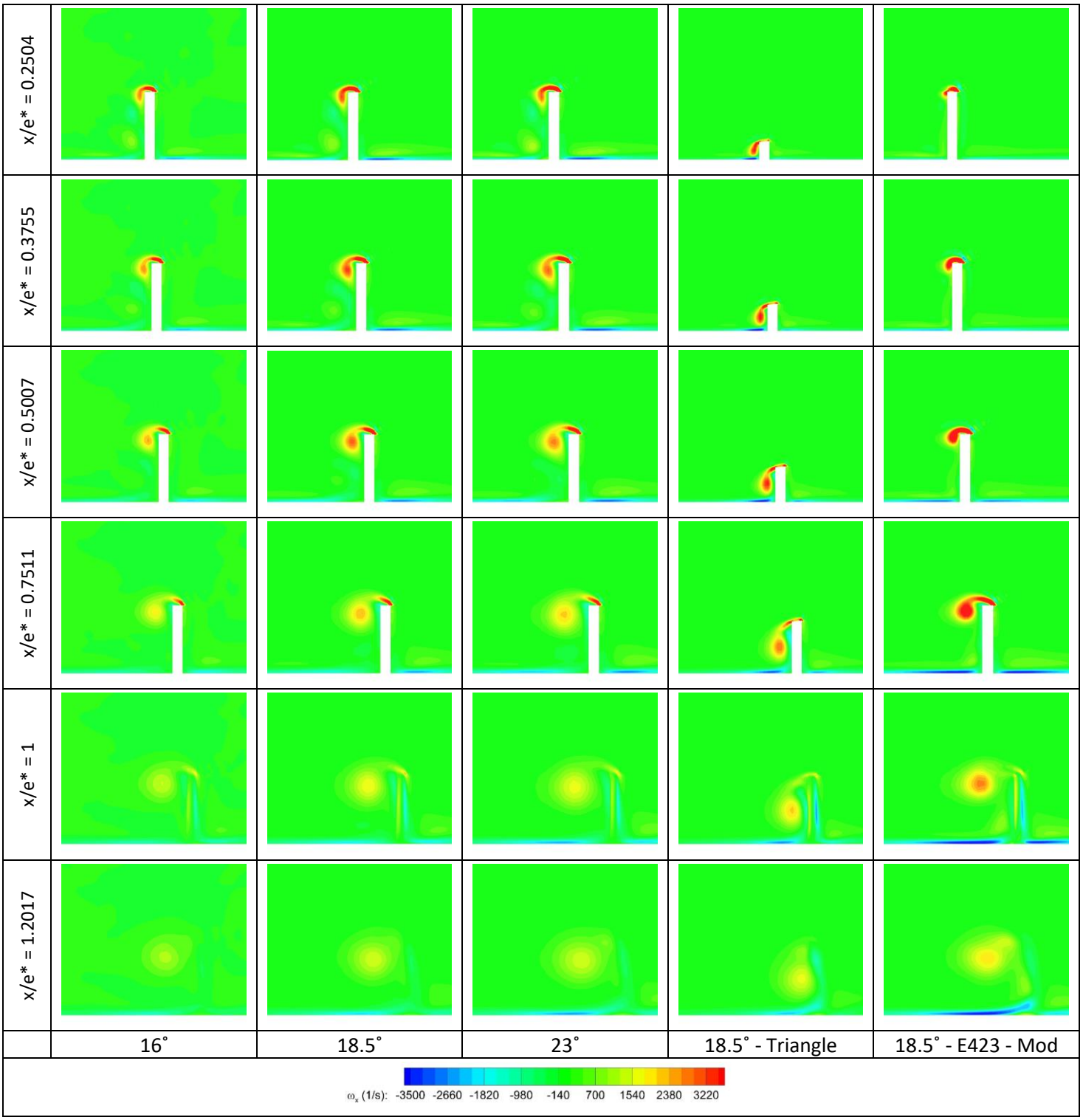

Figure 4-12: Time-averaged vorticity field on MVG vanes with LES

The vorticity contours from the time-averaged flow field at six different points along the formation of the vortex on 5 simulation MVG vanes are shown in Fig. 4-12. Between the rectangular vanes placed at 16˚, 18.5˚, and 23˚, the formation process of the vortex is very similar but strength of the vorticity

varies. There is a larger difference in the vortex formation on the triangle vane in comparison to the rectangular vanes. Due to the shape of the triangular vane, the vortex forms very quickly in comparison to the rectangular vane but very close to the wall. As the vortex continues to grow and form on the triangular vane, the vortex migrates upwards but continues to stay at half the vane height. The distance of the vortex from the wall as it leaves the triangular vane has a very negative effect which will be seen in downstream behavior of the vortex that will be discussed later. The e423 – mod vane also behaves differently from the rectangular vanes. The vortex formation is suppressed until about the mid-point of the vane, the vortex quickly forms on the latter half of vane. Even though the vortex formation is delayed, the vortex is noticeably stronger. The position of the vortex as it leaves the vane is similar to the vortex from the rectangular vanes.

The pressure on the vane is a driving force of the vortex formation and the pressure field at 0.25h, 0.5h, 0.75h, and 0.95h is shown in Fig. 4-13. The MVG vane acts exactly as an airfoil, one side has a high-pressure system and the other side has a low-pressure system. The high/low pressure systems on the vane cause a pressure differential. At the tip of the vane, the pressure causes the flow to wrap around it, generating vorticity in the flow. On the rectangular vane, the pressure differential is the largest near the leading edge of the vane which as observed in Fig. 4-12 is where vorticity in the flow is the strongest. Further downstream on the vane, the pressure differential weakens leading to a slower growth of the vortex. On the triangular vane, the pressure differential is weaker but is more constant. The pressure differential on the e423 – mod vane is both stronger and more evenly distributed than the differential found on the rectangular vane. As with the rectangular vane, there is pressure bubble on the leading edge of the vane, but the pressure differential between the suction and pressure side is reduced immediately behind the leading edge. After the quick reduction of the pressure differential, the differential on the e423 – mod vane quickly grows in strength and remain stable until the trailing edge of the vane. The behavior of the pressure causes the suppress vortex formation on the front half of the vane and quick growth of the vortex on the latter half of the vane.

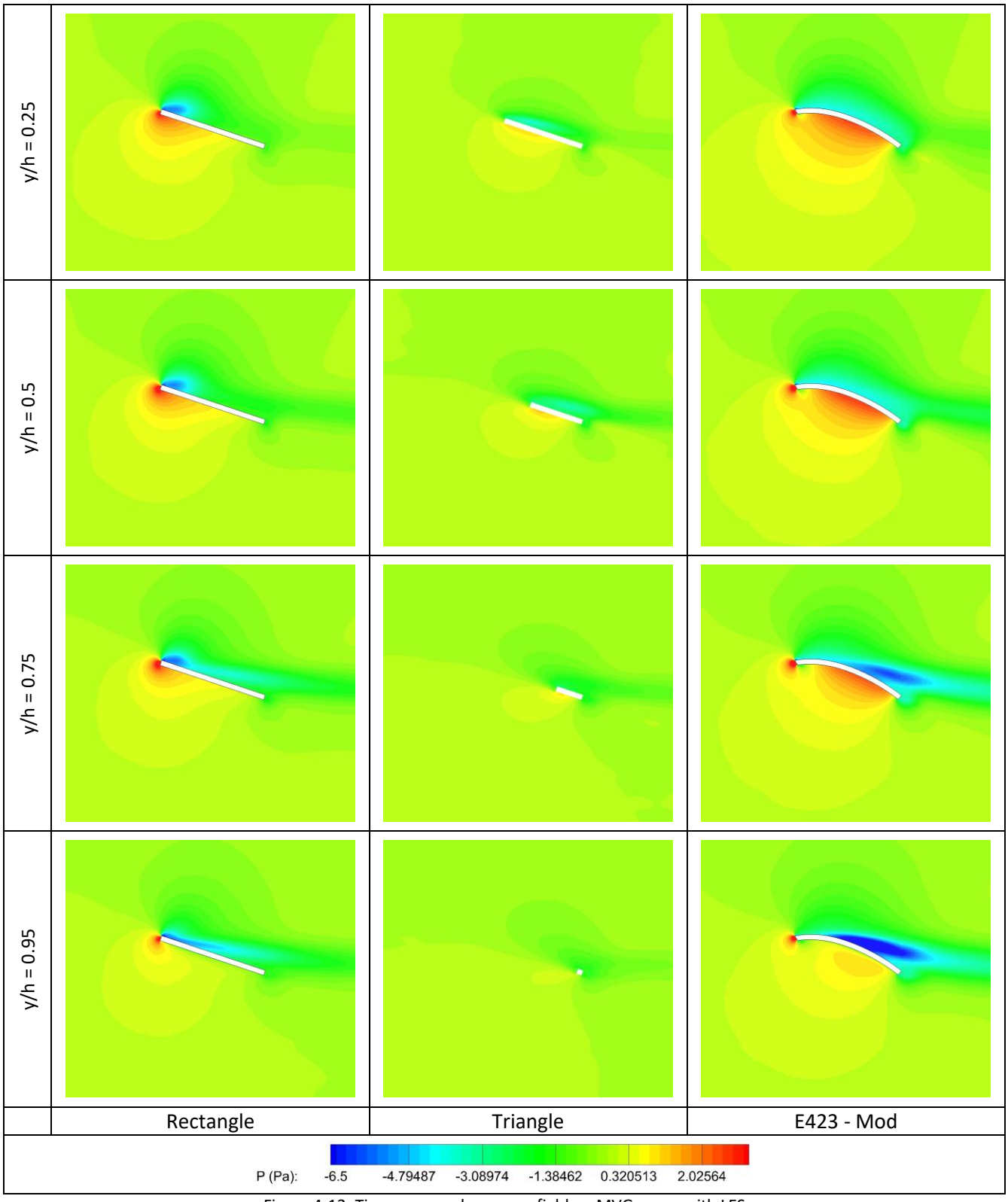

Figure 4-13: Time-averaged pressure field on MVG vanes with LES

The vortex parameters of the downstream vortex are shown in Figs. 4-14, 4-15, 4-16, and 4-17. Included in Figs. 4-14, 4-15, and 4-16 are RANS results for rectangle and triangle vanes at 18.5˚, RANS results are represented by a thin line and LES results are represented by a bold line. The peak vorticity quickly decays downstream of the vane, Fig. 4-14. As depicted in Fig. 4-12, the vortex from the e423 – Mod vane had the largest initial peak vorticity and the peak vorticity remained the strongest in the downstream flow. The rectangular vanes had slightly weaker peak vorticity and altering the vane angle of these vanes affected the peak vorticity. The vortex peak vorticity from the triangular vane had higher initial peak vorticity than the rectangular vane but quickly diminishes to become the weakest peak vorticity.

The circulation of the vortices is plotted in Fig. 4-15. The circulation of the vortex from the e423 – Mod vane was the strongest throughout the measured downstream domain. The rectangular vanes yielded vortices with slightly weaker circulation and increasing the vane angle increased the circulation. The vortices with the higher circulation decayed the fastest leading to rectangular vanes placed at 16˚ and 18.5˚ to have similar circulation at 20h+. The rectangular vane at 23˚ and the e423 – Mod vane also greatly weakened, but they still contained very strong circulation. The vortex from the triangular vane in contrast had a weaker circulation and weakens quickly in comparison to the vortices from the rectangular vanes. By 30h, the circulation of the vortex from the triangular vortex was nearly zero.

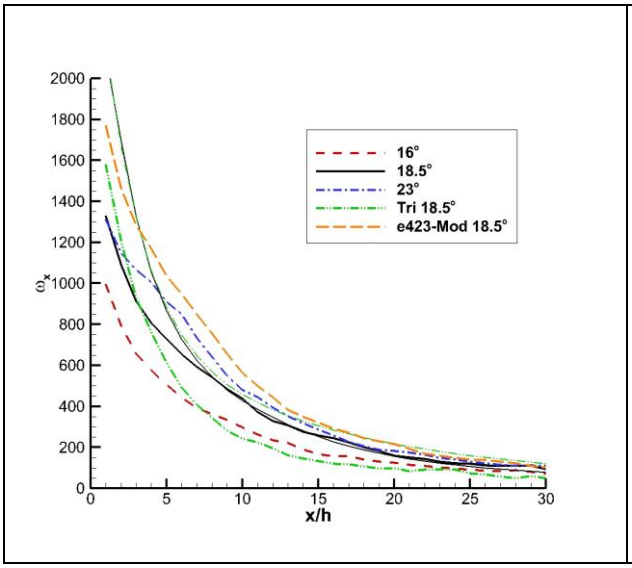

Figure 4-14: Vorticity

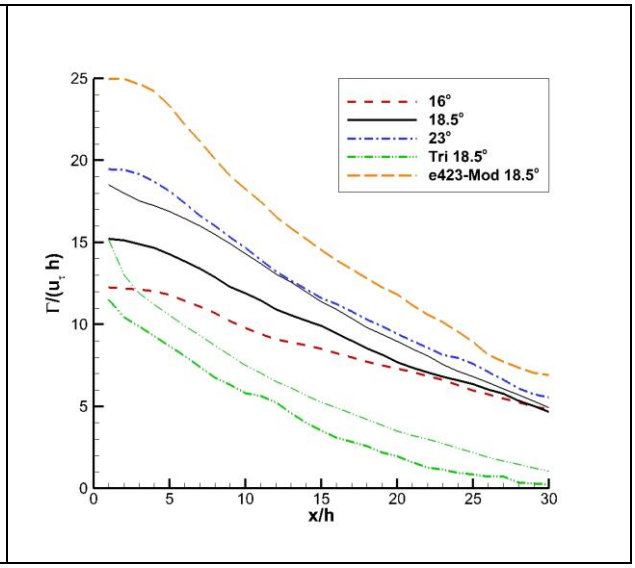

Figure 4-15: Circulation

The trajectory of the vortices is plotted in Fig. 4-16. The vortices from the rectangular vanes and the e423 – Mod vane leave the vane at about 0.8h from the wall; the vortices then move closer to the wall before moving away from the wall. As observed in Fig. 4-12, the vortex from the triangular vane forms

close to the wall and as it leaves the vane, it is less than 0.6h from the wall. The vortex from the triangular vane was not observed to dip closer to the wall as it travels downstream and was observed to move away from the wall quickly. Besides the vertical displacement of the vortices, the vortices also traveled horizontally. Near the vane, the vortices traveled the fastest in the horizontal direction. Further downstream, the rate at which vortices moved in the horizontal direction slowed. The vortices with the strongest circulation were displaced the most in the horizontal direction. For the horizontal and vertical positions of the vortices, the position of the vortices was well defined near the vane but further downstream the position became much harder to pinpoint as the core decayed and multiple 'high' vorticity regions form. The uncertainty of the vortex position leads a zigzag motion in the vortex trajectory. This problem was found to occur while using both the peak vorticity and minimum of Lamba-2 criteria as the indicator the vortex core.

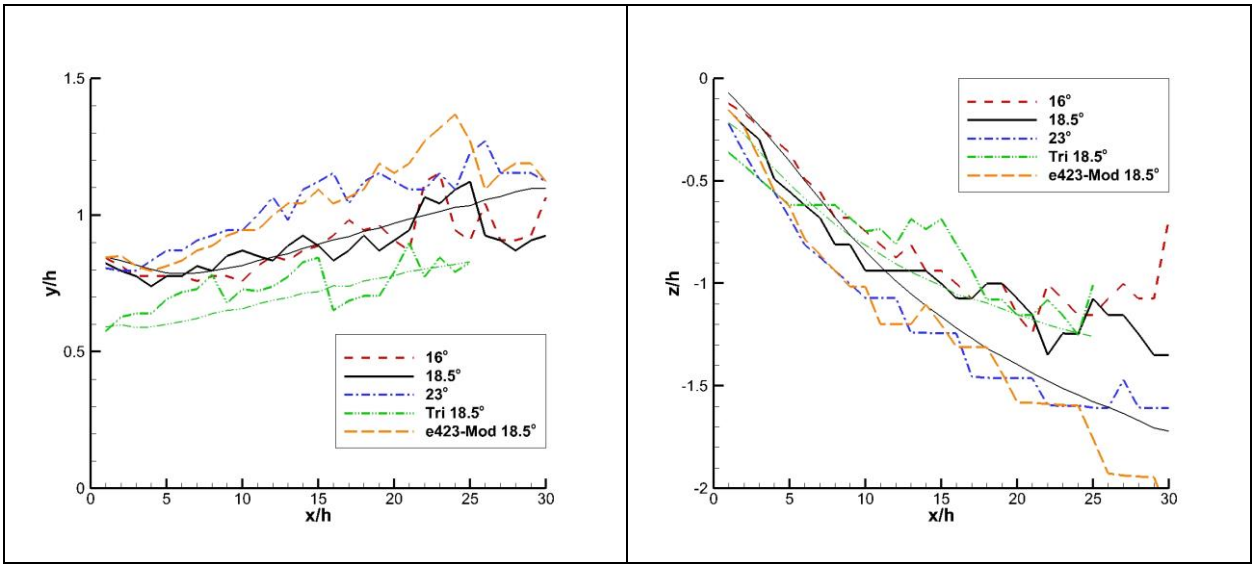

Figure 4-16: Vortex trajectory (Right – vertical, Left – horizontal)

To supplement the vortex circulation plotted in Fig. 4-15, the decay rate of the circulation is calculated and plotted in Fig.4-17. The rectangular vanes and the e423 – Mod vane initially had a low decay rate. At about 2h to 12h, the vortices from the rectangular vanes and the e423 – Mod vane experience their maximum decay rate. The e423 – Mod vane experienced the strongest decay and the rectangular vane at 23˚ experienced the second strongest decay. In contrast, the rectangular vane at 16˚ experienced the lowest decay rate. This suggests the circulation decay rate is proportional to the circulation strength. Further downstream, the vortices experience a lower decay rate in circulation. The vortex generated from the triangular vane in contrast experiences the greatest decay soon after its

formation. The rapid decay of the vortex from the triangular vane is due the vortex being in close proximity to the wall after it's formed.

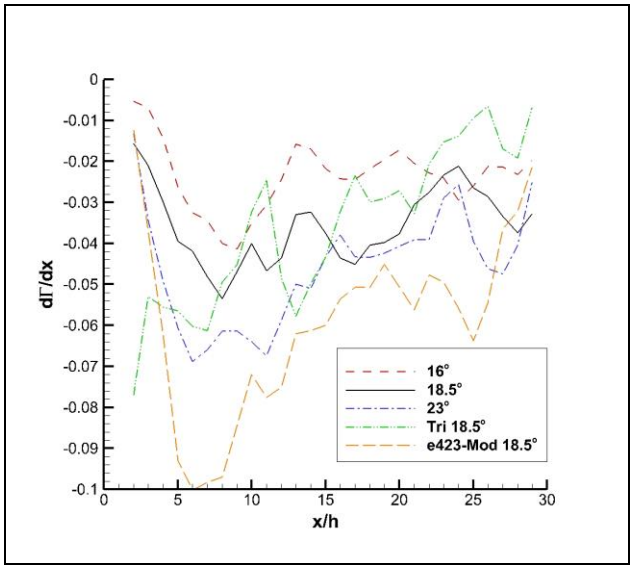

Figure 4-17: Circulation decay rate

To visualize the vortex parameters shown in the previous figures, vorticity, skin friction, normal Reynold stresses, and turbulent kinetic energy are shown in Figs. 4-18, 4-19, 4-20, and 4-21, respectively. As with the vorticity on the vane itself shown in Fig. 4-11, the instantaneous, downstream flow field is also very chaotic and the vortex is deformed by the turbulence of the boundary layer. The position of the vortex core wanders in the vertical and spawnwise direction which has been documented in literature previously [30]. Multiple vortex cores are also present in the instantaneous solution with the cores being more concentrated than the time-averaged solution. Time averaging the vortex structure however yields a more orderly but less concentrated structure. The isocline of 2.5% of the peak vorticity at 1h is shown in Fig. 4-18 to aid in visualizing the growth of the time-averaged vortex. Besides the main vortex, the time-averaged field shows a secondary vortex that forms on the pressure side of the vane. The secondary vortex decays quickly due to its proximity to the wall and by 10h the vortex has completely decayed.

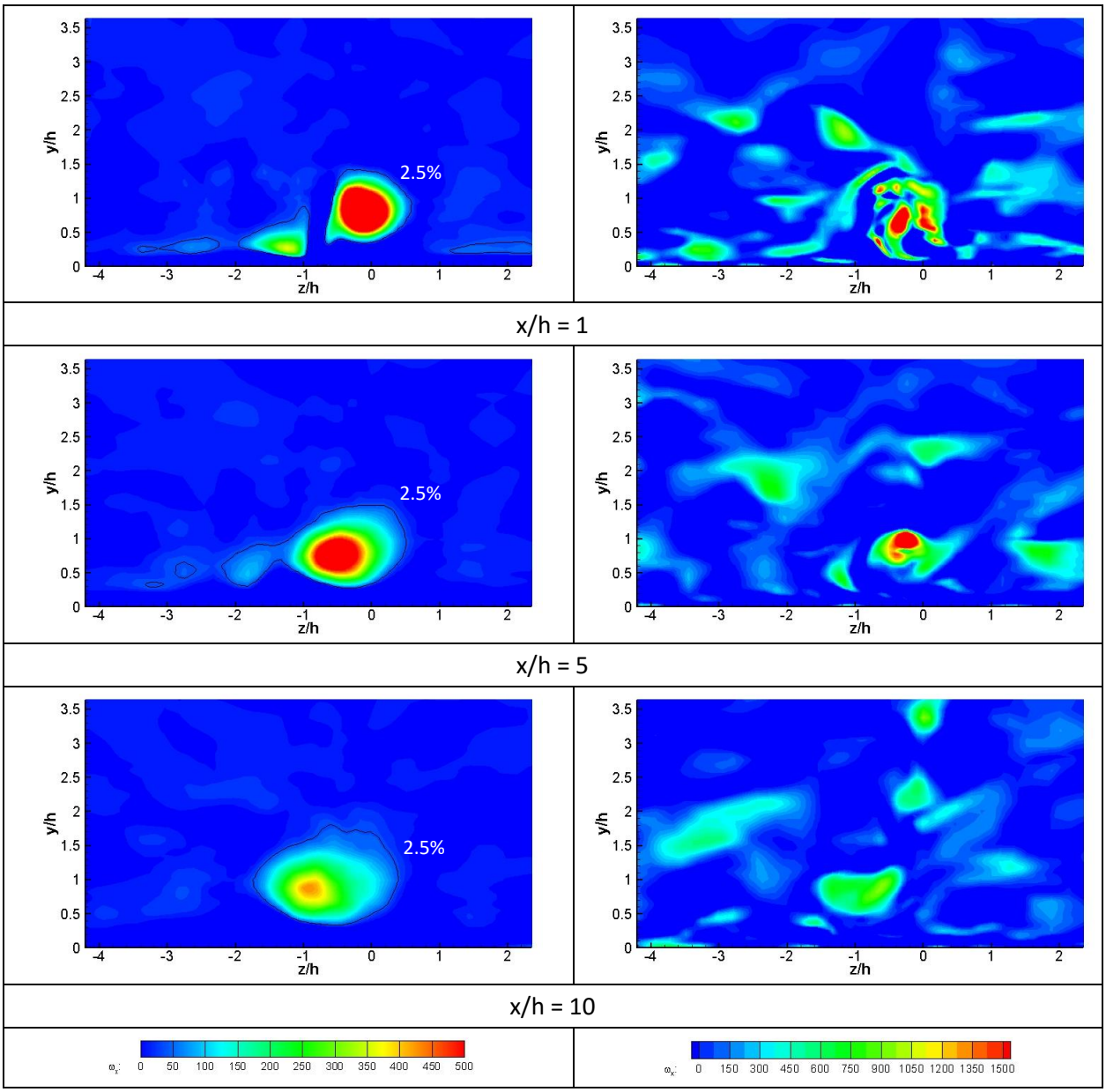

Figure 4-18: Downstream time-averaged and instantaneous vorticity with LES (Right – time-averaged, Left – instantaneous)

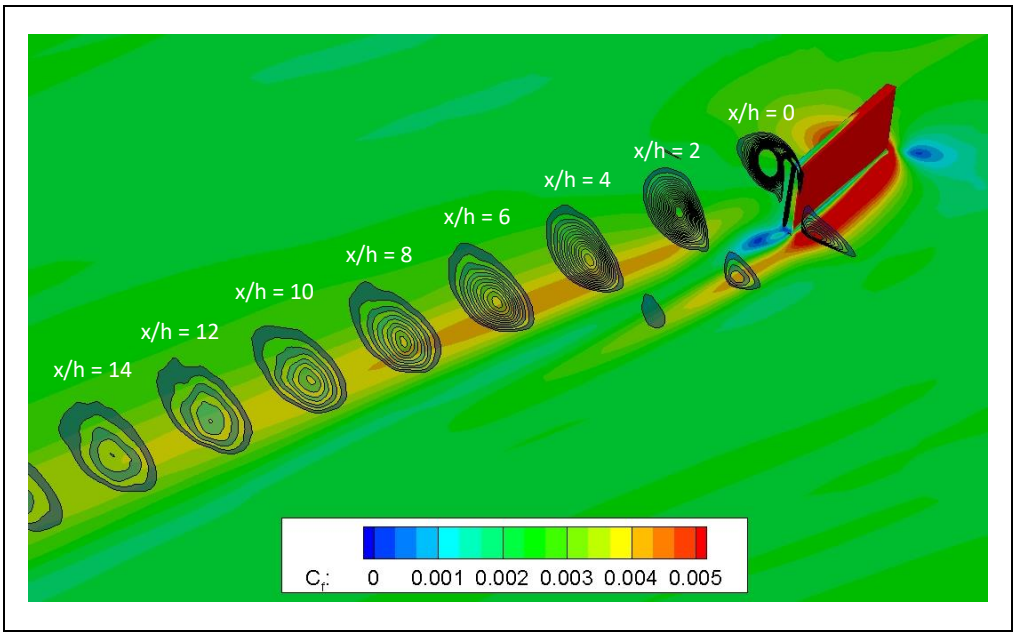

Figure 4-19: Time-averaged vortex effect on the skin friction with LES

The skin friction is a useful metric to express the effect that vortex has on the near-wall boundary layer and the effect that the wall has on the vortex. Shown in Fig. 4-19 is the skin friction contours on the wall along with the vortex structure. Once the vortex leaves the vane, the vortex rapidly diffuses and grows in size, and starts to interact with the wall which is signified by its effect on the wall friction. The vortex is also observed to move closer to the wall as was seen in Fig. 16. These two factors cause the vortex to interact strongly with the wall while it continues to diffuse between 2h and 8h. Unsurprisingly, this is where the fastest decay in the circulation was observed in Fig. 4-15 and 4-17, and peak vorticity in Fig. 4-14. After 8h, the skin friction reduces, signifying that the vortex interaction with the wall has been reduced. The reduction in the interaction is from the vortex moving away from the wall and a reduction in the circulation which decreases the ability for the vortex to circulate flow near the wall. The reduction in the interaction between the wall and the vortex is also expressed as a reduction in circulation decay in Fig. 4-17. After the intense interaction with the wall, the vortex slowly moves further away from the wall while it slowly decays in the boundary layer.

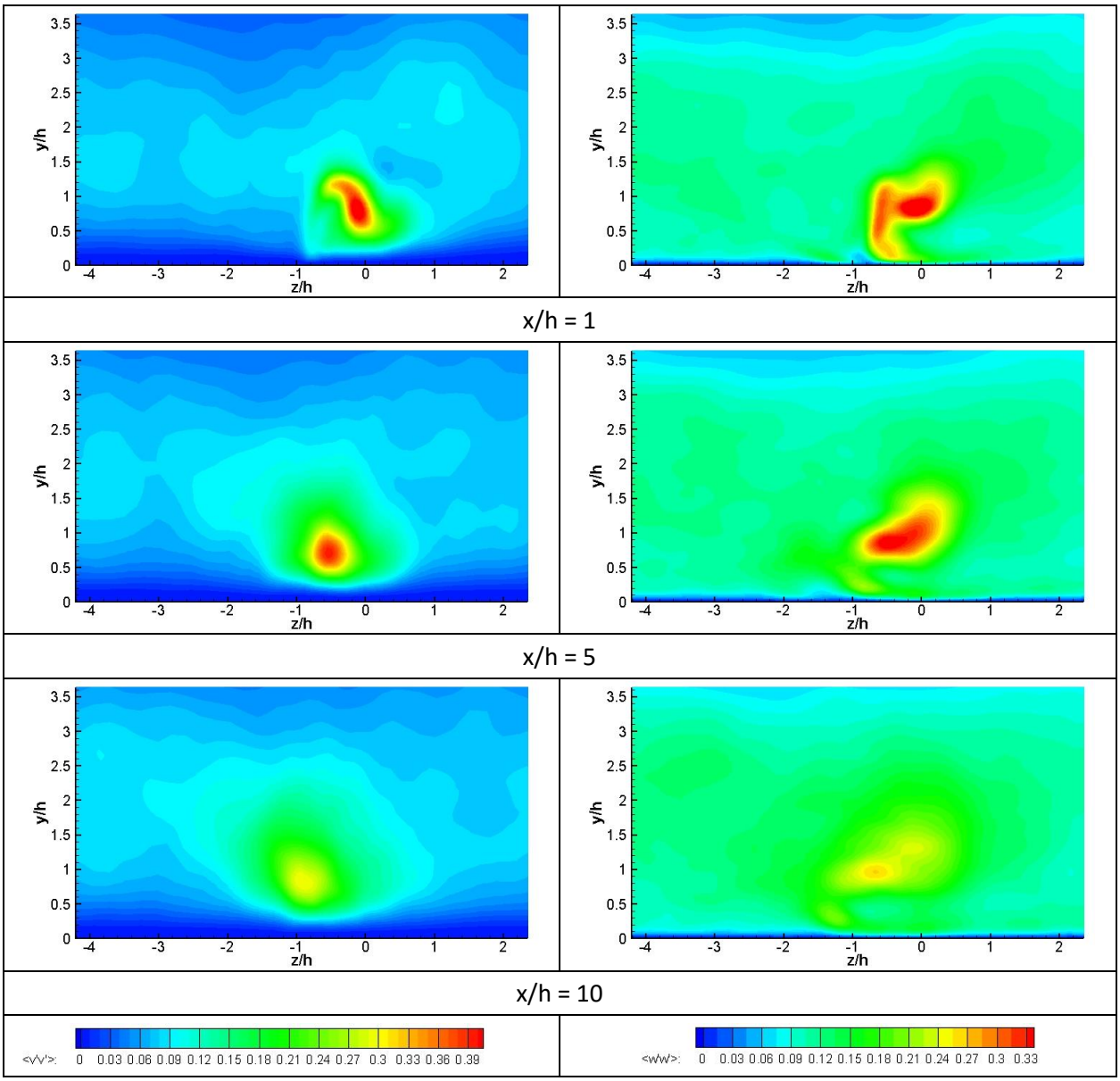

Figure 4-20: Normal Reynold stresses with LES (Right - $\langle v'v' \rangle$, Left - $\langle w'w' \rangle$)

The normal Reynolds stresses at three stations behind the vane is shown in Fig. 4-20. Unsteadiness of the vortex in the turbulent boundary layer induces differences in the *v* (vertical) and *w* (spanwise) velocity components, or v' and w', respectively. Immediately downstream of the vane at 1h, the Reynolds stresses are influenced by the wake of the vane, particularly $\langle w'w' \rangle$. Further downstream, $\langle v'v' \rangle$ obtains a radial distribution while $\langle w'w' \rangle$ has an oval or stretched distribution. The radial distribution of $\langle v'v' \rangle$ is expected due to the random nature of the turbulence. In contrast, movement of the vortex in the spanwise direction is unconstrained allowing for $\langle w'w' \rangle$ to have more of an ellipse distribution. In magnitude, $\langle v'v' \rangle$ is slightly stronger. At 10h, the stresses retain the same distribution but the magnitude of both has weakened. In the case of a solitary vortex, the vortex interactions lay with the wall and the

turbulence in the boundary layer. Angele and Grewe [30] experimentally observed similar behavior in the vortices, however their work was directed at vortices in counter-rotating pairs. To see whether the wake of the vane has an effect on the trajectory of the vortex, more work needs to be conducted on the instantaneous flow field.

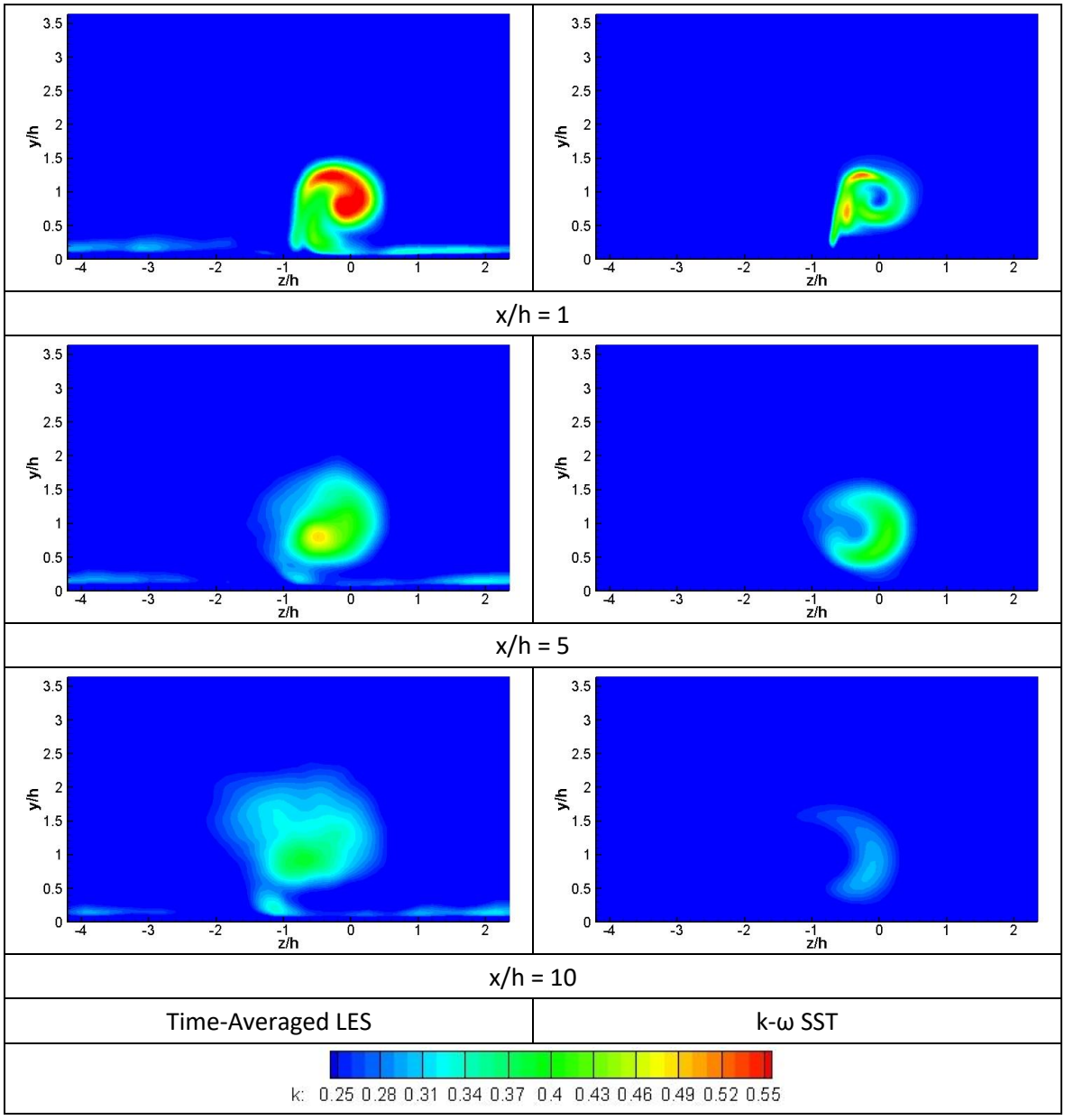

Figure 4-21: Turbulent kinetic energy

Finally, comparing the RANS results to the time-averaged LES results presented in Fig. 4-14, 4-15, and 4-16, RANS had mixed results in comparison to the presented LES results. For the peak vorticity, Fig. 4-14, RANS over predicted the vorticity and the vortex circulation, Fig. 4-15, when compared to the LES results. Looking back to Fig. 4-11, it is visibly noticeable that RANS predicted much stronger vorticity when

the vortex formed. Although the convergence study in section 4.2.1 matched quite well to the published experimental results, this study was conducted at a much higher Reynolds number. However, the vortex trajectory matches very well to what LES predicted, Fig.4-12. The turbulent kinetic energy from the time-averaged LES results and the k-ω SST model are compared in Fig. 4-21. For LES, the peak turbulent kinetic energy is found in the vortex core, the turbulent kinetic energy decays as the vortex moves downstream. In contrast, the turbulent kinetic energy predicted by the k-ω SST model forms a ring around the vortex core. The k-ω SST predicted a much lower value than LES, and by 10h, the turbulent kinetic energy of the vortex has significantly decayed.

4.3.2 Shape Dependence

The shape of a MVG vane is a key component in the formation of the vortex and characteristic of the MVG. Altering the shape of the vane is therefore a potential path to increasing the efficiency and performance of a MVG. In order to study the vane shape, the assumption that a MVG can be broken down into the formation of the vortex (MVG) and the downstream vortex is made. This assumption is similar in concept to the jBAY model. From this assumption, the evolution of the vortex can be defined as a function of the initial state of the vortex after it forms on the MVG. This allows for the formation of the vortex on the MVG to be studied and optimized around a desired initial vortex state. Ashill et al. [111] stated that the effectiveness of a MVG is the strength of the vortex and the improvement in the shape factor of the boundary layer per unit of drag. Vortex circulation is a measure of the transfer of flow in the boundary layer; an increase of momentum transfer in the boundary layer improves the shape factor, making it a suitable metric for efficiency based. Thus, the efficiency of a MVG in this study is taken to be equal to the ratio of the circulation of the vortex at 10h to the drag of the MVG vane. The vortex circulation was measured at x/h = 10 because this is the distance between the MVG and point of separation that Lin et al. [17] found to be the most effective.

The setup for this study is similar to the setup used in the previous sections. ANSYS Fluent was used with the k-ω SST turbulence model to solve for a steady-state solution with the SIMPLEC pressure solver. The convective terms were discretized with a 2nd-order upwind scheme. The MVG vanes were placed on a flat plate with a freestream velocity of 34 m/s and a zero-pressure gradient. The domain extended 125 mm and 800 mm downstream of the MVG. A velocity inlet was used upstream of the MVG and a boundary layer profile of 35mm was imposed on the inlet. The boundary layer profile was generated by a prior RANS simulation of a flat plate with an inlet turbulent intensity of 1% and an imposed velocity

to obtain the desired boundary layer thickness. Periodic boundary conditions were imposed 200 mm apart in the spawnwise direction. No-slip boundary conditions were enforced on the wall and the MVG. The domain extended 200 mm vertically from the wall. The generated meshes had a maximum y^+ of 1 on the wall and 5 on the MVG.

The MVG shape was altered by changing the length (e), the angle (α), and the actual shape. The vane length was tested at 3h, 5h, and 7h. The angle of the vane relative to the freestream velocity was rotated between 16˚ and 29˚. Lastly, the shape of the vane was tested in the form of a rectangle, triangle, the NACA0012 airfoil, e423 airfoil, and a modified version of the e423 airfoil. Airfoil shaped vanes were tested with the idea that MVG vanes operate in a similar manner to wings and using a more aerodynamic shape may increase circulation and decrease drag. The non-rectangle vanes were tested with a length of 3h.

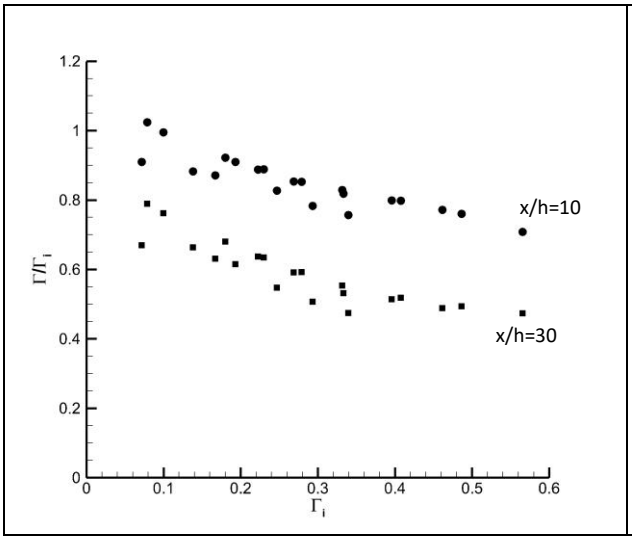

Figure 4-22: Dependency of downstream circulation on initial circulation

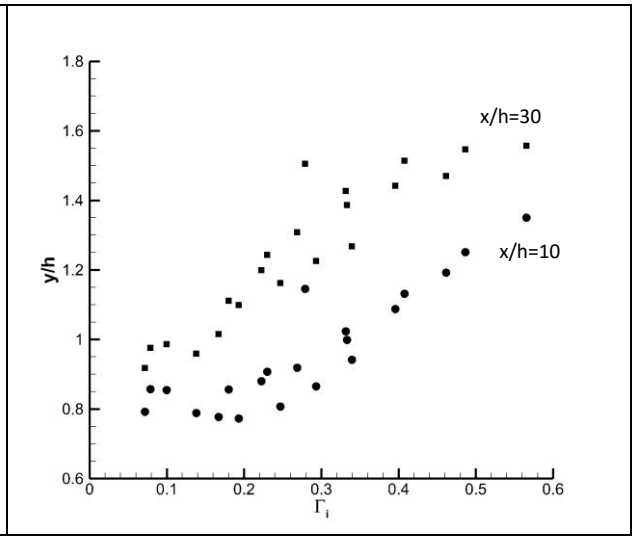

Figure 4-23: Dependency of downstream position on initial circulation

Before looking at the dynamics of vortex formation on the MVG, the downstream behavior of the vortex will be studied to see how well this assumption holds. Varying the angle of MVG vane between 10˚ to 29˚ and using vane lengths (e/h) of 3, 5, and 7, the vortex behavior downstream of the MVG was recorded. Shown in Fig. 4-22 is the circulation and in Fig. 4-23 the y-position of the vortex downstream of the MVG with respect to the initial circulation. The vortex circulation at a given point downstream of the MVG follows a logarithmic function with the initial circulation and as expected, the stronger circulation vortices decay faster. However, the circulation generated by the e/h=3 and e/h=5,7 vanes differs slightly. The y-trajectory of the vortex follows a similar pattern as the vortices propagated downstream except that the trend is less pronounced.

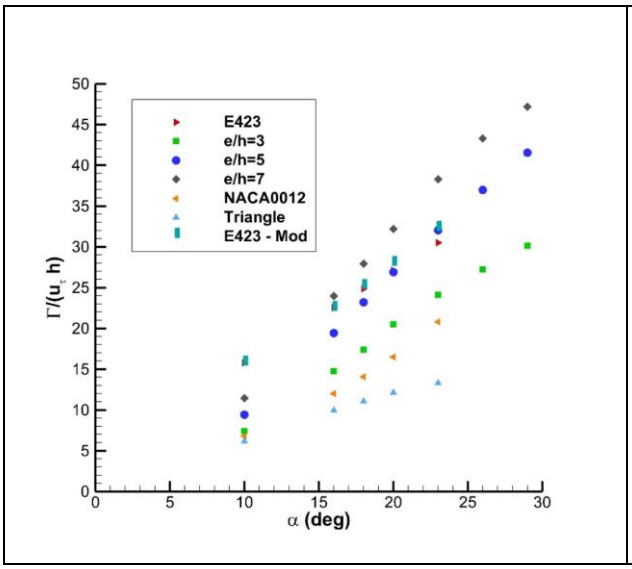

Figure 4-24: Initial circulation dependence on vane angle

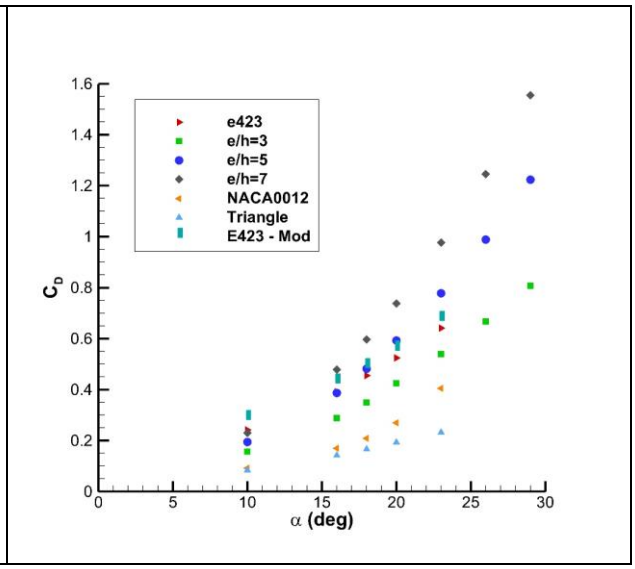

Figure 4-25: Drag dependence on vane angle

From Fig. 4-24, the initial circulation of the generated vortex increases with an increase of angle. At low angles of attack, initial circulation is a linear function of the angle. Increasing the vane angle above 20˚ shows a diminishing increase of circulation. The precise angle at which circulation began to experience a diminishing increase of circulation varied with the vane shape. Comparing the vanes, the triangle vanes were observed to produce the weakest circulation. The airfoil shaped vanes gave mixed results, the E423 and E423-Mod produced much stronger vortices while the NACA 0012 produced weaker vortices when compared to rectangle vanes. Increasing the length of the vane increased the initial circulation of the vortex.

The benefits of MVGs are not without a loss of energy (drag) in the flow and the implementation of MVGs has to be judged on their improvement to the flow versus the drag they themselves add to the overall system. Shown in Fig. 4-25 is the drag coefficient of the vane per angle. The drag of vortex on the wall downstream was neglected and only the drag of the vane itself was considered. Similar to the vortex circulation generated by the vane, the drag increases with vane angle. However, unlike the vortex circulation, the rate at which the drag increases in conjunction with the vane angle.

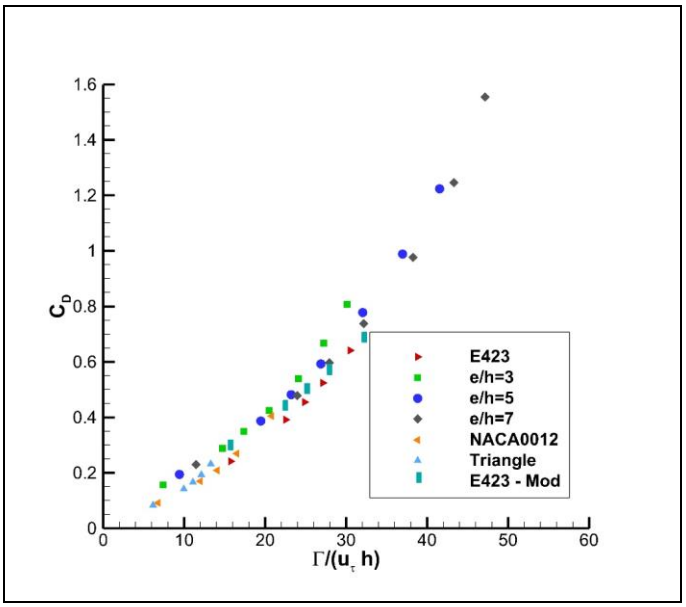

Figure 4-26: Drag coefficient vs initial circulation

A plot can be created from plotting the circulation of the generated vortex versus the drag of the vane as shown in Fig. 4-26. From the plotted data, the drag of the vane is observed to increase as an exponential function of the initial circulation. This exponential relation is observed for each vane shape and as a global set. Two distinct groups can be observed in the plotted data. Rectangle vanes had a slightly higher drag to circulation ratio due to a flow separation problem that will be discussed later while the airfoil shaped and triangle vanes had a better drag to circulation ratio. Furthermore, increasing the vane angle decreases its efficiency by a combination of a diminishing return of circulation increase and an increase of drag. The efficiency of a given vane decreases significantly after 18˚/20˚ and it becomes practical to adopt a new vane shape that generates a stronger vortex.

To provide better insight into the results that were shown previously, the streamwise vorticity and velocity contours are shown in Fig. 4-27 and 4-28. In the figures, the flow fields at 5 streamwise points along the vane for four different MVG shapes were studied. The vanes had an angle of 18˚ relative to the flow direction. For the rectangle vanes and triangle vanes, initial vortex formation occurs on the forward section of the vane. By x/e* = 0.2504, the vortex has begun to roll up, and by x/e* = 0.5007 the vortex has begun to detach from the vane surface. Similarly, the vortex formation occurs near the leading edge of the triangle vane but the vortex continues to grow until the trailing edge of the vane. The vortex at the trailing edge of the triangle vane is closer to the wall than the vortex of the other vanes. In contrast, the vortex formation for the NACA0012 and E423 shaped vanes are delayed until on the second half of the vane.

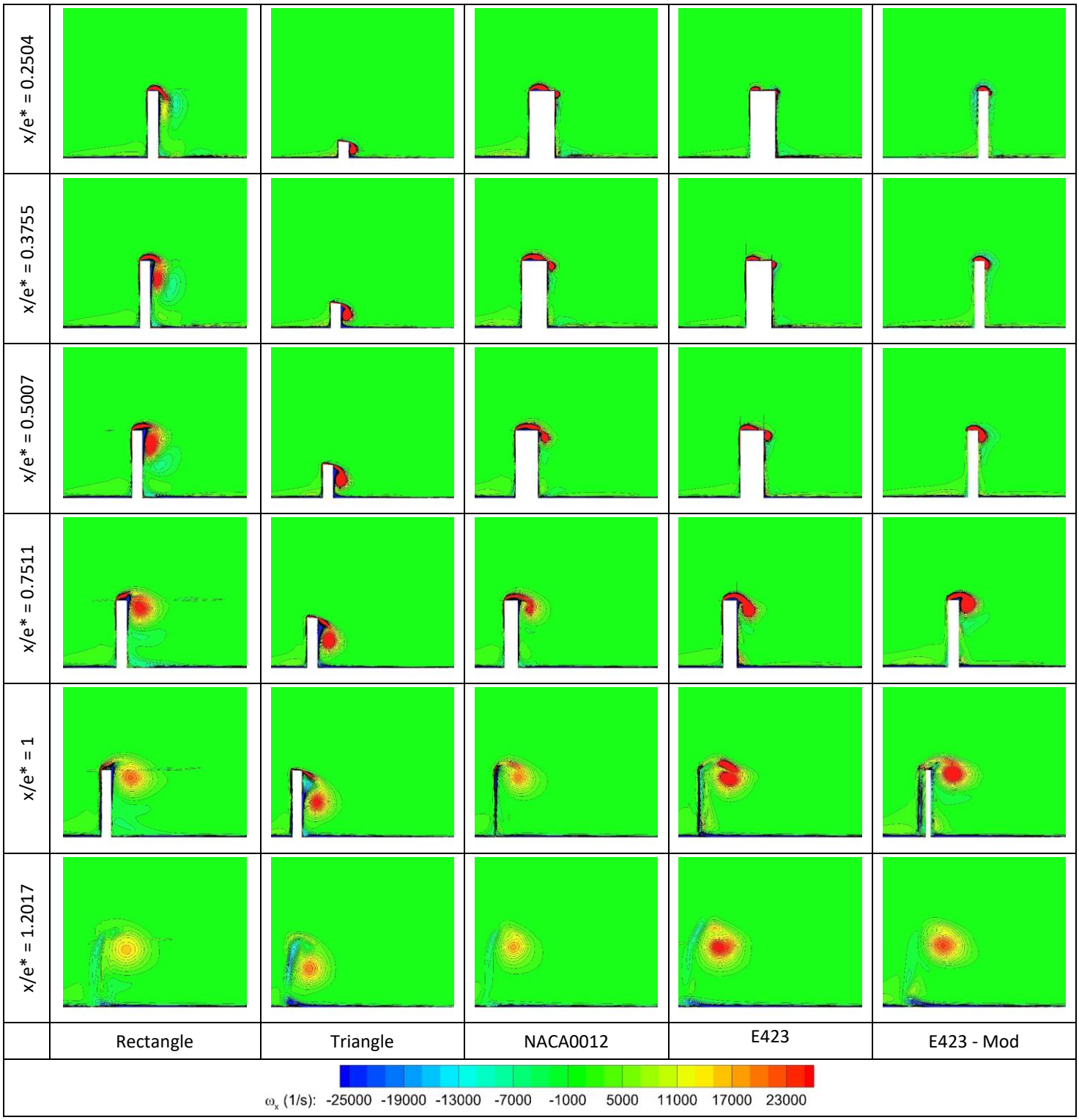

Figure 4-27: ω_x at selected streamwise stations

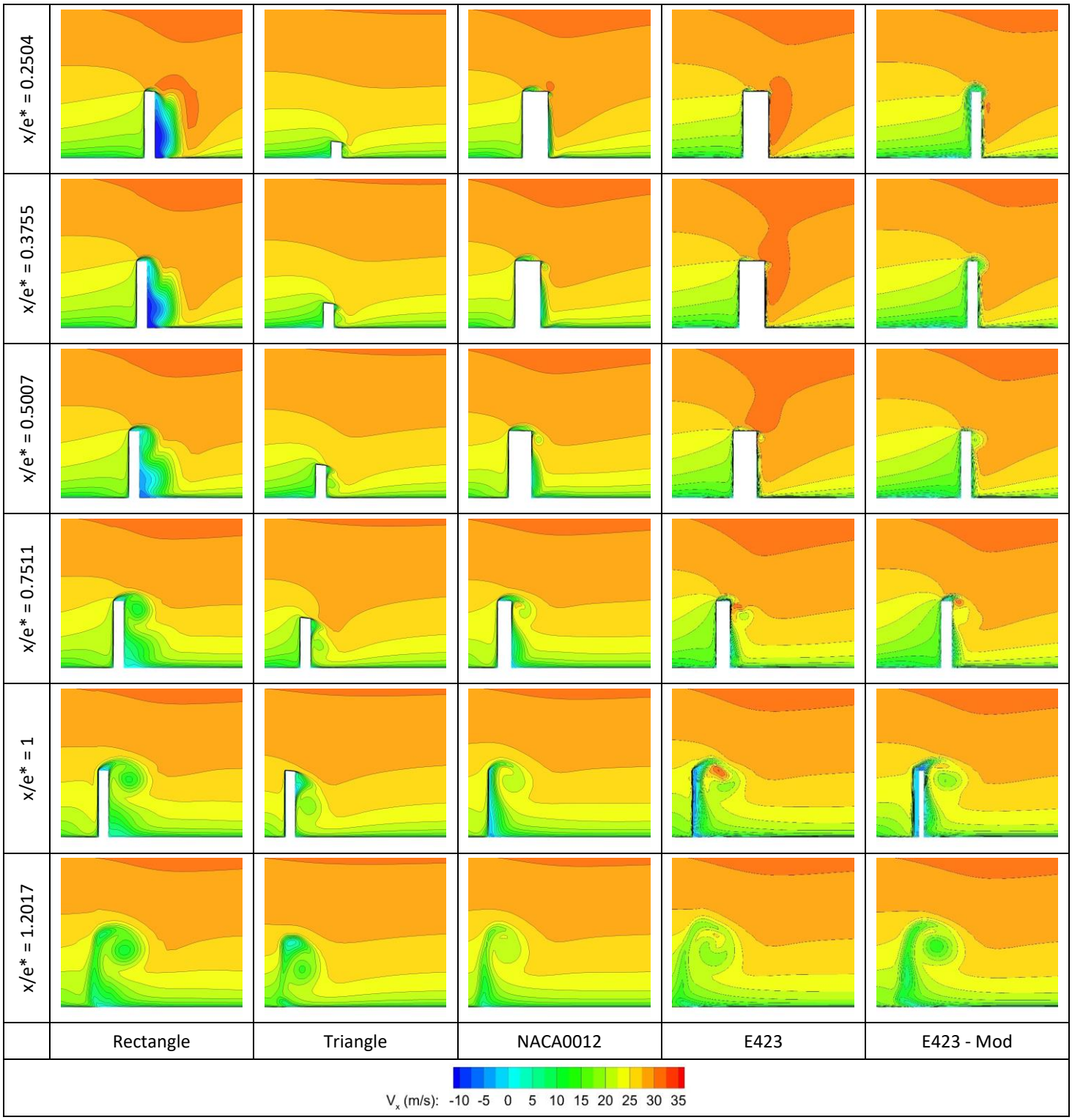

Figure 4-28: V_x at selected streamwise stations

Further insight can be obtained by studying the velocity contours in Fig. 4-29. Rectangle vanes have a noticeable separation bubble on the leading edge of the vane. The separated flow is not suppressed until the vortex has gained sufficient strength at approximately x/e* = 0.5007. The separated flow increases the drag of the MVG vane. For other vanes, the flow remains attached due to a more efficient form. The aerodynamic shape of the vane also plays a role in the vortex formation. The accelerated flow on the forward part of the e387 and NACA0012 vanes' suction side prevents the flow from rolling up, and the flow only rolls up and the vortex forms when the flow decelerates on aft part of the vane. In contrast, the rectangle vane has a separation bubble on the forward section of the vane which allows for the flow to roll up and to form a vortex immediately.

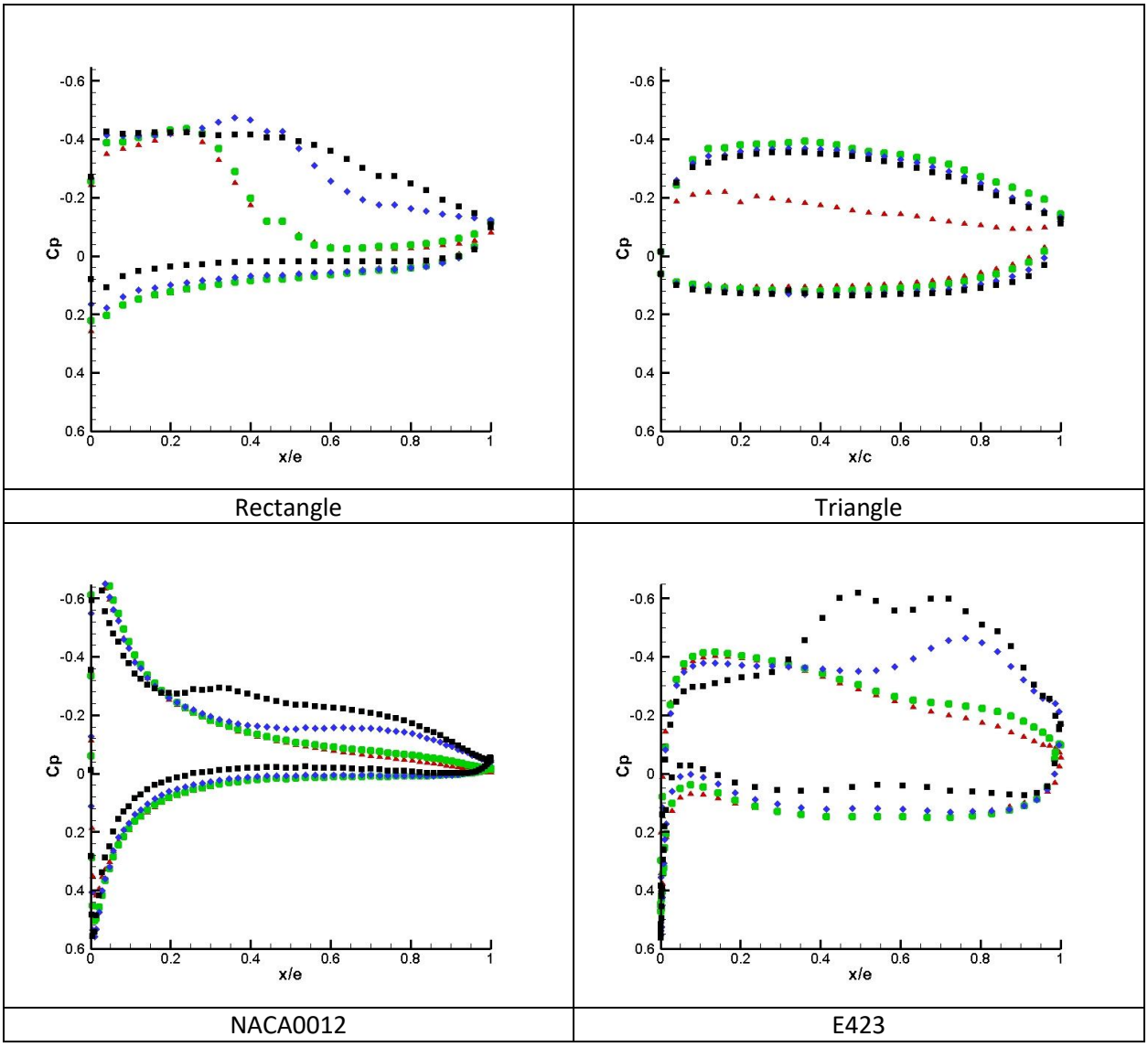

Figure 4-29: Pressure distribution on MVG vanes (▲ – y=0.25h, ● – y=0.5h, ♦ – y=0.75h, ■ – y=0.9h)

The pressure distribution on the vanes at y = 0.25h, 0.5h, 0.75h, and 0.9h are shown in Fig. 4-29. The pressure differential, much as on an aircraft wing, is the driving force of vortex formation on a VG vane. A positive pressure system forms on one side and a negative pressure system forms on the other. On the rectangle vane, the pressure differential is disrupted at half the length of the vane, approximately where the separation bubble is suppressed. The reduction in the pressure differential on the vane consequently causes the vortex formation to stop. The other vanes do not suffer such a collapse in the pressure distribution. The triangle and the e423 vanes maintain the pressure differential along the length of the vane allowing for the vortex formation to continue to the trailing edge of the vane. The continuous pressure differential similarly occurs on the NACA0012 airfoil, but the pressure differential is much weaker leading to a formation of a weaker vortex.

4.3.3 Reynolds Number Effect

Ashill et al. [21] tested MVGs over a wide range of Reynolds numbers to see what effect that the Reynolds number had on the circulation, as noted in the first chapter. Ashill et al. found that above a h^+ of 1,000, the non-dimensional circulation was nearly constant. Below h^+ of 1,000, the non-dimensional circulation trended toward zero, but Ashill et al. main focus was above h^+ of 750. The following section seeks to add to this knowledge and resolve the MVG's Reynolds number below a 1,000.

To study the effect that MVG's Reynolds number has on device's circulation, drag, and other parameters, a similar setup that was used in section 4.3.2. The device's Reynolds number was altered by varying the freestream velocity while maintaining the boundary layer thickness at 35mm. The mesh resolution was altered to the keep the y^+ to less than 1 on the wall and less than 5 on the vane. The rectangle vanes were placed at 18˚ and 23˚ relative to the flow and the vanes had a length of 3h and 7h.

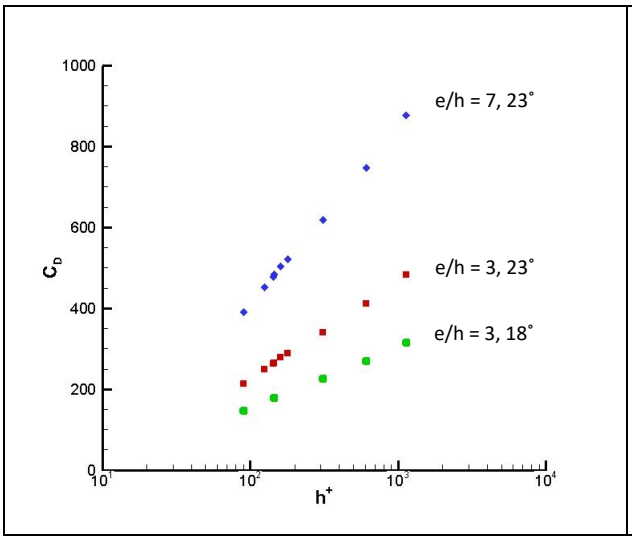

Figure 4-30: MVG vane's drag coefficient relationship with Reynolds number

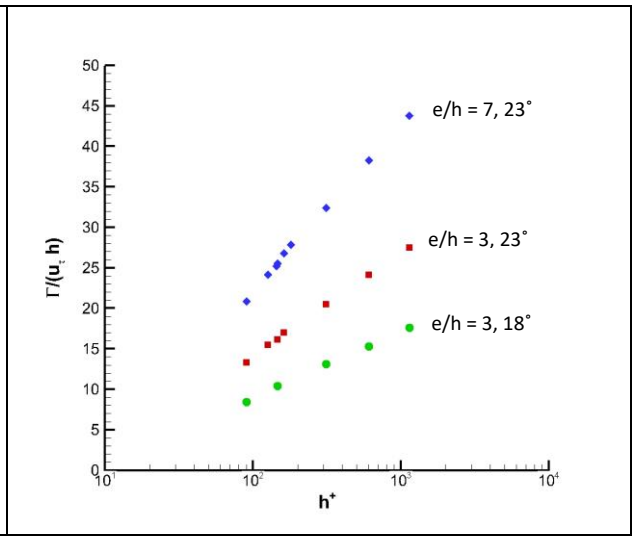

Figure 4-31: Initial circulation relationship with Reynolds number

Altering the freestream velocity led to a MVG's Reynolds number of $90 < h^+ < 1{,}150$ as shown in Fig. 4-30 and 4-31. Fig. 4-30 demonstrates the relationship of the MVG vane's drag coefficient with its Reynolds number and Fig. 4-31 demonstrates the relationship of the circulation at 10h behind the MVG vane. The drag coefficient is based on the friction velocity and the height of the vane. Both properties of the MVG vane have a distinctive logarithmic relation with its Reynolds number. This relationship holds true for both vane lengths and angles.

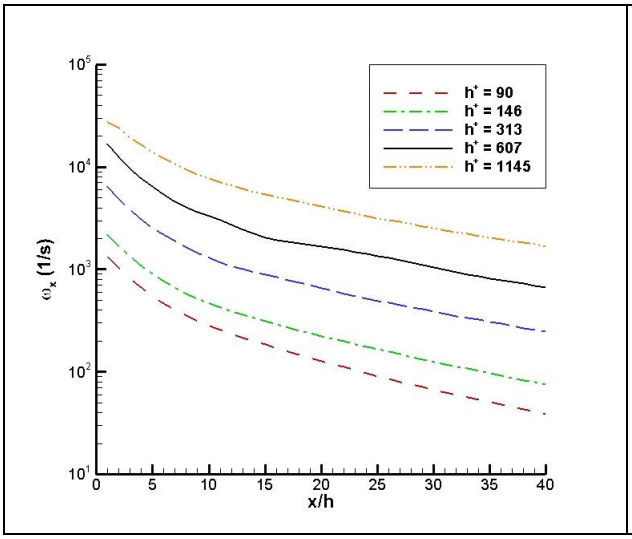

Figure 4-32: Downstream vorticity

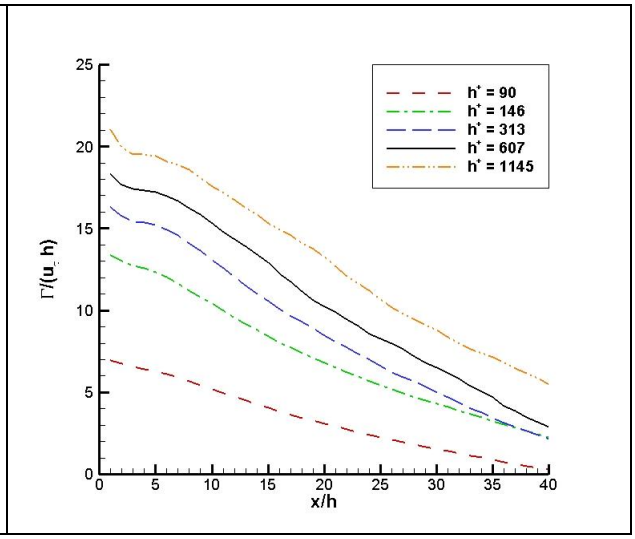

Figure 4-33: Downstream circulation

It is of most interest to study the downstream behavior of a vortex at varying Reynolds numbers. Taking the results from the MVG vane that was placed at 18˚ and had a length of 3h, the peak vorticity, circulation, trajectory, decay, and vortex area was recorded and plotted in Figs. 4-32, 4-33, 4-34, 4-35, 4-

36, and 4-37, respectively. The peak vorticity of a vortex in Fig. 4-32 increases with an increase of Reynolds number. The circulation of a vortex in Fig. 4-33 increases similarly, with an increase of Reynolds number as was noted earlier in Fig. 4-31.

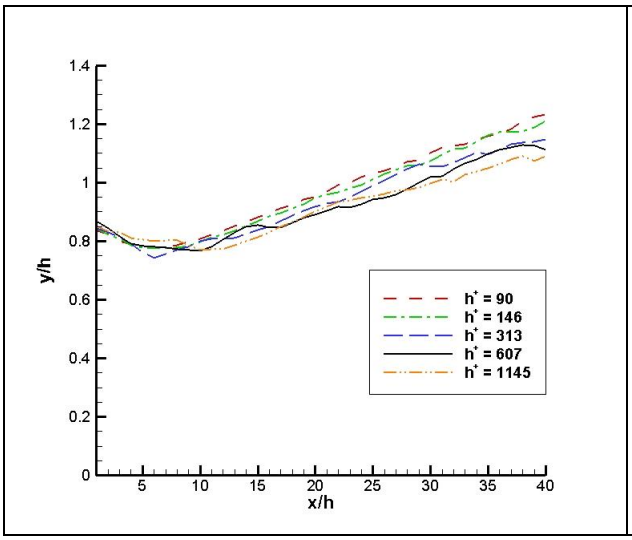

Figure 4-34: Vertical trajectory

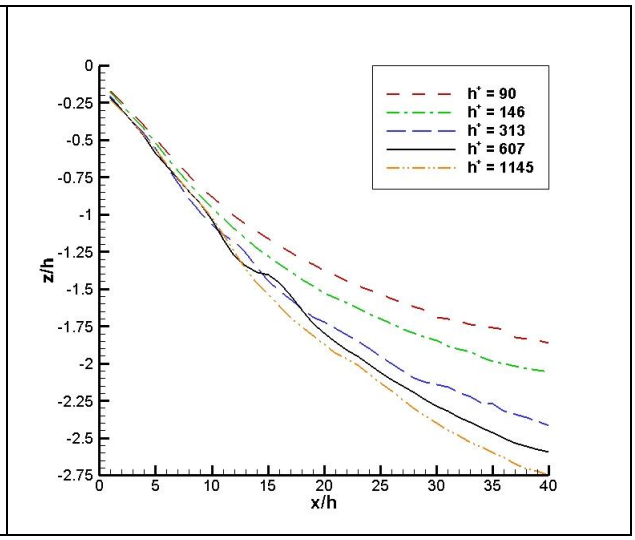

Figure 4-35: Horizontal trajectory

The vertical trajectory of the vortex in Fig. 4-34 was found to be rather independent of the Reynolds number, particularly near the vane. Further downstream, x/h > 10, the vortices from the smaller Reynolds number cases projected away from the wall faster than the vortices from the larger Reynolds number cases. The effect on the Reynolds number had a more profound effect on the horizontal, or streamwise, trajectory. The horizontal trajectory, shown in Fig. 4-35, travels to the right with initial momentum that was gained from its formation. The higher Reynolds number cases were found to travel to the right the farthest while the lower Reynolds number cases travelled the least.

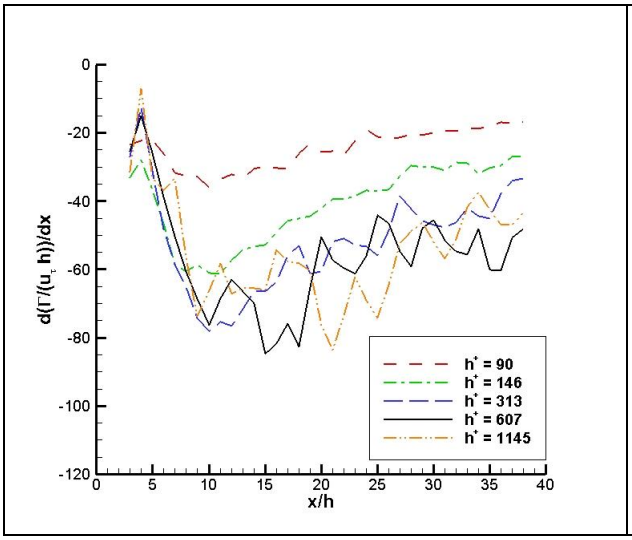

Figure 4-36: Circulation decay rate

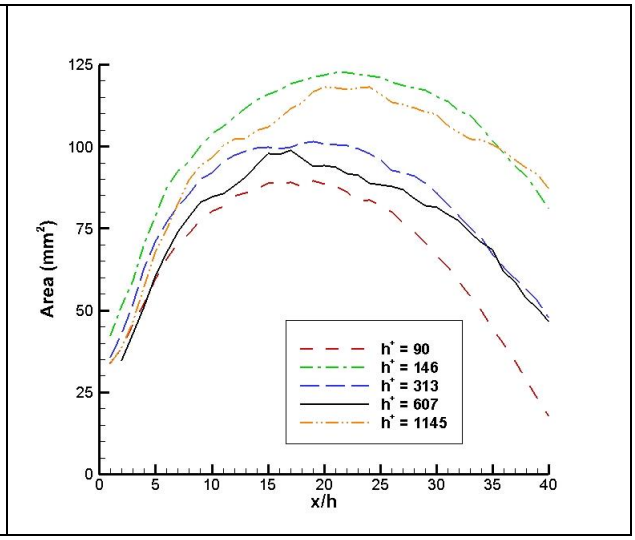

Figure 4-37: Vortex area

About 10h behind the vane, the circulation decay peaks as observed in Fig. 4-36. After 10h behind the vane, the circulation decay rate slows and steadily decays the vortex. The peak decay rate occurs when the vertical position of the vortex is nearest to the wall and the interaction with the wall is strongest as shown in Fig. 4-34. As the vortex propagates away from the wall, the decay rate slightly slows. An increase of Reynolds number had the effect of increasing the magnitude of the circulation decay rate. The area of the vortex core was observed to be independent of the Reynolds number as shown in Fig. 4-37. The vortex at the Reynolds number of 2,062 was observed to have the smallest vortex core while the vortex at the Reynolds number of 3,510 had the largest vortex core; the other three cases fell within these two extremes.

Studying the overall influence that the Reynolds number has on the MVG and its vortex, the Reynolds number controls the strength of vorticity and likewise the circulation. Since the strength of the vortex dictates the path of the vortex, the Reynolds number has an effect on the vortex's trajectory.

4.3.4 Vane Thickness

In the previous sections, an arbitrary thickness of h/7 was chosen, except for the airfoil shaped vanes; it is of interest to determine the effect that the vane thickness has on the vortex parameters. A secondary goal is to determine whether a MVG vane can be modelled with zero thickness (a thin wall), which would decrease the computational cost of modelling a MVG.

The numerical setup was similar to that of section 4.3.2. The freestream velocity was set to 34 m/s and a turbulent boundary layer thickness of 35mm is imposed at the inlet of the domain. The mesh was constructed to ensure that y^+ on the wall was less than 1 and less than 5 on the vane. The tested rectangular MVG vane had a length of 3h and was placed at 23˚.

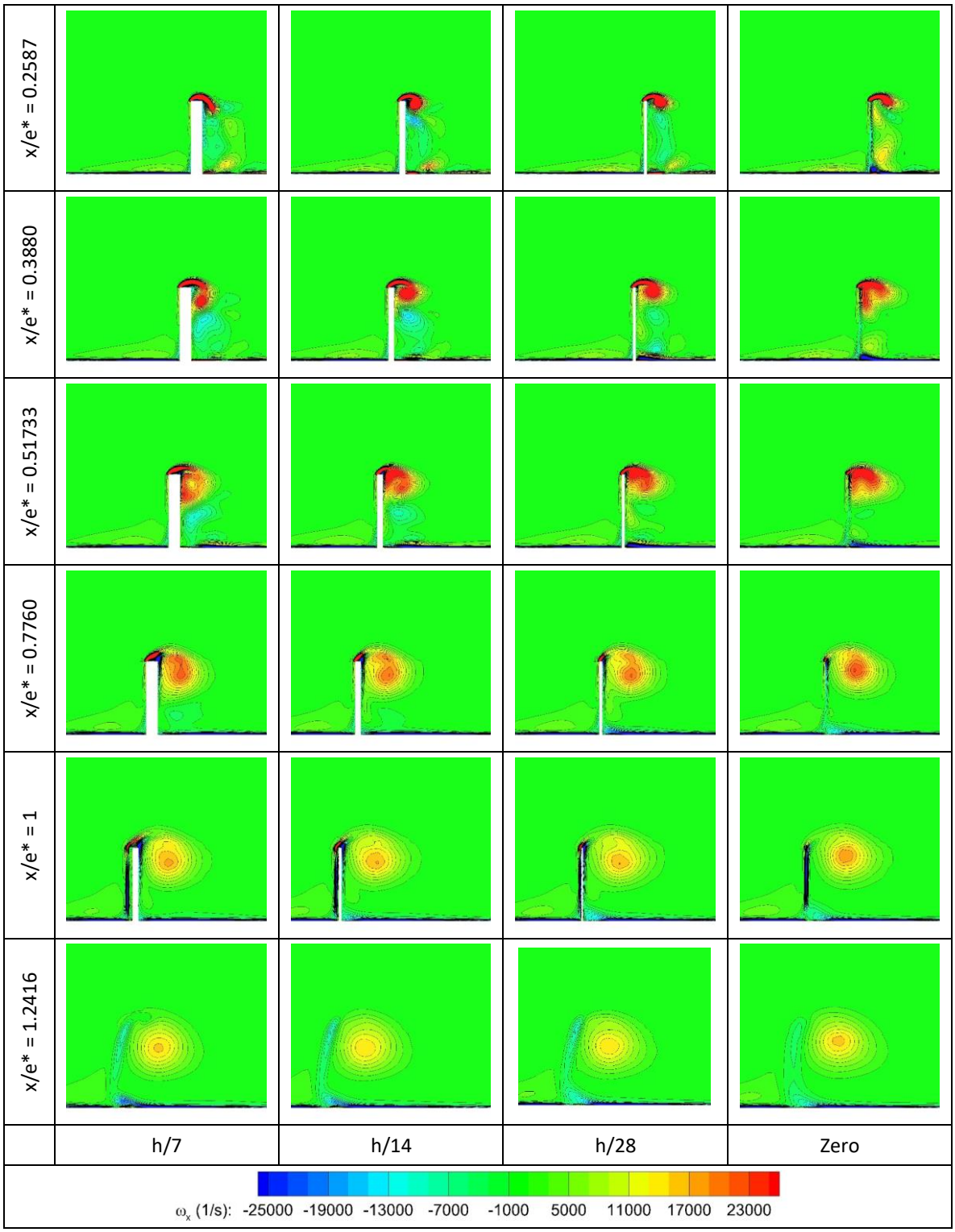

Figure 4-38: ω_x at selected streamwise stations

The vortex parameters downstream of the vane are shown in Fig. 4-39, 4-40, 4-41, and 4-42. Overall, vortices from the four different vane thicknesses follow a similar trend, however there is variation between the thicknesses. The vortex from the vane with a thickness of h/7 was observed to dip towards

the wall far greater at x/h = 5 while vortex from the vane with zero thickness displayed the least amount of dip in it vertical path. Further downstream when the vertical path of the vortex recovers and propagates away from the wall, the vertical trajectory becomes nearly independent of the thickness. In contrast, the horizontal path expressed less variation. Directly behind and far downstream of the vane, there is very little variation while in the region of 5h to 20h there is a slight variation in the horizontal trajectory. For both the vertical and horizontal trajectory, vanes of thickness h/14 and h/28 displayed a nearly identical trajectory.

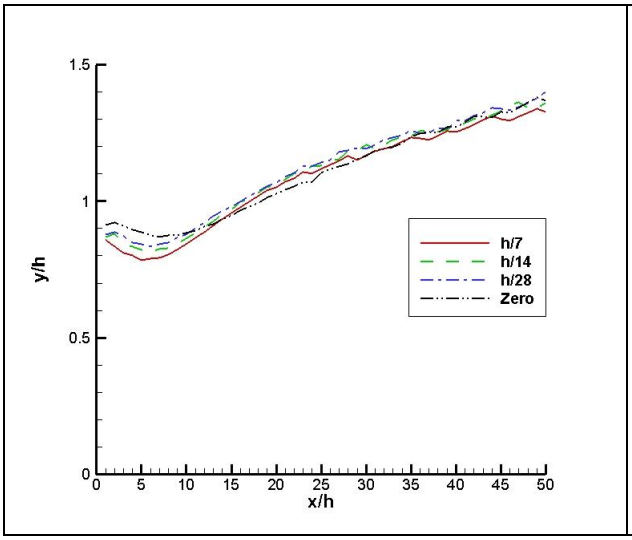

Figure 4-39: Vertical trajectory of vortex

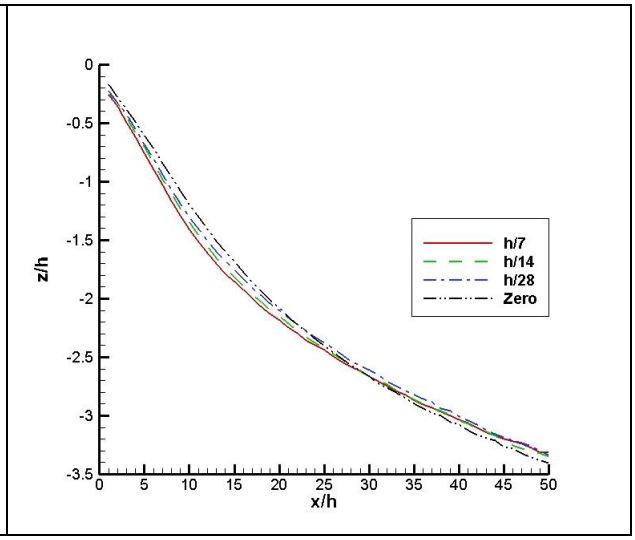

Figure 4-40: Horizontal trajectory of vortex

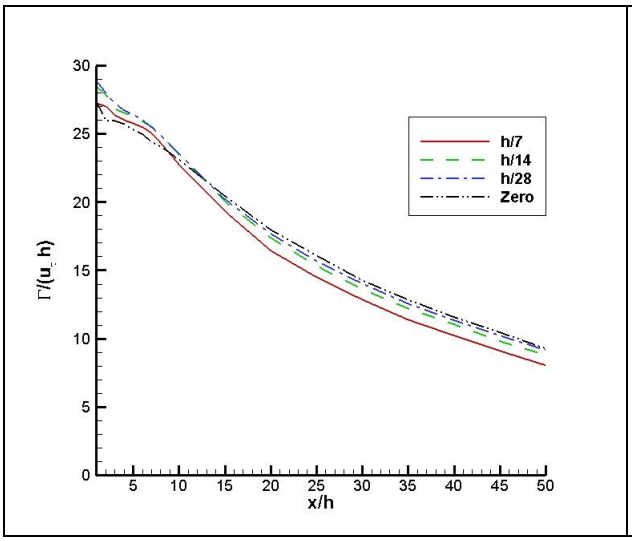

Figure 4-41: Circulation of vortex

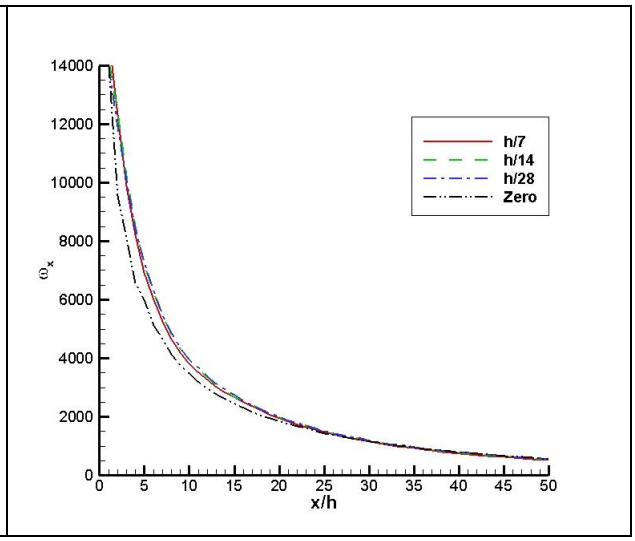

Figure 4-42: Vorticity of vortex

For the downstream circulation, Fig. 4-41, there is a slight variation immediately downstream of the vane. Upon the formation of the vortices, circulation from the vane with zero thickness was the lowest

while the vanes with thickness of h/14 and h/28 had the strongest circulation. The circulation of the vortex from the vane with a thickness of h/7 decayed much more than the others from being closer to the wall, which is also led to a much weaker downstream vortex. The three vortices showed similar circulation strength further downstream. The peak vorticity, Fig. 4-42, is nearly identical for vanes with non-zero thickness. The vortex from the vane with zero thickness displayed a lower peak vorticity in comparison to other vortices. In conclusion, vanes with thicknesses of h/14 and h/28 were found to perform the best. Making the simplification of assuming the vane has zero thickness does not affect the solution significantly.

4.3.5 Height Variation of Rectangular MVG

Lin et al. [1] experimentally tested MVG vanes in a counter-rotating array with heights 0.1h, 0.2h, and 0.4h on an airfoil section. Lin et al. [1] found that 0.2δ was the optimum height to control separation for the tested conditions. Lowering the height to 0.1δ led to MVG to be within the inner boundary layer reducing its effect on the separation. Increasing the height of the MVG to 0.4δ increases the drag on it while leading to no improvement in controlling separation. Other authors in literature have reached similar conclusions. However, in prior published research, authors have looked at the overall effect that MVG of different heights had on the study application and no interest has been given to behavior that MVG height has on the downstream vortex parameters. Furthermore, the boundary layer thickness in many applications may be difficult to calculate or variable in time leading to the height ratio of the MVG to the boundary layer thickness to differ from 0.2. These two factors prompt an interest in how the height of the MVG affects the downstream vortex parameters.

For this study, the height of the vane relative to the boundary layer thickness was tested at 0.1δ, 0.15δ, 0.2δ, 0.25δ, 0.3δ, and 0.4δ. The same setup was used as the previous studies in sections 4.3.2, 4.3.3, and 4.3.4. The boundary layer thickness at the MVG was 35 mm and the freestream velocity was 34 m/s.

Non-dimensionalizing the trajectory of the vortex with the height of the vane leads to very similar path for all 6 vane heights, as shown in Fig. 4-43. The vertical trajectory in particular is very similar among the 6 vanes. Once the vortex leaves the vane, the vortex core moves towards the wall as shown before and is the closest to the wall at 5h to 10h behind the vane. After 10h behind the vane, the vortex moves away from the wall. Also within the first 10h, the horizontal displacements for the 6 vortices follow the

same path. After 10h, the vortices begin to spread out and the vortices from the larger vanes propagate the further in the horizontal direction while the vortices from the smallest vanes propagate the least.

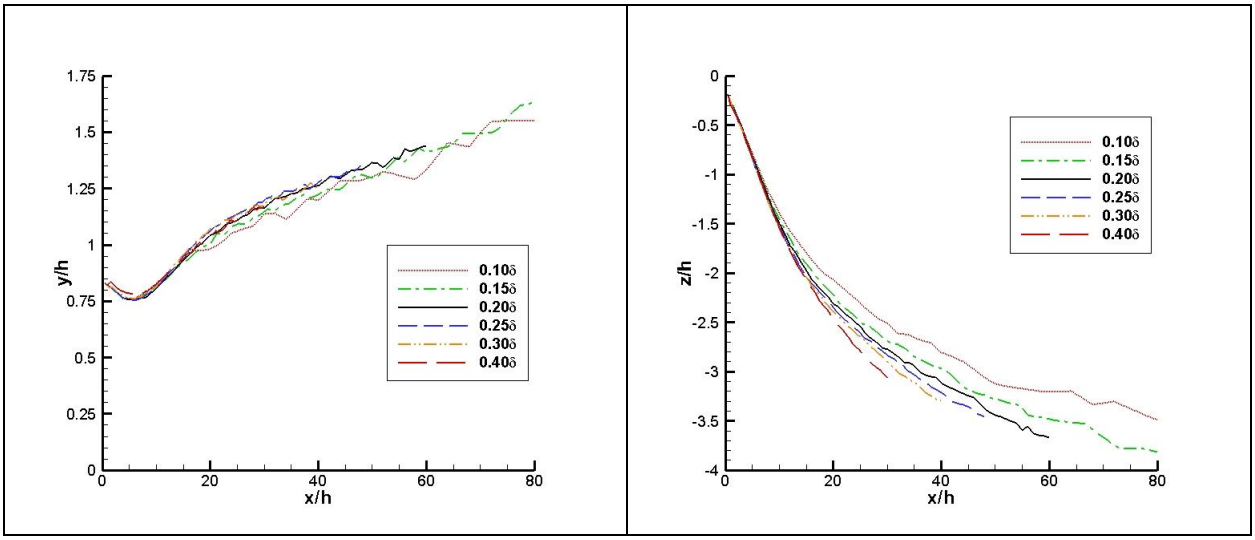

Figure 4-43: Vortex trajectory (Right – vertical, Left – horizontal)

Although the trajectories of the 6 vortices behave very similarly, the circulation of the vortices differ greatly. Shown in Fig. 4-44 is the circulation of the 6 vortices. The larger vanes produce the strongest circulation while the smaller vanes produce the weakest circulation. The larger vanes encounter higher velocity from the vane being higher in the boundary layer. The higher velocities on the vane cause a larger pressure differential on the vane that in turn generates a higher vorticity and circulation in the flow. The smaller vanes in contrast have a lower presence in the boundary layer and experience a lower velocity. By about 20h behind the vane, the vortices have lost half their strength. However, the degradation of the circulation slows and the vane with height 0.1h still has a presence up to 80h. Although it appears the vortices from the smaller vanes have a similar 'life time' to the vortices from the larger vanes, albeit with weaker strength, this is misleading. Since the distance traveled by the vortices is non-dimensionalized by the height of the vane, the unit distance for a smaller vane corresponds to an actual distance much smaller than for a unit distance of a larger vane. This results in the vortex from a smaller vane to decay and dissipate faster than vortex from a larger vane. Therefore, in dimensional distance, the vortex from the larger vanes affects the boundary layer much farther downstream and with much more strength than their smaller counterparts. For a smaller vane to have an effect on the separation, it must be placed much closer to the separation than a larger vane.

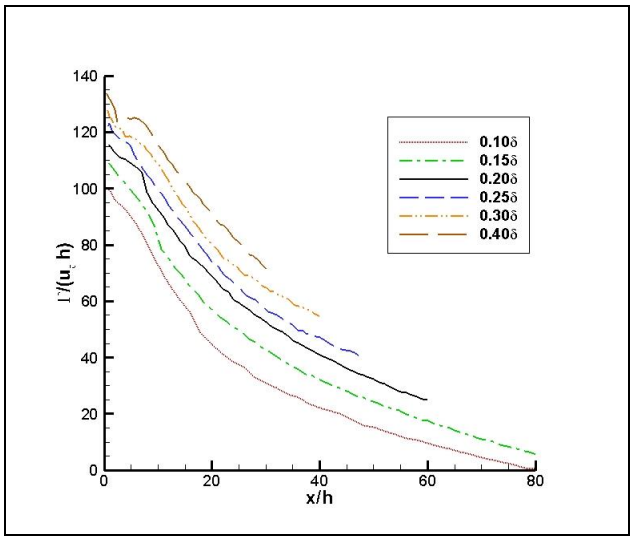

Figure 4-44: Circulation

Finally, shown in Fig. 4-45 is the circulation at two stations downstream of the vane in comparison to the drag coefficient of the vane. The circulation is sampled at 1h, 20h, and 20h* downstream of the vane, h* is a constant height unit of 0.007 mm. Firstly, the plotted data corresponds to the trend published by Lin et al. [1]. One h behind the vane, the drag coefficient increases with no gain of circulation above a vane height of 0.25h, below a vane height of 0.2h the drag coefficient decreases with a decrease of circulation. At 20h behind the vane, the circulation is weaker but the same trend at 1h is observed in circulation to drag points. A more interesting comparison is made if a constant height of 0.007 mm (h* = 0.2δ) is used to scale the distance behind the vane instead of scaling with height of the vane. With this change, the vortices from the larger vanes experience less decay while the vortices from the smaller vanes experience much more decay. In order words, the smaller vanes become less attractive due to a higher decay while the taller vanes become more attractive due to a lower decay in circulation.

Assessing all the data in respect with varying the height of MVG vane, the optimum height is found to be between 0.2δ to 0.3δ. Lowering the vane height below this range leads to the vortex to decay too fast and must be placed very close to the separate region to have any effect on the separation. Increasing the vane height above this range leads to a negligible increase of circulation while the drag increases greatly but the decay in circulation is much smaller allowing for the vortex to have an effect much further downstream. Therefore, the optimum height may be dependent on the particular application.

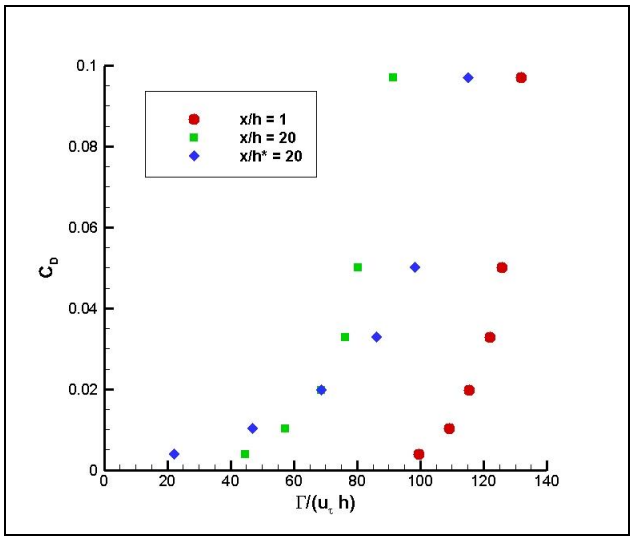

Figure 4-45: Circulation vs Drag

4.4 Conclusion

In this chapter, the dynamics of a MVG vane embedded in a turbulent boundary layer were studied in depth. Experimental wind tunnel tests were conducted to validate computational models on the drag of a vane. From the experimental data, drag from similar computational models was found to compare well to experimentally derived values. Further preliminary work looked at the sensitivity of a MVG to the mesh resolution and found that the flow field around a MVG and the downstream vortex was fairly insensitive to the mesh resolution over the range tested.

Beyond the preliminary studies, a set of LES simulations was conducted for MVG vanes with three different shapes and angles. The dynamics of the vortex formation and behavior of the downstream vortex were discussed. The vortices were found to decay the quickest at a distance of x/h = 2 to 10. The instantaneous path of the vortices was found to be greatly dictated by the turbulence of the boundary layer. RANS models were also conducted of the same setup and were found to over predict the circulation and the vorticity in comparison to the time-averaged LES results. The poor RANS results are contrary to the comparison made in section 4.2.1 to the experimental results of Yao et al. [29]. However, the comparison made to Yao et al. [29] experimental results was conducted at a high Reynolds number (Re = 16533 or h^+ = 607) while the comparison made with the LES results was conducted at a very low Reynolds number (Re = 2900 or h^+ = 125) and thus it is proposed that the accuracy of RANS modelling of a MVG breaks down at the low Reynolds number.

Further work looked at how the shape and angle of a MVG vane impacted their effectiveness. Testing 5 different vane shapes at a range of angles, it was found that triangle vanes were the most effective in terms of downstream circulation per drag of the MVG vane. However, triangle vanes produce much weaker vortices than the other vanes. NACA0012 followed by the e423/e423-mod vanes had slightly inferior circulation per drag, but had much stronger vortices. Rectangles vanes were found to suffer from flow separation on the leading edge which reduced their efficiency. Furthermore, the circulation generated by a MVG vane can be increased by increasing the angle vane, but increasing the angle beyond 18˚/20˚ was observed to decrease the circulation to drag ratio. The circulation to drag ratio of MVG vanes as a whole is limited by the induced drag of the vortex which follows an exponential function of circulation. This leads to conclusion that the weakest vortex producing vanes have the best efficiency without consideration to the required strength of the vortex downstream to suppress flow separation.

The last three studies on MVG dealt with the effect that Reynolds number, the thickness of the vane, and the height of the vane had on the vortex. Circulation and drag of the vane were found to have a logarithmic relation with the device's Reynolds number. A vane with a thickness of h/14 and h/28 was found to produce the best vortex, but there was no wide variation between the tested thicknesses. Moreover, the thickness of the vane can be neglected to reduce computational costs of a simulation and still yield an accurate downstream vortex. Finally, the vortices from vanes a variety of heights were found to behave similarly when the spatial distances were non-dimensionalized with the vane's height. This however translates in the smaller vane's vortex to decay faster than a larger vane's vortex. If actual distances are considered, vanes with the height of 0.2δ and 0.3δ had the best circulation to drag ratio.

The knowledge learned from these studies on MVG are applied later in chapters 5 and 6 where they are applied on an airfoil suffering flow separation and a centrifugal compressor undergoing rotating stall. Rectangle and e423-mod vanes are applied in these chapters; triangle vanes aren't considered due to their weakly generated vortices.

5. Flow Control on E387 Airfoil

Before applying MVG to the complicated case of controlling rotating stall in a centrifugal compressor, a short study was conducted on using MVG to control flow separation on the Eppler 387 (e387) airfoil. Implementing MVG in an intermediary case such as on the e387 airfoil allows for MVG to be studied in a realistic application. The e387 airfoil was also designed for a Reynolds number sufficiently low to study effectively with LES, allowing for a far more in-depth study into the dynamics of a MVG.

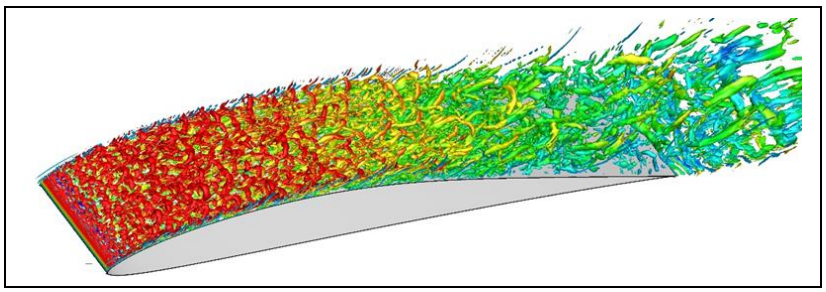

Figure 5-1: Lambda-2 criterion of the turbulent flow on e387 airfoil

The e387 airfoil and similar airfoils are commonly used to for wind turbines and UAVs. At low Reynolds numbers (<500,000) and high angles of attack, the e387 airfoil suffers laminar separation on the leading edge of the airfoil due to the airfoil curvature and an adverse pressure gradient. The flow then transitions to a turbulent flow causing the flow to reattach; further downstream on the airfoil, the flow separates again in presence of another adverse pressure gradient. These flow features have led to the e387 airfoil to be extensively tested. These flow features of the e387 airfoil can be observed in Fig. 5-1 with the airfoil placed at a high angle of attack. Volkers [112] experimented with the airfoil at Reynolds numbers of 60,000 to 500,000. McGhee et al. [113] conducted wind tunnel experiments on the airfoil at Reynolds numbers of 60,000 to 460,000. McGranahan and Selig [114] used oil flow visualization experiments to determine the separation and reattachments points at Reynolds numbers of 200,000 to 500,000.

5.1 Numerical Setup

The airfoil was placed at an angle of attack of 12˚ in a flow to give the airfoil a Reynolds number of 200,000. To keep the mesh size of the simulation within reasonable limits, the domain size was sacrificed. A velocity inlet was imposed 3c upstream and a pressure outlet was imposed 5c downstream of the airfoil. Periodic boundaries were enforced 0.15c in the spanwise direction. The geometry of the computational domain is shown in Fig. 5-2. A c-mesh topology with hexa cells was used to mesh the

domain. To determine the sensitivity of the simulation to the mesh resolution, Mesh 1 and 2 were generated with 24.2 and 34.8 million cells, respectively. Mesh 1 had a maximum y^+ of 3.0 and an average y^+ of less than 0.4. The grid resolution in the streamwise (x^+) and the spanwise (z^+) were both less than 20. Mesh 2 had a maximum y+ of 1.4 and an average of less than 0.4. The grid resolution in the streamwise (x^+) and spanwise (z^+) was less than 15.

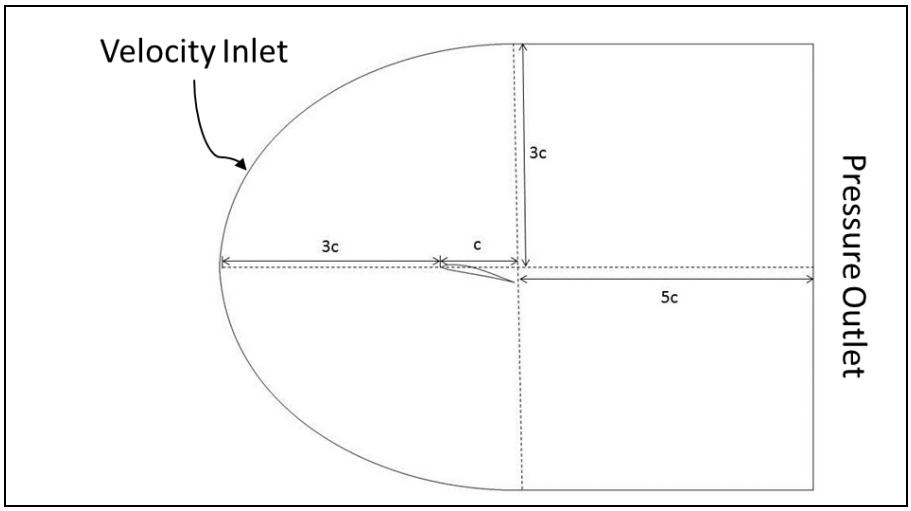

Figure 5-2: Numerical setup of e387 airfoil

For the simulation, *Code_Saturne* was run with LES and the subgrid eddy viscosity was modelled with the DSM (Dynamic Smagorinksy-Lilly) and WALE (Wall-Adapting Local Eddy-viscosity) models. Without a predetermined Smagorinsky constant, the constant Smagorinksy-Lilly subgrid model was not considered. An implicit 2nd-order Crank-Nicholson time scheme and a 2nd-order spatial discretization schemes were used. To ensure numerical stability and accuracy, the CFL number was kept below 0.65. The simulation was allowed to run for 2 flow through periods before statistics of the flow were taken, the flow was averaged over a further 2 flow through periods.

5.2 Baseline

A baseline case was carried to establish the sensitivity of the simulation to the mesh resolution and to give a comparison to cases utilizing MVG's to suppress flow separation. Shown in Table 5-1 is a comparison of the computed drag and lift to the experimental values determine by McGhee et al. [113] and Selig et al. [115]. The numerically derived lift coefficient was overestimated and the drag coefficient was underestimated compared to the published values. There was a slight difference between the computed values of Mesh 1 and 2, and the DSM and WALE subgrid models yielded nearly the same values.

	AoA	C_L	C_D
Selig et al. [115]	12.17˚	1.215	0.0733
McGhee et al. [113]	12.09˚	1.174	-
Mesh 1 - DSM	12.00˚	1.309	0.0510
Mesh 1 - WALE	12.00˚	1.310	0.0504
Mesh 2 - DSM	12.00˚	1.353	0.0571

Table 5-1: Comparison of published experimental drag and lift to LES results

The reason for the under predicted drag and overestimated lift can be seen in the predicted flow features and pressure distribution. Table 5-2 compares the laminar separation, the turbulent reattachment, and the turbulent separation points to what was experimentally observed by McGranahan et al. [114]. The distances given in Table 5-2 are given as fraction of the airfoil chord. The predicted laminar separation bubble is drastically under-predicted on the leading edge by much as a third. Increasing the mesh resolution on the airfoil yielded a larger separation bubble, but the separation bubble was still only half the size that was observed experimentally. The turbulent separation point was better predicted by the numerical simulation although increasing the mesh resolution did not improve the predicted separation point. In the results that McGranahan et al. [114] published, the turbulent separation point drastically changed from 10.10˚ to 12.10˚ suggesting a strong sensitivity in the turbulent separation point at that angle of attack.

	AoA	Laminar Separation	Turbulent Reattachment	Turbulent Separation
McGranahan et al. [114]	12.10˚	0.000	0.050	0.450
McGranahan et al. [114]	10.10˚	0.000	0.070	0.700
Mesh 1 - DSM	12.00˚	0.002	0.0158	0.630
Mesh 1 - WALE	12.00˚	0.002	0.0174	0.720
Mesh 2 - DSM	12.00˚	0.007	0.0293	0.765

Table 5-2: Comparison of published experimental separation and reattachments points to the LES results

The dynamics of the flow are further illustrated in the skin friction and pressure distribution in Fig. 5-3 and 5-4, respectively. From Fig 5-3, the skin friction near leading edge drops to zero which denotes the laminar separation; the skin friction increases when the flow transitions to a turbulent flow and reattaches. The skin friction steadily decreases from the curvature of the airfoil and the adverse pressure until once again the skin friction reaches zero which denotes the turbulent separation. Between the two subgrid models, the WALE model predicts a stronger skin friction. Increasing the mesh resolution shows a slight increase of skin friction. The differences in the pressure distribution, Fig. 5-4, were less noticeable between the two subgrid models and mesh resolutions. However, the numerical results predicted a more

negative pressure distribution than was observed by McGhee et al. [113]. The stronger suction on the airfoil leads to a stronger lift.

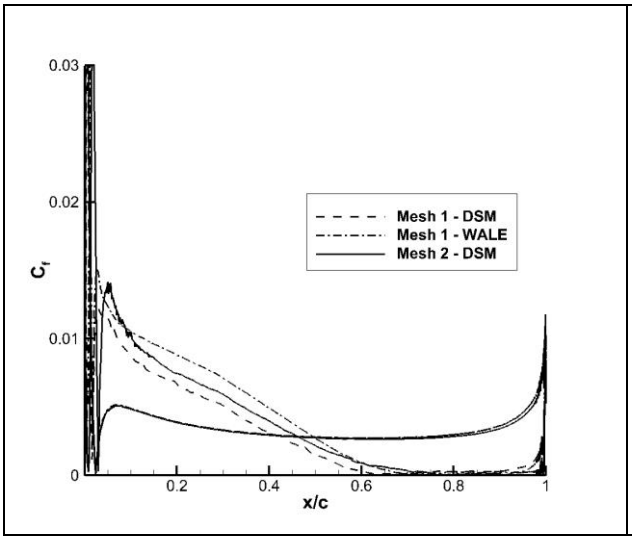

Figure 5-3: Skin friction on e387

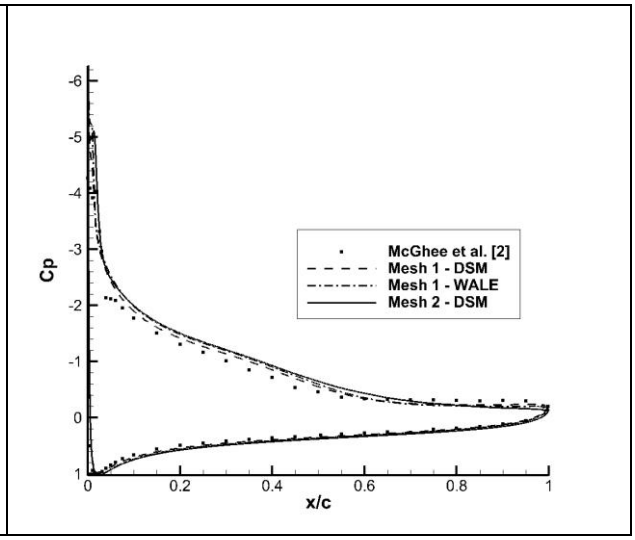

Figure 5-4: Pressure coefficient distribution on e387

A graphic illustration of the skin friction on the upper surface, or suction side, of the airfoil is shown in Fig. 5-5. The instantaneous and time-averaged skin friction is compared. In the time-average results, the flow features are easily discernable while the instantaneous results are much more chaotic.

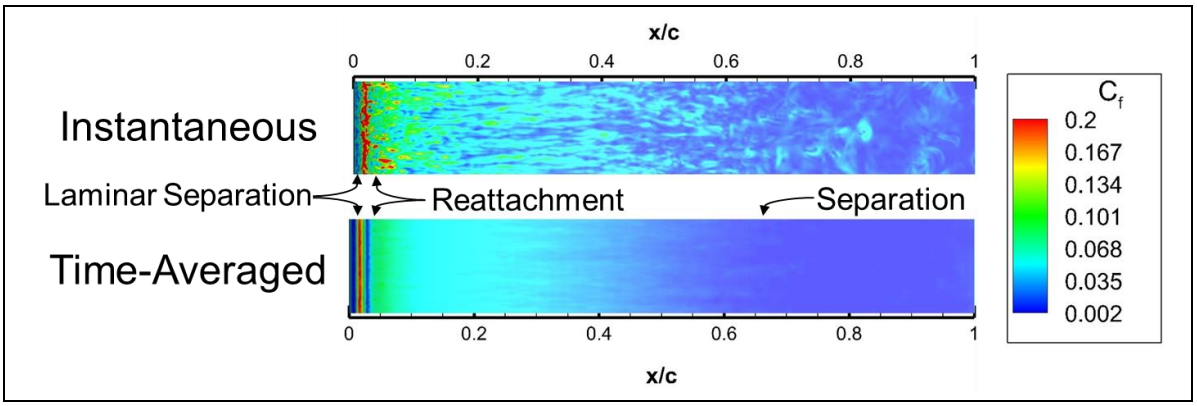

Figure 5-5: Instantaneous and time-averaged skin friction on e387 airfoil

It can be concluded from the position of the flow features and the pressure distribution that the overestimation of the lift and under prediction of the drag is due to the under prediction of the laminar separation bubble and the turbulent separation point. The under prediction of these flow features leads to a more favorable pressure distribution on the airfoil, which generates more lift. Although it is hard to pinpoint the culprit of this problem without further study, the leading cause may be the small domain size. While it is preferable to have an accurate prediction of the flow on the e387 airfoil at the tested

conditions, the main goal of this study is to observe the behavior of a MVG on airfoil that has adverse flow conditions. The baseline results are therefore sufficient to give a good comparison to the MVG study.

5.3 Flow Control

To study the impact of using MVG vanes to control the turbulent flow separation, the same computational setup was used from the baseline study. The rectangular MVG vanes that were used had a height (h) of 0.01c and a length of 3h. Three vane angles were tested at 18.5 ˚, 23˚, and 14˚, Case 1, 2, and 3, respectively. The Reynolds number based on the freestream velocity and the height of MVG was approximately 2,000. The Reynolds number based on the friction velocity and the height of the MVG vane, h^+, was 108.9. The meshes that were generated for the three MVG configurations used a similar mesh resolution to Mesh 2 in the baseline study. To resolve the flow around the MVG vane, the mesh resolution was increased near the vane and in the streamwise direction. Due to strong and complex flow around the a MVG vane, the mean y^+ on the vane was 8. The meshes for the three cases had approximately 40.6 million cells. A view of the mesh surrounding the MVG on the airfoil is shown in Fig. 5-6.

Similar to the baseline case, the numerical simulation was allowed to run for a two downwash periods before statistics were taken. The drag and lift were monitored along with the overall flow field to ensure that the flow field had reached a 'converged' state. The flow field was then averaged over a further three downwash periods, the results are presented in the following sections. The analysis of the vortex was conducted by extracting planes normal to the airfoil surface from the time-averaged flow field. From the extracted planes, the vortex was evaluated using methods that were described in section 4.1.

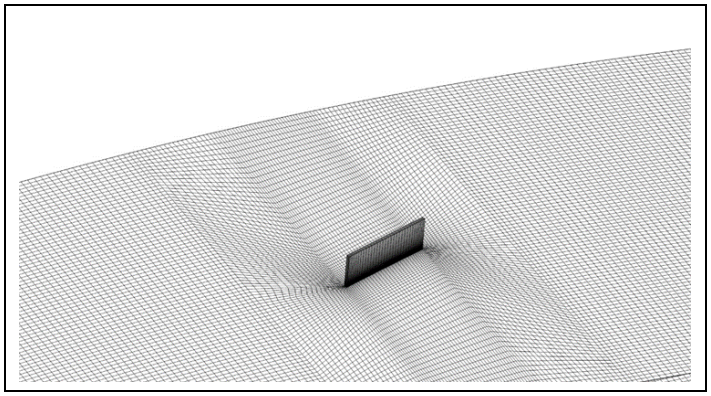

Figure 5-6: MVG mesh on the e387 airfoil

5.3.1 Vortex Parameters

The vortex from Case 1 is visualized in Fig. 5-7 with the contours of the normal vorticity with respect to the wall. High vorticity is represented by red and low vorticity by blue. As with the simulated vortex in section 4.4.1, the peak vorticity quickly diminishes downstream of the vortex but the vortex grows in cross-sectional area. Although the vortex moves away from the wall as it travels downstream, the vortex follows the curvature of the wall. Eventually the vortex dissipates to the extent that it is indistinguishable from the turbulence of the boundary layer.

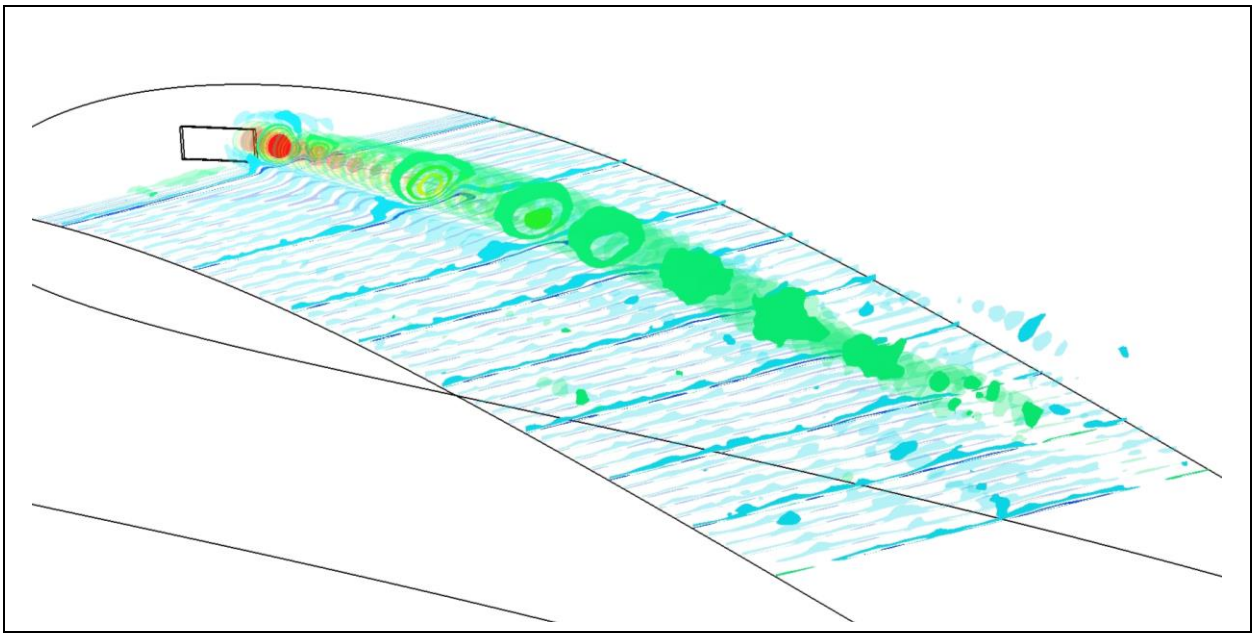

Figure 5-7: Vortex from Case 1

To quantify the behavior of the vortex shown in Fig. 5-7 along with the other two MVG cases, the peak vorticity, circulation, trajectory, circulation decay, and cross-sectional area are plotted in Fig. 5-7, 5-8, 5-9, 5-10, 5-11, and 5-12, respectively. The MVG on the e387 airfoil behaved similarly to the MVG behavior on a flat plate that was observed in chapter 4. By increasing the vane angle the peak vorticity was increased. The peak vorticity of the vortices declines very rapidly within the first 10h behind the vane but the decline is much slower further downstream. The decline of the peak vorticity is due to the diffusion of the vorticity in the vortex. Similarly, the circulation of the vortex sees a decline too but at a much slower rate than the peak vorticity. As with the observations made in chapter 4, an increase of vane angle corresponds to an increase of initial circulation. Increasing the angle from 14˚ to 18.5˚ increased the initial circulation strength by 149% and increasing the angle further to 23˚ led to a further increase of 135% from 18.5˚. About 25h downstream of the MVG, the circulation of the three cases were nearly equivalent.

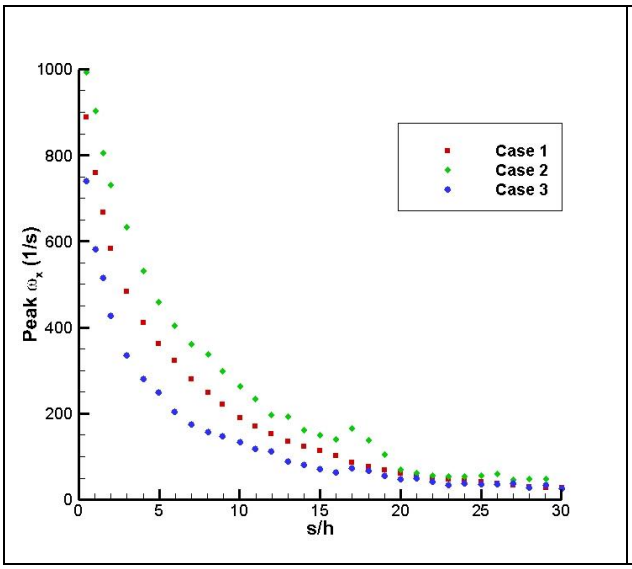

Figure 5-8: Peak vorticity

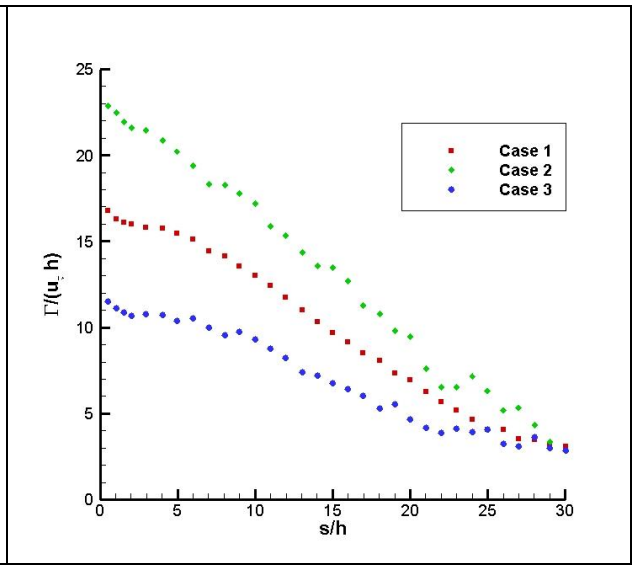

Figure 5-9: Vortex circulation

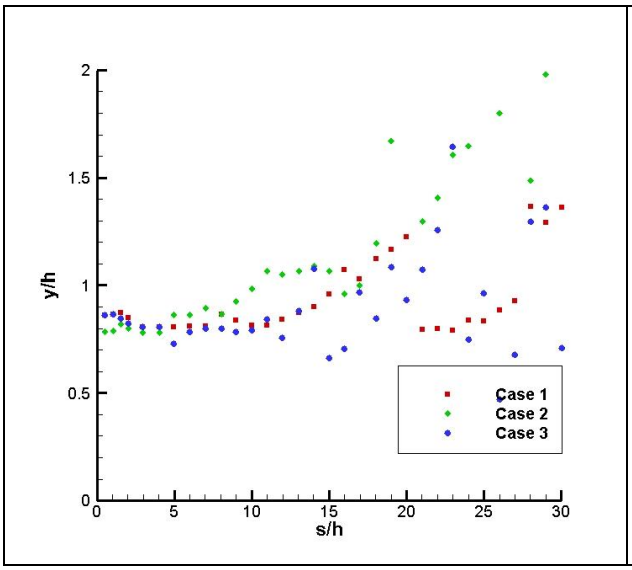

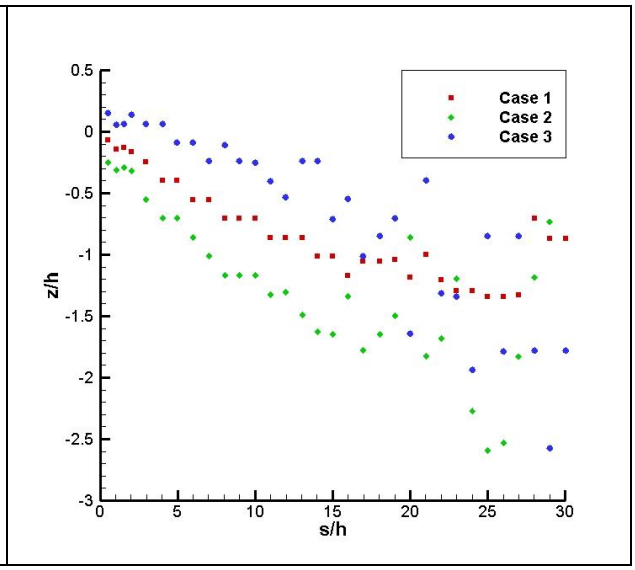

Figure 5-10: Trajectory of vortex (right – vertical, left – horizontal)

Shown in Fig. 5-10 is the trajectory of the vortex for the three cases. In the direction normal to the airfoil surface, the vortices are observed to go slightly towards the wall in the first 10h behind the vane while following nearly the same path. After the initial 10h, the vortices are observed to move away from the wall. The vortex from Case 2 moved away from the wall the fastest while the vortex from Case 3 moved the slowest away from the wall. In the streamwise direction, or horizontal direction, all vortices propagated to the right due to the vane angle while the vortices moved in the streamwise direction. Case 2 with the vane at 23˚ show the vortex moving the furthest while Case 3 with the vane at 14˚ shows the least amount of movement in the streamwise direction. Within the first 10h to 15h behind the vane, the

vortex paths were very predictable, but further downstream, the vortex position became increasingly difficult to measure leading to much variation in the position of the vortex core.

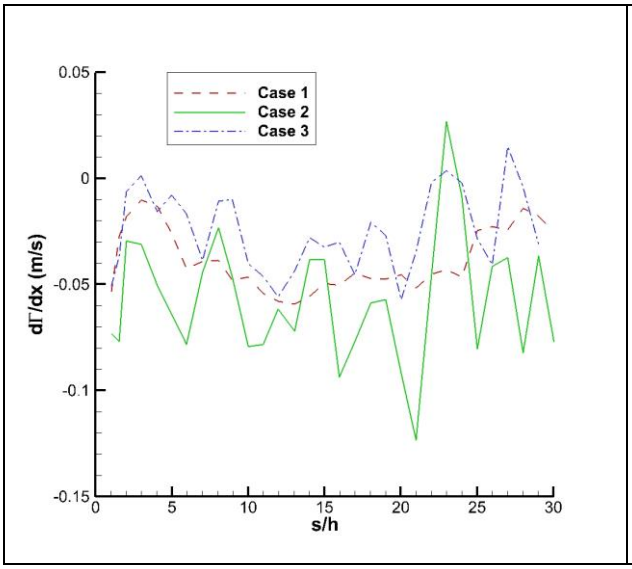

Figure 5-11: Circulation decay

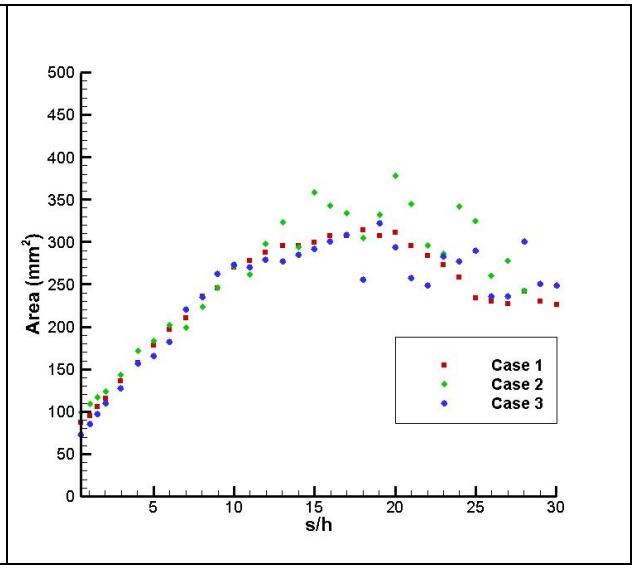

Figure 5-12: Vortex area

The decay of the circulation was calculated and plotted in Fig. 5-11. Unlike the circulation for the vortices on a flat plate that was shown in Fig. 4-17, there was no observable peak decay immediately behind the vane. Case 2 appears to have a nearly constant decay rate in the measured domain while Cases 1 and 3 showed a peak at around 12h. The cross-sectional area of the vortex is plotted in Fig. 5-12. The areas of the three vortices are quite similar with the stronger vortex of Case 2 being slightly larger while the smaller vortex of Case 3 being slightly smaller. As the vortices propagate downstream, their size increases nearly linearly with the distance. After 15h, the vortices appear to reduce in size but this may be due to the clipping of the vorticity.

To provide some further insight into the vortex parameters presented in the plots above, the vorticity and Reynolds stresses are shown for several downstream slices. In Fig. 5-13, a comparison is made between the instantaneous LES, time-averaged LES, and RANS solution. Similarities can be made to the comparison made of a vortex on a flat plate in Fig. 4-18. As with the previous comparison, the instantaneous flow is very irregular and turbulent, making it difficult to differentiate the vortex from the surrounding turbulence structures. Averaging the flow over time removes the turbulent fluctuations resulting in a clearly defined vortex. As with the vortices on a flat plate, a secondary vortex is formed off the pressure side of the vane and is present in s/h = 1 slice. Due to the secondary vortex being closer and weaker in magnitude compared to the main vortex, it decays very rapidly and by s/h = 5 it has nearly decayed. The main vortex diffuses and stretches into an oval from s/h = 1 to 5, this process continues until

by s/h = 20 when it is barely visible in the vorticity contours. Although the RANS modelling of this case will be discussed in more detail later, RANS is able to predict the vortex structure quite well. However, RANS predicts a much weaker primary and secondary vortex than the LES.

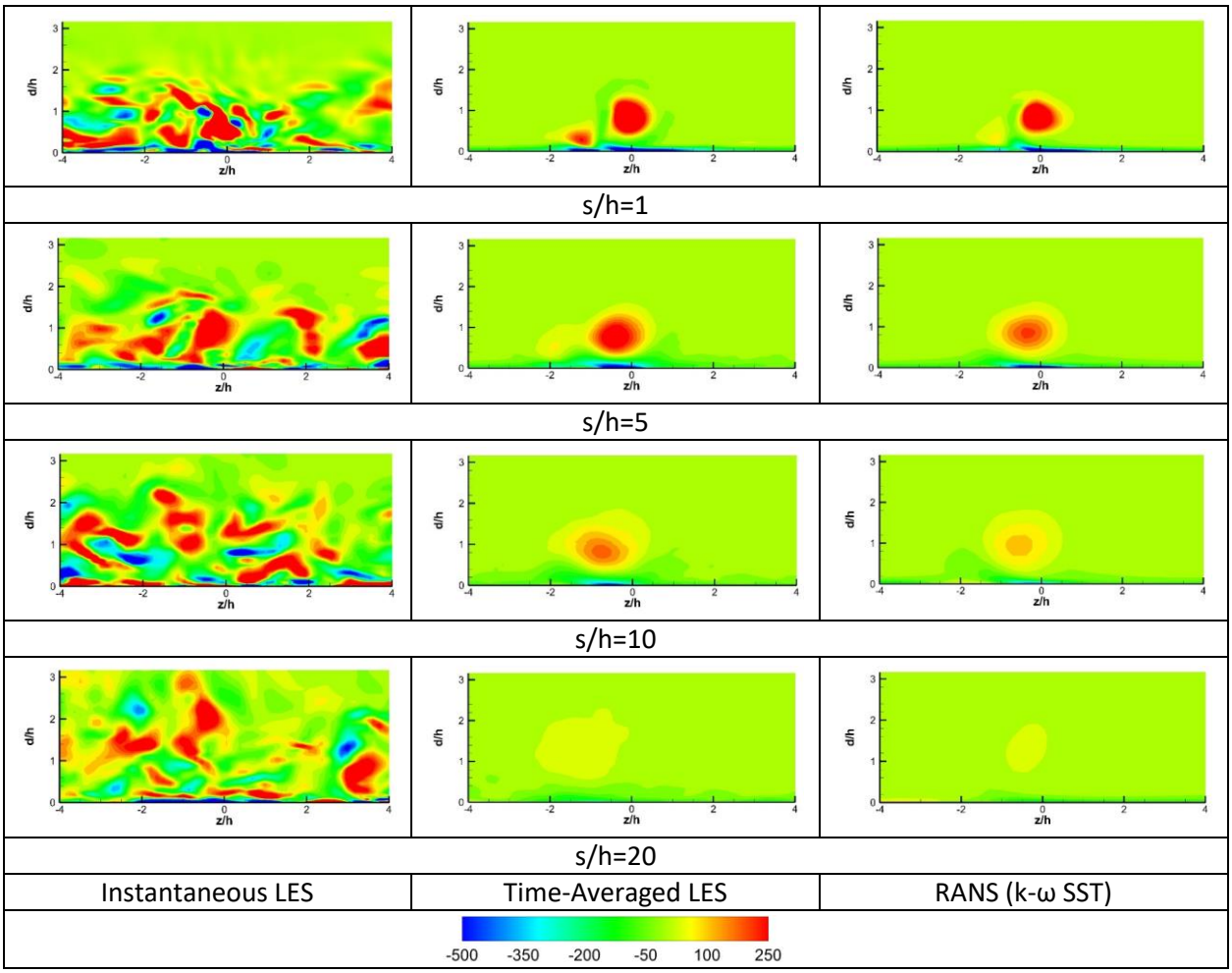

Figure 5-13: Vorticity at selected planes for instantaneous and time-average LES results for Case 1 and steady-state RANS

Contours of the normal Reynolds stresses at 1h, 5, and 10h behind the vane are shown in Fig. 5-14. The initial distribution and magnitude of $\langle v'v' \rangle$ and $\langle w'w' \rangle$ are similar to what was observed in Chapter 4, Fig. 4-20. At 1h, the Reynolds stresses are influenced by the wake of the vane. As the vortex moves downstream, the distribution of the stresses behave differently from the vortex on a flat plate. At 5h, the distribution of $\langle v'v' \rangle$ evolves into two peaks, and further downstream at 10h, the nearest peak of $\langle v'v' \rangle$ to the wall has nearly dissipated. The primary distribution of $\langle w'w' \rangle$ correlates with the vortex core and a secondary structure of $\langle w'w' \rangle$ are observed near the wall.

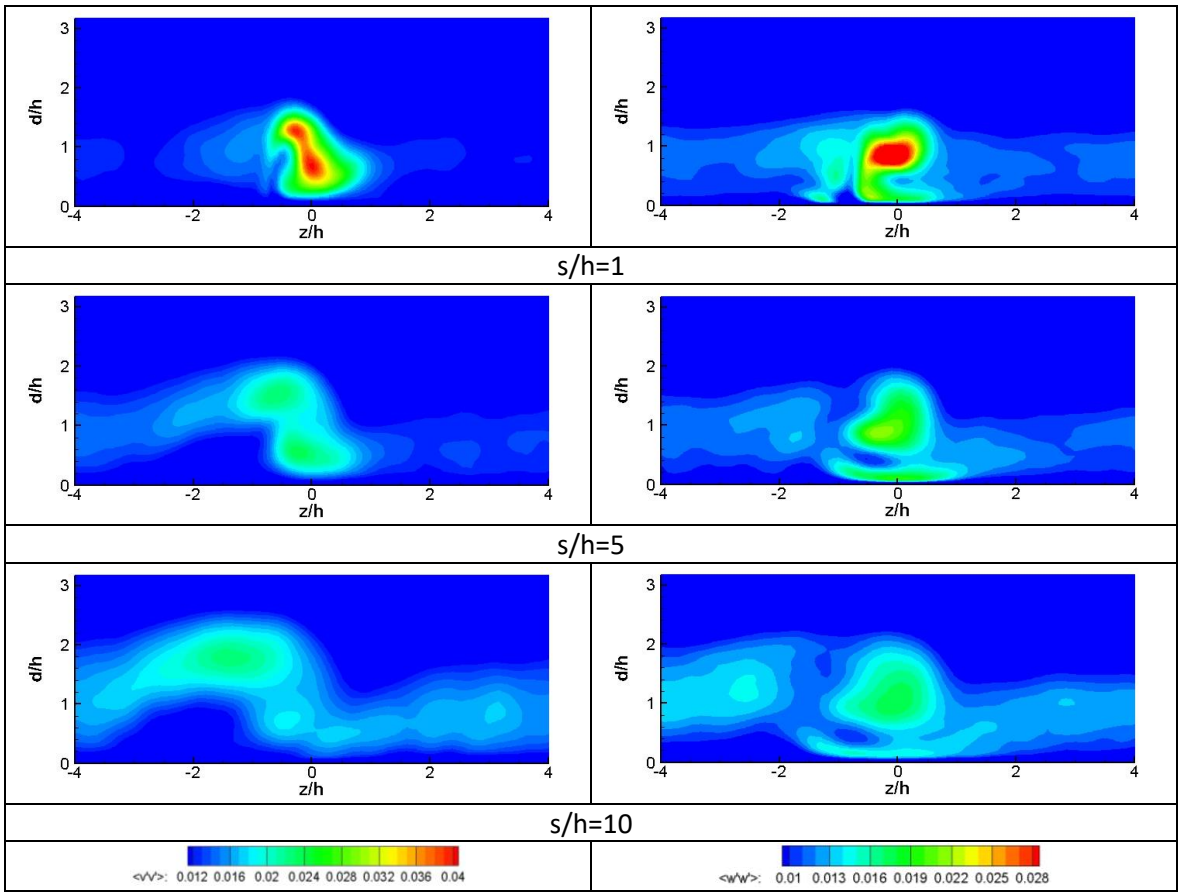

Figure 5-14: Normal Reynold stresses (Right - $\langle v'v' \rangle$, Left - $\langle w'w' \rangle$)

5.3.2 Skin friction

As noted before, the vortex embedded in the boundary layer transfers momentum from the outer boundary layer into the near-wall boundary layer. As a direct consequence of the transfer momentum, or circulation, there is in an increase of skin friction which is the main component in the decay of a vortex [5]. The increase of skin friction has also been used as a metric of the effectiveness of a MVG by previous researchers. Shown in Fig. 5-15 is the skin friction at s/h = 2, 5, 10, 20, 30, and 40 behind the MVG. As observed by pervious researchers, the vortex induces an increase of local skin friction which indicates circulation within the boundary layer. The vortices for all three cases have an effect on the skin friction up to 40h behind the MVG. Initially, the vortices have a strong effect on the wall that is confined to a narrow band, but as the vortex propagates downstream, the vortices diffuse and their effect on the wall weakens while spreading out. As expected, the stronger vortices generate a stronger skin friction, but have a faster decay rate. By s/h = 20, the vortices from Case 1 and 2 have nearly equal effect on the skin friction.

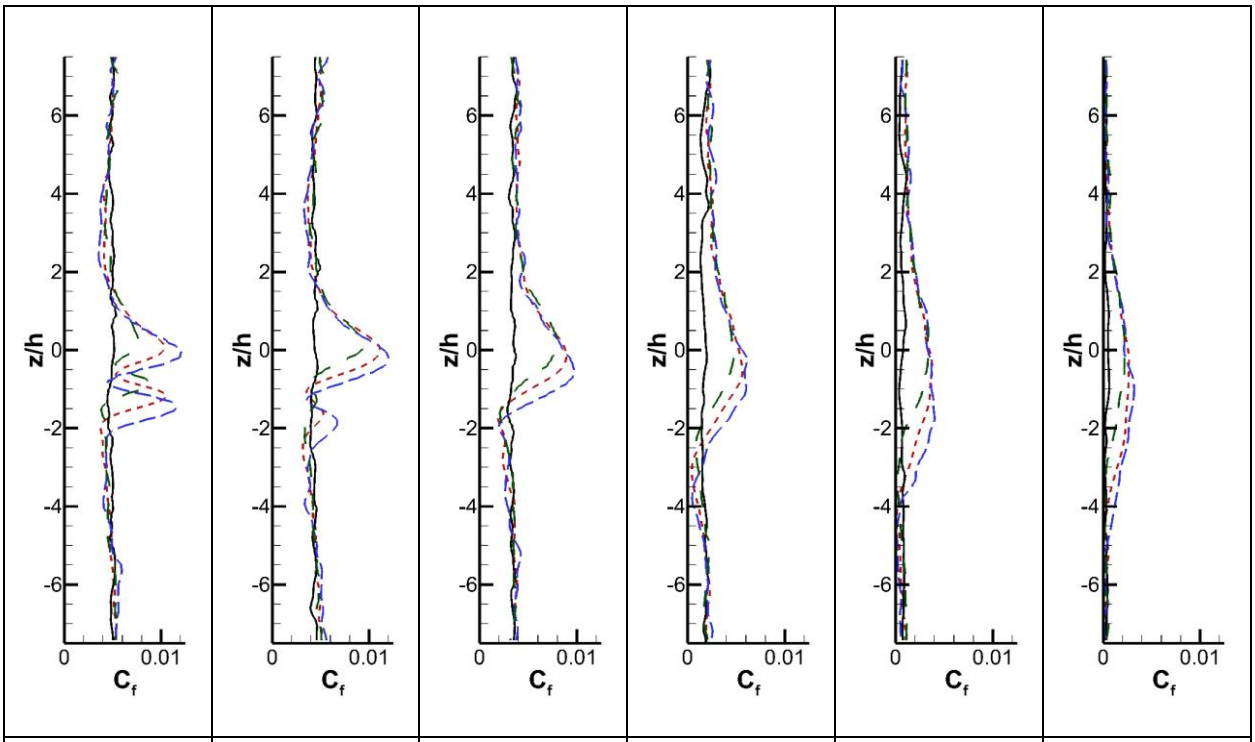

s/h=2	s/h=5	s/h=10	s/h=20	s/h=30	s/h=40

Figure 5-15: Time average skin friction at selected streamwise points (------ Baseline, - - - - Case 1, -- -- -- Case 2, -- -- -- Case 3)

Contours of the skin friction on the upper surface of the e387 airfoil are shown in Fig. 5-16 for the baseline case and for the three MVG configurations tested. The increase in skin friction from the vortex interaction with the wall is observable for all the three cases. Immediately behind the MVG there is a region of strong skin friction which signifies a strong interaction between the vortex and wall. This region of strong skin friction is strongest for Case 2 and the weakest for Case 3, which also have the strongest and weakest vortices, respectively. Although the higher skin friction represents greater circulation in the boundary layer, it also represents loss of energy and the weakening of the vortex. It can easily be inferred that a strong vortex can be overall counterproductive if the vortex decays too quickly before the vortex reaches the region of separated flow.

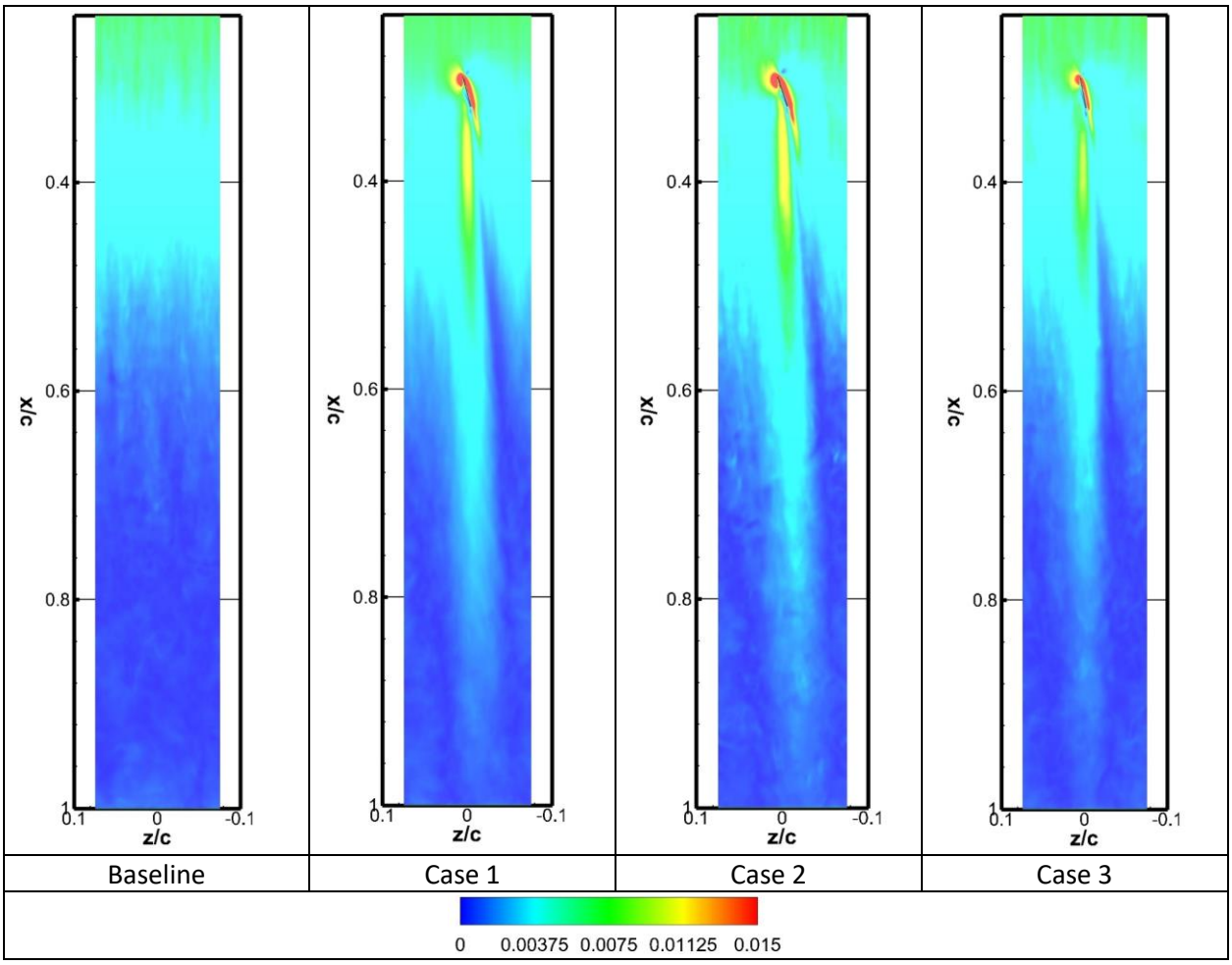

Figure 5-16: Skin friction contours

5.3.3 Drag and Lift

The improvement in the drag and lift of airfoil with use of flow control is the most important metric on the effectiveness of the flow control. Table 5-3 shows the effect that the three MVG cases have on the lift and drag of the airfoil compared to the baseline case. In relation to the baseline case, all three cases improved the lift and drag of the airfoil. Case 2 had the greatest increase in lift and lowest reduction in drag while Case 3 had the smallest change in both values. Case 3 had the best improvement of the lift-to-drag ratio.

	MVG Angle	C_L	C_D	L/D
Baseline	-	1.353	0.0571	23.70
Case 1	18.5˚	1.420	0.0534	26.59
Case 2	23.0˚	1.429	0.0536	26.66
Case 3	14.0˚	1.410	0.0528	26.70

Table 5-3: MVG configuration effect on drag and lift

5.4 RANS Modelling

To supplement the work in the previous section and assess the accuracy of RANS turbulence models in predicting MVG on the e387 airfoil, a parallel study was made with the k-ω SST turbulence model. In chapter 4, it was shown that RANS was sufficiently capable of modelling MVG and their generated vortex on a flat plate. In this study, the k-ω SST model is evaluated in an application where an adverse pressure gradient is present along with a wall curvature and an adverse boundary layer.

The same setup from the previous LES simulations was reused for the RANS models; however, the mesh resolution was reduced. The SIMPLEC solver from ANSYS Fluent was used to solve for a steady-state solution with the k-ω SST turbulence model. A 2nd-order upwind scheme was used for the convective terms and a 2nd-order centered scheme for the diffusion terms.

5.4.1 Baseline

The k-ω SST is evaluated firstly on the baseline e387 airfoil to establish the suitability of the model to predict the flow on the e387 airfoil. Three different meshes were generated with cell counts of 8.2 million, 6.8 million, and 4.3 million, Mesh B1, B2, and B3, respectively. The coarsest mesh was constructed with a y^+ of no more than 5 while the finest with a y^+ of no more than 2.

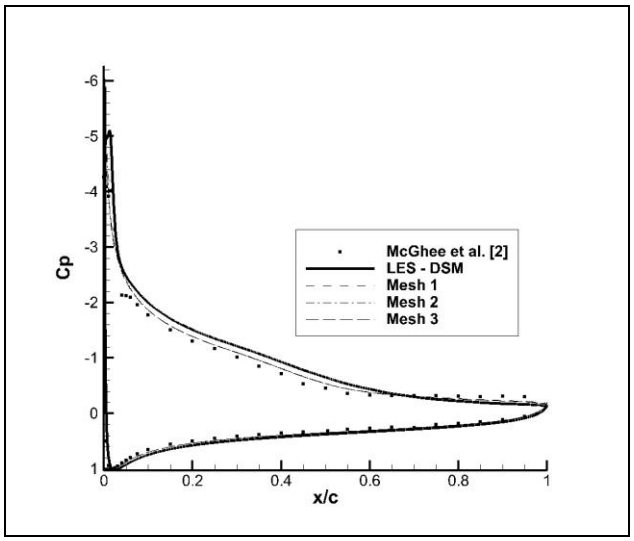

Figure 5-17: Pressure coefficient distribution, RANS vs LES

The pressure coefficient on the airfoil was plotted in Fig. 5-17 along with the LES results from the previous section and the experimental results of McGhee et al. [113]. Pressure distribution from the three different mesh resolutions shows no variation. As expected with a steady-state RANS model, the k-ω SST does not predict separation bubble on the leading edge of the airfoil. The RANS model does however

predict a pressure distribution that more closely matches the experimental results on the upper surface of the airfoil than the LES results. Presented in Table 5-4 is the drag and lift coefficients. There is a very small variation with respect to three different mesh resolutions and the predicted coefficients are in-between those of the LES and experimental results. With the exception of the leading-edge separation bubble, the k-ω SST model matches satisfactorily to the LES and experimental results.

	AoA	C_L	C_D
Selig et al. [115]	12.17˚	1.215	0.0733
McGhee et al. [113]	12.09˚	1.174	-
Mesh 2 - DSM	12.00˚	1.353	0.0571
Mesh B3	12.00˚	1.295	0.0593
Mesh B2	12.00˚	1.294	0.0591
Mesh B1	12.00˚	1.299	0.0602

Table 5-4: Comparison of RANS predictions of the drag and lift to LES and experimental results

5.4.2 Flow Control

Seeing that the k-ω SST model performed decently well in predicting the flow on the e387 airfoil, a subsequent case was setup to match the Case 1 of section 5.3. As with Case 1, a MVG vane was placed on the airfoil at 18.5˚ relative to the freestream. To gauge the sensitivity of the k-ω SST model to the mesh resolution, three meshes were generated with 14.0 million, 8.8 million, and 6.2 million cells, or Mesh F1, F2, and F3, respectively. The meshes were adapted from the previous section, but the mesh density was increased in the spanwise direction and around the vane to resolve the flow around vane.

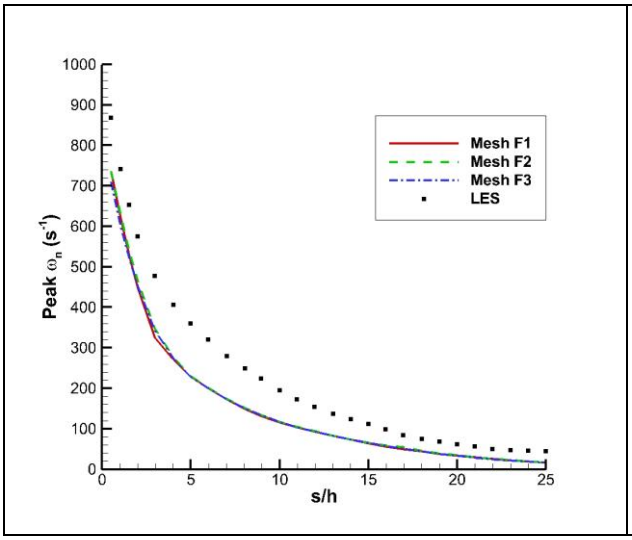

Figure 5-18: Peak Vorticity

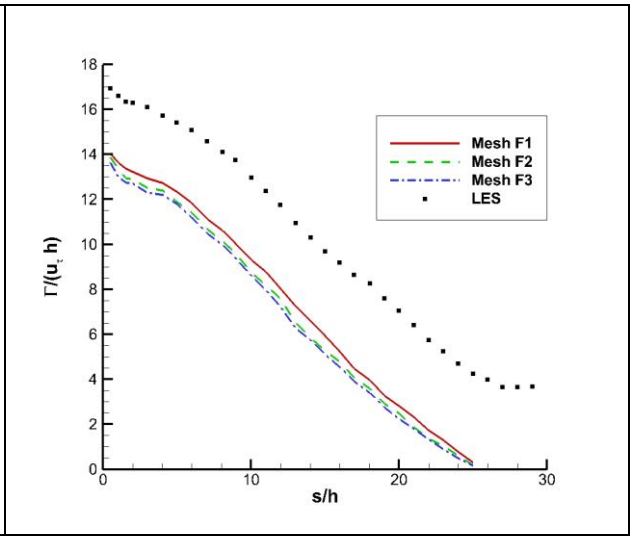

Figure 5-19: Circulation

The peak vorticity, Fig. 5-18, was independent of the mesh density but the k-ω SST was found to under predict the vorticity when compared to the LES. The circulation, Fig. 5-19, predicted by the k-ω SST was also less than what was predicted by LES by about 18%. The densest mesh, Mesh F1, gave a slightly higher circulation in comparison to the other two meshes.

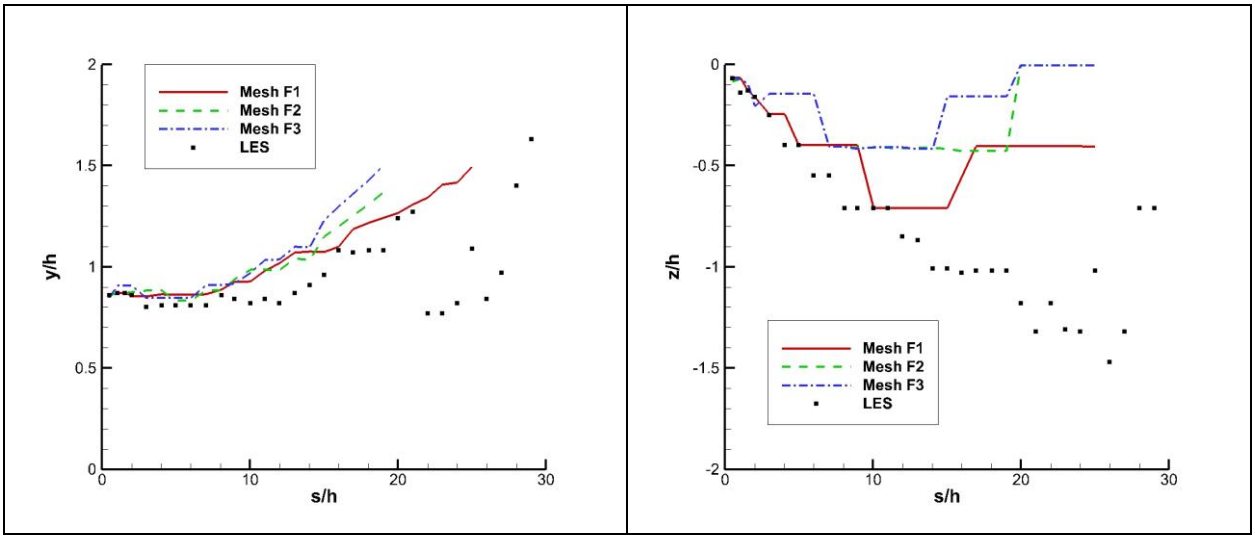

Figure 5-20: Trajectory of vortex (right – vertical, left – horizontal)

For the trajectory, RANS predicts the initial path of the vortex well in comparison to the LES in Fig. 5-20. After 4h behind the vane, RANS predicts that the vortex propagates away from the wall faster than LES. Initially the three meshes show good agreement among themselves but the coarser meshes predict the vortex propagating away from the wall faster. For the horizontal path of the vortex, RANS predicted the vortex stop propagating in the streamwise direction after 5h to 10h downstream of the vortex while LES predicted the flow the vortex continuing to propagating at least up 30h.

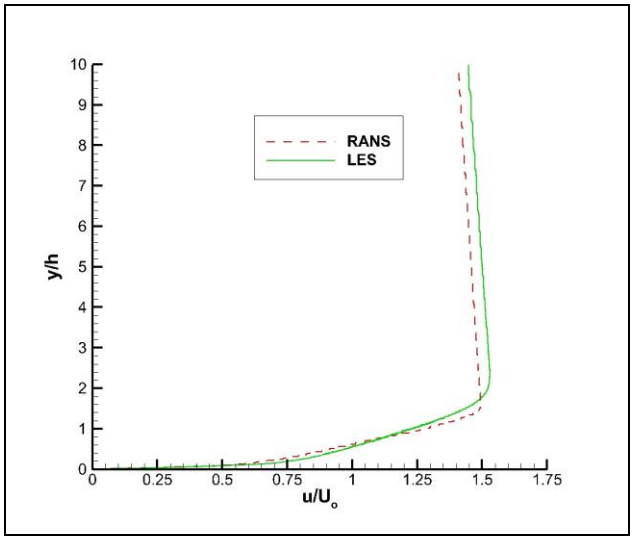

Figure 5-21: Upstream Boundary Layer

An explanation for why the k-ω SST model under predicts the vorticity and the circulation when compared to the time-averaged LES results is partly due to the upstream boundary layer. Shown in Fig. 5-21 is the boundary profile at s/h = 7.48, LES predicts a boundary layer with a higher velocity, which from the prior chapter it was shown that the velocity of the flow correlates with the circulation strength. Essentially, the underlying difference in results between LES and RANS is due to the numerical physics of both methods. LES directly resolves the flow on the airfoil, simulating the upstream laminar separation bubble and turbulent transition while the k-ω SST assumes the flow is completely turbulent from the onset. This results in the two different boundary layer profiles in Fig. 5-21.

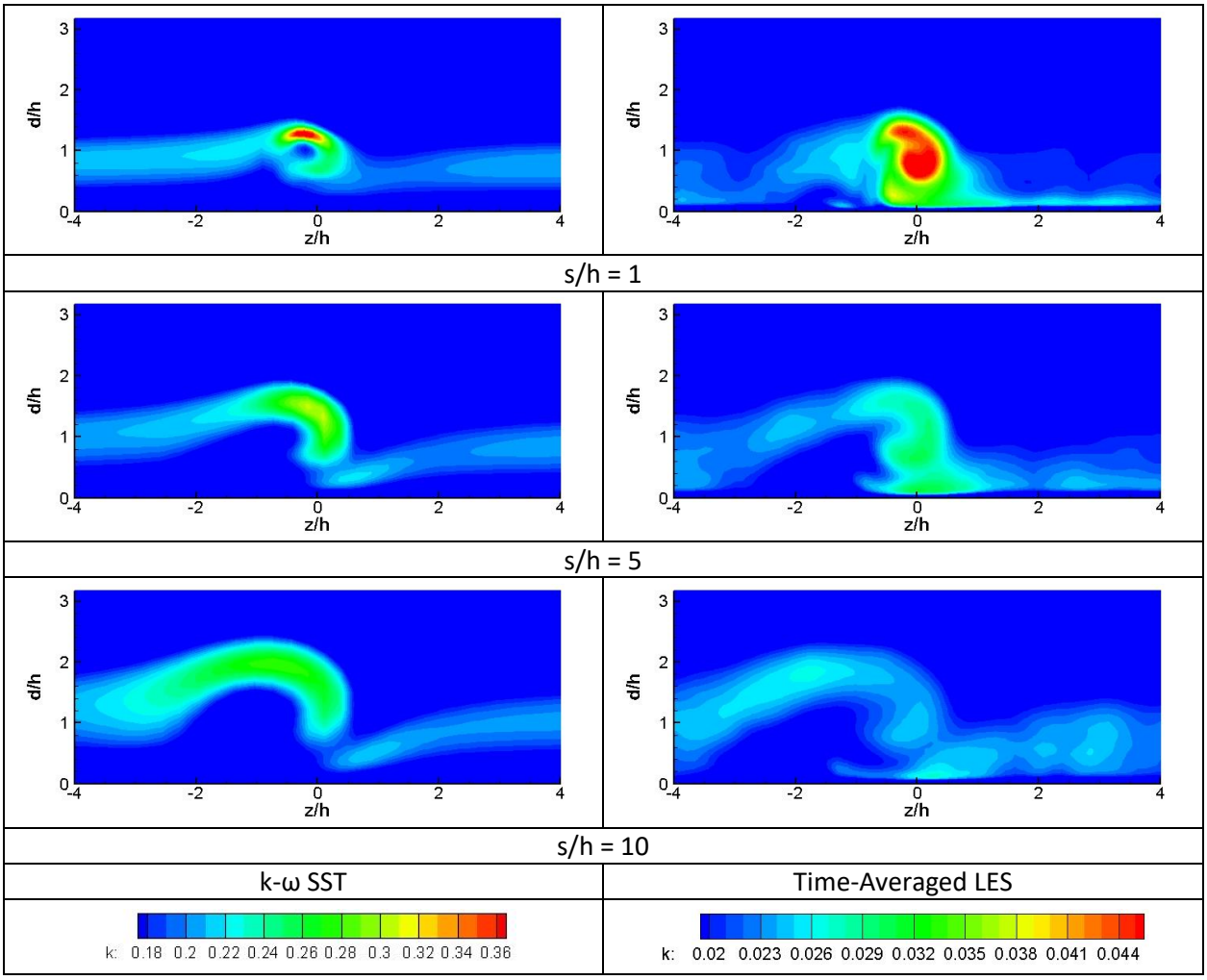

Figure 5-22: Turbulent Kinetic Energy (Top – k-ω SST, Bottom – LES)

Lastly is the turbulent kinetic energy of the flow and the vortex in Fig. 5-22. Making a good comparison between LES and k-ω SST model is complicated by the k-ω SST model overestimating the amount of the turbulence within the boundary layer. The k-ω SST model over predicts the turbulent kinetic energy by a factor of 10, which also influences the difference observed in the boundary layer profile

in Fig. 5-21. After adjusting the contour plots of the LES results and the k-ω SST model, similar but differing structures can be observed. The time-averaged LES results show that the peak turbulent kinetic energy is within the core at s/h=1. The turbulent kinetic energy in the vortex core dissipates further downstream. By s/h=10, the turbulence in the vortex core has diminished significantly. The peak turbulent kinetic energy has shifted away from the core and to the updraft and downdraft of the vortex. The k-ω SST predicts little turbulent kinetic energy in the vortex core, but in a ring around the vortex core at s/h=1. As the vortex develops, the turbulent kinetic energy wraps around the core, similarly to what LES predicts, but with greater intensity. It may be worthwhile to use a transition model, such as the k-kl-ω Transition or the Transition SST models, that does not assume that the flow is fully turbulent to see whether similar levels of turbulent kinetic energy are seen in the flow when compared to LES.

5.5 Conclusion

The e387 airfoil was placed at an angle of attack of 12˚ and was simulated with LES. The time-averaged flow field was found to compare well with published, experimental results. Three different MVG vane configurations were then placed on the e387 airfoil, upstream of the flow separation. In the instantaneous flow field, the turbulence in the boundary layer had strong influence on the vortex and dominating the vortex. As with the LES results in chapter 4, time-averaging exposes the vortex structure in the boundary layer. The vortex had an effect on the skin friction of up to 40h behind the vane while the circulation of the vortex was measurable up to 30h behind the vane. The vortex had the strongest influence on the wall from approximately 5h to 15h behind the vane. Comparing the downstream vortices and the effects that they had on the airfoil, the optimum MVG angle was found to be 18.5˚. This matches the conclusion reached in the previous chapter and from prior published works. However, the MVG at 14˚ was found to lead to the best improvement in lift-to-drag ratio.

Contrary to the previous comparison between LES and RANS in chapter 4, RANS under predicted the vortex strength in comparison to LES. Part of the discrepancy between RANS and LES is due to RANS predicting a weaker boundary layer on the airfoil which causes the MVG to encounter lower velocity and generate a weaker vortex. The k-ω SST model also assumes that the flow is fully turbulent and over predicts the turbulent kinetic energy of the flow which further hampers the solution. In the initial 5h to 10h behind the MVG, RANS matches well to the vortex trajectory of the time-averaged LES results. After this distance, RANS predicted the vortex propagated away from the airfoil surface faster while moving less in the horizontal direction in contrast to the LES results.

6. Modelling NACA CC3

A high-speed centrifugal compressor was modelled with a vaneless and a vaned diffuser from choke to near stall conditions. The compressor with a vaned diffuser was modelled at an operating point below the stall line to induce rotating stall.

6.1 Introduction

The NASA CC3 centrifugal compressor was developed by Detroit Diesel Allison from 404-III compressor that operated at 1.658 kg/s (3.655 lbm/s) and 36,015 rpm. The 404-III compressor was scaled to obtain the CC3 compressor which has an operating point of 4.536 kg/s (10 lbm/s) and 21789 rpm. At the design conditions, the total pressure ratio across the compressor was 4:1. The aerodynamic and mechanical specifications of the compressor with a vaned diffuser is given by McKain and Holbrook [49]. The project was sponsored later by NASA as a test case for flow inside a high-speed centrifugal compressor. Photo of the NASA CC3 compressor with a vaned diffuser is displayed in Fig. 6-1.

Figure 6-1: NASA CC3 compressor [116]

The CC3 compressor is composed of 15 blades with 15 splitter blades matched to a diffuser with 24 wedge vanes as shown in Fig. 6-3. The impeller can also be paired with a diffuser that is vaneless as shown in Fig. 6-2. The impeller blades have a backsweep of 50˚ and the leading edge of the splitter blades are located 30% of the chord of the main blades. The inlet tip diameter is 210 mm and the inlet blade height is 63 mm. The exit diameter of the impeller blades is 432 mm and the exit blade height is 17 mm. The tip clearance of the main and splitter blades is a constant 0.2 mm. The diameter of the leading edge of the vanes of the diffuser is 465 mm. The impeller geometry was constructed with the published geometry for hot conditions at design point.

The compressor has been extensively studied by NASA and other researchers in literature. Skoch et al. [1] obtained additional compressor performance and PIV data of the internal flow of the compressor. Wernet et al. [117] experimentally investigated surge and stall using PIV measurements. Kulkarni et al. [118] numerically modelled a single passage of the CC3 compressor with a vaneless diffuser. Shahin et al. [118] used LES to simulate a third of the compressor at deep surge conditions. Spakovszky [52] observed a four-lobed pre-stall resonance that rotated at a frequency of -0.27 times the rotor frequency in the opposite direction of the impeller rotation. Furthermore, Spakovszky [52] states that the compressor will experience 'classic' surge, or a surge cycle that passes in and out of rotating stall. This behavior has been observed by a number of experimental studies on the CC3 compressor [52, 117]. Halawa et al. [53, 54] found that separated flow on the leading edge of the impeller blade and non-uniform flow in the impeller passageway cause random fluctuations in the flow at the inlet of the diffuser; this lead to the development of stall. Halawa et al. [53, 54] also noted a potential connection between stall and surge, and vaneless space between impeller and diffuser being the source of surge.

In this chapter, a single passageway of the CC3 compressor is modelled to determine the degree of mesh sensitivity and to provide an additional validation for the new compressible flow algorithm. In the second part of the chapter, the full compressor is modelled with a vaned diffuser from the near choke to stall/surge. The unsteady simulation near stall is of particular interest to compare how the results match previous works and to obtain better understanding of rotating stall in the compressor.

6.2 Numerical Setup

The NASA CC3 compressor was modelled with both Fluent and the new compressible flow algorithm developed by the author for *Code_Saturne*. A validation study was conducted with a single passage of the NASA CC3 using a vaneless diffuser. From this study the optimum mesh resolution was discovered and used to model the full compressor with a vaned diffuser. The CC3 compressor with a vaneless diffuser is shown in Fig. 6-2 and with a vaned diffuser in Fig. 6-3.

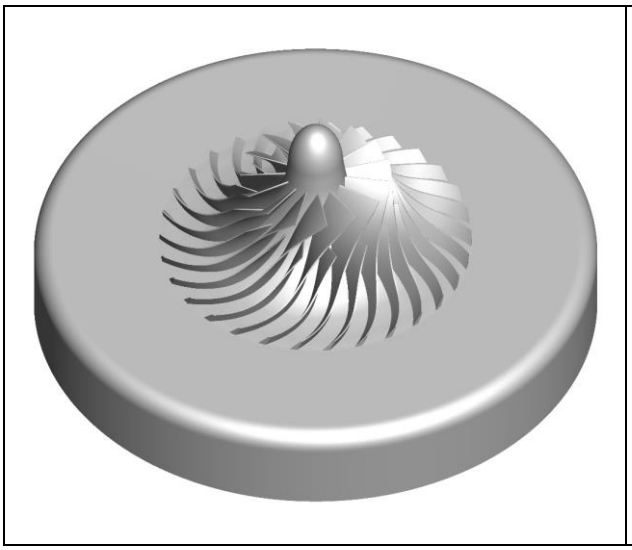

Figure 6-2: CC3 with a vaneless diffuser

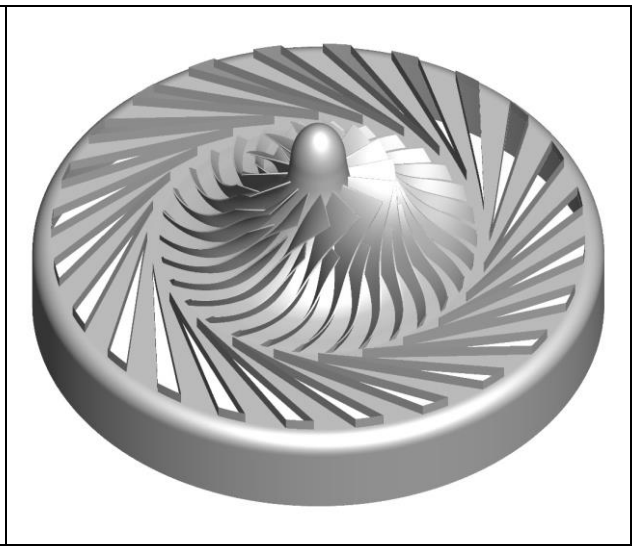

Figure 6-3: CC3 with a vaned diffuser

The geometric data for the hot flow conditions was used to construct the compressor in Autodesk Inventor. The geometry was imported into ANSYS ICEM where a block-based, hexa mesh was generated and was converted to unstructured mesh of CGNS and msh formats. Four different mesh densities were generated to determine the mesh sensitivity and to pick the optimum mesh resolution. It is desirable to have the best mesh resolution to resolve flow, however this has to be balanced against the global mesh size and time step requirements which dictates the computational cost of the model. The size of each mesh is shown in Table 6-1.

	Impeller	Inlet	Diffuser	Tip Gap	Avg y^+
Mesh A	102,216	20,141	40,480	3	62
Mesh B	436,833	137,376	214,016	4	38
Mesh C	732,769	146,454	309,600	5	30
Mesh D	982,288	199,848	315,744	6	30

Table 6-1: Mesh resolution for NASA CC3

In the implementation of the boundary conditions, a total pressure of 101,325 Pa and a total temperature of 288.15 K were imposed at the inlet. A turbulence intensity of 0.2% was imposed at the inlet. The static pressure was specified at the outlet to obtain the desire flow conditions. The static pressure at the outlet was manipulated by Eq. 6-1 to obtain the desire mass flow rate. Eq. 6-1 is derived from the Bernoulli's equation [59] and multiplied by a dampening factor of 0.1. The dampening factor has the dual purpose of maintaining a more stable flow field at the outlet and dampening out the pressure perturbations between the inlet and outlet of the domain.

$$dP = 0.1 * 0.5 * \left(\dot{m}_{current}^2 - \dot{m}_{target}^2\right)/(\rho A^2) \quad (6\text{-}1)$$

The walls of the main and splitter blades and the hub of the impeller had a velocity equal to the rotational velocity of the rotating domain. The shroud of the impeller had a velocity vector of null. The vaneless and the vaned diffusers used a no-slip boundary condition for the walls. For the modelling of a single passage of the CC3 compressor with a vaneless diffuser, rotated periodic boundary conditions were used, as shown in Fig. 6-4. Mesh joining was used to join the meshes of the inlet, impeller, and diffuser domains together. The complete CC3 compressor with a vaned diffuser used a domain topology similar to the topology shown in Fig. 4-6. For the full CC3 compressor with a vaned diffuser, a sliding mesh interface was used between the impeller and diffuser domains to allow for the mesh of the impeller to be rotated.

The compressor was modelled at a design speed of 21,789 rpm. The time step of the simulation was set to $2x10^{-7}$ s to keep the CFL number below 2. As with prior simulations, a 2nd-order MUSCL scheme was used for the convective terms and a 1st-order implicit scheme for time. The AUSM+-up scheme was used for the mass flux discretization and convective pressure terms. Turbulence was modelled with the k-ω SST model with a wall function. The simulation was initialized by taking the flow field from a prior model on a coarser mesh and interpolating the flow field onto the new mesh. The model was run for several revolutions until the difference in mass flow rate between the inlet and outlet was less than 1%, and the total pressure at the inlet and outlet converged.

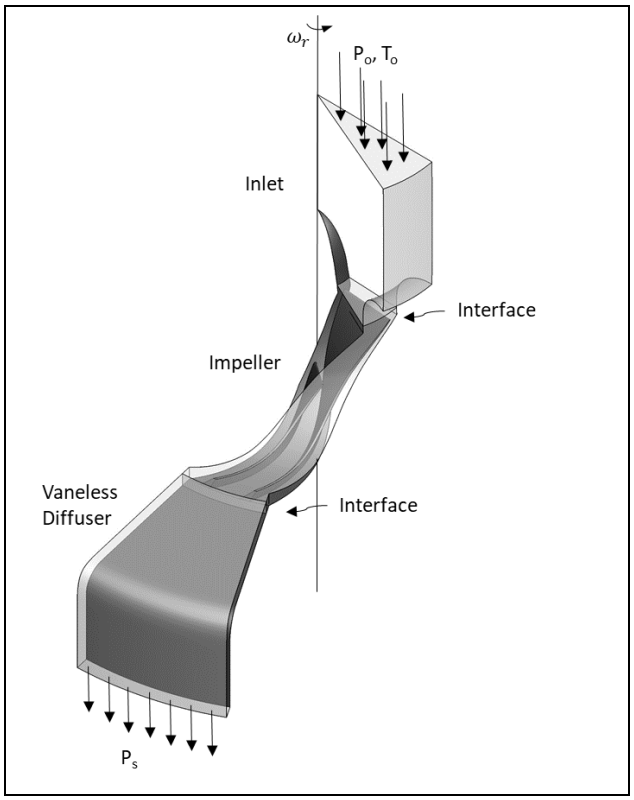

Figure 6-4: Domain of CC3 with a vaneless diffuser

6.3 NASA CC3 with a Vaneless Diffuser

A single passage of the NASA CC3 was modelled with a vaneless diffuser. First the sensitivity of the solution to the mesh density was studied. With the mesh that offered the best compromise between size and accuracy, the operating range of the compressor was obtained and the internal flow of the compressor was studied.

6.3.1 Mesh Sensitivity

Four mesh resolutions are given in Table 6-1 and modelled with a single impeller passageway at the operating design point of the compressor. The compressor was matched with a vaneless diffuser. The sensitivity of the mesh resolution was assessed by the pressure distribution on the impeller blades and the predicted performance of the compressor at the design mass flow rate of 4.54 kg/s. The pressure distribution on the main and splitter blades are plotted in Fig. 6-5. The pressure was measured at 75% of span from the hub and was non-dimensionalized by the inlet total pressure. For both the main and splitter blades, there is very small deviation between the four tested meshes.

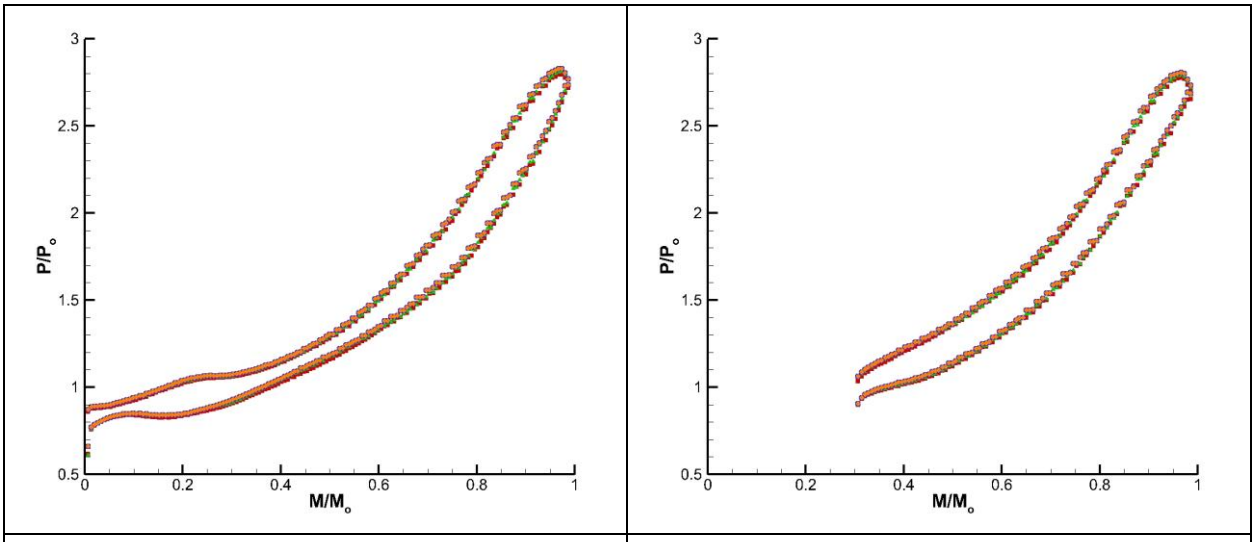

Main Blade	Splitter Blade

Figure 6-5: Blade pressure distribution (♦ - Mesh A, ● – Mesh B, ▲ – Mesh C, ■ – Mesh D)

The total pressure ratio and the adiabatic efficiency were compared between the different mesh resolutions and published experimental measurements in Table 6-2. Similar to the pressure distributions on the blades, there was only a slight deviation between the overall performances of the four mesh densities. In comparison to experimental measurements, the new compressible flow algorithm in *Code_Saturne* overestimated the total pressure ratio and the adiabatic efficiency. ANSYS Fluent was also

used to model the compressor with the same meshes. ANSYS Fluent also overestimated the total pressure ratio and adiabatic efficiency at the operating design point. Due to the little mesh sensitivity between the three highest resolution meshes, it was decided to conduct the rest of the study with Mesh C.

	Total Pressure Ratio		Adiabatic Efficiency	
	Code_Saturne	Fluent	*Code_Saturne*	Fluent
Mesh A	4.18	4.18	90.99%/89.31%	89.31%
Mesh B	4.28	4.18	91.56%	88.16%
Mesh C	4.18	4.32	91.98%/89.85%	88.89%
Mesh D	4.48	4.32	91.13%	88.73%
Exp [1]	3.97		83.2%	

Table 6-2: Mesh sensitivity at operating design point

6.3.2 Compressor Operating Range and Internal Flow

The full operating range of the compressor was modelled with Mesh C from near choke until the compressor experienced rotating stall. The total pressure ratio and adiabatic efficiency is plotted against experimental results of Skoch et al. [1] and ANSYS Fluent in Fig. 6-6 and 6-7. *Code_Saturne* does a good job of predicting the total pressure ratio curve, even better than ANSYS Fluent. ANSYS Fluent overpredicts the total pressure ratio at the operating point, but near stall and choke, it matches the experimental data well. For the adiabatic efficiency, Code_Saturne matches the results of ANSYS Fluent, but both solvers overpredicts the efficiency by about 2% in comparison to the experimental results.

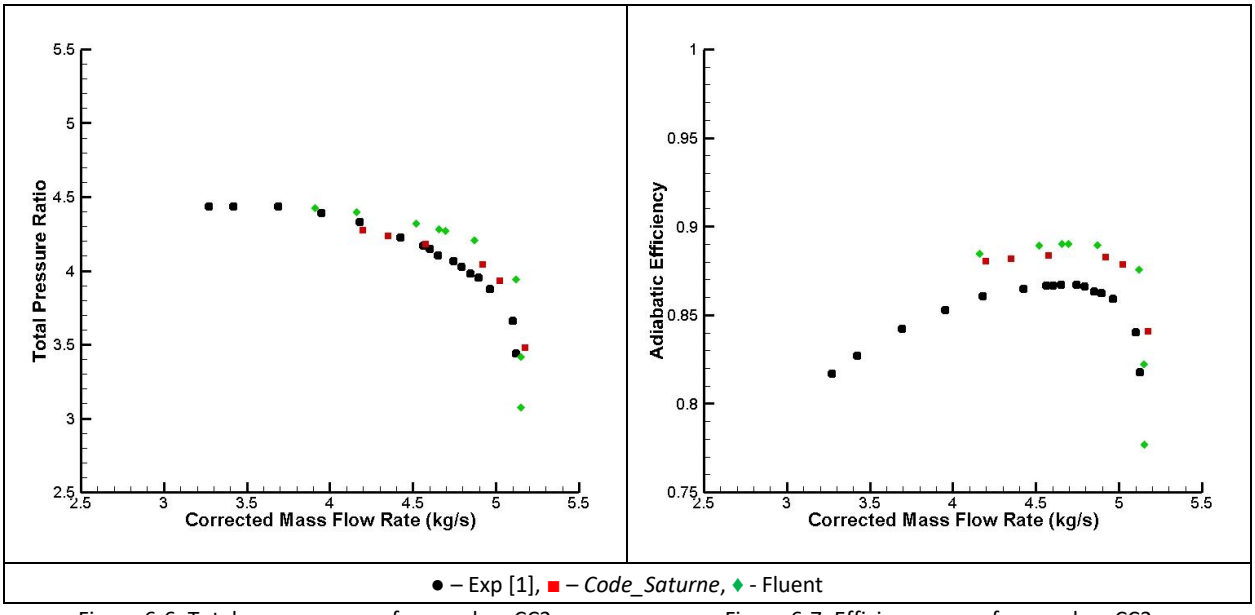

Figure 6-6: Total pressure curve for vaneless CC3

Figure 6-7: Efficiency curve for vaneless CC3

At the design operating point, the meridional planes are extracted from the flow field that was modelled with the new compressible flow algorithm in *Code_Saturne* and Fluent. The location of seven meridional planes in the impeller are presented in Fig. 6-8. A comparison of the meridional planes from *Code_Saturne* and Fluent models are made in Figs. 6-9 and 6-10.

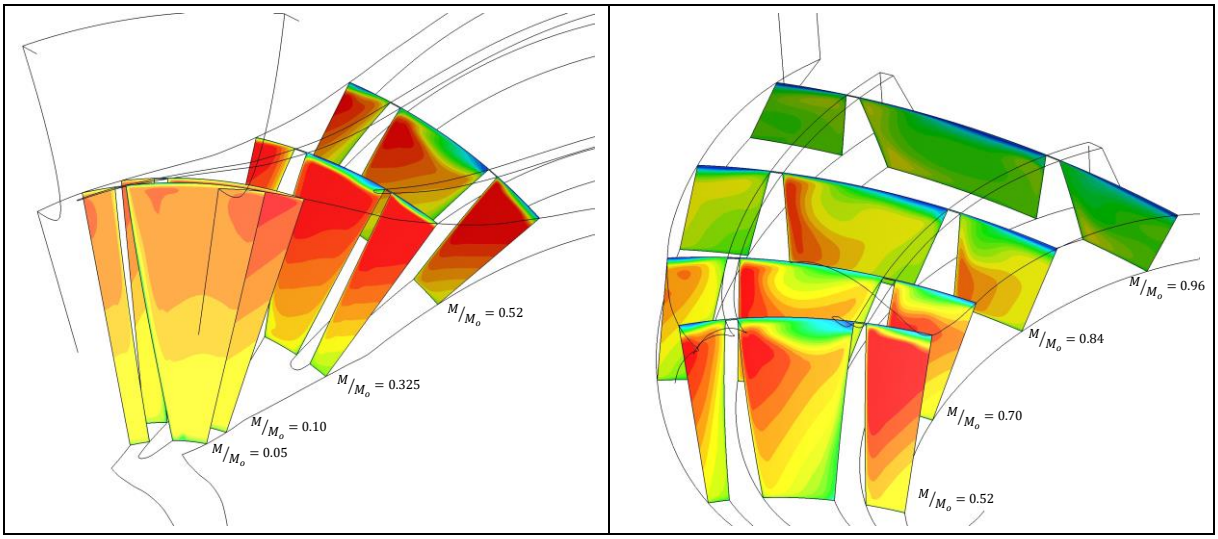

Figure 6-8: Meridional planes for CC3 – *Code_Saturne*

The flow of the impeller passage is initially uniformed but the boundary layer and secondary flow start to shape the passageway flow. The predicted flow field matches the experimental observations made by Skoch et al. [1]. In the initial meridional planes of 5% and 10% in Fig. 6-9, the flow is relatively uniform. The boundary layer on the blades and hub decelerates the flow; the flow at the corner of the hub and pressure side of the blade decelerates the most. Along the shroud, a pool of low velocity flow collects. The impeller blade scraps this pool of low velocity as it collects towards the suction side of the blade. The splitter blade 'splits' the flow and the low velocity flow is predominately diverted to the left of the splitter blade. Further downstream, the pool of the low velocity flow increases in size and continues to drift towards the suction side of the blades. The flow on the pressure side of both the splitter and the main blades continues to decelerate. By M/M_o = 96%, the averaged meridional velocity has diminished. Corresponding to the meridional velocity plotted in Fig. 6-9 is the tangential velocity plotted in Fig. 6-10. Starting at M/M_o = 32.5%, the flow starts leaking from the tip gap. The 'jet' from the tip gap increases in strength and size in later meridional planes and corresponds to the pool of low velocity in Fig. 6-9. By M/M_o = 96%, the tangential velocity has stratified in the passageway with high tangential velocity in the upper part of the passage and lower tangential velocity in the lower part. In this final meridional plane, the flow in the passageway has begun to circulate. Both the new algorithm in *Code_Saturne* and Fluent predicted very similar meridional and tangential velocity flow fields throughout the compressor.

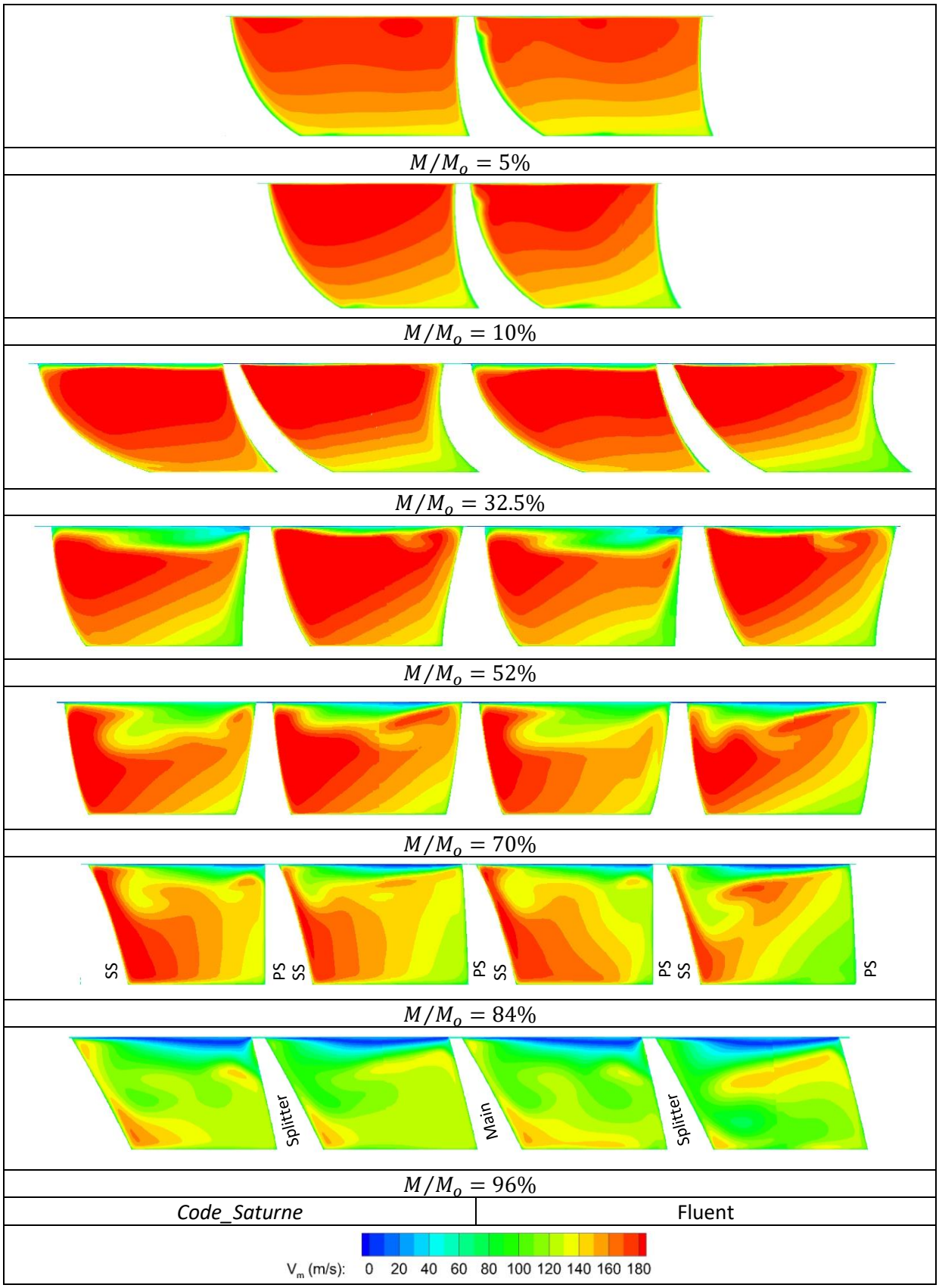

Figure 6-9: Meridional planes for NASA CC3 with a vaneless diffuser – Meridional velocity

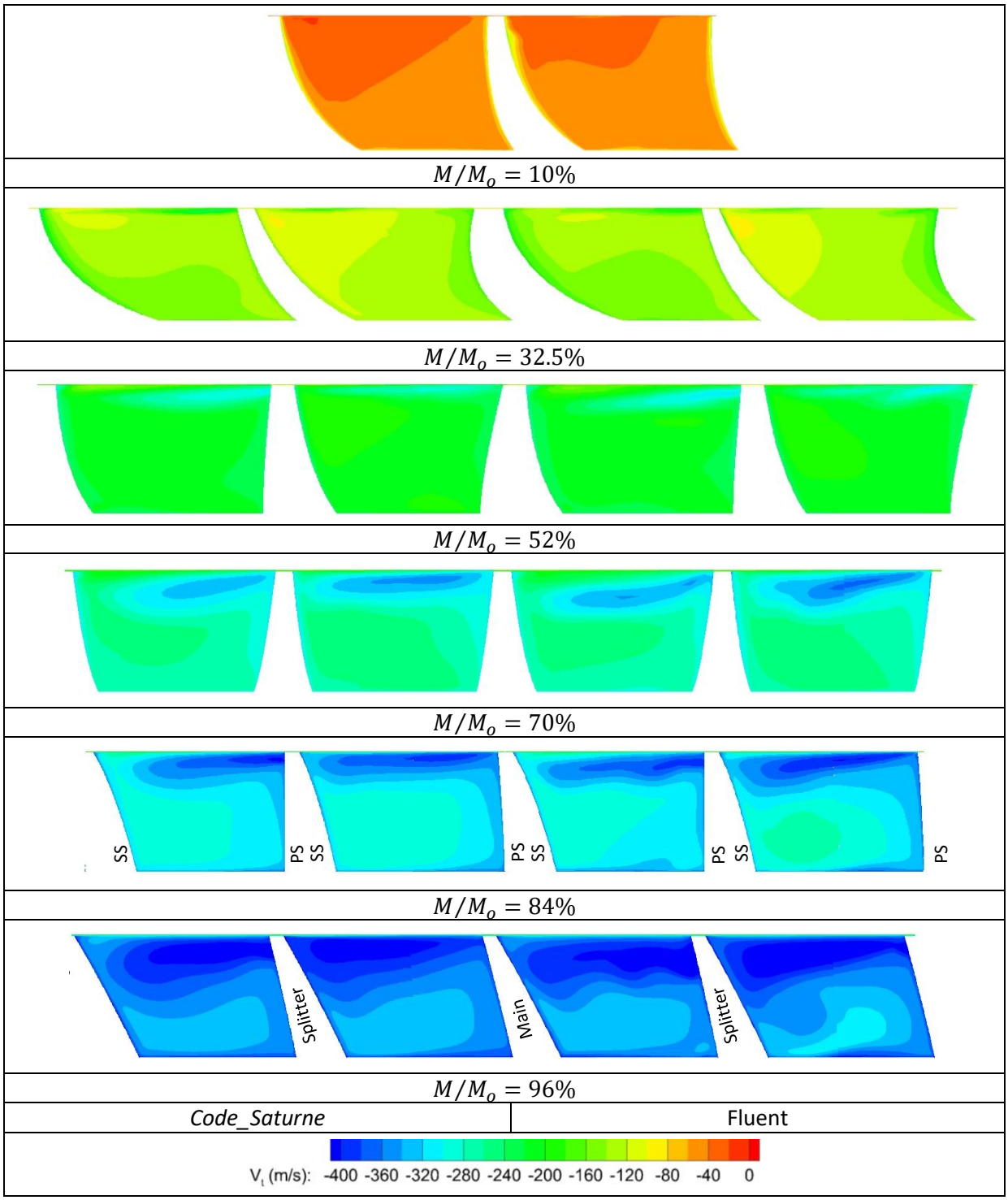

Figure 6-10: Meridional planes for NASA CC3 with a vaneless diffuser – Tangential velocity

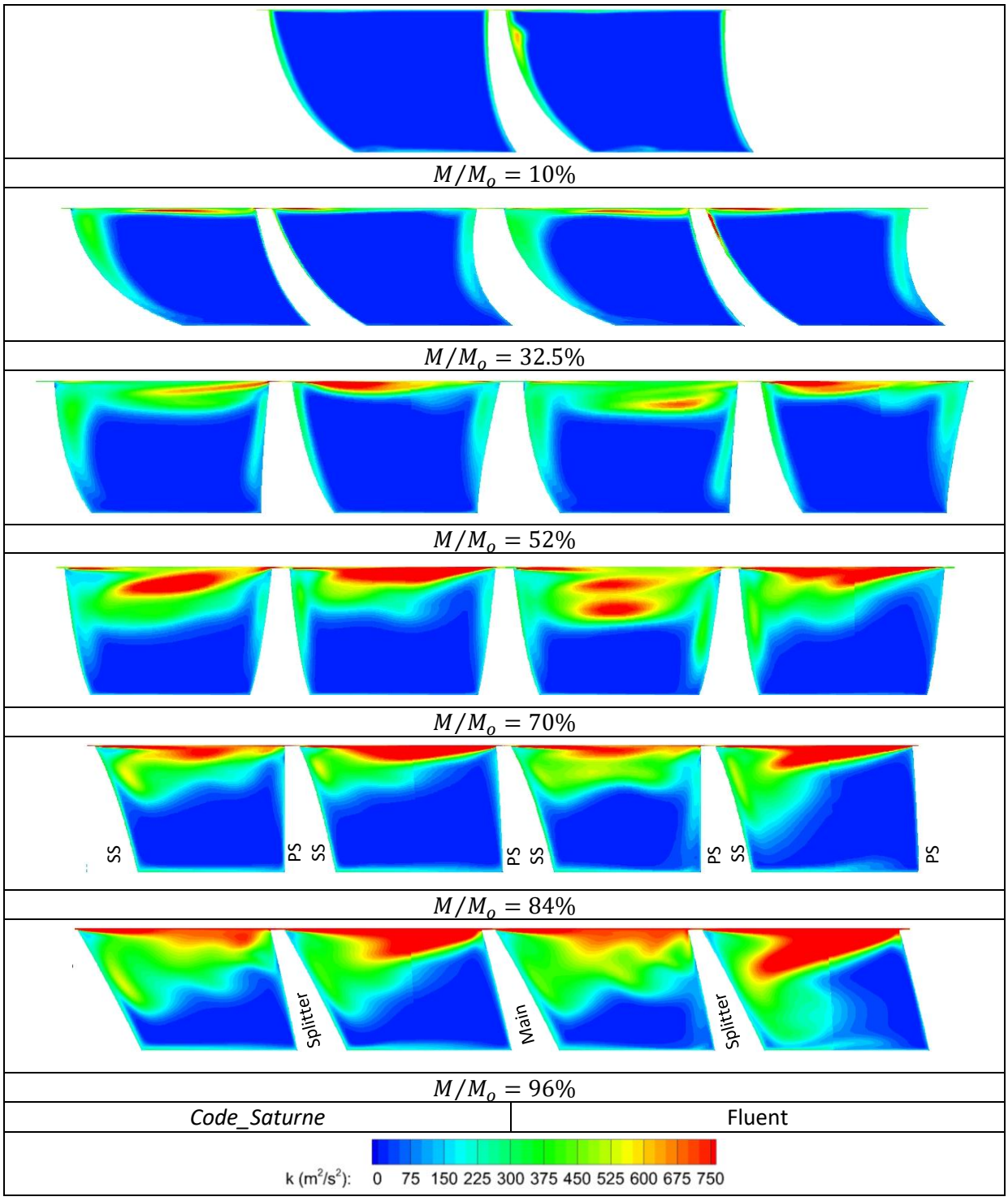

Figure 6-11: Meridional planes for NASA CC3 with a vaneless diffuser – Turbulent kinetic energy

The turbulent kinetic energy at the design operating point is shown in Fig. 6-11. Comparing the turbulent kinetic energy (TKE) between *Code_Saturne* and Fluent, there is a slight difference. At M/M_o = 10%, Fluent predicted a much thicker TKE distribution on the suction side (SS) of the blade while *Code_Saturne* predicted a thinner and uniformed distribution on the SS. On the pressure side (PS) of the

blade, both solvers predicted a similar distribution of TKE. Further downstream, TKE is produced by the secondary flow from the tip gap and TKE accumulates on suction side of the blade. Fluent predicted the TKE diffuses slightly more than *Code_Saturne*, but overall both solvers predicted quite similar distributions.

The radial and tangential velocity at the r/r_{TE} = 1.0791 in the diffuser is shown in Fig. 6-12. This is the equal radial distance of the leading distance of the leading edge of the vanes for a vaned diffuser. At this radial distance, the velocity components are still greatly non-uniform from the wake of the blades and the jet of the passageway. Further downstream the components eventually become uniform in the theta direction; however, this non-uniformity becomes detrimental in the next section where the vaned diffuser has to adjust to the non-uniform flow especially at off-design conditions.

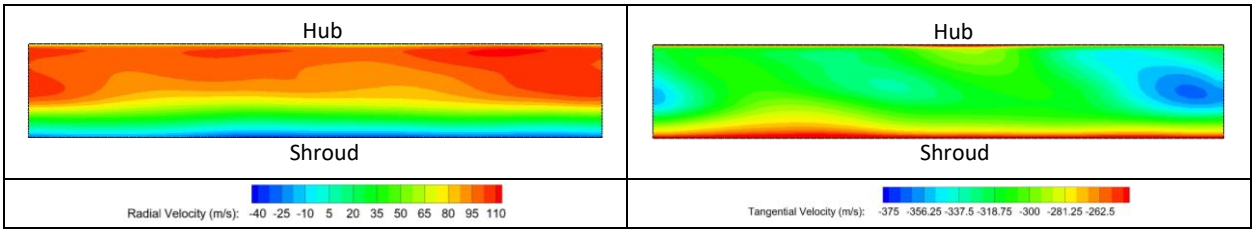

Figure 6-12: Velocity at r/r_{TE} = 1.0791

6.4 NASA CC3 with a Vaned Diffuser

The use of the new compressible flow algorithm written for *Code_Saturne* was shown to give good results with respect to modelling a single passageway of the NASA CC3 with a vaneless diffuser in the previous section. Attention is now focused on modelling the full compressor with a vaned diffuser. The compressor was modelled at three points: near choke, design point, and near stall. The total pressure ratio and adiabatic efficiency is plotted in Fig. 6-13 and Fig. 6-14 against the experimental results of Skoch et al. [1]. The new algorithm predicted a higher total pressure and adiabatic efficiency than what was experimentally observed. The divergence between the predicted total pressure ratio by *Code_Saturne* and experimental data increases as the mass flow rate is increased.

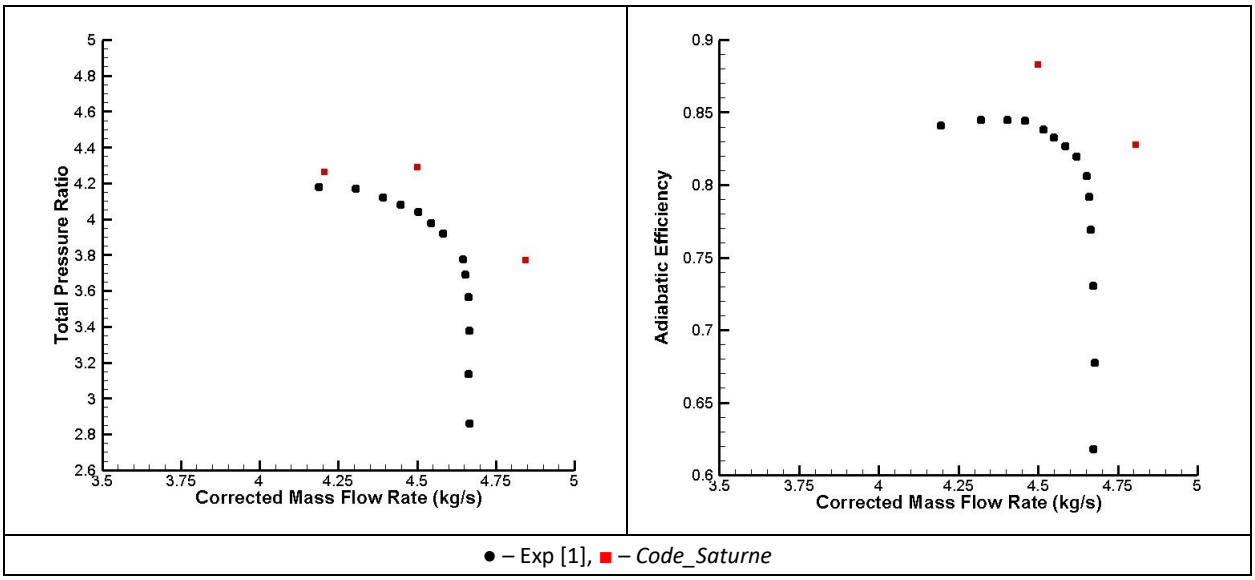

Figure 6-13: Total pressure curve for vaned CC3

Figure 6-14: Efficiency curve for vaned CC3

6.4.1 Off-Design and Design Condition

Meridional planes where extracted from the time-averaged flow within the impeller at the same locations as shown in Fig. 6-8. The meridional planes were extracted from the flow field at design and off-design operating conditions and are displayed in Fig. 6-15. At the design operating condition, the structure of the flow was very similar to the flow structure found for the case with a vaneless diffuser in Fig. 6-9. Although similar, the boundary layer for this case was noticeably larger than the previous case with a vaneless diffuser. Unfortunately, there are no published PIV results of the internal flow of the impeller to compare against.

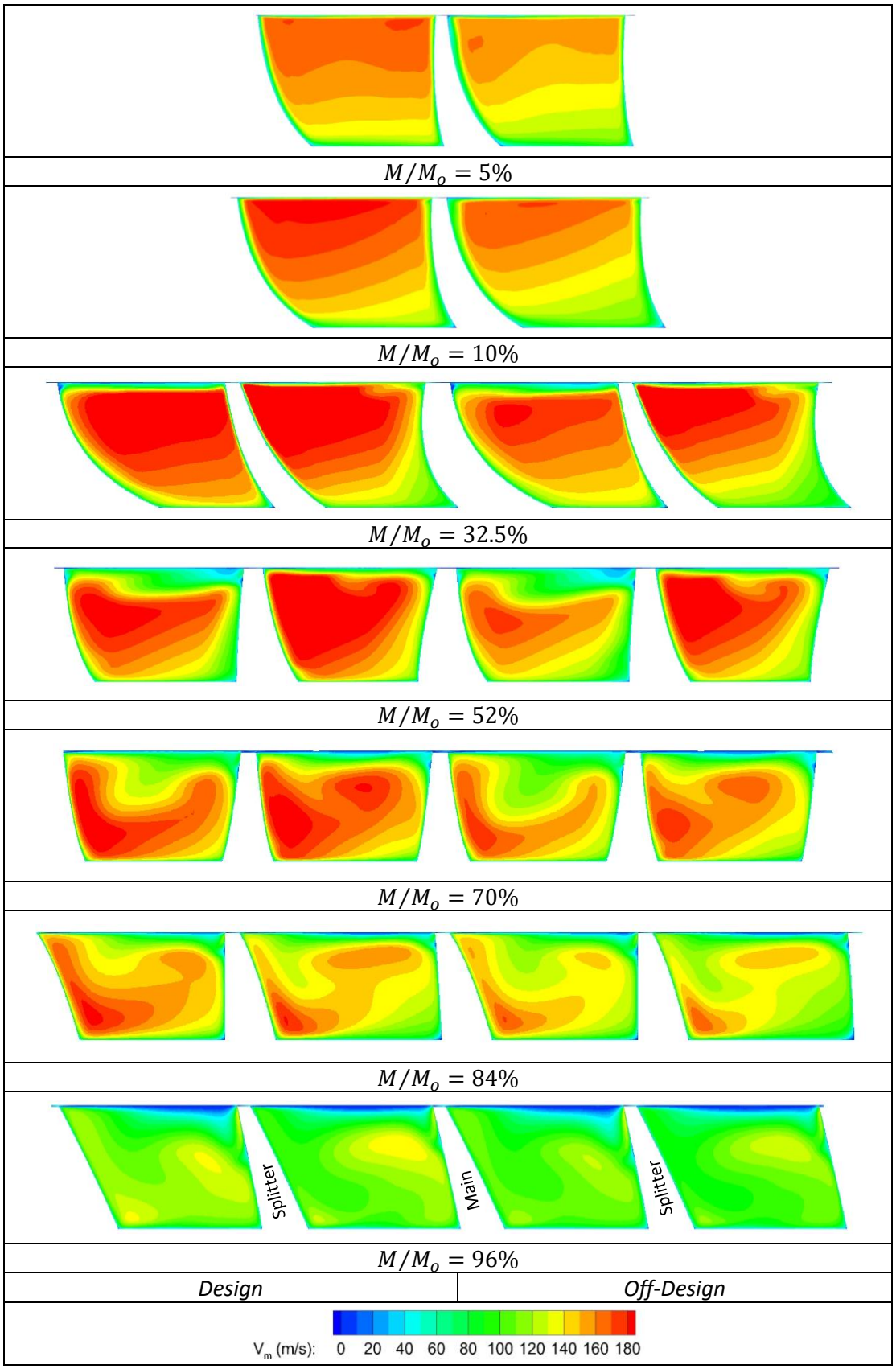

Figure 6-15: Meridional planes for NASA CC3 with a vaned diffuser

Comparing the design to the off-design operating condition, the flow structure was very similar except for the meridional velocity being weaker and the boundary layer has slightly thickened. Bigger differences occur in the pressure distribution in the vaned diffuser, Fig. 6-16. The pressure gradient across the vaned diffuser between the design and off-design operating conditions has considerably grown leading to a state where the vaned passages are akin to a compressed spring waiting to be unleased.

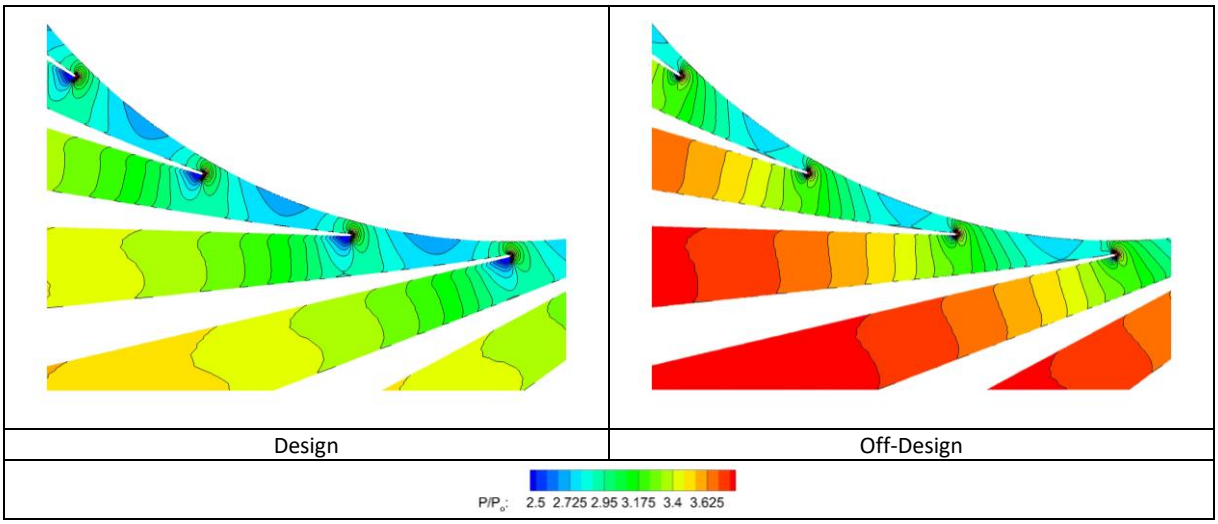

Figure 6-16: Pressure distribution in a vaned diffuser at design and off-design conditions

6.4.2 Rotating Stall

To force the compressor into rotating stall, the mass flow rate was dropped to 3.8 kg/s which is in the general range that Wernet et al. [117] and Halawa et al. [53] observed rotating stall. Rotating stall quickly formed in the compressor and the compressor was modelled until surge occurred. The pressure inside of the impeller and diffuser was monitored to capture any instability inside the compressor.

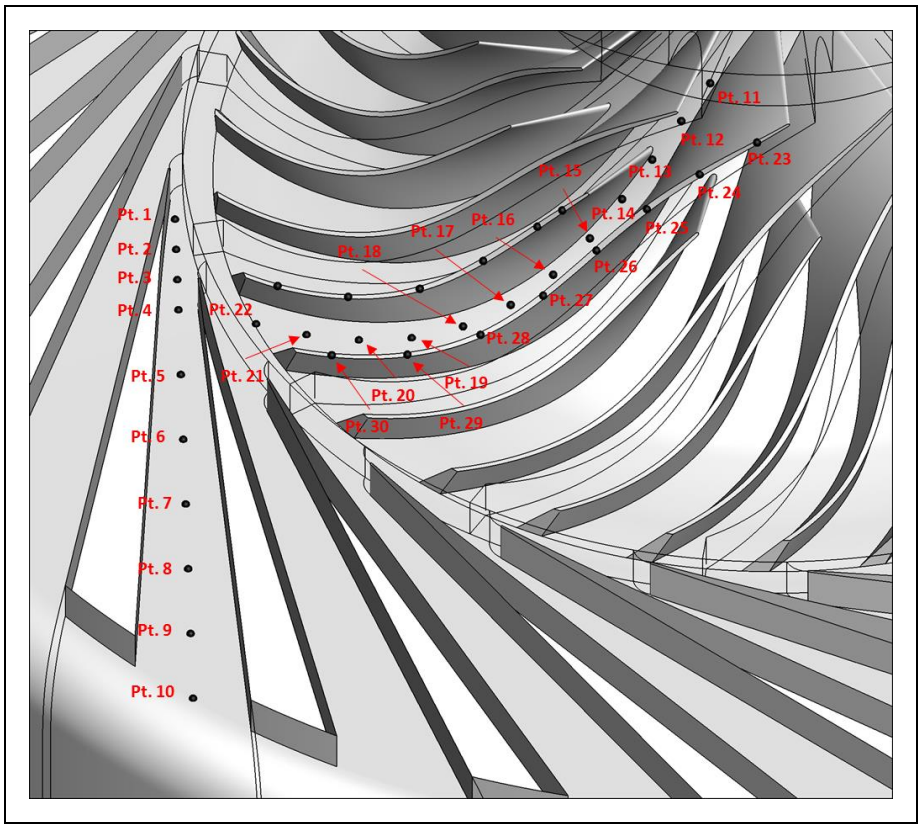

Figure 6-17: Sampling points in the CC3 compressor

Inside the compressor, the pressure was monitored at several points as shown in Fig. 6-17. The pressure at selected monitoring points from Fig. 6-17 are plotted in Fig. 6-18 based upon the distinct flow characteristic observed at these points. The plotted monitoring points are located throughout the impeller and the vaned diffuser. The perturbations in the monitored pressure grow as the rotating stall progresses into surge. The pressure at points in the impeller that are near the inlet have a long-term perturbation while progressing downstream in the impeller, secondary perturbations form on the top of the long-term perturbations. The period of the pressure perturbations at the monitor points at the leading edge of the main blade, P23 and P26, are out of phase of the pressure perturbations at the hub, P11, and downstream monitoring points on the main blade, P29 and P30. The frequency of the pressure perturbation at the monitoring points in the impeller was 1546.5 to 1718 Hz. The frequency of the pressure perturbations of the monitoring points in the diffuser, P3 and P6, was found to be approximately 1031 Hz, although it is suspected that there is a lower frequency in the pressure perturbations based on the pressure contours. Most of the higher frequency perturbations in the diffuser and in the downstream section of the impeller are from the impeller/diffuser interaction.

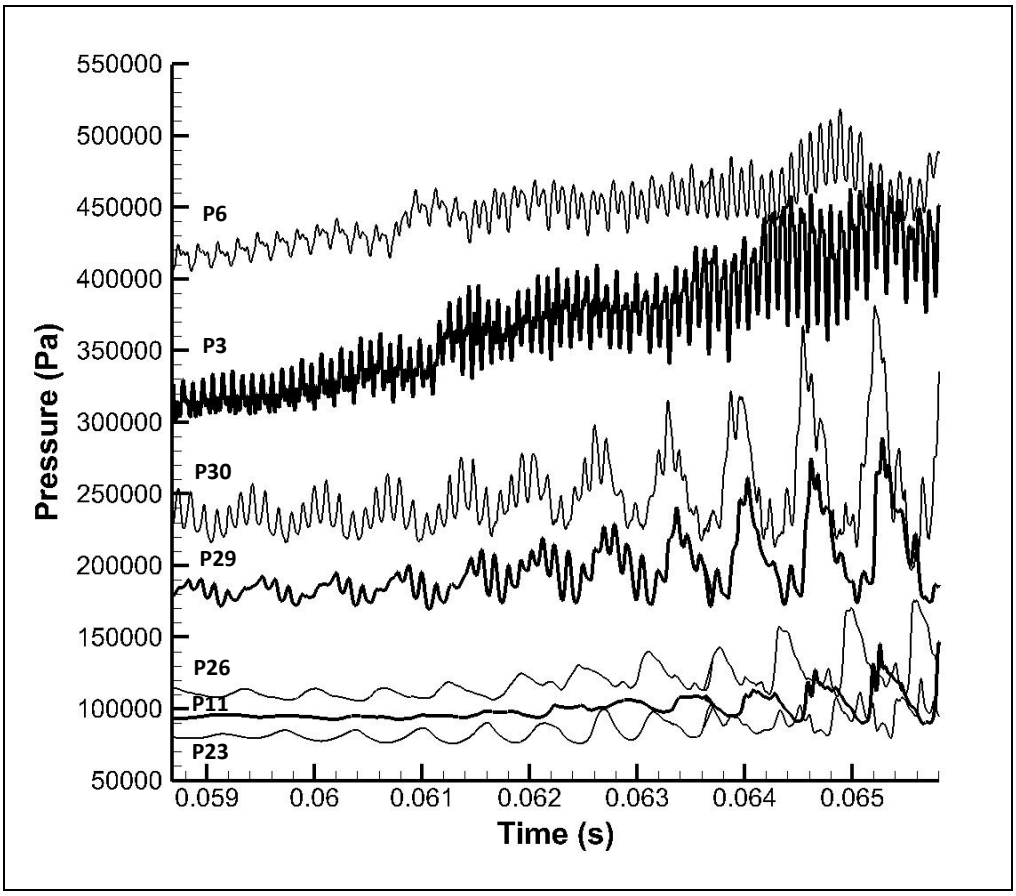

Figure 6-18: Pressure monitor

The pressure field at 70% span from the hub is shown in Fig. 6-19. In Fig. 6-19, the pressure at the off-design operating point of 4.2 kg/s and rotating stall at 3.8 kg/s is shown. At the off-design point of 4.2 kg/s, the pressure distribution around the compressor is still nearly uniform. The pressure field of the diffuser shows some non-uniformity, but the flow is still able to accommodate these perturbations. With the reduction of the mass flow rate to 3.8 kg/s, the momentum of the flow is unable to support the pressure gradient across the compressor. Rotating stall was observed to form quickly with four rotating stall cells in the impeller and the diffuser. The rotating cells in the impeller were observed to rotate at approximately 0.0587 times the rotational speed of the impeller. The rotational speed of the stall in the diffuser could not be calculated. The stall in the impeller was observed to be out of phase with the stall in the diffuser.

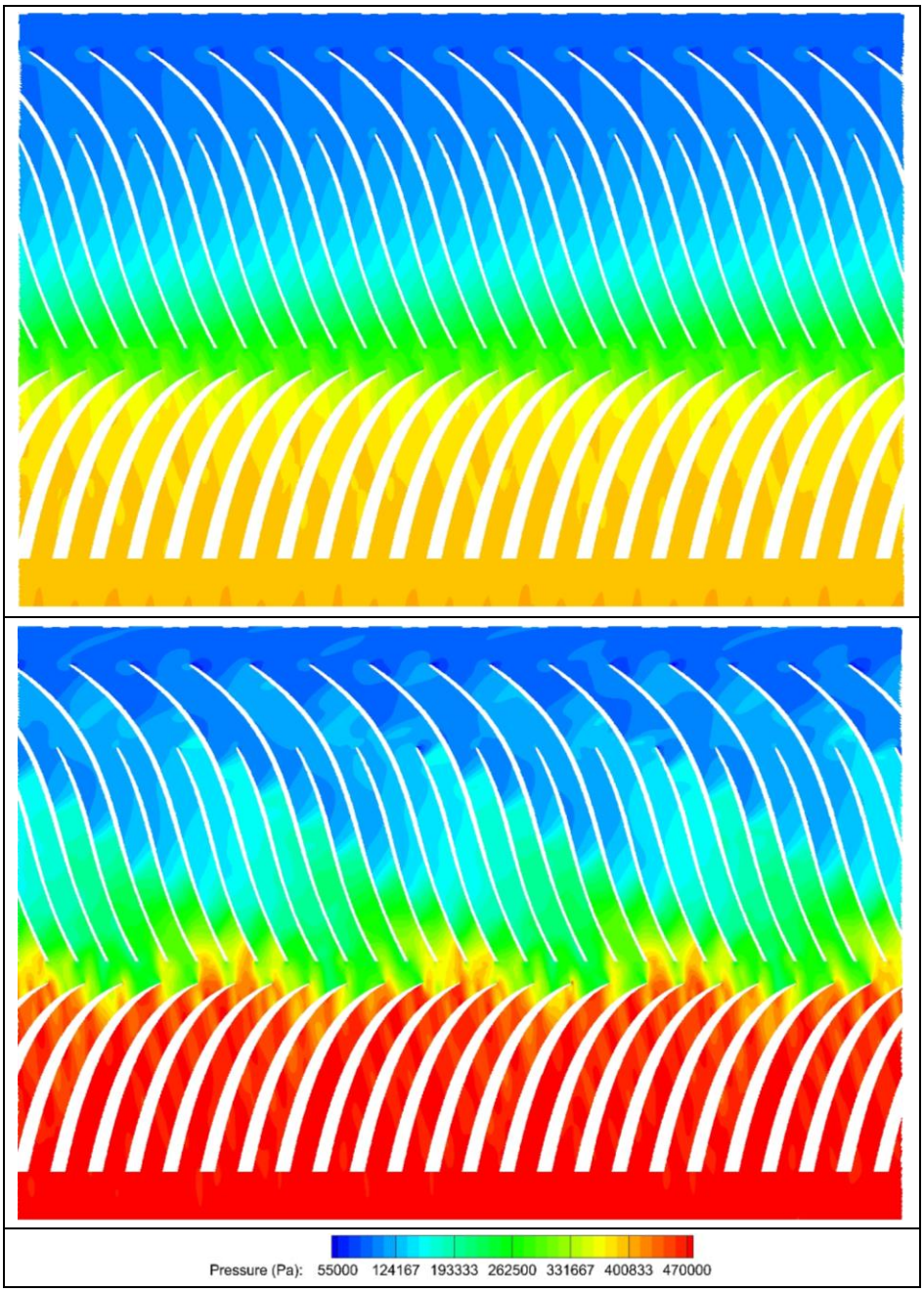

Figure 6-19: Pressure distribution at 70% span (Top - $\dot{m} = 4.2\ kg/s$, Bottom - $\dot{m} = 3.8\ kg/s$)

Taking a second look at the pressure perturbations from the monitoring points in Fig. 6-17, the pressure points on the impeller blade edge from the leading edge to the trailing edge, P 23 to P 29, are plotted in Fig. 6-20. The explanation behind the prior observation that the pressure perturbations in the impeller are out of phase in Fig. 6-18 becomes clear. The pressure perturbations originate from the exit of the impeller and propagate upstream in the impeller. Combining the pressure monitors in the Fig. 6-20 to the pressure contours in Fig. 6-19, the high pressure from the stalled diffuser passages sends 'waves'

upstream into the impeller. The individual pressure 'waves' are denoted by dotted line in Fig. 6-20 to illustrate the propagation of the 'waves.'

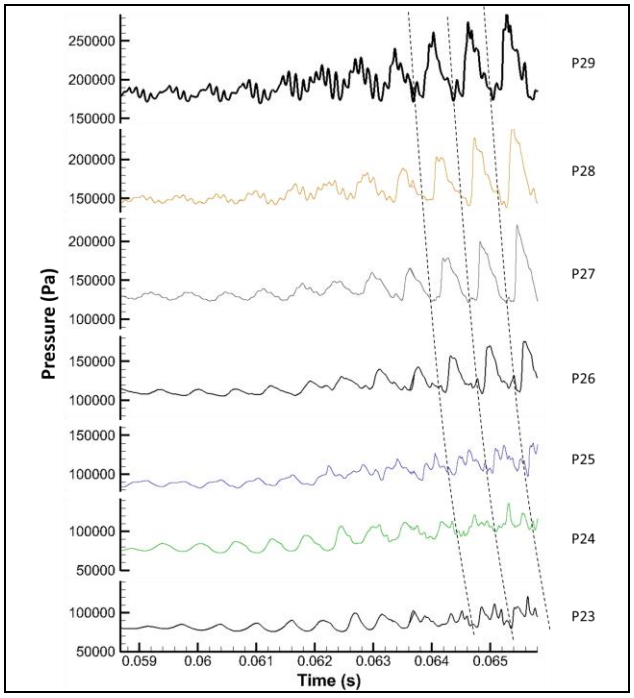

Figure 6-20: Pressure perturbation in the impeller

Turning attention to the velocity field of the compressor, a different set of events are observed to occur in the impeller. The meridional velocity at 70% span from the hub is plotted in Fig. 6-21. The stalled diffuser passages are clearly visible with the stalled flow leaking into the vaneless space between the impeller and the diffuser. However, the area of interest is in the impeller. At the leading edge of the main impeller blade, a change in direction of the oncoming flow is met by the flow separating from the impeller blade and an acceleration of the flow to accommodate the separation bubble. As the impeller blade rotates and passes the disturbance, the flow angle returns to normal extinguishing the separation bubble. From this process, a packet of high momentum flow propagates downstream. In half of a revolution, the packet of high momentum flow encounters the vaneless region between the impeller and diffuser and matches a set of unstalled diffuser passages.

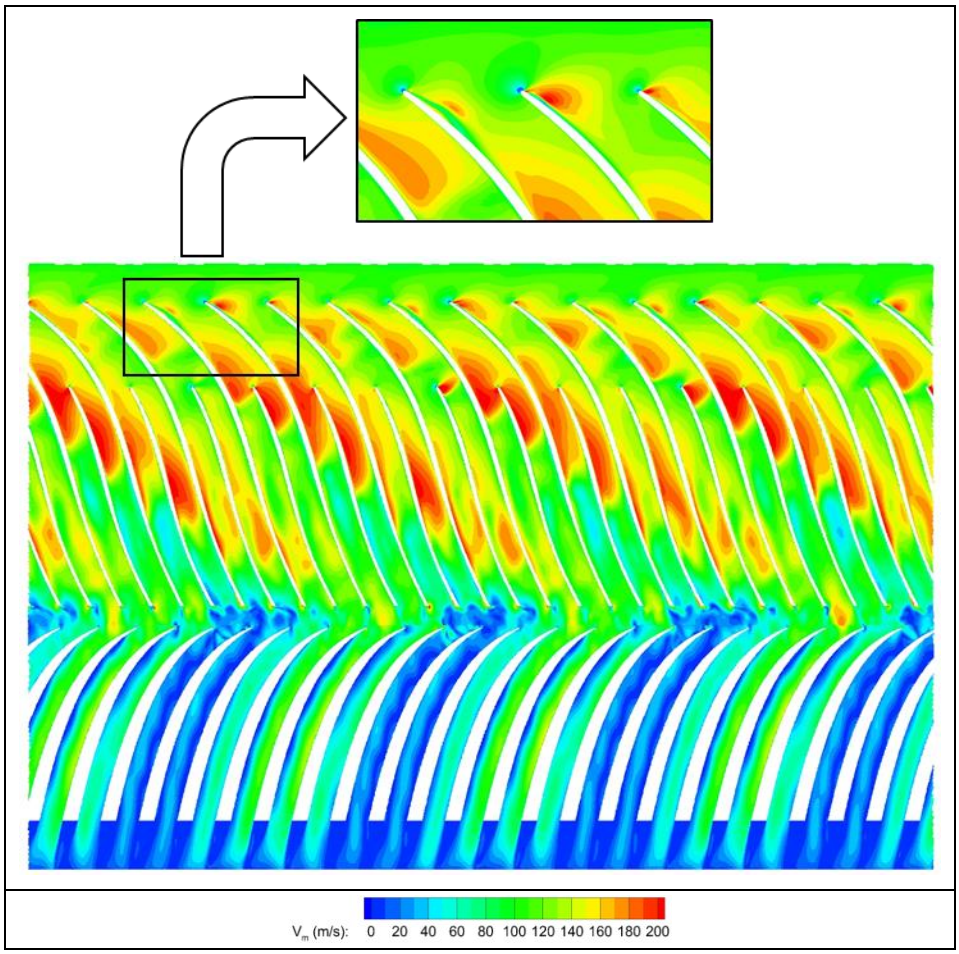

Figure 6-21: Meridional velocity at 70% span from the hub

6.5 Conclusion

The NASA CC3 compressor was modelled with a vaneless and vaned diffuser. A single passage of the impeller with a vaneless diffuser was modelled first to determine the proper mesh resolution and comparison was made with published experimental results. Modelling the single passageway from choke to stall, the total pressure ratio curve and adiabatic efficiency curve were calculated. The new algorithm in *Code_Saturne* was found to predict total pressure ratio very well in comparison to published experimental results. *Code_Saturne* predicted an adiabatic efficiency curve that nearly matches results from ANSYS Fluent, but both solvers over predict the efficiency by about 2%. There was a strong discrepancy in the turbulent kinetic energy between *Code_Saturne* and ANSYS Fluent which may explain the over prediction of the performance of the compressor for *Code_Saturne*.

The full compressor was modelled with a vaned diffuser at the operating design point, near choke, and near stall. The modelled compressor was found to over predict the total pressure ratio and adiabatic

efficiency when compared to published experimental results. It is theorized that the mesh for the vaned diffuser wasn't sufficient given that the mesh for the compressor with a vaneless diffuser gave very good results. The mass flow rate of the compressor was reduced to below the stall line to induce rotating stall and modeled until the compressor progressed into surge. Four stall cells were observed in the impeller and the diffuser, the rotating stall cells in the impeller were measured to rotate at 0.0587 times the rotational speed of the impeller. In the analysis of rotating stall in the compressor, two competing processes are observed that dictate the rotating stall. From the exit of the impeller blades, pressure perturbations are observed to emanate from the vaneless region between the impeller and diffuser when the impeller rotates pass a stalled set of diffuser passages. The pressure perturbations propagate upstream to the entrance of the impeller and alters the flow angle of the incoming flow. At the leading edge of the impeller blade, the disturbed incoming flow causes a formation of a separation bubble, and the flow is accelerated to accommodate the separation bubble. The entrance of the impeller passage passes the disturbance and the flow returns to normal, extinguishing the separation bubble. Through this action, a packet of high momentum flow propagates downstream and eventually encounters the vaneless region between the impeller and diffuser and into a set of unstalled diffuser passages. This process provokes a question on whether the leading edge of the impeller blade controls the rotating stall in the compressor or the vaneless region/vaned diffuser. This suggests the rotating stall in the compressor is a mutual interaction that settles to a quasi-stable equilibrium before the system is brought out of rotating stall or pushed into surge.

7. Flow Control in NASA CC3

7.1 Introduction

In the previous chapter the NASA CC3 was modelled and rotating stall was observed and studied. As noted in the Chapter 1, prior researchers [50-54] have used jets in the inlet of the vaned diffuser to suppress the instabilities present. As discussed in the introduction chapter, passive vortex generators are tested in the inlet of the compressor to assess their capability to suppress the instabilities in the impeller. The implementation of flow control within the NASA CC3 compressor is conducted in two stages. An optimization study was pursued to determine the optimum configuration for VG in the inlet of the compressor. The optimum configuration is then implemented in the full compressor to access the ability of VG to suppress flow instabilities and improve the operating range of the compressor. The VG optimization study was conducted with ANSYS Fluent while modelling of the full compressor with VG implemented was done with *Code_Saturne*.

7.2 Numerical Setup

As with the previous chapter, the new compressible flow algorithm that was discussed in chapter 2 and written for *Code_Saturne* was used to model the flow inside the CC3 compressor. Identical to the simulations in the previous chapter, time was advanced with a 1st-order implicit scheme. A 2nd-order MUSCL scheme was used for the convective terms of density, total energy, and momentum. A time step of $2x10^{-7}$ s was selected to keep the maximum CFL number below 2. For the optimization study in section 7.3, ANSYS® Fluent was used due to it is efficiency in solving steady-state, compressible problems. The SIMPLEC method was used to solve for the results was presented in section 7.3. A 2nd-order upwind scheme was used for density, energy, and momentum convective terms in Fluent. Turbulence was modelled with the k-ω SST model. For both the optimization study with Fluent and the full compressor modelling with *Code_Saturne*, a total pressure inlet of 101325 Pa and a total temperature of 288.15 K were imposed at the inlet. A static pressure at the outlet was imposed and manipulated with Eq. 6-1 to obtain the desired mass flow rate. Periodic boundary conditions were used in between the passages for the optimization study. The exact composition of the mesh is described in detail in the following sections.

7.3 Vortex Generator Optimization Study

To determine the best MVG configuration to control the internal flow of a compressor, it is preferable to model the complete compressor at an operating point where rotating stall occurs, unfortunately this approach would cost an astronomical amount of computational power. To conduct an optimization study within the resources available, some simplifications were made to the numerical setup. This was accomplished by eliminating the impeller blades and cutting the passage at M = 52% meridional plane. The meridional plane of 52% was at least 103 boundary layer thicknesses downstream of the VG and allowed for sufficient distance for the vortices to travel downstream without the outlet interfering with the vortices. With the simplified domain, the boundary layer was able to form in the inlet and interact with the VG. The vortices propagated downstream in the boundary layer and were analyzed at the approximate location of the leading edge of the impeller blade.

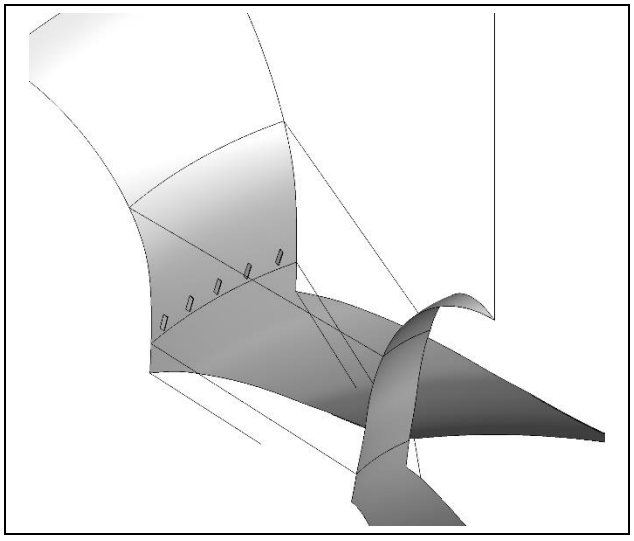

Figure 7-1: Domain for VG optimization study

The trailing edge of the MVG was placed at -127.71 cm upstream of the leading edge of the impeller blade. A profile of the total pressure at this plane, with and without the impeller blade, is shown in Fig. 7-2. The total pressure from the simplified case matches well to a case where the impeller blades are modelled. The boundary layer thickness at this location on the shroud was 0.9739 mm. The height of the vanes was 0.6443δ, 0.8δ, 1.3043δ, and 1.9364δ, or 0.2988%, 0.3710%, 0.6050%, and 0.8981% of the inlet tip radius of the impeller blade, respectively. The placement of the vanes was constrained by the mesh interface to allow motion between the impeller blades and the MVG. In the inlet passageway, or 24˚ of the full circumference of the compressor, arrays of 1 to 7 vanes were tested.

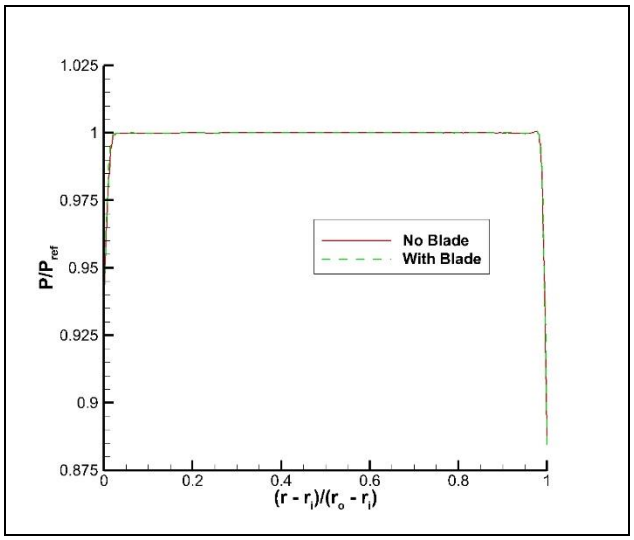

Figure 7-2: Total pressure profile at z = -127.71 cm

7.3.1 Mesh Sensitivity

To determine sensitivity of the model to the resolution of the mesh, three mesh densities were generated as shown in Table 7-1. The mesh sensitivity was conducted with a vane height of 1.3043δ and at 18.5˚. The vane was placed in the middle of the domain on the shroud. Between Mesh A and B, the loss in total pressure ratio across the model was similar. The finest mesh, Mesh C, observed a lower loss in total pressure, 0.02% when compared to the other two meshes.

Mesh	Number of Cells	Total Pressure Ratio
A	107,831	-0.4762%
B	783,741	-0.4787%
C	2,140,065	-0.4584%

Table 7-1: Sensitivity to mesh resolution

The boundary layer profile was extracted at 127.71 cm downstream of the vane, or the approximated axial position of the leading edge of the main impeller blade (z = 0 m). The boundary profiles are plotted in Fig. 7-3. Increasing the mesh density from Mesh A to B saw a significant change in the boundary profile, further increase in mesh density to Mesh C saw further changes in the profile. The outer boundary layer saw a near convergence for Mesh B and C, convergence on the inner boundary layer remained elusive. Similar trends are observed in the sensitivity of the circulation to the mesh density, Fig. 7-4. Circulation of the vortices was measured from 1h to 30h downstream of the vane. The coarsest mesh, Mesh A, grossly underestimated the circulation. Mesh B and C gave similar prediction for the circulation strength but Mesh C still gave a slightly higher circulation strength. Ideally, it would preferable to keep increasing the mesh densities until the properties of the vane and the vortex are independent of the mesh

resolution; however, Mesh C demonstrates that the mesh density needed to achieve this goal is very high. To keep within limits of the available computational resources, a mesh resolution similar to Mesh B is used for the following sections.

It should also be noted that the interface between the inlet and impeller domain was located at about 10h. In the numerical solution of the flow, the interface was observed to diffuse the vortex when the vortex crossed the interface. Although the interface had an observable effect on the vortex, the circulation in Fig. 7-4 showed little influence by the interface.

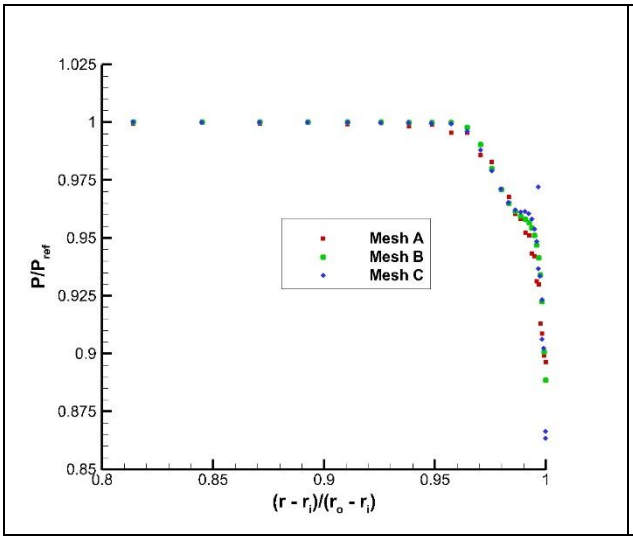

Figure 7-3: Boundary layer profile sensitivity to mesh resolution

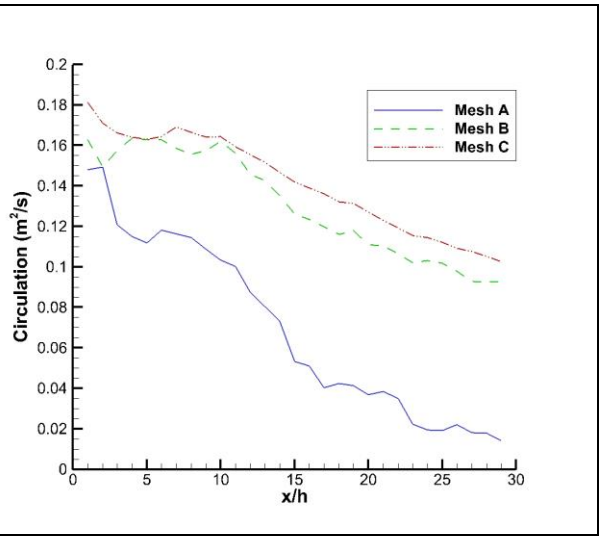

Figure 7-4: Circulation sensitivity to mesh resolution

7.3.2 Simplified Case – Co-Rotating

With determination of the mesh sensitivity of VG in the inlet of an 'impeller,' the implementation of co-rotating, rectangle vanes are considered. The vanes were placed at 18.5˚ relative to the axial direction while the vane height and count are considered. The effects of VG height and vane count per passageway was evaluated by the boundary layer profile at z = 0 m (axial position of the leading edge of the impeller) and the total pressure loss. Plotted in Fig. 7-5 is the boundary layer for the total pressure at z = 0 m for the different VG configurations along with a case without any VG. The boundary layer at this position was spatially averaged in the theta direction over a 24˚ arc. As expressed previously in earlier chapters, the vortices in the boundary layer transfer momentum from the outer boundary layer to inner boundary layer. The transfer in momentum is expressed in the boundary layer profiles as an increase of the total pressure near the wall with a reduction in the total pressure in the outer boundary layer. The smallest VG, with a height of 0.6443δ, saw a small transfer in momentum. Increasing the VG height lead

to an increase of momentum transfer and increasing the vane count also lead to an increase of momentum transfer. As the vane height became greater than the boundary layer thickness, the vortices were capable of transferring more momentum into the boundary layer.

It was originally envisioned to use a smaller VG's than 0.6443δ, but given that VG's with height of 0.6443δ had only a very slight impact on the downstream boundary layer, this idea was dismissed. By increasing the vane height further, the boundary layer saw diminishing returns and greater vane heights were not sought.

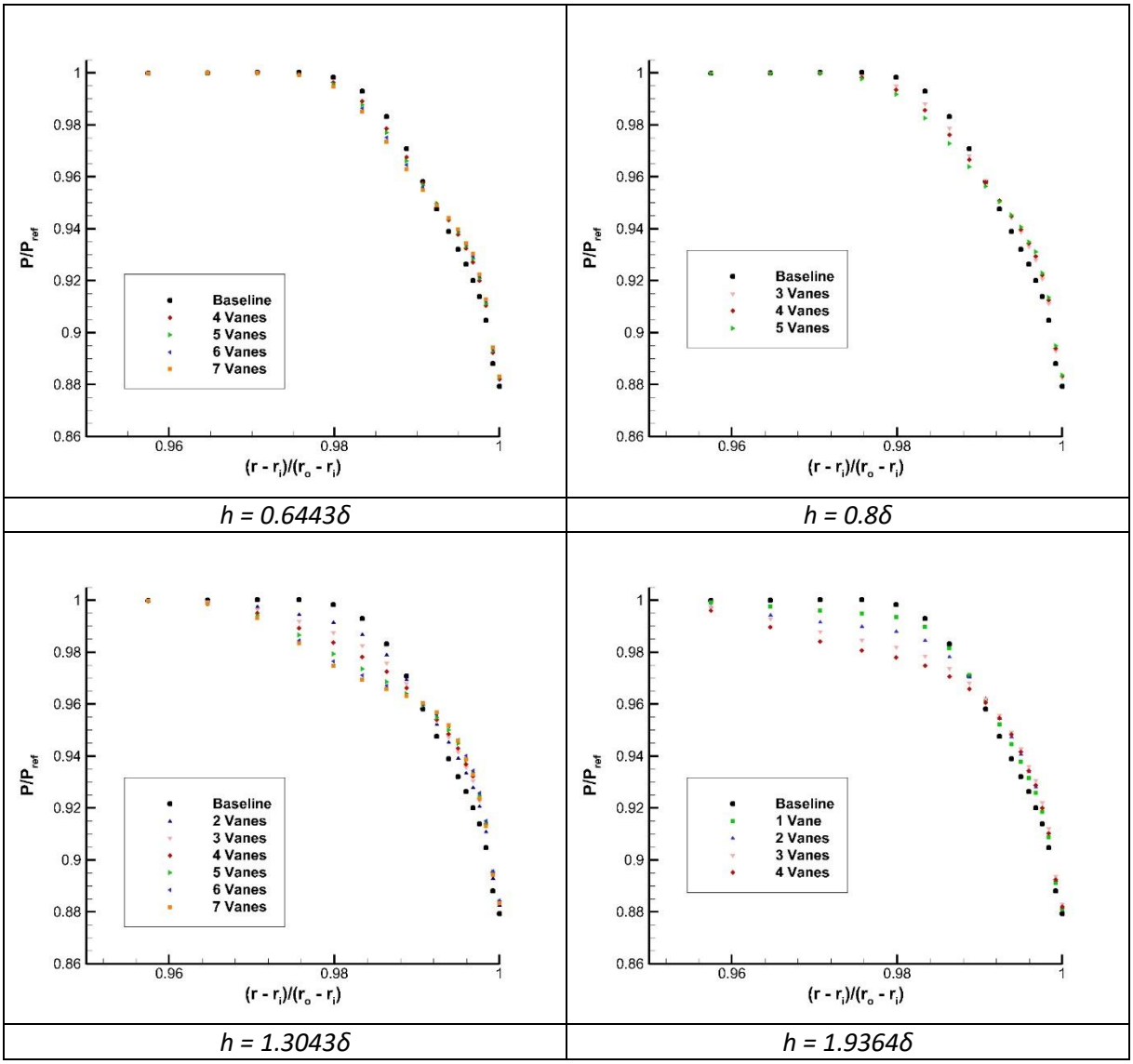

h = 0.6443δ | *h = 0.8δ*

h = 1.3043δ | *h = 1.9364δ*

Figure 7-5: Boundary profiles at z = 0

To determine the amount of energy loss from MVG vanes, the change in total pressure ratio was calculated between the inlet and outlet the domain. Plotted in Fig. 7-6 is the pressure ratio for the three

different vane heights in comparison to the baseline case without any vanes. Without any vanes, a total pressure loss of -0.46% was measured. MVG vanes with a height of 0.6443δ caused no discernable change in the total pressure loss. The slightly taller vanes with a height of 1.3043δ caused a slight increase of total pressure loss, with the largest increase above the baseline being 0.04%. The tallest vanes lead to the greatest increase of total pressure loss, with the largest increase above the baseline being 0.08%. Increasing the vane count also increased the total pressure loss.

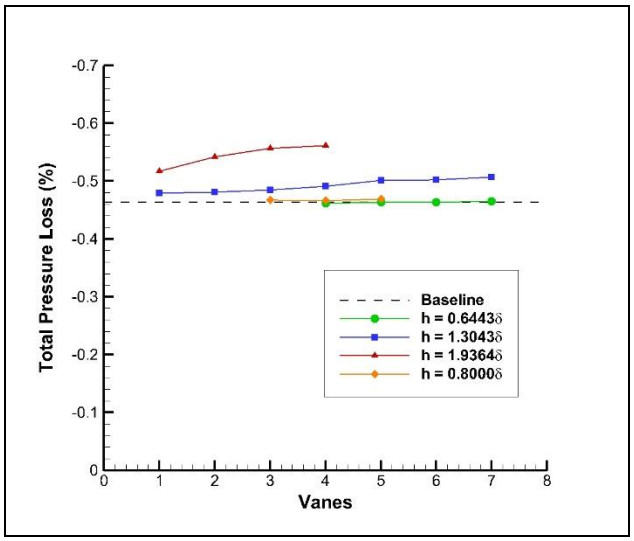

Figure 7-6: Total Pressure Loss

Combing the results of the boundary layer profile in Fig. 7-5 and the total pressure loss in Fig. 7-6, the best vane height that strikes the best balance between momentum transfer in the boundary layer and losses can be determined. The vane with a height of 1.3043δ was considered the best compromise as it had less of an effect on the pressure loss than the taller vane while still having a very significant effect on the boundary layer when compared to the smaller vanes. A vane with a height of 0.8δ was a secondary choice and may be considered in future work. In the vane count per 24˚ arc, 5 vanes were considered optimum, as increasing the vane saw no changes in the boundary layer profile while decreasing the vane count saw a reduction in the momentum transfer in the boundary layer. Fig. 7-7 displays the axial velocity contours for 5 co-rotating vanes with heights of 0.8δ and 1.3043δ.

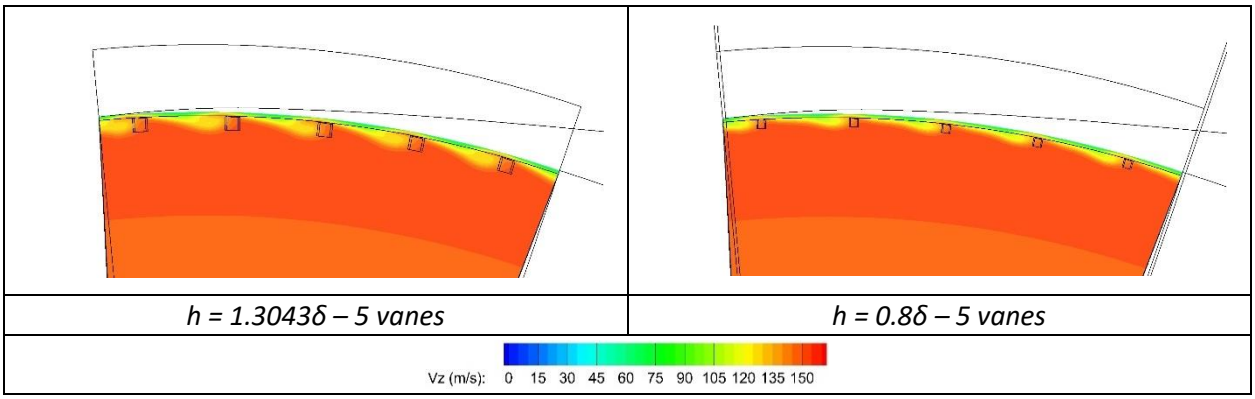

Figure 7-7: Axial flow at z = 0 m

7.3.3 Simplified Case – Counter-Rotating

In section 7.3.2, co-rotating vanes were considered and was found to be capable of transferring momentum in the boundary layer at the location of the leading edge of the impeller blade. Counter-rotating, rectangle vane pairs were experimented with to determine their relative effectiveness to co-rotating vanes. A pair of vortex generators with heights of 1.3043δ was placed in the same axial location as the co-rotating vanes. In the first numerical experiment, the spacing (w) between the vanes were varied between 2h and 4h.

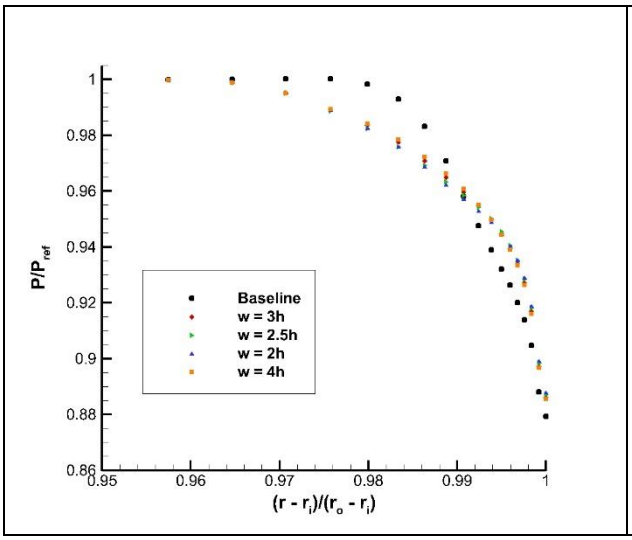

Figure 7-8: Vane pair spacing – boundary profile

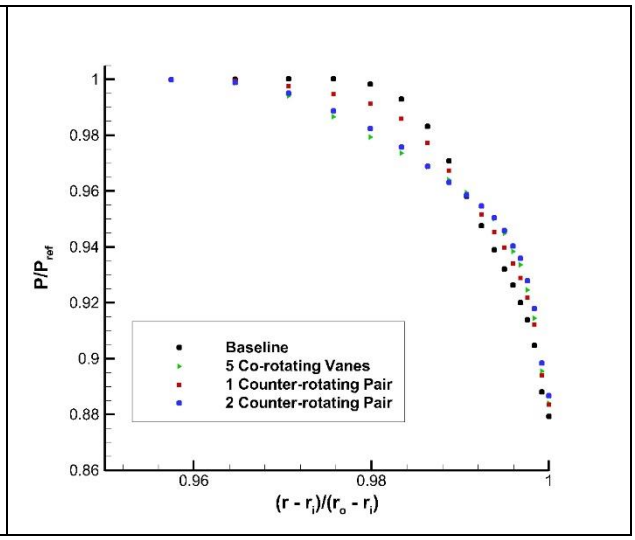

Figure 7-9: Multiple vane pairs – boundary profile

The boundary layer profile was extracted at z = 0 m and the boundary layer was spatially averaged over a circumference width of w + xh and was centered on the vortex pair. The boundary profile was plotted in Fig. 7-8. From the plot, there is a slight deviation between the spacing tested with the smaller spacing giving better transfer in momentum than widely spaced vanes. An additional model was conducted with two vane pairs with vane pairs evenly spaced in the 24˚ section of the inlet; the spacing

in the vane pair was 2.5h. The spacing (s) between the vane pairs were 9.53h, or 12˚. The boundary layer profile was plotted against a single counter-rotating pair and 5 co-rotating vanes in the 24˚ section in Fig. 7-9. The single counter-rotating pair was unable to match the co-rotating vanes in transferring the momentum in the boundary layer; however, introducing a second counter-rotating pair yielded very similar results to that of the 5 co-rotating vanes.

The pressure losses for the two cases are shown in Figs. 7-10 and 7-11. In regards to the vane spacing of the counter-rotating pairs, there was little difference in the pressure losses. Comparing the losses to co-rotating vanes, one and two counter-rotating vanes saw slightly higher loses than comparative co-rotating vanes. In combination with slightly less momentum transfer in the boundary layer and slightly higher pressure losses, counter-rotating vanes are less efficient than co-rotating vanes.

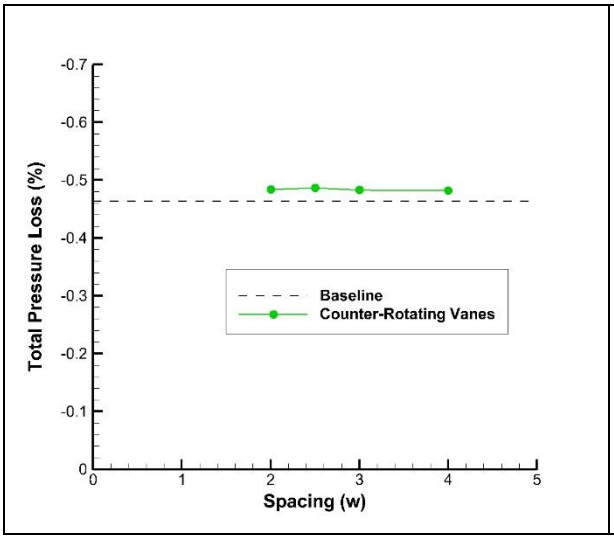

Figure 7-10: Pressure Loss for counter-rotating vane spacing

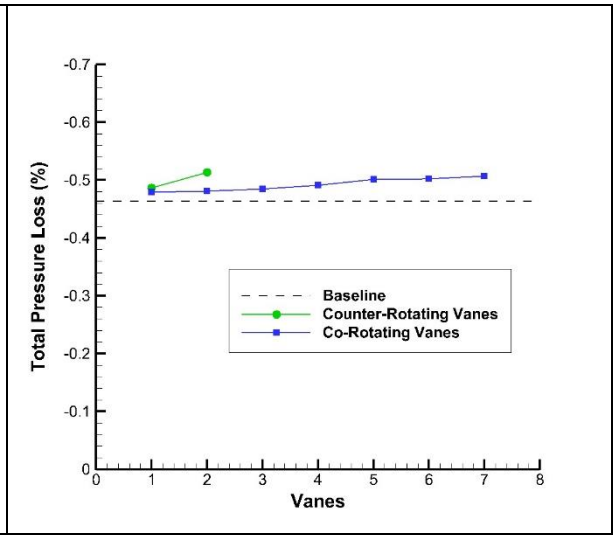

Figure 7-11: Pressure Loss for counter-rotating vanes

7.3.4 Simplified Case – E423

Continuing from work in section 4.4.2, it was hypothesis that the ability of a VG vane to transfer momentum in the boundary layer could be increased by using the e423 shaped vanes. E423 vanes were found to have greater circulation than similar rectangular vanes while having a corresponding lower drag in section 4.4.2. To determine whether using e423 shaped vanes could yield better results than using simple rectangular vanes, e423 shaped vanes were modelled with heights of 0.8δ and 3 to 5 vanes per the 24˚ arc. Conforming to expectations, the e423 vanes transferred momentum in the boundary layer better than rectangular vanes. Three e423 vanes were found to be approximately equivalent to four rectangular vanes.

As discussed in Chapter 4, circulation is not without a cost, and the stronger circulation produced by the e423 vanes led to a slight increase in pressure loss as shown in Fig. 7-13. The pressure loss was about 0.006% higher for e423 vanes when compared to rectangular vanes and the losses were nearly constant between 3 to 5 vanes. Furthermore, the pressure losses from the e423 vanes were less than if the rectangular vane height was increased from 0.8δ to 1.3043δ to obtain an increase of boundary layer transfer. These results demonstrate that using alternative vane shapes, specifically e423 vanes, can potentially increase the effectiveness of VG in transferring momentum in the boundary layer while reducing pressure losses.

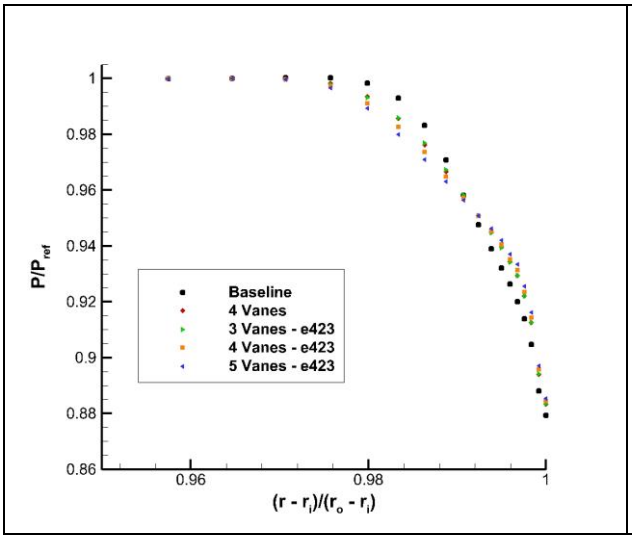

Figure 7-12: Boundary profile for e423 Vane

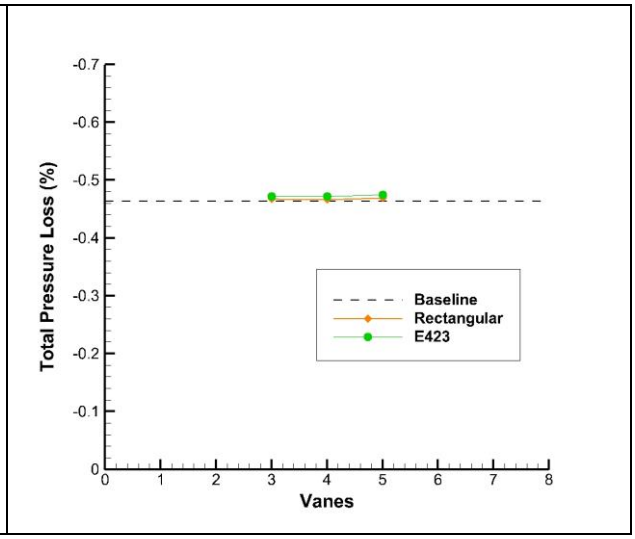

Figure 7-13: Pressure Loss for e423 vane

7.4 MVG Effect on Rotating Stall

To determine the effect that the VG configurations that were investigated in the previous section has controlling instabilities in the compressor, a selection was made on the best configuration to accomplish this task. Although it was desirable to test many different configurations to determine their effectiveness in extending the operating range of the compressor, finite computational resources limit the number of configurations that could be tested. A VG array of 5 vanes per 24˚ arc with a height of 1.3043δ was chosen. Future work should consider vane heights of 0.8δ along with counter-rotating vanes and co-rotating e423 vanes which demonstrate the potential to be as effective as the chosen configuration.

The numerical setup for modelling the CC3 compressor with a vaned diffuser and implementation of VG was similar to the model used in the previous chapter to investigated rotating stall. The generated

mesh size was slightly increased in the inlet and impeller to better resolve the VG vanes and the vortices. The mesh resolution was also increased to improve the interpolation of the flow across the sliding interface separating the stationary inlet domain and the rotating impeller domain. View of the VG implemented in the inlet of the CC3 compressor is shown in Fig. 7-14.

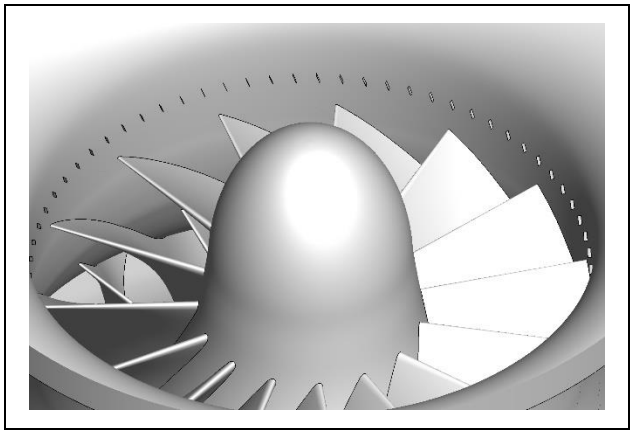

Figure 7-14: VG inside the NASA CC3

The total pressure and adiabatic efficiency is plotted in Figs. 7-15 and 7-16, respectively. As with the baseline compressor with a vaned diffuser, total pressure ratio and adiabatic efficiency is over predicted in comparison to published experimental results. However, the results demonstrate the extension of the operating range by the use of VG implemented in the inlet of the compressor.

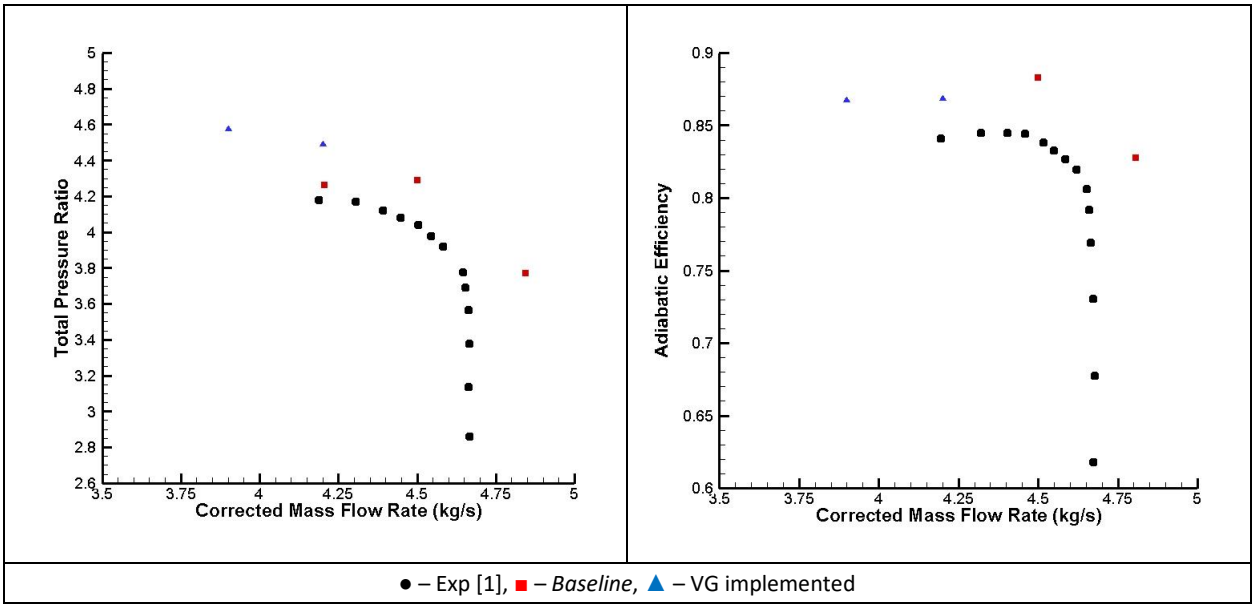

Figure 7-15: VG effect on pressure curve

Figure 7-16: VG effect on efficiency curve

The pressure contours at 70% span from the hub is shown in Fig. 7-17. The pressure contours are extracted from the instantaneous flow at operating mass flow rate of 3.9 kg/s. In contrast to the pressure

contours of Fig. 6-16 and in section 6.4.2 when rotating stall was observed, the pressure in the compressor is very uniformed.

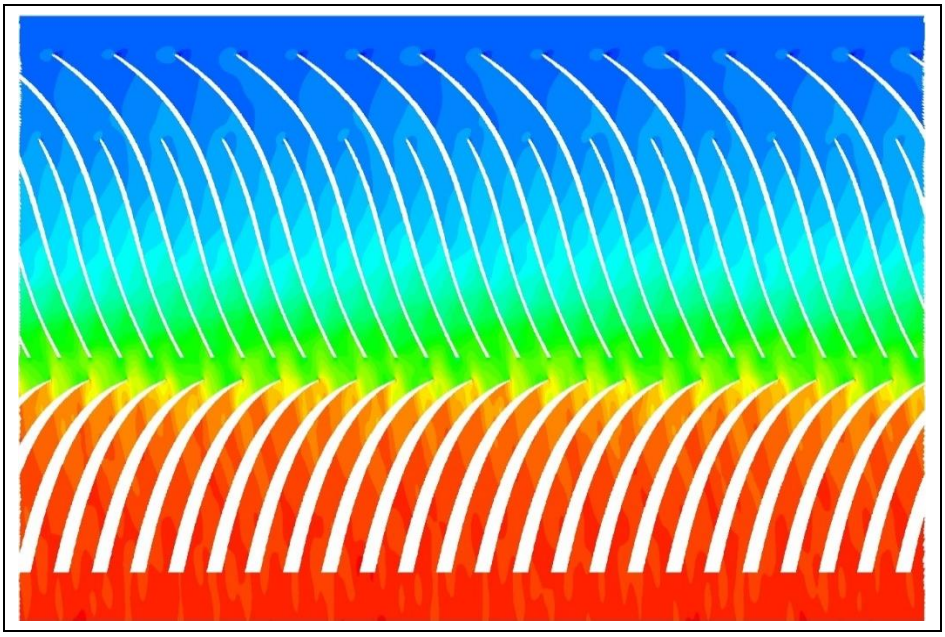

Figure 7-17: Pressure distribution at 70% span

7.5 Conclusion

The NASA CC3 compressor that was modelled in Chapter 6 was re-modelled with vortex generators applied to the inlet. In the section 7.3, simplifications were made to the compressor by removing the impeller blades for a single passageway to allow for an optimization study of the VG to be conducted. The optimization study looked at co-rotating rectangular vanes with heights between 0.6443δ and 1.9364δ, counter-rotating vane pairs, and co-rotating e423 vanes with a height of 0.8δ. Co-rotating rectangular vanes with a height of 1.3043δ and 5 vanes per 24˚ inlet arc were chosen. However, co-rotating rectangular vanes with a height of 0.8δ, two counter-rotating vane pairs, and co-rotating e423 vanes were found to be potentially as effective.

From the optimization study, the chosen VG configuration was tested with the full compressor at operating condition and where rotating stall was present. Initial results indicate that placing vortex generators in the inlet suppresses rotating stall.

8. Summary and Conclusions

8.1 Summary

The research presented in this thesis sought to implement vortex generators into the inlet of a high-speed centrifugal compressor to increase its operating range and to suppress instabilities in the compressor. To achieve the goals of this project, a new compressible flow algorithm was written in the open source code *Code_Saturne* by the author in order to model the compressible flow in rotating reference frame. The new algorithm used the SIMPLEC method for the compressible Navier-Stokes equations. An AUSM^{+}-up scheme was implemented into the algorithm to discretize the mass flow rate and convective terms of the pressure correction equation. To increase the order of accuracy of the algorithm, a 2nd-order MUSCL scheme was also implemented. These improvements to the *Code_Saturne* are detailed in Chapter 2 along with an algorithm to recycle a turbulent inflow for large-eddy simulation of a turbulent flow on a flat plate. The new compressible flow algorithm was tested and validated with a shock tube problem, inviscid channel flow with a bump, RAE2822 airfoil, Sajben diffuser, and NASA LSCC. The latter three cases used the k-ω SST and Spalart-Allmaras models with a wall function to model the turbulence. For the shock tube problem and inviscid channel flow, the algorithm gave a good prediction of the flow. For the more complex cases of the RAE2822 airfoil and Sajben diffuser, the algorithm gave reasonable prediction of the flow field, however the wall needed to be resolved to give an accurate prediction of the shock/boundary-layer interaction. In the final case, the NASA low-speed centrifugal compressor was modelled and the new algorithm predicted a flow field that matched reasonably well to published experimental results and to a corresponding model made with Fluent.

With a construction of an algorithm to model the flow of a high-speed compressor, attention was given to the flow dynamics of a MVG and the optimum configuration for a MVG. These studies were conducted in a turbulent boundary layer on a flat plate with a zero-pressure gradient. Initial work found a MVG and its vortex was fairly insensitive to the mesh resolution and compared very well to published experimental results. Experimental wind tunnel tests were also conducted to validate RANS ability to accurately predict the drag of a MVG. Further work used LES to simulate three different MVG shapes and angles in a turbulent boundary layer on a flat plate. Among the findings of the simulations, the vortices were found to decay the quickest at a distance of x/h = 2 to 10 and the instantaneous path of the vortices were greatly dictated by the turbulence of the boundary layer. Comparing RANS to the time-averaged LES results, RANS over predicted the circulation and the vorticity which is contrary to the comparison made

to published experimental results. Although the comparison made with published experimental results was conducted at a high Reynolds number (Re = 16533 or h^+ = 607), the comparison made with the LES results was conducted at a very low Reynolds number (Re = 2900 or h^+ = 125). It is concluded that the accuracy of RANS modelling of a MVG breaks down at low Reynolds numbers.

To complete the study of MVG on a flat plate, an optimization study was conducted with several different vane shapes and angles considered. The effectiveness of the MVG vane was measured by the ratio of the downstream circulation per drag of the vane. Triangular vanes were found to be the most effective however their vortices were weak compared to other tested vanes. Vanes in the form of the NACA0012 followed by the e423/e423-mod vanes had slightly inferior circulation per drag, but had much stronger vortices. The effectiveness of traditional rectangular vanes was diminished by flow separation on the leading edge of the vane. In regards to the vane angle, 18˚/20˚ was found to be the optimum. The circulation to drag ratio was limited by the induced drag of the vortex which led to the conclusion that the vanes producing the weakest vortex were the most efficient but this had to be balanced with the required strength of the vortex to affect the downstream flow. Further work looked into the effect that the Reynolds number, the thickness of the vane, and the height of the vane had on the generated vortex. The circulation and drag of the vane was found to have a logarithmic relation with the device's Reynolds number. The vane thickness of h/14 and h/28 produced the best vortices, but variations between the vane thicknesses were small. Finally, the vortices from vanes with a variety of heights were found to behave similarly when the spatial distances were non-dimensionalized with the vane's height. This however translates in the smaller vane's vortex to decay faster than a larger vane's vortex. If the actual distances are considered, vanes with the height of 0.2δ and 0.3δ had the best circulation to drag ratio.

To offer further insight into the dynamics of a MVG and apply the lessons learned in studying a MVG on a flat plate, a MVG was applied to an e387 airfoil that was suffering flow separation. The MVG was found to have an effect on the skin friction of up to 40h behind the vane while the circulation of the vortex was measurable up to 30h behind the vane. The vortex was observed to have the strongest influence on the wall from 5h to 10h behind the vane. Conforming to the findings of a MVG on a flat plate, the optimum vane angle was found to be at 18.5˚, although the MVG placed at 14˚ was found to cause the best improvement in lift-to-drag ratio.

Attention was returned to modelling a high-speed centrifugal compressor, the NASA CC3 compressor with a vaned and vaneless diffuser, with the new compressible flow algorithm written in *Code_Saturne*. A single passageway of the impeller was matched with a vaneless diffuser and was

modelled from near choke to near stall. The pressure curve and adiabatic efficiency curve were compared to published experimental results and results from ANSYS Fluent. The new algorithm gave very good results for the total pressure ratio, but over predicted the adiabatic efficiency by about 2%. However, ANSYS Fluent over predicted the adiabatic efficiency by about 2% too with the same mesh. Focus was turned to modelling the complete compressor with a vaned diffuser. The compressor was modelled at three points in the operating range of the compressor and the compressible flow algorithm was found to under predict the total pressure ratio of the compressor. The mass flow rate of the compressor was reduced below the stall line to induce rotating stall. Four stall cells were observed in the impeller and the diffuser; the rotating stall cells in the impeller were measured to rotate at 0.0587 times the rotational speed of the impeller. In the analysis of rotating stall in the compressor, pressure perturbations were observed emanating from stalled vane diffuser passages and propagate upstream into the impeller. The pressure perturbations negatively affect the incoming flow into the impeller causing a formation of a separation bubble on the leading edge of the blade. To accommodate the separation bubble, the flow accelerates. A packet of high momentum flow detaches as the impeller passage moves out of rotating stall. The packet of high momentum flow travels downstream until it reaches the diffuser, suppressing stall in the diffuser passages the packet interacts with. It is still under investigation whether rotating stall in the impeller or diffuser controls the flow structure of the compressor at rotating stall.

With rotating stall observed in the compressor, an optimization study of vortex generators was conducted on a simplified model. In the optimization study, co-rotating rectangular vanes with a height of 1.3043δ and 5 vanes per 24˚ inlet arc were chosen. However, co-rotating rectangular vanes with a height of 0.8δ, two counter-rotating vane pairs, and co-rotating e423 vanes were found to be potentially as effective. The chosen vortex generator configuration was implemented in the full compressor at an operating condition where rotating stall was present. Initial results indicate that placing vortex generators in the inlet of centrifugal compressor suppresses rotating stall.

8.2 Future Work

For future work, there are number of areas that need to be considered further that this thesis was unable to answer within its limits. Although the new compressible flow algorithm written in *Code_Saturne* was found to be adequate to modelling compressible flow in a compressor and variety of other applications, there are some shortcomings that need to be address. In the modelling of a compressor,

the pressure and velocity fields became decoupled if there was a poor guess for the initial flow field or the CFL number was pressed above 3. Further work needs to be done in the algorithm to make a stronger coupling between the pressure and velocity fields in a segregated algorithm or the implementation of a fully-coupled algorithm. This may alleviate the dependency of the algorithm on the CFL number to a greater degree. Going deeper into the algorithm of *Code_Saturne* that was not touched in this thesis is the efficiency of the linear solvers and the gradient reconstruction. Both processes took majority of the processing time per time step and any reduction in either process will greatly reduce the computation time. Furthermore, there is a least-squares gradient reconstruction in *Code_Saturne* that is up to 40% cheaper than the iterative gradient reconstruction which was primarily used, but the least-squares gradient reconstruction was found to be very sensitive to skewed mesh. A potential solution is to the increase the robustness of the least-squares method and the order of accuracy on a skewed mesh to make this method an alternative to the iterative gradient reconstruction used. The second issue found with the new compressible flow algorithm in *Code_Saturne* was the turbulence models. In the validation studies in Chapter 3, the turbulence model was observed to slightly over predict the turbulence of the flow. The turbulence models used were adapted from the incompressible flow algorithm and further validation work should to be conducted to assess their suitability for a highly compressible flow. The accuracy of the wall function used for the turbulence models should also to be assessed for compressible flows. All of the work that was conducted was with the wall unresolved, a future modelling should be conducted with a wall resolved mesh to study any improvement in the flow predictions.

The high-fidelity simulations of MVG in Chapters 4 and 5 offered useful insight into the flow dynamics of MVG, however there were some shortcomings. In section 4.4.1, RANS greatly overestimated the circulation and vorticity when compared to LES at the Reynolds number of 2,900. It is not known for certain whether this problem is due to the inability of RANS to model the flow at such a low Reynolds numbers. It would be desirable to observe whether the discrepancy between LES and RANS exists at higher Reynolds numbers. In the simulation of the e387 airfoil and MVG on the airfoil, the discrepancy was reversed and RANS underestimated the strength of the vortex. It would be noteworthy to see if different RANS models yield better results than the k-ω SST model, particularly transitional models that can better predict the upstream flow. Work should also be explored on the effect that the domain size has on the results.

Although the current modelling of a high-speed centrifugal compressor and rotating stall was satisfactory, a number of points should be addressed with future work. The most outstanding point is the

insufficient resources committed to the baseline case and the case with VG at rotating stall. More computational time needs to be committed in order to obtain a better understanding of rotating stall and to ensure that the VG implemented suppresses rotating stall instead of merely postponing it. Furthermore, in addition to the changes suggested above to providing a more efficient solver, a wall resolved solution should be sought. Resolving the wall would provide a better prediction of the losses in the compressor and simulation of rotating stall. The ultimate goal is to use LES with or without a wall function to simulate the dynamic flow of a compressor. Although a wall resolved solution with LES would require an extreme amount of computational resources (on the order of 0.5 to 1 billion cells), a wall resolved solution with RANS or LES with a wall function to simulate a complete compressor is reachable. On the implementation of vortex generators in a centrifugal compressor, it was demonstrated that vanes with smaller heights, counter-rotating vane pairs, and non-rectangular vanes had the potential to affect the downstream flow as much as the tested VG configuration. Future studies should look at whether these alternative configurations are more effective than the implemented configuration. Ultimately, experimental testing needs to be conducted to validate whether the improvements in the computational results are accurate.

Appendix A

Spalart-Spur Rotation/Curvature Correction for k-ω SST Model

As discussed in Section 2.2.4.3, the rotation/curvature correction used for the k-ω SST model was rewritten in *Code_Saturne* to exactly replicate the correction given by Smirnov and Menter [75]. The original correction for the k-ω SST model was found overproduce turbulence in a boundary layer of a rotating flow; the revised correction fixes this problem.

To validate the revised correction, the numerical experiment of Kristoffersen and Anderrson [119] was replicated. Kristoffersen and Anderrson conducted a DNS simulation of rotating channel flow, the numerical setup of the simulation is given in Fig. A-1. The Reynolds number of 5800 was based on the bulk velocity and the channel width was imposed; the Rossby number of the rotation flow was tested from 0 to 0.5. The generated mesh used for the validation study had 128x81 nodes in the streamwise and vertical directions, respectively. The wall boundary layer was resolved with a y^+ of less than 1. The flow was model with the incompressible module of *Code_Saturne* with the original and revised rotation/curvature correction for the k-ω SST model. To give a comparison to the results of *Code_Saturne*, Fluent was used with similar numerical setup.

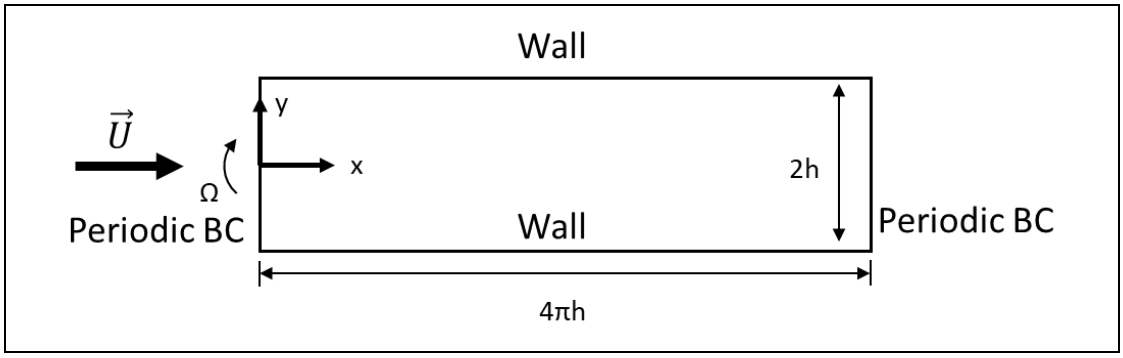

Figure A-1: Computational domain for rotating flow

The velocity and turbulent viscosity profiles of the channel flow are plotted in Fig. A-2 and A-3, respectively. The velocity profiles in Fig. A-2 are plotted for Rossby numbers of 0, 0. 5, 0.1, 0.2, and 0.5. With no rotation in the flow, both versions of the correction and Fluent matches the DNS data perfectly. As the rotational speed of the channel was increased, the profiles of the old correction and the revised correction diverge. The velocity profile from the old correction matches the DNS data marginally better, however there is good agreement between the revised correction and Fluent. Testing was done with other turbulence models (v2-f, k-ε, and Spalart-Allmaras) using other rotation/curvature corrections and similar

discrepancy to that of the revised correction were found. The turbulent viscosity profiles in Fig. A-3 are plotted for Rossby numbers of 0.1 and 0.5. At Ro=0.1, the old correction greatly overpredicted the turbulent viscosity when compared to the revised correction. At Ro=0.5, the old correction continued to overpredict the turbulent viscosity but to lesser degree in comparison to the revised correction.

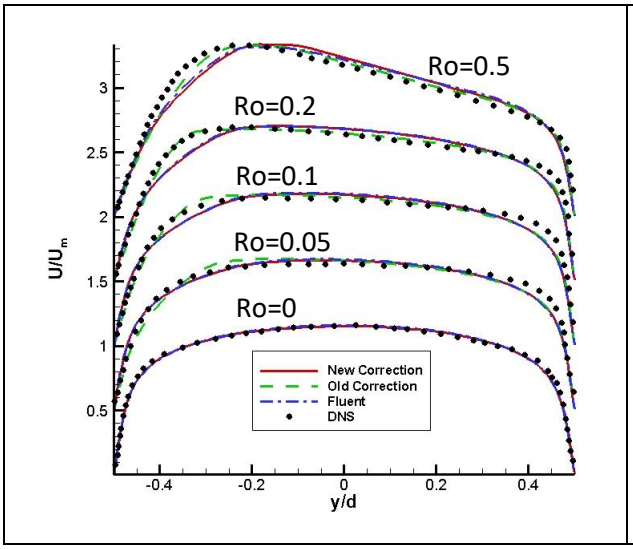

Figure A-2: Velocity profiles

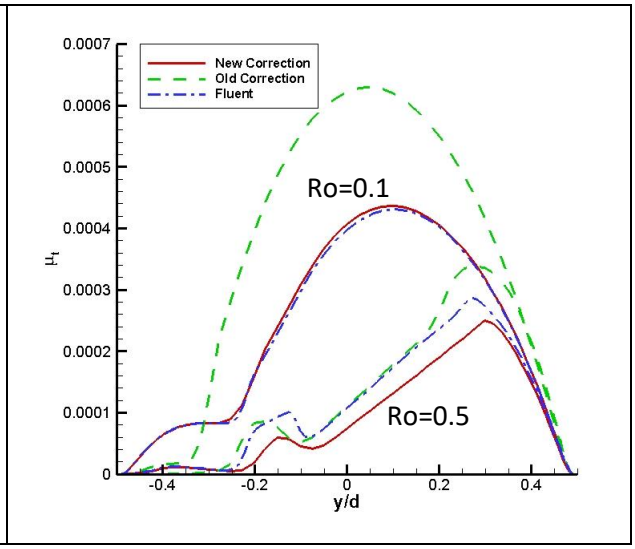

Figure A-3: Turbulent viscosity profiles

The revised rotation/curvature correction for the k-ω SST model limits the turbulent production in a rotating flow in comparison to the old correction. For the test case of a rotating channel flow, the old correction did a slightly better job of predicting the velocity profile than the revised correction. Due to the inherit limits of RANS modelling, the predicted rotating channel flow doesn't exactly match the DNS data of Kristoffersen and Anderrson, but the revised rotation/curvature correction achieves the objective of limiting turbulence production in a rotation flow.

9. References

[1] G. J. Skoch, P. S. Prahst, M. P. Wernet, J. R. Wood, and A. J. Strazisar, "Laser Anemometer Measurements of the Flow Field in a 4:1 Pressure Ratio Centrifugal Impeller," NASA and U.S. ARL1997.

[2] P. Frigne and R. Van Den Braembussche, "Distinction Between Different Types of Impeller and Diffuser Rotating Stall in a Centrifugal Compressor With Vaneless Diffuser," *Journal of Engineering for Gas Turbines and Power,* vol. 106, no. 2, pp. 468-474, 1984.

[3] I. J. Day, "Stall Inception in Axial Flow Compressors," *Journal of Turbomachinery,* vol. 115, no. 1, pp. 1-9, 1993.

[4] B. d. Jager, "Rotating stall and surge control: a survey," in *Proceedings of 1995 34th IEEE Conference on Decision and Control*, 1995, vol. 2, pp. 1857-1862 vol.2.

[5] N. M. McDougall, N. A. Cumpsty, and T. P. Hynes, "Stall Inception in Axial Compressors," *Journal of Turbomachinery,* vol. 112, no. 1, pp. 116-123, 1990.

[6] T. R. Camp and I. J. Day, "A Study of Spike and Modal Stall Phenomena in a Low-Speed Axial Compressor," no. 78682, p. V001T03A109, 1997.

[7] Z. S. Spakovszky and C. H. Roduner, "Spike and Modal Stall Inception in an Advanced Turbocharger Centrifugal Compressor," *Journal of Turbomachinery,* vol. 131, no. 3, pp. 031012-031012-9, 2009.

[8] J. N. Everitt and Z. S. Spakovszky, "An Investigation of Stall Inception in Centrifugal Compressor Vaned Diffuser," *Journal of Turbomachinery,* vol. 135, no. 1, pp. 011025-011025-10, 2012.

[9] M. W. Müller, H. P. Schiffer, M. Voges, and C. Hah, "Investigation of Passage Flow Features in a Transonic Compressor Rotor With Casing Treatments," no. 54679, pp. 65-75, 2011.

[10] C. Hah, "Steady and Unsteady Flow Effects of Circumferential Grooves Casing Treatment in a Transonic Compressor Rotor," presented at the International Gas Turbine Congress 2011, Osaka, 2011.

[11] W. Jansen, A. F. Carter, and M. C. Swarden, "Improvements in Surge Margin for Centrifugal Compressors," in *Centrifugal Compressors, Flow Phenomena and Performance*no. AGARD–CP–282): Advisory Group for Aerospace Research and Development, 1980.

[12] H. D. Taylor, "The elimination of diffuser separation by vortex generators," United Aircraft Corporation1947.

[13] L. J. Lina and W. H. Reed, "A Preliminary Flight Investigation of the Effects of Vortex Generators on Separation Due to Shock," Langley Aeronautical Laboratory, Washington1950.

[14] D. Rao and T. Kariya, "Boundary-layer submerged vortex generators for separation control - An exploratory study," in *1st National Fluid Dynamics Conference*(Fluid Dynamics and Co-located Conferences: American Institute of Aeronautics and Astronautics, 1988.

[15] J. Lin, F. Howard, and G. Selby, "Turbulent flow separation control through passive techniques," in *2nd Shear Flow Conference*(Shear Flow Conference: American Institute of Aeronautics and Astronautics, 1989.

[16] J. C. Lin, "Control of Turbulent Boundary-Layer Separation using Micro-Vortex Generators," presented at the 30th AIAA Fluid Dynamics Conference, Norfolk, 1999.

[17] J. Lin, F. Howard, D. Bushnell, and G. Selby, "Investigation of several passive and active methods for turbulent flow separation control," in *21st Fluid Dynamics, Plasma Dynamics and Lasers Conference*(Fluid Dynamics and Co-located Conferences: American Institute of Aeronautics and Astronautics, 1990.

[18] E. Canepa, D. Lengani, F. Satta, E. Spano, M. Ubaldi, and P. Zunino, "Boundary Layer Separation Control on a Flat Plate With Adverse Pressure Gradients Using Vortex Generators," no. 4238X, pp. 1211-1220, 2006.
[19] J. C. Lin, F. G. Howard, and G. V. Selby, "Small Submerged Vortex Generators for Turbulent Flow Separation Control," *Journal of Spacecraft and Rockets,* vol. 27, no. 5, pp. 503-507, 1990.
[20] J. Lin, F. Howard, and G. Selby, "Exploratory study of vortex-generating devices for turbulent flow separation control," in *29th Aerospace Sciences Meeting*(Aerospace Sciences Meetings: American Institute of Aeronautics and Astronautics, 1991.
[21] P. R. Ashill, J. L. Fulker, and K. C. Hackett, "Research at DERA on Sub Boundary Layer Vortex Generators (SBVGs)," presented at the 39th Aerospace Sciences Meeting and Exhibit, Reno, 2001.
[22] P. R. Ashill, J. L. Fulker, and K. C. Hackett, "Studies of Flows Induced by Sub Boundary Layer Vortex Generators (SBVGs)," presented at the 40th AIAA Aerospace Sciences Meeting & Exhibit, Reno, NV, 2002.
[23] J. C. Lin, S. K. Robinson, R. J. McGhee, and W. O. Valarezo, "Separation control on high-lift airfoils via micro-vortex generators," *Journal of Aircraft,* vol. 31, no. 6, pp. 1317-1323, 1994/11/01 1994.
[24] G. Godard and N. Stanislas, "Control of a decelerating boundary layer. Part 1: Optimization of passive vortex generators " *Aerospace Science and Technology,* vol. 10, no. 3, pp. 181-191, 2006.
[25] W. R. Pauley and J. K. Eaton, "Experimental study of the development of longitudinal vortex pairs embedded in a turbulent boundary layer," *AIAA Journal,* vol. 26, no. 7, pp. 816-823, 1988/07/01 1988.
[26] R. D. Mehta, I. M. M. A. Shabaka, A. Shibl, and P. Bradshaw, "Longitudinal Vortices Imbedded in Turbulent Boundary Layers," presented at the AIAA 21st Aerospace Sciences Meeting, Reno, NV, 1983.
[27] I. M. M. A. Shabaka, "Longitudinal vortices imbedded in turbulent boundary layers. Part 1. Single vortex," *Journal of Fluid Mechanics,* Article vol. 155, pp. 37-57, 1985.
[28] J. Liu, U. Piomelli, and P. Spalart, "Interaction between a spatially growing turbulent boundary layer and embedded streamwise vortices " *Journal of Fluid Mechanics,* vol. 326, pp. 151-179, 1996.
[29] C.-S. Yao, J. C. Lin, and B. G. Allan, "Flow-Field Measurement of Device-Induced Embedded Streamwise Vortex on a Flat Plate," presented at the 1st AIAA Flow Control Conference, St. Louis, MO, 2002.
[30] K. P. Angele and F. Grewe, "Instantaneous Behavior of Streamwise Vortices for Turbulent Boundary Layer Separation Control," *Journal of Fluids Engineering,* vol. 129, no. 2, pp. 226-235, 2006.
[31] R. D. Mehta, "Longitudinal vortices imbedded in turbulent boundary layers part 2. vortex pair with common flow' upwards," *Journal of Fluid Mechanics,* Article vol. 188, pp. 529-546, 1988.
[32] E. E. Bender, B. H. Anderson, and P. J. Yagle, "Vortex Generator Modelling for Navier–Stokes Codes," *ASME Paper No. FEDSM99-6929,* 1999.
[33] A. Jirasek, "Vortex-Generator Model and Its Application to Flow Control," *Journal of Aircraft,* vol. 42, no. 6, pp. 1486-1491, 2005.
[34] F. Wallin and L.-E. Eriksson, "A Tuning-free Body-Force Vortex Generator Model," in *44th AIAA Aerospace Sciences Meeting and Exhibit*(Aerospace Sciences Meetings: American Institute of Aeronautics and Astronautics, 2006.
[35] B. G. Allan, C.-S. Yao, and J. C. Lin, "Numerical Simulation of Vortex Generator Vanes and Jets on a Flat Plate," presented at the 1st Flow Control Conference, St. Louis, MO, 2002.

[36] E. Wik and S. T. Shaw, "Numerical Simulation of Micro Vortex Generators," presented at the 2nd AIAA Flow Control Conference, Portland, OR, 2004.
[37] M. Manolesos, G. Papadakis and S. Voutsinas, "Assessment of the CFD capabilities to predict aerodynamic flows in presence of VG arrays," *Journal of Physics: Conference Series,* vol. 524, no. 1, 2014.
[38] L. Florentie, A. H. van Zuijlen, S. J. Hulshoff, and H. Bijl, "Effectiveness of Side Force Models for Flow Simulations Downstream of Vortex Generators," *AIAA Journal,* pp. 1-12, 2016.
[39] L. R. Owens, B. G. Allan, and S. A. Gorton, "Boundary-Layer-Ingesting Inlet Flow Control," *Journal of Aircraft,* vol. 45, no. 4, pp. 1431-1440, 2008.
[40] Y. Zhang, S. Hu, X.-F. Zhang, M. Benner, A. Mahallati, and E. Vlasic, "Flow Control in an Aggressive Interturbine Transition Duct Using Low Profile Vortex Generators," *Journal of Engineering for Gas Turbines and Power,* vol. 136, no. 11, pp. 112604-112604-8, 2014.
[41] G. A. Mitchell, "Experimental Investigation of the Performance of Vortex Generators Mounted in the Supersonic Portion of a Mixed-Compression Inlet," NASA, Washington, D.C.1971.
[42] M. Vyas, S. Hirt, R. Chima, D. Davis, and T. Wayman, "Experimental Investigation of Micro Vortex Generators on a Low Boom Supersonic Inlet (Invited)," in *29th AIAA Applied Aerodynamics Conference*(Fluid Dynamics and Co-located Conferences: American Institute of Aeronautics and Astronautics, 2011.
[43] S. Tournier, J. Paduano, and D. Pagan, "Flow Analysis and Control in a Transonic Inlet," in *23rd AIAA Applied Aerodynamics Conference*(Fluid Dynamics and Co-located Conferences: American Institute of Aeronautics and Astronautics, 2005.
[44] A. Hergt, R. Meyer, M. W. Müller, and K. Engel, "Loss Reduction in Compressor Cascades by Means of Passive Flow Control," no. 43161, pp. 269-280, 2008.
[45] A. Hergt, R. Meyer, and K. Engel, "Effects of Vortex Generator Application on the Performance of a Compressor Cascade," *Journal of Turbomachinery,* vol. 135, no. 2, pp. 021026-021026-10, 2012.
[46] C. H. Law, A. J. Wennerstrom, and W. A. Buzzell, "The Use of Vortex Generators as Inexpensive Compressor Casing Treatment," 1976.
[47] R. V. Chima, "Computational Modeling of Vortex Generators for Turbomachinery," no. 3610X, pp. 1229-1238, 2002.
[48] R. A. Gomes and R. Niehuis, "Aerothermodynamics of a High-Pressure Turbine Blade With Very High Loading and Vortex Generators," *Journal of Turbomachinery,* vol. 134, no. 1, 2011.
[49] T. F. McKain and G. J. Holbrook, "Coordinates for a High Performance 4:1 Pressure Ratio Centrifugal Compressor," NASA, Lewis Research Center 1997.
[50] G. J. Skoch, "Experimental Investigation of Centrifugal Compressor Stabilization Techniques," NASA, Washington, D.C.2003.
[51] G. J. Skoch, "Experimental Investigation of Diffuser Hub Injection to Improve Centrifugal Compressor Stability," NASA, Washington, D.C. 2004.
[52] Z. S. Spakovszky, "Backward Traveling Rotating Stall Waves in Centrifugal Compressors," *Journal of Turbomachinery,* vol. 126, no. 1, pp. 1-12, 2004.
[53] T. Halawa, M. Alqaradawi, O. Badr, and M. S. Gadala, "Numerical Simulation of Stall Development Into Surge and Stall Control Using Air Injection in Centrifugal Compressors," no. 46094, p. V002T11A003, 2014.
[54] T. Halawa, M. S. Gadala, M. Alqaradawi, and O. Badr, "Optimization of the Efficiency of Stall Control Using Air Injection for Centrifugal Compressors," *Journal of Engineering for Gas Turbines and Power,* vol. 137, no. 7, pp. 072604-072604-10, 2015.
[55] A. Stein, S. Niazi, and L. N. Sankar, "Computational Analysis of Stall and Separation Control in Centrifugal Compressors," *Journal of Propulsion and Power,* vol. 16, no. 1, pp. 65-71, 2000.

[56] Y. Fournier, J. Bonelle, C. Moulinec, Z. Shang, A. G. Sunderland, and J. C. Uribe, "Optimizing Code_Saturne computations on Petascale systems," *Computers & Fluids,* vol. 45, no. 1, pp. 103-108, 2011.
[57] "Code_Saturne 4.0.0 Theory Guide," 2015.
[58] *Code_Saturne*. Available: www.code-saturne.org/cms/
[59] "ANSYS Fluent User's Guide," ANSYS, Inc 2011.
[60] F. M. White, *Viscous Fluid Flow*, 3rd ed. McGraw-Hill Education, 2006.
[61] H. Tennekes and J. L. Lumley, *A First Course in Turbulence*. The MIT Press, 1972.
[62] H. Schlichting and K. Gersten, *Boundary-Layer Theory*, 8th ed. Springer, 2000.
[63] R. S. Rogallo and P. Moin, "Numerical Simulation of Turbulent Flows," *Annual Review of Fluid Mechanics,* vol. 16, pp. 99-137, 1984.
[64] D. R. Chapman, "Computational aerodynamics development and outlook," *AIAA,* vol. 17, no. 12, pp. 1293-1313, 1979.
[65] J. Smagorinsky, "General Circulation Experiments with the Primitive Equations I. The Basic Experiment," Washington, DC 1963.
[66] M. Germano, U. Piomelli, P. Moin, and W. H. Cabot, "Dynamic Subgrid-Scale Eddy Viscosity Model," *Physics of Fluids A,* vol. 3, no. 7, pp. 1760-1765, 1991.
[67] F. Nicoud and F. Ducros, "Subgrid-Scale Stress Modelling Based on the Square of the Velocity Gradient Tensor," *Flow, Turbulence and Combustion,* vol. 62, no. 3, pp. 183-200, 1999.
[68] P. Spalart and S. Allmaras, "A one-equation turbulence model for aerodynamic flows," in *30th Aerospace Sciences Meeting and Exhibit*, Reno, NV, 1992: AIAA.
[69] B. E. Launder and D. B. Spalding, *Lectures in mathematical models of turbulence*. London; New York: Academic Press, 1972.
[70] F. R. Menter, "Two-Equation Eddy-Viscosity Turbulence Models for Engineering Applications," *AIAA,* vol. 32, no. 8, pp. 1598-1605, 1994.
[71] D. C. Wilcox, "Multiscale Model for Turbulent Flows," *AIAA,* vol. 26, no. 11, pp. 1311-1320, 1988.
[72] F. R. Menter, "Improved Two-Equation k-omega Turbulence Models for Aerodynamic Flows," 1992.
[73] F. R. Menter, M. Kuntz, and R. Langtry, "Ten Years of Industrial Experience with the SST Turbulence Model," *Turbulence, Heat and Mass Transfer 4,* pp. 625-632, 2003.
[74] P. R. Spalart and M. L. Shur, "On the Sensitization of Turbulence Models to Rotation and Curvature," *Aerospace Science and Technology,* vol. 1, no. 5, pp. 297-302, 1997.
[75] P. E. Smirnov and F. R. Menter, "Sensitization of the SST Turbulence Model to Rotating and Curvature by Applying the Spalart-Shur Correction Term," *ASME Journal of Turbomachinery,* vol. 131, 2009.
[76] B. Van Leer, "Towards the ultimate conservative difference scheme. V. A second-order sequel to Godunov's method," *Journal of Computational Physics,* vol. 32, no. 1, pp. 101-136, 1979.
[77] A. Harten, "High Resolution Schemes for Hyperbolic Conservation Laws," *Journal of Computational Physics,* vol. 49, no. 3, pp. 357-393, 1983.
[78] P. K. Sweby, "High Resolution Schemes Using Flux Limiters for Hyperbolic Conservation Laws," *SIAM Journal on Numerical Analysis,* vol. 21, no. 5, pp. 995-1011, 1984.
[79] P. L. Roe, "Characteristic-based schemes for the Euler equations," *Annual Review of Fluid Mechanics,* vol. 18, pp. 337-365, 1986.
[80] G. D. Van Albada, B. Van Leer, and W. W. Robers, "A comparative study of computational methods in cosmic gas dynamics," *Astronomy and Astrophysics,* vol. 108, no. 1, pp. 76-84, 1982.
[81] T. J. Barth and D. C. Jespersen, "The design and application of upwind schemes on unstructured meshes," in *27th Aerospace Sciences Meeting*, Reno, NV, 1989: AIAA.

[82] S. Spekreijse, "Multigrid Solution of Monotone, Second Order Discretization of Hyperbolic Conservation Laws," *Mathematics of Computation,* vol. 49, no. 179, pp. 135-155, 1987.
[83] C. Bruner and R. Walters, "Parallelization of the Euler equations on unstructured grids," in *13th Computational Fluid Dynamics Conference*, Snowmass Village, CO, 1995: AIAA.
[84] M. S. Darwish and F. Moukalled, "TVD Schemes for Unstructured Grids," *International Journal of Heat and Mass Transfer,* vol. 46, no. 4, pp. 599-611, 2003.
[85] M. Liou and C. Steffen, "A new flux splitting scheme," *Journal of Computational Physics,* vol. 107, pp. 23-39, 1993.
[86] M. Liou, "A Sequel to AUSM: AUSM$^+$" vol. 129, ed: Journal of Computational Physics, 1996, pp. 364-382.
[87] M. Liou, "A sequel to AUSM, Part II: AUSM$^+$-up for all speeds," *Journal of Computational Physics,* vol. 214, pp. 137-170, 2006.
[88] A. J. Chorin, "A Numerical Method for Solving Incompressible Viscous Flow Problems," *Journal of Computational Physics,* vol. 14, pp. 12-26, 1967.
[89] S. V. Patankar and D. B. Spalding, "A Calculation Procedure for Heat, Mass and Momentum Transfer in Three-Dimensional Parabolic Flow," *International Journal of Heat Mass Transfer,* vol. 15, pp. 1787-1806, 1972.
[90] C. M. Rhie and W. L. Chow, "Numerical Study of the Turbulent Flow Past an Airfoil with Trailing Edge Separation," *AIAA,* vol. 21, no. 11, pp. 1525-1532, 1983.
[91] F. Archambeau, J. Hérard, and J. Laviéville, "Comparative study of pressure-correction and Godunov-type schemes on unsteady compressible cases," vol. 38, ed: Computers & Fluids, 2009, pp. 1495-1509.
[92] C. M. Xisto, J. C. Páscoa, P. J. Oliveira, and D. A. Nicolini, "A hybrid pressure–density-based algorithm for the Euler equations at all Mach number regimes," *International Journal for Numerical Methods in Fluids,* vol. 70, no. 8, pp. 961-976, 2012.
[93] J. Tannehill, D. Anderson, and R. Pletcher, *Computational Fluid Mechanics and Heat Transfer*, 2nd ed. Taylor & Francis, 1997.
[94] B. Francois, M. Costes, and G. Dufour, "Comparison of Chimera and Sliding Mesh Techniques for Unsteady Simulations of Counter Rotating Open-Rotors," in *20th ISABE Conference*, Gothenburg, 2011: ISABE.
[95] E. Sergent, "Vers une méthodologie de couplage entre la simulation des grandes échelles et les modèles statistiques," 2002.
[96] A. Smirnov, S. Shi, and I. Celik, "Random Flow Generation Technique for Large Eddy Simulations and Particle-Dynamics Modeling," *Journal of Fluids Engineering,* vol. 123, no. 2, pp. 359-371, 2001.
[97] T. Lund, X. Wu, and K. Squires, "Generation of Turbulent Inflow Data for Spatially-Developing Boundary Layer Simulations," *Journal of Computational Physics,* vol. 140, pp. 233-258, 1998.
[98] E. Bohr, "Inflow Generation Technique for Large Eddy Simulation of Turbulent Boundary Layers," Rensselaer Polytechnic Insitute, Troy, 2005.
[99] G. A. Sod, "A Survey of Several Finite Difference Methods for Systems of Nonlinear Hyperbolic Conservation Laws," *Journal of Computational Physics,* vol. 27, no. 1, pp. 1-31, 1978.
[100] A. Rizzi and H. Viviand, "Numerical Methods for the Computation of Inviscid Transonic Flows with Shock Waves," in *Notes on Numerical Fluid Mechanics*, vol. 3, 1981.
[101] P. H. Cook, M. A. McDonald, and M. C. P. Firmin, "Aerofoil RAE 2822 - Pressure Distributions, and Boundary Layer and Wake Measurements," in *Experimental Data Base for Computer Program Assessment - Report of the Fluid Dynamics Panel Working Group 04*no. AGARD-AR-138): Advisory Group for Aerospace Research and Development, 1979, p. 624.

[102] J. T. Salmon, T. J. Bogar, and M. Sajben, "Laser Doppler Velocimeter Measurements in Unsteady, Separated, Transonic Diffuser Flows," *AIAA Journal,* vol. 21, no. 12, pp. 1690-1697, 1983.
[103] M. D. Hathaway, R. M. Chriss, A. J. Strazisar, and J. R. Wood, "Laser Anemometer Measurements of the 3-D Rotor Flowfield in the NASA Low-Speed Centrifugal Compressor," NASA 1995.
[104] J. R. Wood, P. W. Adam, and A. E. Buggele, "NASA Low-Speed Centrifugal Compressor for Fundamental Research," NASA 1983.
[105] P. P. Rautaheimo, E. J. Salminen, and T. L. Siikonen, "Numerical Simulation of the Flow in the NASA Low-Speed Centrifugal Compressor," *International Journal of Turbo and Jet Engines,* vol. 20, no. 2, pp. 155-170, 2003.
[106] J. Jeong and F. Hussain, "On the Identification of a Vortex," *Journal of Fluid Mechanics,* vol. 285, pp. 69-94, 1995.
[107] A. Kendall and M. Koochesfahani, "A Method for Estimating Wall Friction in Turbulent Boundary Layers," presented at the 25th AIAA Aerodynamic Measurement Technology and Ground Testing Conference, San Francisco, CA, 2006.
[108] V. C. Patel, "Calibration of the Preston Tube and Limitations on its use in Pressure Gradients," *Journal of Fluid Mechanics,* vol. 23, no. 1, pp. 185-208, 1965.
[109] J. H. Preston, "The Determination of Turbulent Skin Friction by Means of Pitot Tubes," *Journal of Royal Aeronautical Society,* vol. 58, no. 518, pp. 109-121, 1954.
[110] "Quality Assessment for Wind Tunnel Testing," AGARD, Neuilly Sur Seine, France 1994.
[111] P. R. Ashill, J. L. Fulker, and K. C. Hackett, "A Review of Recent Developments in Flow Control," *The Aeronautical Journal,* vol. 109, no. 1095, pp. 205-232, 2005.
[112] D. F. Volkers, "Preliminary Results of Windtunnel Measurements on Some Airfoil Sections at Reynolds Numbers between 0.6×10^5 and 5.0×10^5," Delft University of Technology, Delft, The Netherlands1977.
[113] R. J. McGhee, B. S. Walker, and B. F. Millibard, "Experimental Results for the Eppler 387 Airfoil at Low Reynolds Numbers in the Langley Low-Turbulence Pressure Tunnel," 1988.
[114] B. D. McGranahan and M. S. Selig, "Surface Oil Flow Measurements on Several Airfoils at Low Reynolds Numbers," presented at the AIAA Applied Aerodynamics Conference, Orlando, FL 2003.
[115] M. S. Selig and B. D. McGranahan, "Wind Tunnel Aerodynamic Tests of Six Airfoils for Use on Small Wind Turbines," 2004.
[116] G. J. Skoch, "Centrifugal Compressor Flow Range Extension Using Diffuser Flow Control," ed, 2000.
[117] M. P. Wernet, M. M. Bright, and G. J. Skoch, "An Investigation of Surge in a High-Speed Centrifugal Compressor Using Digital PIV," NASA, Glenn Research Center 2002.
[118] S. Kulkarni, T. S. Beach, and G. J. Skoch, "Computational Study of the CC3 Impeller and Vaneless Diffuser Experiment," NASA, Glenn Research Center 2013.
[119] R. Kristoffersen and H. I. Andersson, "Direct simulations of low-Reynolds-number turbulent flow in a rotating channel," *Journal of Fluid Mechanics,* vol. 256, pp. 163-197, 1993.